Investigation of Oxidation in Nonaqueous Lithium–Air Batteries

By
Jonathon R. Harding
M.S. Chemical Engineering Practice, Massachusetts Institute of Technology, June 2012
B.S. Chemical Engineering, North Carolina State University, December 2008

SUBMITTED TO THE DEPARTMENT OF CHEMICAL ENGINEERING IN PARTIAL
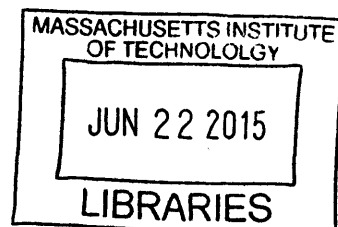FULLFILLMENT OF THE REQUIREMENTS FOR THE DEGREE OF

DOCTORATE OF PHILOSOPHY IN CHEMICAL ENGINEERING

AT THE

MASSACHUSETTS INSTITUTE OF TECHNOLOGY

JUNE 2015

Signature of Author: _ **Signature redacted**

Department of Chemical Engineering
May 1, 2015

Certified by: __ **Signature redacted**

Yang Shao-Horn
Professor of Mechanical Engineering
Thesis Supervisor

Certified by: ____ **Signature redacted**

Paula T. Hammond
Professor of Chemical Engineering
Thesis Supervisor

Accepted by: **Signature redacted**

Richard D. Braatz
Professor of Chemical Engineering
Chairman, Committee for Graduate Students

1

Investigation of Oxidation in Nonaqueous Lithium–Air Batteries

By

Jonathon R. Harding

Submitted to the Department of Chemical Engineering
on May 1, 2015, in Partial Fulfillment of the Requirement for the Degree of
Doctor of Philosophy in Chemical Engineering

Abstract

The demand for clean energy in portable applications is driving the development of high specific energy batteries, which will enable automobiles powered by electricity derived from renewable energy sources such as solar and wind. Lithium–air batteries are a promising avenue for advancing the energy storage capabilities beyond that of current lithium-ion technology. These batteries face a number of challenges which prevent their practical implementation in devices. This thesis explores possible mitigations for two of these challenges: (1) the high charging overpotential and (2) the volatility and poor oxygen conduction of liquid electrolytes in Li–air batteries.

In the first part, Vulcan carbon-based electrodes were developed where chemically-synthesized lithium peroxide was included during the electrode preparation process. Variants of these electrodes which further included noble metal catalyst nanoparticles (Au, Pt, and Ru) were also prepared, and Pt and Ru were both demonstrated to begin oxidizing Li_2O_2 500 mV lower than required for carbon-only or Au-containing electrodes. Using a differential electrochemical mass spectrometer (DEMS) designed and built over the course of this thesis, we showed that Ru-containing electrodes produce oxygen throughout the oxidation of Li_2O_2, while Pt generated both carbon dioxide and oxygen, indicative of electrolyte decomposition. These results served as a foundation for future efforts to develop solid catalysts for the oxidation of Li_2O_2 in Li–air batteries.

In the second part, Li–O_2 devices using a solid electrolyte based on poly(ethylene oxide) (PEO) were developed. The discharge performance at room temperature and 60 °C was characterized, with dramatically higher discharge capacity and rate capability achievable at the elevated temperature. DEMS was used to show that the gases evolved during charging in argon were sensitive to the temperature of charging, with additional carbon dioxide observed at and above 50 °C. Finally, the autoxidation of PEO at 60 °C in Li–O_2 environments was studied, where NMR and DEMS measurements showed that the rate of PEO autoxidation increases with increasing applied potential, and that this reaction has a significant impact after only one charging cycle, identifying another condition that must be met for stable and practical Li–air batteries.

Thesis Supervisor: Yang Shao-Horn
Title: Gail E. Kendall Chair in Mechanical Engineering

Thesis Supervisor: Paula T. Hammond
Title: David H. Koch (1962) Professor in Engineering

Acknowledgements

A very large number of people helped me with this thesis; without them, this work would never have been completed and I am deeply grateful for their support and guidance through the years.

First, I want to thank Profs. Yang Shao-Horn and Paula Hammond for their mentorship and support throughout my time at MIT. Yang's dedicated focus on me and my project throughout the years were critical in my development as a researcher, a professional, and a person. She provided the support and opportunity for me to learn an entirely new field and explore my own talents and skills. Her constant advocacy for and critiques of my research unquestionably made the work stronger. Paula's unwavering support and positive attitude were also essential for my success; I always appreciated the opportunities to get a new perspective on the direction of my work, and always appreciated the immensely positive attitude that she brings to everything she does.

I also want to thank my committee, Profs. Martin Bazant and William Green, who always provided good ideas and challenging perspectives during my too-infrequent committee meetings and whose teaching continued to aid me long after the final exam. I am also grateful to Claude Lupis and Bob Hanlon, my directors at practice school, who provided mentorship and leadership for all of us dropped into a new and challenging environment. I also appreciated the opportunity to teach 10.302 with Prof Alan Hatton, Prof. William Tisdale, and William Dalzell, and to my fellow TAs Tanya and Kunle. I thoroughly enjoyed the teaching opportunity, and the energy that everyone put into helping educate a new generation of chemical engineers.

I also want to thank the many current and former lab members who made this research possible. Prof. Yi-Chun Lu was an excellent mentor and leader of the Li–air team, and helped me immensely as a new graduate student. Yasuhiro Tsukada was extremely helpful in completing the

work into Li_2O_2-preloaded electrodes shown in Chapter 2. Carolyn Joseph was an excellent UROP who was always ready and willing to help me out with anything in lab. On my more recent work, I want to thank Chibueze Amanchukwu for his work in further testing and developing polymer-based Li–air batteries, and as a source of further intellectual insights into the chemical reactivity of various materials in Li–air. I also thank Koffi Pierre Yao, who provided immense assistance both in continuing the Li_2O_2-preloaded work, and in designing and constructing the DEMS air cell described in Chapter 3. Finally, I thank Shuting Feng for all her assistance and energy these past several months as she is beginning her own journey in graduate school.

Beyond my research, I want to thank all the members of both the Shao-Horn and Hammond labs for making working in either lab an enjoyable experience. The excitement, energy, and comradery that both labs exhibited were critical for my success. Not only did I know that I could count on any member of the lab to help when I needed it, I enjoyed socializing with all of them both in and out of the lab.

I also want to thank my friends from outside of lab at MIT, too many to name here. I met most of them during my first semester as a student here, and built many close friendships with them since then. I always looked forward to the many activities we did and spending time with them.

Finally, I want to thank Erika Bruno and to my family, for their support and love over the past years. Erika was always there for me, and made coming home at the end of the day something to look forward to. My family, and especially my parents, Mark and Margaret Harding, were always there for me, and provided the support, love, and advice I needed to be successful throughout my life, including here at MIT.

Table of Contents

List of Figures

15

List of Tables

17

List of Abbreviations

Abbreviation	Definition
^{1}H-NMR	Proton NMR
Au/C	Gold nanoparticles on VC
BHT	Butylated hydroxytoluene
CNT	Carbon nanotube
DEMS	Differential electrochemical mass spectrometer
DME	1,2-dimethoxyethane
EC	Ethylene carbonate
EIS	Electrochemical impedance spectroscopy
EV	Electric vehicle
FEP	Fluorinated ethylene propylene
GIXD	Grazing incidence X-ray diffraction
HEV	Hybrid electric vehicle
Li-ion	Lithium-ion
Li-Nafion	Lithiated Nafion®
LiTFSI	Lithium *bis*(trifluoromethane)sulfonimide
MS	Mass spectrometer
MW	Molecular weight
NMR	Nuclear magnetic resonance
NP	Nanoparticle
OCV	Open-circuit voltage
OER	Oxygen evolution reaction
ORR	Oxygen reduction reaction
P4M***	Codes used to identify electrolytes used in Chapter 4, see Table 4-1
PAN	Polyacrylonitrile
PC	Propylene carbonate
PEGDME	Poly(ethylene glycol) dimethyl ether
PEO	Poly(ethylene oxide)
PHEV	Plug-in hybrid electric vehicle
Pt/C	Platinum nanoparticles on VC
Pyr$_{14}$TFSI	1-butyl-1-methylpyrrolidinium *bis*(trifluoromethane)sulfonamide
RGA	Residual gas analyzer
Ru/C	Ruthenium nanoparticles on VC
SAIT	Samsung Advanced Institute of Technology
SEM	Scanning electron microscopy
SS	Stainless steel
UHV	Ultra-high vacuum
V$_{Li}$	Volts *versus* lithium
VC	XC-72 Vulcan carbon
VC***	Codes used to identify electrodes used in Chapter 4, see Table 4-2
XRD	X-ray diffraction

18

Chapter 1

Introduction

1.1 Motivation

Climate change, including the increase of the global surface temperature (Figure 1-1), is a significant concern for society's future,[1] and the effects of climate change (including sea-level rise and dramatic changes to local climates) are expected to have a large impact on the global economy over the next century.[2] Climate change has been linked to the growing concentration of carbon dioxide and other greenhouse gases in the global atmosphere (Figure 1-2), although a very small[3] and shrinking[4,5] number of climate scientists remain unconvinced. The continued widespread combustion of fossil fuels is a significant source of the greenhouse gases,[1] which motivates the development and widespread implementation of non-fossil fuel energy sources, such as wind, solar, biomass, geothermal, and, more controversially, nuclear energy. These technologies are now a significant source of electrical energy (Figure 1-3), and in 2014 accounted for 32.6% of the total electricity produced in the U.S.[6] In the past 15 years, energy production from wind and solar technologies has dramatically increased; energy derived from solar and wind have increased 5.5 and 29 times respectively, between 2000 and 2015.

However, of these technologies, only biomass (largely in the form of ethanol additives) has been widely adopted in the transportation sector, which continues to source 95% of its energy from fossil fuels.[6] This is largely due to the transient, low-density, and often stationary nature of other renewable energy sources and the enormous safety concerns associated with the concept of nuclear powered cars. Therefore, it is desirable to electrify the transport system, which would link the large amount of energy consumed on transportation with the gradual increase in electrical energy generation from clean sources.

While some forms of transportation can be electrified (such as buses and regional trains) by directly connecting vehicles to the electrical grid, this is not feasible for automobiles, which must

20
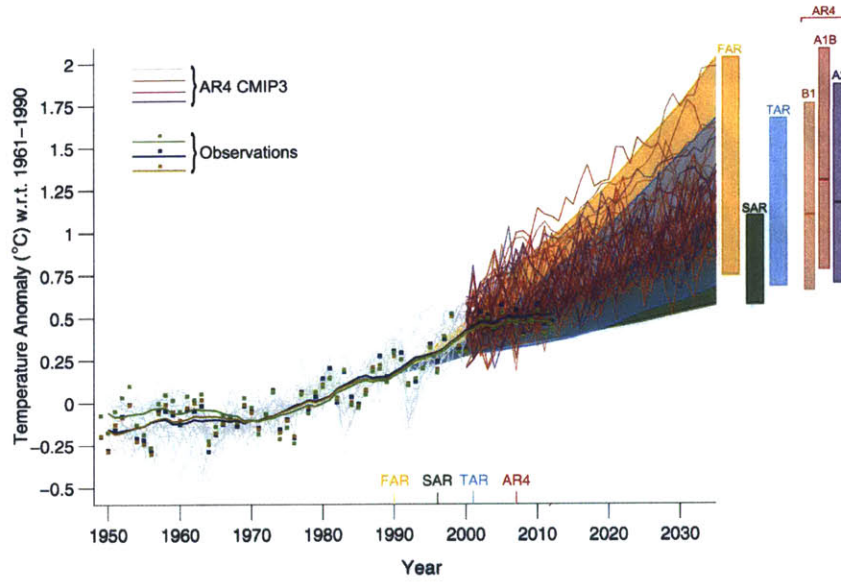
Figure 1-1. Estimated changes in the observed globally and annually averaged surface temperature anomaly relative to 1961–1990 (in °C) since 1950 compared with the range of projections from the first four IPCC assessments. Reproduced from Ref. 1.
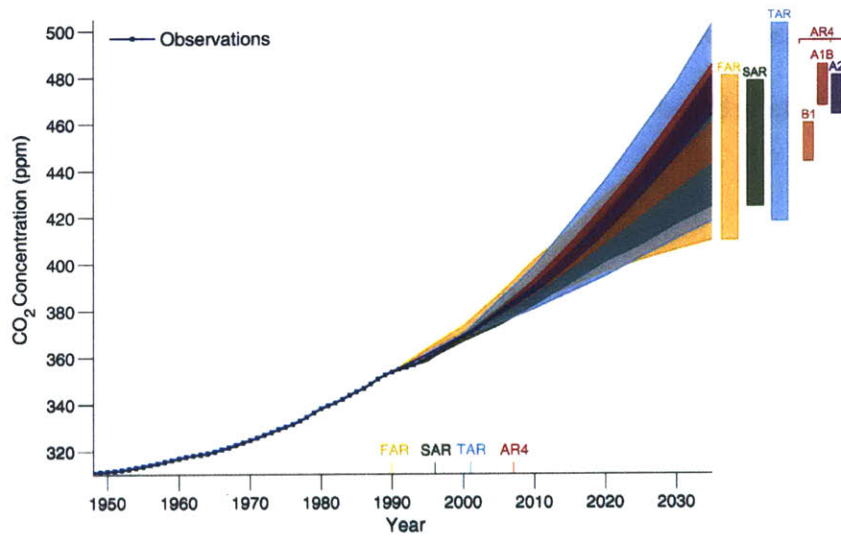
Figure 1-2. Observed globally and annually averaged CO_2 concentrations in parts per million (ppm) since 1950 compared with projections from the first four IPCC assessments. Reproduced from Ref. 1.
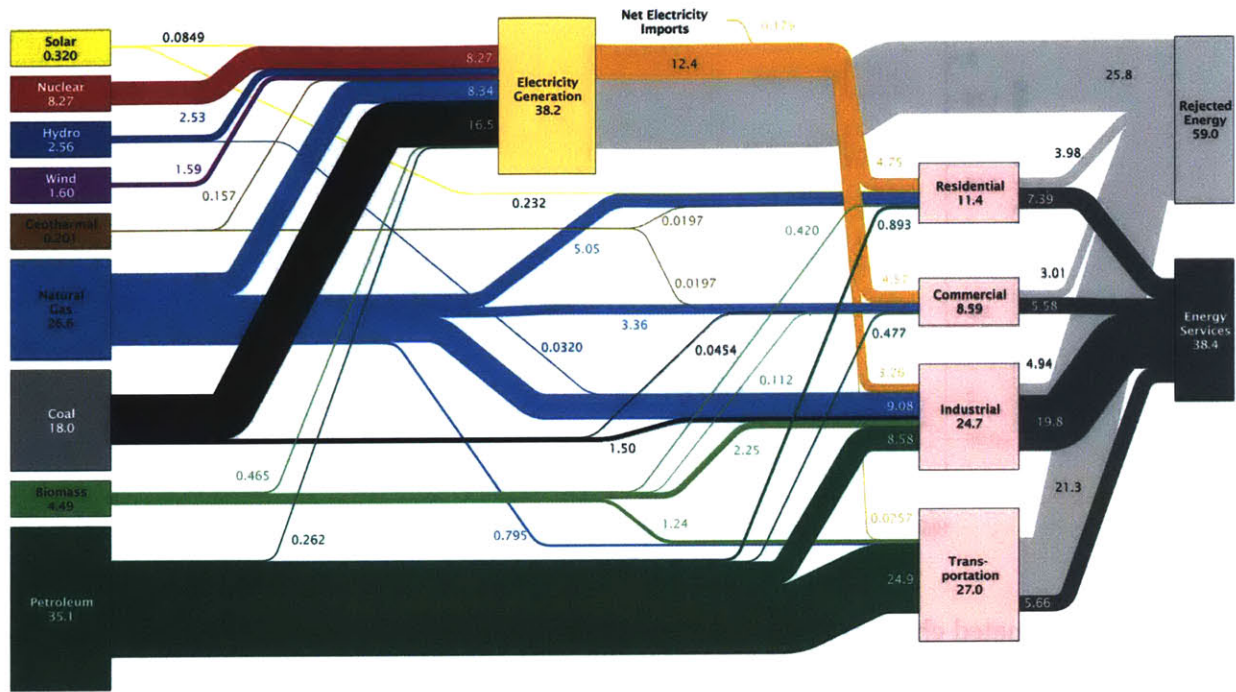
Figure 1-3. Estimated US Energy Use in 2013: 97.4 Quads (quadrillion BTU). Energy sources are listed on the left and energy consuming sectors are listed near the right in pink. Colored bars indicate the use of each source in a particular sector, and the width of these bars is proportional to consumption. Data is based on DOE/EIA-0035(2014-03), March, 2014.[7] Reproduced from Ref. [8].

be capable of travelling individually and independently from the grid. Thus, technologies are needed that store electrical energy with sufficient density for automotive applications. Conceptually, this can be achieved either through the electrochemical production of fuels (*e.g.* hydrogen via electrolysis of water) or using on-board electrochemical devices to store energy taken from the grid (*e.g.* lithium-ion batteries). While both of these pathways are potentially viable options that are being extensively investigated,[9–11] in this thesis we choose to focus on new battery technologies.
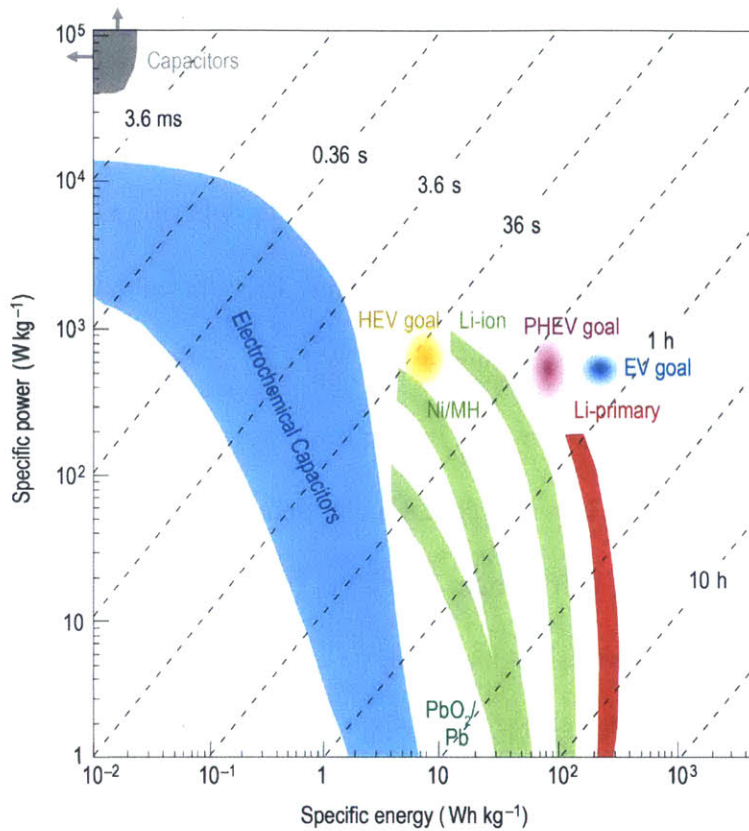
Figure 1-4. Specific power against specific energy for various electrical energy storage devices. Adapted with permission from Simon and Gogotsi.[12] HEV, PHEV, and EV goals were obtained from USCAR.[13]

Three classes of vehicles are currently being developed that rely on on-board batteries for some or all of their energy storage: hybrid electric vehicles (HEV), plug-in hybrid electric vehicles (PHEV), and electric vehicles (EV). As shown in Figure 1-4, current lithium-ion (Li-ion) batteries are capable of meeting the performance targets of HEVs, although efforts are ongoing to develop electrochemical capacitors that are capable of meeting this need.[14–16] PHEVs and EVs are both currently available, but are strictly limited by the performance and cost of Li-ion batteries. The EVs currently available from Tesla Motors are undeniably impressive, but the high cost and limited

availability of their vehicles makes them niche luxury items, and the battery in the Tesla Model S is estimated to make up 30% of the vehicle's curb weight.[17]

As shown in Figure 1-4, industry targets for EV battery performance[13] require batteries with at least double the specific energy of Li-ion batteries. This presents a significant materials challenge, as the lithium intercalation compounds used in the positive electrode of Li-ion batteries have a limited capacity for lithium ions,[18] which in turn limits the specific energy of devices using these compounds.[19] High voltage lithium intercalation compounds are being investigated in an effort to increase the energy stored per unit lithium,[18,20,21] but new electrolyte materials need to be found that are stable with these materials.[22] An alternative to finding higher voltage intercalation materials is to use conversion reactions, in which lithium ions are reacted with other species in the battery to spontaneously form new compounds while discharging. Two such systems have been of great interest recently are lithium–sulfur and lithium–air (Li–air) batteries.[23] However, because oxygen is significantly lighter than sulfur (16 g/mol O *vs.* 32 g/mol S), Li–air batteries have a higher theoretical specific energy and are the focus of this thesis.

Figure 1-5 shows a comparison of the theoretical energy density between traditional Li-ion batteries (using a $LiCoO_2$ positive electrode) and Li–air batteries.[19] If combined with a lithium metal anode, Li–air batteries are theoretically capable of achieving 3-4× enhancement in specific energy over current Li-ion batteries, while matching their volumetric energy density. Even when compared to lithium metal-based Li-ion batteries, Li–air batteries may achieve twice the specific energy density. It should be noted that development of practical devices using lithium metal or other high capacity negative electrodes (such as silicon) is required for the high performance of Li–air batteries; carbon-based Li–air batteries have only minimal theoretical improvements over

Li-ion. Developing rechargeable lithium batteries with high capacity anodes is the subject of intense research by a number of groups,[24–26] but is not the focus of this thesis. Other work has shown similar results; a detailed engineering analysis of Li–air and advanced Li-ion devices by Gallagher *et al.* show that open Li–air batteries may be able to achieve ~1.5× higher specific energy than advanced Li-ion batteries, while more than doubling the volumetric energy density of current Li-ion batteries.[20]
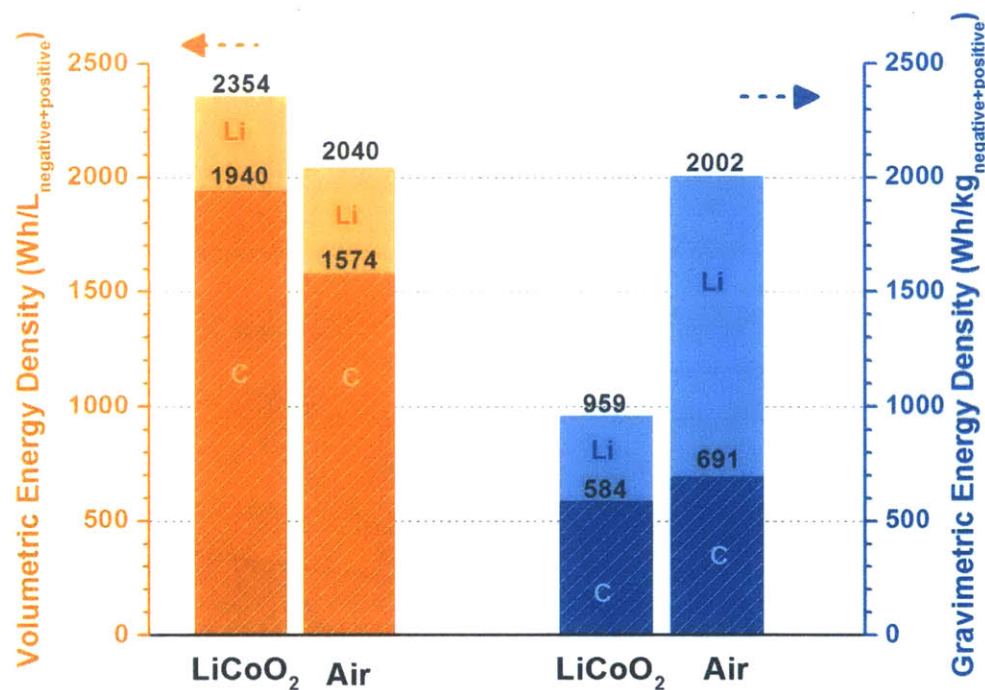
Figure 1-5. Estimated theoretical gravimetric and volumetric energy density of $LiCoO_2$ and O_2 (Li_2O_2) as the positive electrode with carbon (C_6) or Li as the negative electrode. An additional two times excess lithium is assumed for the lithium negative electrode. Reproduced with permission from Lu *et al.*[19]

1.2 Principles of Operation for Lithium–Air Batteries

Li–air batteries (and closely related Li–O₂ batteries, which use purified oxygen rather than air) operate by reacting lithium with gaseous oxygen electrochemically, allowing work to be performed as electrons are transferred from the lithium negative electrode to the oxygen positive electrode (Figure 1-6). Although this reaction can be performed in aqueous as well as nonaqueous environments, nonaqueous Li–air batteries have received greater attention owing to their higher achievable specific energy density.[27] In general, the desired discharge product is lithium peroxide, which is produced by the overall reaction:[28]

$$2\text{Li}(s) + \text{O}_2(g) \leftrightarrow \text{Li}_2\text{O}_2(s) \quad \text{where } E° = 2.96 \, V \, vs. \, \text{Li} \quad\quad (1\text{-}1)$$
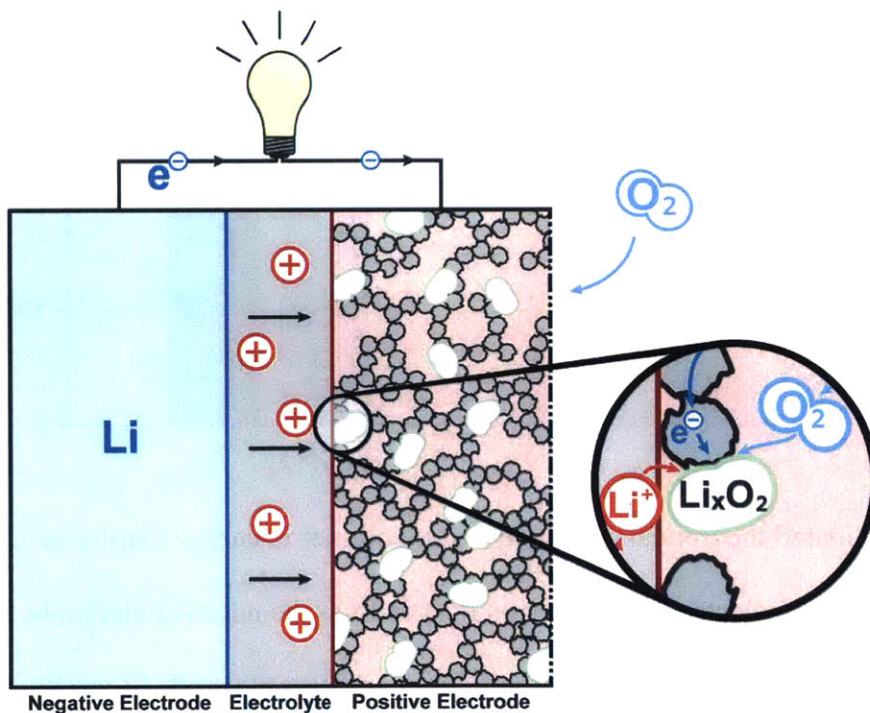
Figure 1-6. A schematic of the theoretical discharge behavior of a nonaqueous Li–air or Li–O₂ battery. Lithium ions are generated at the negative electrode and react with oxygen at the positive electrode to produce solid lithium oxides, such as lithium peroxide or lithium oxide.

Reaction 1-1 proceeds electrochemically, where lithium ions are generated at the interface between the electrolyte and negative electrode and diffuse through the electrolyte, while electrons are transported through an external circuit. In the positive electrode, lithium ions, electrons, and oxygen react to spontaneously produce solid Li_2O_2, which is deposited throughout the electrode (Figure 1-6). The reaction in the positive electrode is believed to obey the following reaction scheme:[19]

$$Li^+ + e^- + O_2 \rightarrow LiO_2 \tag{1-2}$$

$$LiO_2 + Li^+ + e^- \rightarrow Li_2O_2 \tag{1-3a}$$

$$2LiO_2 \rightarrow Li_2O_2 + O_2 \tag{1-3b}$$

Although LiO_2 is reactive and unstable, numerous reports have identified its presence in discharging electrodes through direct and indirect methods.[19,29,30] Reactions 1-3a and 1-3b are less well understood, and conditions in which one or the other dominates is the subject of active investigation.[31-34] We also note that although lithium oxide (Li_2O) would theoretically achieve higher specific energy than Li_2O_2, in practice it is not observed as a discharge product,[19] and when added to electrodes has been shown to be very difficult to oxidize.[35,36] For this reason, Li_2O_2 is generally considered the desired discharge product of Li–air batteries, and all the analyses of Li–air performance above assume Li_2O_2 as the discharge product.

In contrast with Li-ion devices, in which the amount of lithium intercalation compounds control the capacity, the porosity of the positive electrode controls the maximum theoretical capacity of Li–air batteries, because Li_2O_2 is spontaneously formed in the electrode void space during discharge. As the cell is discharged, Li_2O_2 has been observed to gradually accumulate, and in some situations this continues until all void space in the electrode is filled (Figure 1-7).[37] The mechanism

controlling the shape and distribution of discharge product is of particular concern owing to the insulating nature of Li_2O_2, and remains a subject of active research.[38,39]
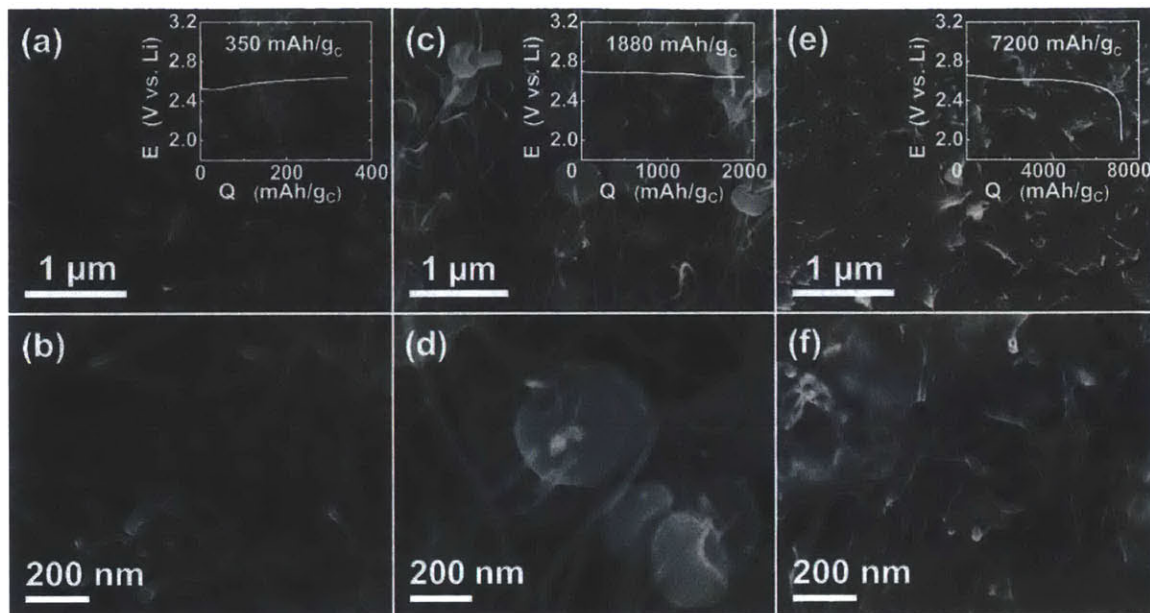
Figure 1-7. Evolution of Li_2O_x discharge product morphology in a carbon nanofiber electrode. Insets show the corresponding discharge voltage profile. Reproduced with permission from Mitchell and Gallant *et al.*[37]

1.3 Challenges for Lithium–Air Batteries

In spite of the promising theoretical performance of Li–air batteries, a host of challenges have been identified that currently prevent their practical implementation.[19] Li–air and Li–O_2 batteries exhibit poor recharge reaction kinetics, and often charge near 4.0 V *vs.* Li (V_{Li}),[40,41] more than 1 V higher than the reversible potential of 2.96 V_{Li} listed in reaction 1-1. Many catalyst materials have been proposed to improve on this charging potential,[28,42–46] some of which are explored in Chapter 2. Additionally, discharge rate capability of Li–air and Li–O2 batteries is below that of Li-ion;[47,48] at very low rates, cells can be discharged to very high depths of discharge, but at higher

rate are only able to access a fraction of capacity. This behavior is linked to the distribution of discharge product within the positive electrode:[38,40] low rates allow large, space-filling particles to form, while higher rates usually restrict the discharge product to form a thin coating on the electrode surface, and efforts to understand the controlling factors of these two behaviors,[38,39] as well as their impact on subsequent charging,[40] is ongoing. The cycle life of Li–O_2 and Li–air batteries is also quite poor, with devices that are deeply discharged often only lasting a handful of cycles.[49,50] Some researchers use limited capacity discharge,[41,42,51] which enhances the cycle life but ultimately results in the same capacity fade after tens of cycles.[51] This behavior is attributed to reactions between the discharge products or intermediates (Li_2O_2, LiO_2, and $O_2^{\cdot-}$) and the electrode and electrolyte;[41,52] several teams of researchers have investigated a large number of electrolyte and electrode material systems in an effort to find a stable combination.[53] The only apparently successful pairing yet demonstrated used a DMSO-based electrolyte with a nanoporous gold electrode,[54] and recent results from our group have shown that Li_2O_2 and DMSO react over the course of hours.[55] Chapter 5 continues this trend and explores the interaction between oxygen and a solid-polymer electrolyte at charging potentials, and Chapter 3 describes the development of equipment that can analyze the gas consumption and production of Li–O_2 cells to directly confirm the reversible operation of such devices.

Additional problems arise when considering true Li–air devices, which are open to air, as opposed to the closed Li–O_2 devices that are frequently used in laboratory research. Li_2O_2 is unstable in air, readily reacting with CO_2 to form Li_2CO_3 and with water to form LiOH, both of which require much higher potentials to oxidize.[35,36] Practical devices will need to develop an air scrubbing system that removes CO_2 and water, or selectively allows the passage of only oxygen.[20] Additionally, electrolyte evaporation is a concern; most of the solvents used in Li–O_2 batteries are

volatile,[56–58] and will escape the cell over time. This is both detrimental to the cell operation (electrical conductivity will eventually be lost) and to the environment where these toxic solvents would be contaminating.[56,58,59] In Chapters 4 and 5 we investigate using a solid, non-volatile polymer electrolyte as a possible solution to this problem and direction for future investigations.

1.4 Thesis Scope

This thesis investigates several faces of oxidation within Li–O_2 batteries. In Chapter 2, we investigate the charging behavior of Li–O_2 cells where chemically-synthesized Li_2O_2 has been included in the positive electrode, with and without the presence of various noble metal catalysts. The use of Li_2O_2-preloaded electrodes controls for variations that may occur during discharge with the different catalysts, and allows their activity in electrochemically oxidizing Li_2O_2 to be studied. We use X-ray diffraction and scanning electron microscopy to confirm the oxidation and removal of Li_2O_2, and show that both Pt and Ru allow the oxidation of Li_2O_2 to occur at much lower potentials than for Au or Vulcan carbon alone.

Chapter 3 describes the design and construction of a differential electrochemical mass spectrometer (DEMS) in our lab. DEMS allows for the quantitative measurement of the consumption and production of gas through all stages of Li–O_2 cell operation. We explore the design of the DEMS system and the decisions made in the process of development. Finally, we demonstrate the capabilities of the DEMS on several Li–O_2 systems, showing results that agree with work published by other groups for carbon electrodes in liquid electrolytes, and confirming that oxygen is the dominant product of Li_2O_2 oxidation in the presence of Ru, while both oxygen and carbon dioxide are produced in the presence of Pt.

In chapter 4, we develop a solid-polymer-based Li–O_2 cell based on poly(ethylene oxide) (PEO). Using solid, non-volatile PEO as the electrolyte solvent allows us to develop a cell that

30

would not be susceptible to solvent evaporation, and allows us to engineer a three-phase electrode with high oxygen transport. We investigate the performance of these cells at room temperature, and consider the various possible causes of their poor performance. We subsequently investigate the discharge performance at 60 °C, finding that carbon loading controls discharge capacity and ultimately approaching the device performance targets. Finally, we use DEMS to investigate the gas evolution during charging under argon at a range of temperatures from 30 to 60 °C, observing a marked increase in the production of unwanted gases at 50 °C and higher.

Finally, Chapter 5 continues the investigation of the behavior of PEO electrolytes under charging conditions, showing that PEO autoxidation is a major reaction in PEO-based $Li-O_2$ cells at 60 °C in oxygen over 100 hour time periods. We use DEMS and nuclear magnetic resonance spectroscopy to determine that the rate of this autoxidation reaction increases with increasing cell potential, and propose a mechanism for this reaction that explains the accelerated rate of oxidation without an observed increase in current. Finally, we demonstrate that this reaction affects the performance of the cells developed in Chapter 4, and use pressure-tracking experiments on the DEMS to show that PEO autoxidation is observed after a single charging cycle. These observations can be used to guide the development of new polymer and liquid electrolytes for Li–air batteries and provide additional constraints that must be met for stable, practical Li–air devices.

Chapter 2

Evidence of Catalyzed Oxidation of Lithium Peroxide for Rechargeable Lithium–Air Battery Applications*

2.1 Introduction

As described in Chapter 1, there are a number of challenges that currently limit the practical uses of Li–air batteries, which include low rate capability (typically 0.1 to 1 mA/cm^2),[60–62] low round-trip efficiency (53–64%,[63] 70%[64]), poor cycle life (10–100 cycles),[64–66] and electrolyte reactivity towards oxygen reduction reaction (ORR) intermediate species.[65,67] In this chapter, we focus on the challenge of the low round-trip efficiency of Li–O$_2$ cells, which has been attributed to the slow oxygen evolution reaction (OER) kinetics in organic electrolytes,[28,43,47,63] and more recently to the morphology of the Li$_2$O$_2$ produced during discharge[19,34,42,68,69] and the buildup of stable byproducts that are more difficult to oxidize.[41,70–72] The discharge voltages of Li–O$_2$ cells are typically in the range of 2.7–2.8 V$_{Li}$ for carbon-based electrodes,[28,37,40,42,47,73,74] slightly below the thermodynamic equilibrium potential (~2.96 V$_{Li}$), which is in good agreement with earlier findings that carbon is a reasonably active catalyst for oxygen reduction in organic electrolytes.[75] In contrast, the charge voltages of Li–O$_2$ cells with carbon-based electrodes are typically much higher than the thermodynamic voltages; early work with carbonate based electrolytes showed an average voltage plateau of ~4.7 V$_{Li}$ on carbon,[63] *versus* ~4.2 V$_{Li}$ on MnO$_x$/C[66] and ~4.0 V$_{Li}$ on λ-MnO$_2$,[60] α-MnO$_2$ nanowires,[64] and Co$_3$O$_4$[63] (70 mA/g$_{carbon}$ or 0.1 mA/cm$_{electrode}$^{2}), with additional work showing that catalysts such as MnO$_2$[64] and PtAu[74] can reduce the charging voltages of Li–O$_2$ batteries. However, these studies employed carbonate-based electrolytes in Li–O$_2$ cell testing, which can produce significant amounts of carbonates and alkyl-carbonates in addition to Li$_2$O$_2$, due to the reactivity between superoxide (an ORR immediate species) and carbonate solvents.[42,67,76,77] More recent work has investigated the catalysis of Li-O$_2$ charging in electrolytes based on 1,2-dimethoxyethane (DME) and its oligomers, and observed a reduction in the charging potential of deeply discharged Li-O$_2$ cells,[44,78,79] especially when carbon-free electrodes are

used.[54,80,81] This is in contrast with work by McCloskey et al.,[42] which showed that catalysts such as Pt, Au and MnO_2 do not appear to influence the charging voltages of Li–O_2 cells with DME. However, these authors examined Li–O_2 cells with exceptionally small capacities (less than 1 monolayer of Li_2O_2, ~130 mAh/g_{Vulcan})* which can be compared to most other studies (in the range from ~1000 to ~10000 mAh/g_{carbon}[37,47,72,82]).

In this chapter, we reexamine the effect of catalysts on the oxidation kinetics of Li_2O_2-loaded electrodes in a DME-based electrolyte, which does not react as readily with ORR intermediate products such as superoxide ions, as shown by Aurbach et al.,[67] and leads to Li_2O_2 formation in Li–O_2 cells.[37,47,83] The use of Li_2O_2-loaded electrodes eliminates concerns that observed changes in charging voltage may be due to changes in discharge product morphology. We show that Li_2O_2 can be completely oxidized upon charging using X-ray diffraction (XRD) and scanning electron microscopy (SEM), where much higher overpotentials are needed for electrodes based on Vulcan carbon and Au/C than those of Pt/C and Ru/C.

After publication of the work presented in this chapter, additional investigations into Li_2O_2-loaded electrodes were performed in our lab, but are not included in this thesis. Yao et al.[46] investigated a variety of transition metal and perovskite materials as more cost-effective catalysts for Li_2O_2 oxidation, and very recently proposed a mechanism to explain the relative activity of various metals and metal oxides as promoters of the electrochemical oxidation of Li_2O_2.[84]

---

* In McCloskey et al.,[42] most results are given on an absolute scale of current and capacity, which makes comparison between their results and other published results challenging. In the supplemental information of that paper, the authors give an approximate value of the carbon loading present in their carbonate free electrodes, reporting that the active cathode material ranged from 3-6 mg in each electrode. The authors define active material as both the carbon and catalyst included in the electrode mass.
Assuming a mass of 3 mg of carbon was added to each electrode on average, and observing that each cell was allowed to discharge to 0.4 mAh in DME gives a result of only 130 mAh/g_{carbon}.

Additional work investigating Li_2O_2-loaded electrodes with various promoters using differential electrochemical mass spectrometry (DEMS) is presented in Chapter 3.

2.2 Experimental

2.2.1 Electrode Preparation

All electrodes consisted of a carbon structure with lithiated Nafion® (Li-Nafion; LITHIon™ dispersion, Ion Power, USA) as a binder deposited on aluminum foil. The carbon structure consisted of pure Vulcan XC72 carbon (VC), 40 wt% Au on VC (Au/C), 40 wt% Pt on VC (Pt/C), or 40 wt% Ru on VC (Ru/C), all of which were purchased from Premetek (USA). 90% phase-pure Li_2O_2 powder (with 10% LiOH, see Section 2.2.2 below; Sigma-Aldrich, USA) was ball-milled in a PULVERISETTE 6 (Fritsch, Germany) at 500 rpm without solvent under dry argon for 5 hours. After ball milling, XRD indicated 4% LiOH in crystalline Li_2O_2 (Figure 2-1). Li_2O_2 electrodes had a ~1:1 mass ratio of Li_2O_2 and carbon (0.99, 1.08, 0.99, and 1.01 g_{Li2O2}/g_{carbon} for VC+Li_2O_2, Au/C+Li_2O_2, Pt/C+Li_2O_2, and Ru/C+Li_2O_2, respectively). Assuming complete oxidation, Li_2O_2 has a capacity of 1168 mAh/g. Therefore, the expected capacity of each set of electrodes was 1160, 1260, 1160, and 1180 mAh/g_{carbon} for VC+Li_2O_2, Au/C+Li_2O_2, Pt/C+Li_2O_2, and Ru/C+Li_2O_2, respectively.

Catalyst/VC and Li_2O_2 were mixed under argon. Li-Nafion and anhydrous isopropanol were added to the mixture, which was sonicated with a probe ultrasonicator in a dry glovebox (MBRAUN, USA, H_2O < 0.1 ppm, O_2 < 1%) until a homogenous slurry was obtained. This slurry was deposited onto aluminum foil in air, and then quickly dried under vacuum. After the isopropanol evaporated, 15 mm diameter electrodes were punched from the electrode sheet in the dry glovebox. These electrodes were then dried in a Büchi B-585 glass vacuum oven (BÜCHI, Switzerland) for at least 8 hours at 70 °C, without exposure to air. Following drying, the electrodes

36

were transferred into an argon glovebox (MBRAUN, USA, $H_2O < 0.1$ ppm, $O_2 < 0.1$ ppm) without exposure to air and stored there until used. Electrodes were weighed individually on a XS205 analytical balance (Mettler-Toledo, USA) before use. For each catalyst, electrodes were prepared with Li_2O_2 (denoted by "+Li_2O_2", e.g. Au/C+Li_2O_2) and without Li_2O_2, which was used to generate background current.

2.2.2 Confirmation of Li_2O_2 Purity

The manufacturer reported 90% phase purity of the Li_2O_2 used in this work. XRD was performed on the Li_2O_2 powder both as purchased and after the ball milling treatment (Figure 2-1). The as purchased powder shows a ~10% phase impurity of LiOH, although the small size of the LiOH peaks and their close proximity to major Li_2O_2 peaks increases the uncertainty of this calculation. Post ball milling, only the (200) LiOH peak is detected, and its area is consistent with a
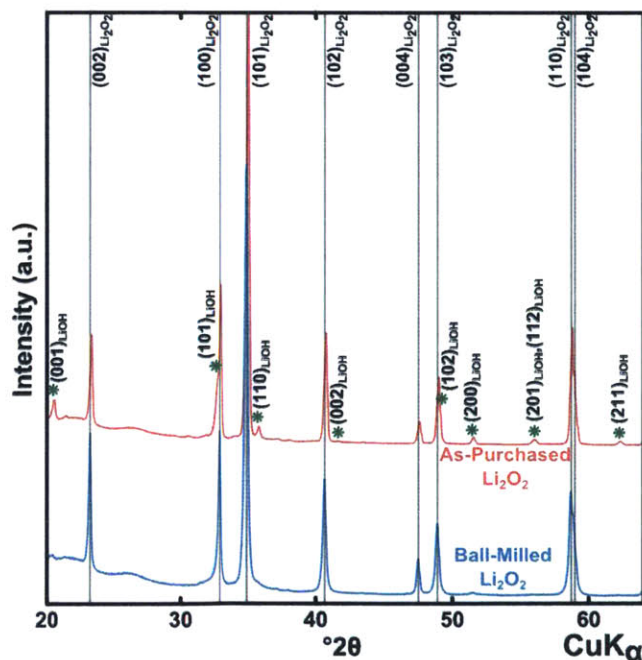
Figure 2-1. XRD spectra of Li_2O_2 powder as-purchased and after ball-milling. Grey vertical lines denote Li_2O_2 lattice planes, and green stars denote LiOH lattice planes.

4% LiOH phase impurity. However, we are not aware of a reasonable pathway for the conversion of LiOH into Li_2O_2 while dry ball milling under argon. We propose that the LiOH was present on the surface of the as purchased Li_2O_2 powder, where ball-milling most effectively reduced LiOH crystal size, thereby reducing its peaks below the XRD detection limit.

For the purposes of estimating the expected cell capacity, this contamination is neglected; the number of Li atoms present changes by only 0.3% by including a 10% LiOH impurity. Additionally, the thermodynamic equilibrium potential for LiOH is 3.3 V_{Li}, below the operating potential of all cells presented here. We therefore assume that LiOH is also oxidized during charging, which is consistent with the agreement between the observed and expected capacities.

2.2.3 Electrochemical Testing

All electrochemical testing was performed using TJ-AK cells (Tomcell Japan Co, Japan), which were prepared in the argon glovebox and held approximately 1 mL of head space. Metallic Li (Chemetall, Germany, ~0.14 mm thickness, 18 mm diameter) was used as an anode with two Celgard 2500 separators (Celgard, USA, 21 mm diameter). The electrolyte consisted of 87.5 µL of 0.1 M $LiClO_4$ in DME (Novolyte, USA; manufacturer reported H_2O < 20 ppm).

Each electrode type was charged potentiostatically at several voltages using either a So-lartron 1470 (Solartron Analytical, UK) or a Bio-logic VMP3 (Bio-logic, France). For each catalyst and at each voltage, electrodes with and without Li_2O_2 were charged to allow the estimation of net current by subtracting background current due to reactions not involving Li_2O_2. Each test began with a 6 h rest at open circuit voltage (OCV), followed by 30 min at 2.9 V_{Li} before switching to the desired test potential. Testing was not time-limited, and when possible cells were allowed to charge until the normalized current was less than twice that of the corresponding background electrode. Integrating the net current with respect to time gave the capacity of the electrode associated

38

with Li_2O_2 oxidation (Figure 2-2). The activity for Li_2O_2 oxidation was compared by net carbon-mass-normalized current for Li_2O_2 oxidation, which was calculated by subtracting the carbon-mass-normalized current of a Li_2O_2-free electrode from the carbon-mass-normalized current of a corresponding Li_2O_2-containing electrode. As the carbon:Li_2O_2 mass ratio was kept nearly equal to 1, currents normalized to carbon are equivalent to those normalized to Li_2O_2. Measurements at each condition were repeated several times, from which an average and a standard deviation of carbon-mass-normalized currents of Li_2O_2 oxidation were obtained.
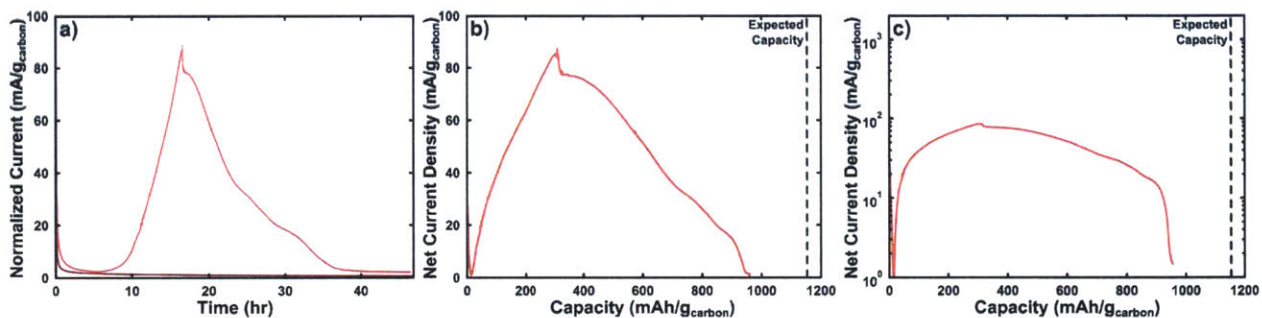
Figure 2-2. Example background subtraction and capacity integration for an Au/C+Li_2O_2 cell charged at 4.3 V. (a) Carbon normalized active and background current *vs.* time, (b) Background subtracted net current *vs.* time, (c) Net current *vs.* capacity on a linear scale, and (d) Net current *vs.* capacity on a log scale as presented in the remainder of the chapter.

Each catalyst was also tested galvanostatically. Each cell was rested at OCV for 6 h before current was applied. The currents were selected on a carbon-normalized basis, and ranged from 5–500 mA/g_{carbon}. Each test was terminated when the cut-off voltage was reached.

A Li-O_2 cell consisting of a lithium metal anode (15 mm in diameter and ~0.45 mm thickness) and a Li-Nafion-bonded air electrode (12.7 mm in diameter) of Pt/C was discharged and

charged at 100 mAh/g$_{carbon}$. A detailed description for the preparation and testing of this cell can be found in the experimental section of Lu *et al.*[47]

2.2.4 Materials characterization

XRD spectra were collected using a X'PERT Pro (PANalytical, Netherlands) with a Cu anode (Cu K$_\alpha$). Samples were held under Kapton®, placed on a zero-background holder, and were prepared in the argon glovebox. XRD was performed on each batch of electrodes in the as-prepared state, after ~50% charging, and in the fully charged state. A continuous scan rate of 1°/min from 20° to 64° 2θ was used for all samples.
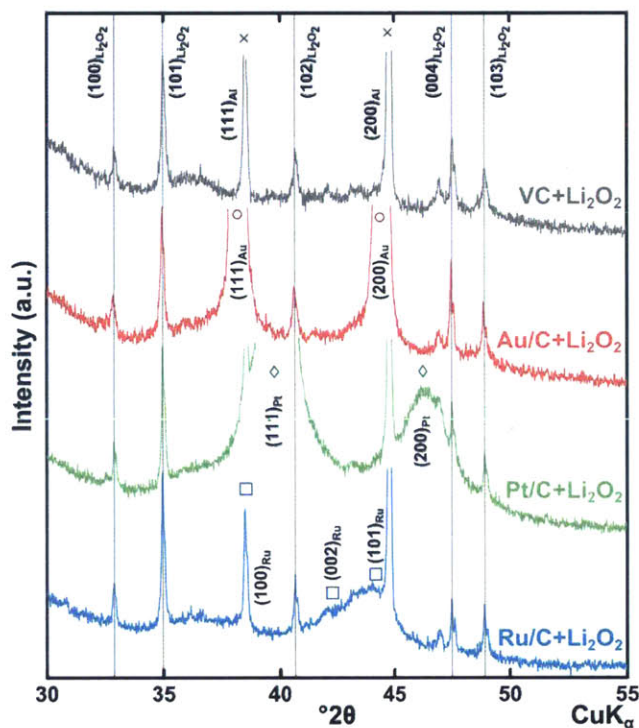
Figure 2-3. XRD spectra of pristine electrodes containing Li$_2$O$_2$ and various catalyst nanoparticles.

2.3 Results and Discussion

2.3.1 Electrode microstructure

Figure 2-3 shows the XRD of pristine Li_2O_2-containing electrodes for each catalyst. XRD analysis of these electrodes shows crystalline Li_2O_2 with space group *P6₃/mmc*. No crystalline form of LiOH, Li2O, or Li2CO3 was observed. SEM imaging reveals that VC or catalyzed VC (Au/C, Pt/C and Ru/C) particles (~50 nm)[47] are uniformly mixed with Li2O2 particles (~350 nm in Figure 2-4), as shown in Figure 2-5. It should be noted that metal catalyst nanoparticles are not visible in these images as they are generally 2 to 10 nm in diameter (Figure 2-6).
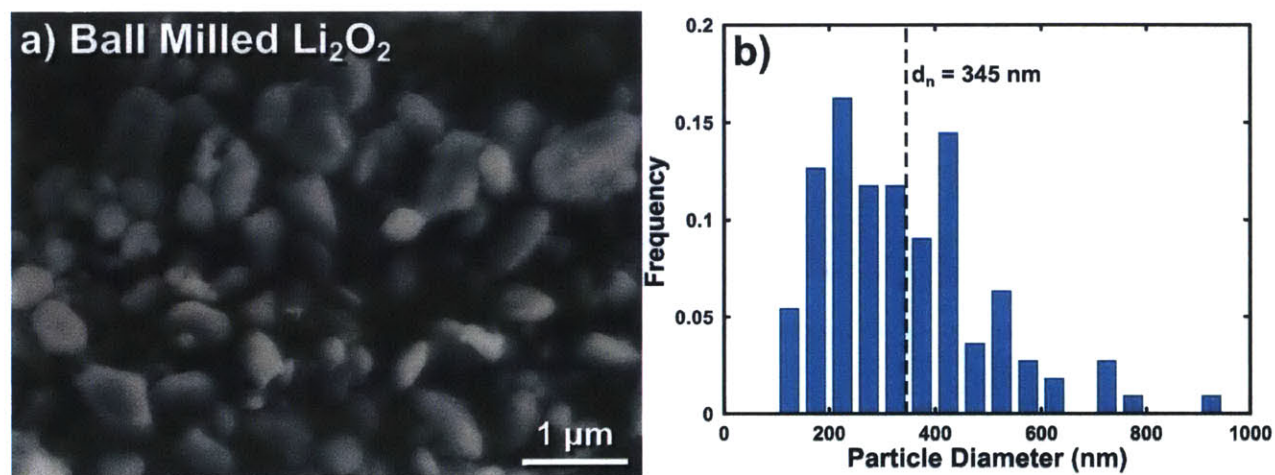
Figure 2-4. (a) SEM of ball-milled Li_2O_2. (b) Particle size distribution of particles present in (a).
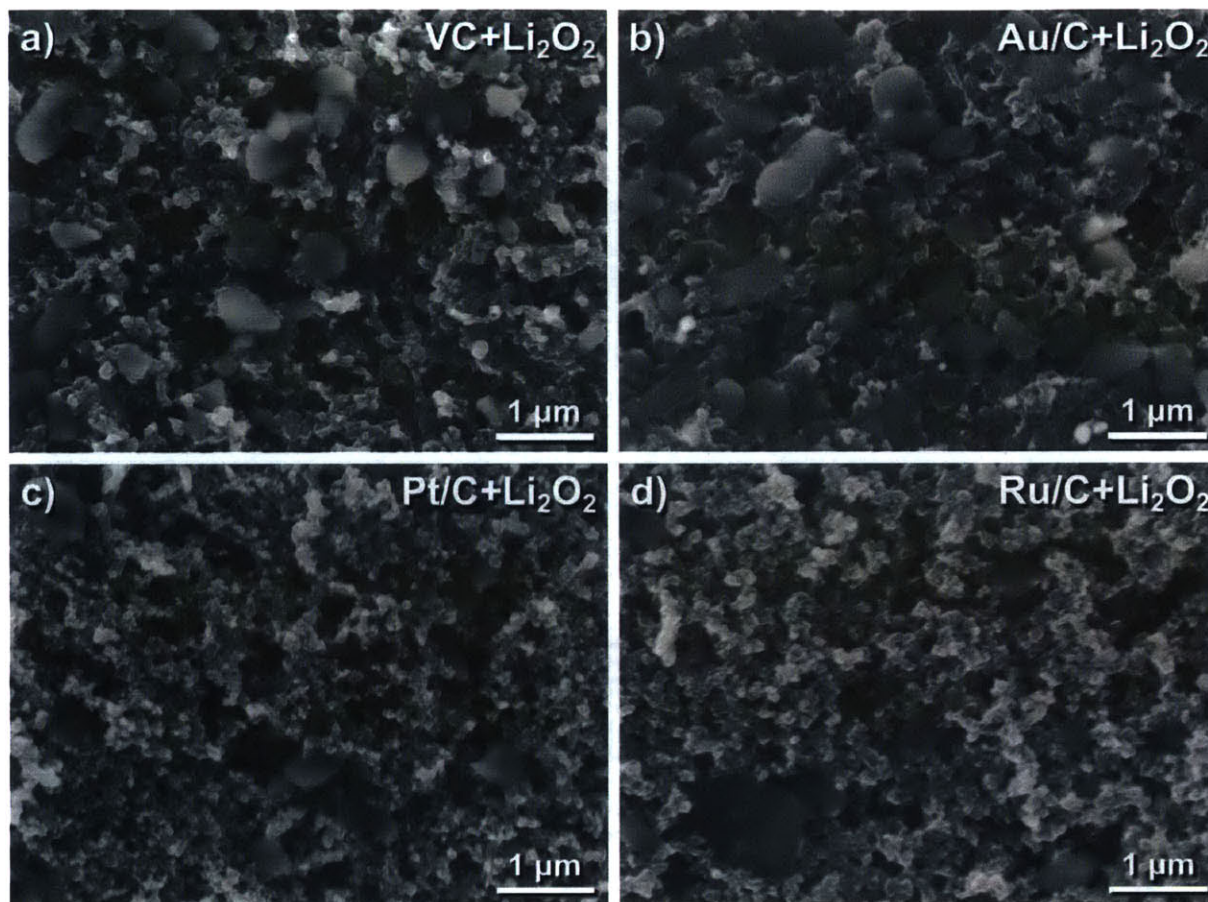
Figure 2-5. SEM images of pristine electrodes containing Li_2O_2: (a) $VC+Li_2O_2$, (b) $Au/C+Li_2O_2$, (c) $Pt/C+Li_2O_2$, (d) $Ru/C+Li_2O_2$. Large smooth particles are Li_2O_2 and small particles are Vulcan carbon. The nanoparticles of Au, Pt and Ru are too small to be visible in these images.
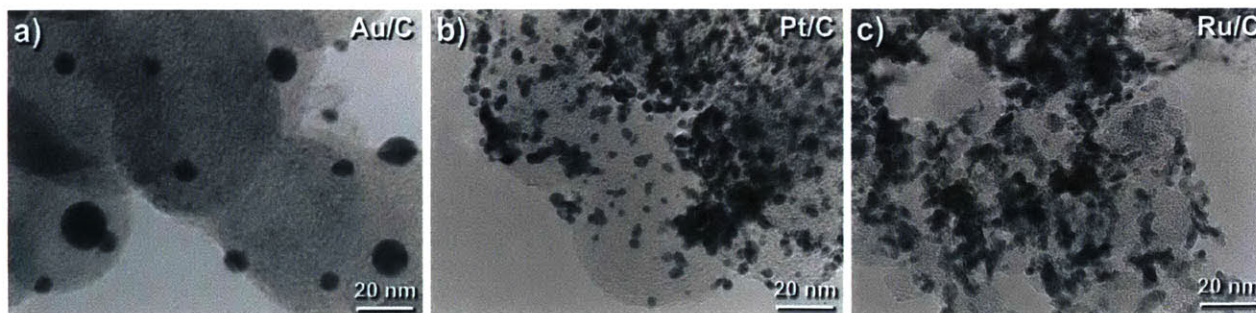
Figure 2-6. TEM of VC supported catalyst. (a) Au on XC72 Vulcan carbon (Au/C), (b) Pt on XC72 Vulcan carbon (Pt/C), (c) Ru on XC72 Vulcan carbon (Ru/C).

42

2.3.2 Li$_2$O$_2$ Oxidation on Vulcan Carbon

Vulcan carbon was found to become active in catalyzing the oxidation of Li$_2$O$_2$ at 4.0 V$_{Li}$ and higher. The net oxidation current obtained from VC+Li$_2$O$_2$ was found to significantly increase with increasing applied potentials, as shown in Figure 2-7. A maximum current of 20 mA/g$_{carbon}$ was reached at 4.0 V$_{Li}$ while 1000 mA/g$_{carbon}$ was obtained at 4.4 V$_{Li}$. Some current waves were noted (*e.g.* currents at 4.3 V$_{Li}$), where the physical origin is not understood and requires further investigation. The total capacities associated with net Li$_2$O$_2$ oxidation currents were found to be very comparable for all applied potentials (~900–1100 mAh/g$_{carbon}$), which translated to 80–95% of the expected capacity based on the amount of Li$_2$O$_2$ in the pristine electrode. It is interesting to note that an average current of ~100 mA/g$_{carbon}$ for Li$_2$O$_2$ oxidation corresponds to voltages between 4.1 and 4.2 V$_{Li}$, which is consistent with reported charging voltage of Li–O$_2$ cells with carbon electrodes.[37]
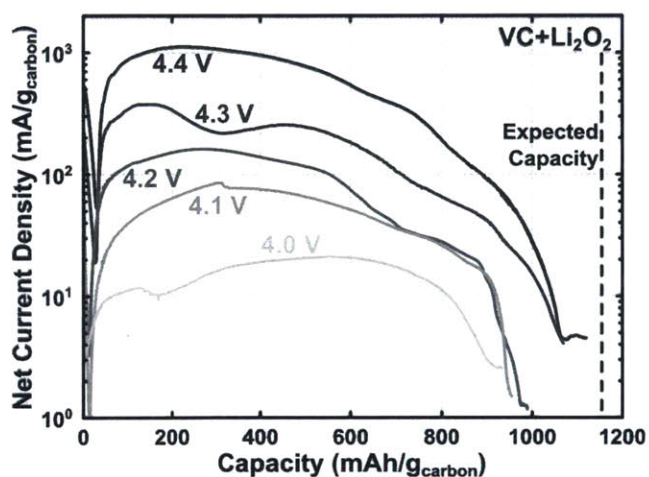
Figure 2-7. Net current density *vs.* capacity for VC+Li$_2$O$_2$ cells charged potentiostatically at select voltages. The expected capacity was estimated from the amount of Li$_2$O$_2$ used in the pristine electrodes.
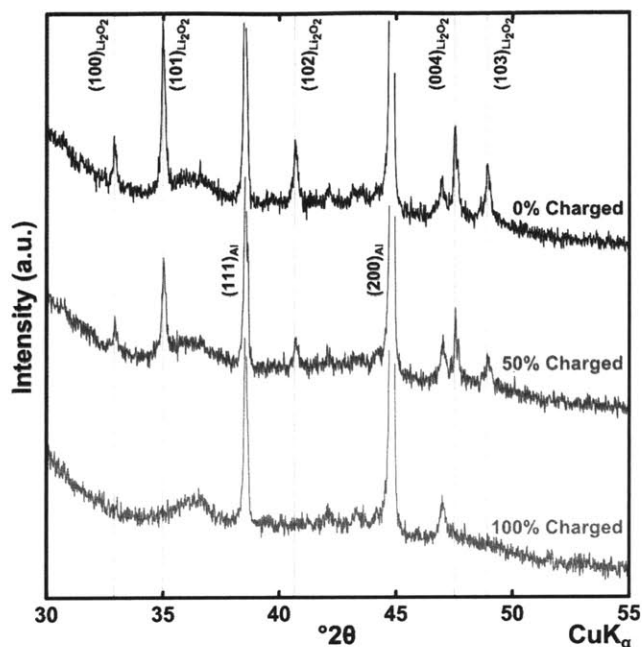
Figure 2-8. XRD data from an as-prepared VC+Li_2O_2 electrode (0% charged), a ~50% charged electrode (4.3 V_{Li}, 515 mAh/g_{carbon}), and a ~100% charged electrode (4.3 V_{Li}, ~1050 mAh/g_{carbon}) showing a reduction then elimination of crystalline Li_2O_2 in the electrode. Grey vertical lines mark the Li_2O_2 peaks.

XRD and SEM analyses show that Li_2O_2 could be removed completely upon charging, which confirms that the measured oxidation currents in Figure 2-7 are associated with oxidation of Li_2O_2. Figure 2-8 shows the XRD spectra of as-prepared, 50% and 100% charged VC+Li_2O_2 electrodes tested at 4.3 V_{Li}, where the peak intensities of Li_2O_2 were found to linearly decrease with increasing charged capacity (Figure 2-9) and Li_2O_2 peaks were no longer visible at ~100% charged capacity. SEM imaging of these electrodes further supports that Li_2O_2 was largely removed upon charging, as shown in Figure 2-10. In comparison to the as-prepared electrode (Figure 2-10a), the number of Li_2O_2 particles was visibly reduced in the 50% charged electrode (Figure 2-10b). Li_2O_2 particles were not visible in the 100% charged electrodes (Figure 2-10c), where holes left behind by the removal of Li_2O_2particles were clearly identified.

44
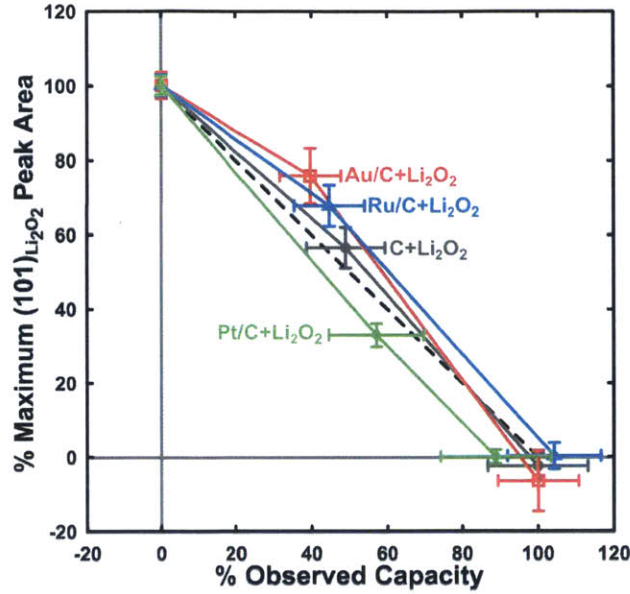
Figure 2-9. Percent reduction of the $(101)_{Li_2O_2}$ diffraction peak area *vs.* percent observed capacity for $VC+Li_2O_2$, $Au/C+Li_2O_2$, $Pt/C+Li_2O_2$, and $Ru/C+Li_2O_2$. The dashed black line marks the ideal 1:1 relationship between increasing charging and peak area reduction.
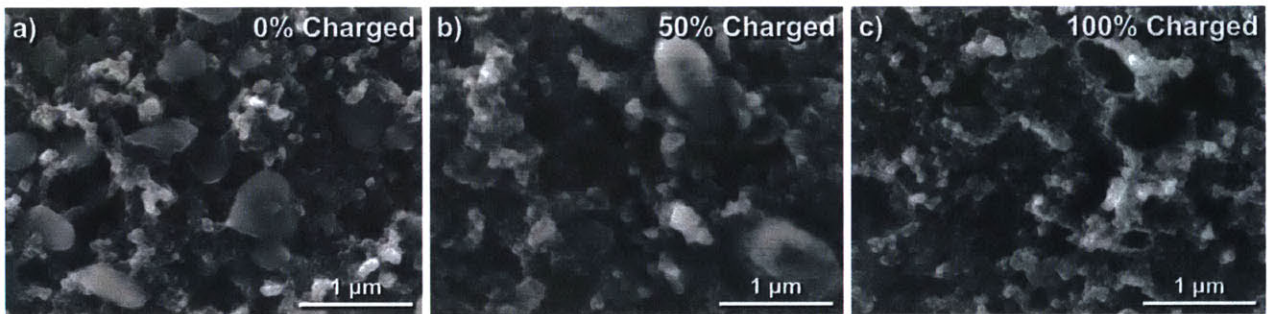
Figure 2-10. SEM images of $VC+Li_2O_2$ electrodes at select states of charge. (a) As-prepared (0% charged), (b) a ~50% charged electrode (4.3 V_{Li}, 515 mAh/g$_{carbon}$), (c) and a ~100% charged electrode (4.3 V_{Li}, ~1050 mAh/g$_{carbon}$).

2.3.3 Li$_2$O$_2$ Oxidation with Catalyzed Vulcan Carbon

2.3.3.1 Charging of Au/C and Li$_2$O$_2$

Au/C was found to be no more active in catalyzing the oxidation of Li$_2$O$_2$ than VC. The net oxidation current densities obtained from Au/C+Li$_2$O$_2$ electrodes at select applied potentials are shown in Figure 2-11a. The capacities obtained from charging Au/C+Li$_2$O$_2$ cells were consistent with the expected capacity based on Li$_2$O$_2$ mass in the pristine electrodes, which indicates nearly complete oxidation of Li$_2$O$_2$ at all applied potentials. This was further confirmed by XRD analyses of charged Au/C+Li$_2$O$_2$ electrodes (Figure 2-12), which showed the absence of Li$_2$O$_2$ peaks for a ~100% charged electrode. Interestingly, the oxidation current densities were fairly constant as a function of time at low voltages similar to that found for VC+Li$_2$O$_2$ while larger current densities were noted to decay with time at higher voltages, where the underlying cause is not understood at this time.

2.3.3.2 Charging of Pt/C and Li$_2$O$_2$.

Pt/C was shown to significantly promote the kinetics of Li$_2$O$_2$ oxidation as well as electrolyte oxidation relative to VC. The net oxidation current densities obtained from Pt/C+Li$_2$O$_2$ electrodes at select applied potentials are shown in Figure 2-11b. The applied potentials were limited to 3.9 V$_{Li}$ and lower due to pronounced electrolyte oxidation at 4.0 V$_{Li}$ and higher. At 3.9 V$_{Li}$, the oxidation current densities reached 1000 mA/g$_{carbon}$, which is 2 orders of magnitude higher than that catalyzed by VC alone at 4.0 V$_{Li}$. Although decreasing applied voltages reduces the oxidation currents, Pt/C remained reasonably active (providing 100 mA/g$_{carbon}$) at 3.6 V$_{Li}$ and became inactive below 3.5 V$_{Li}$. This is consistent with a Pt/C-based Li-O$_2$ cell cycled at 100 mAh/g$_{carbon}$, which completed charging at less than 4.0 V$_{Li}$ (Figure 2-13). High catalytic activity of Pt/C toward Li$_2$O$_2$ oxidation was further confirmed by XRD analysis of charged electrodes, where Li$_2$O$_2$ could be

46

oxidized and removed largely at 3.7 V_{Li} (800 mAh/g_{carbon}), as evidenced by the absence of Li_2O_2

peaks in a fully oxidized electrode (Figure 2-12). The capacities associated with Li_2O_2 oxidation
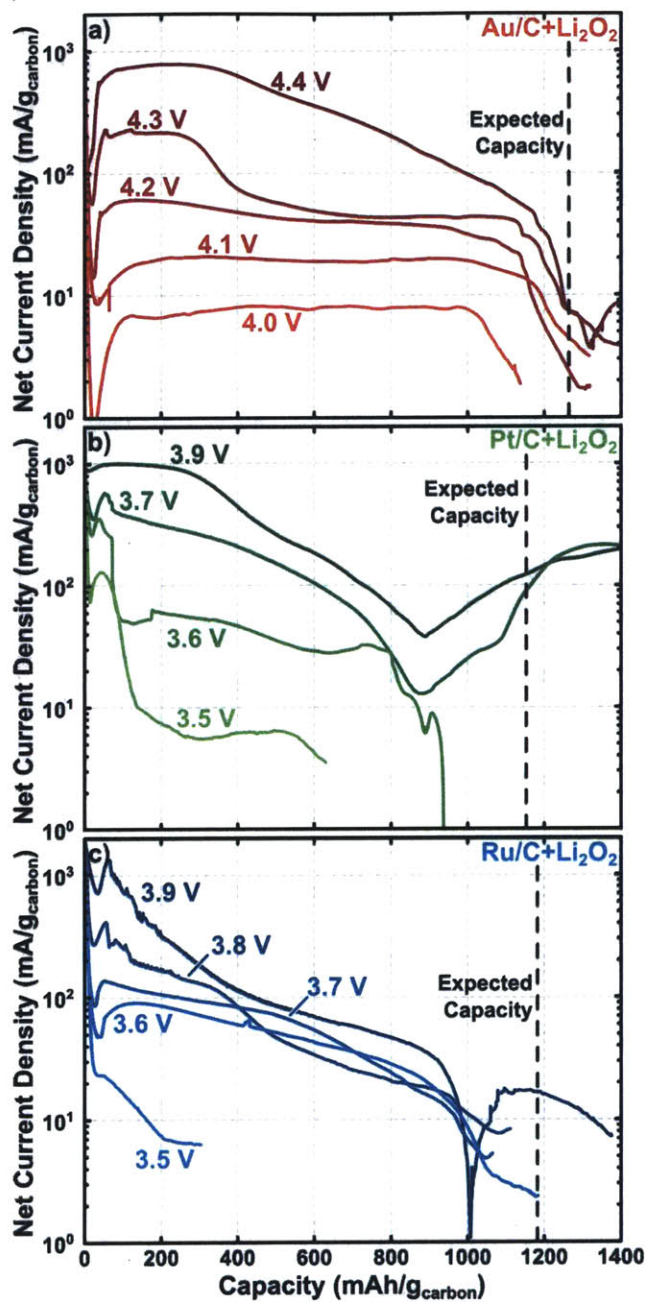
Figure 2-11. Potentiostatic charging profiles of (a) Au/C+Li_2O_2, (b) Pt/C+Li_2O_2, and

(c) Ru/C+Li_2O_2 electrodes at select voltages.
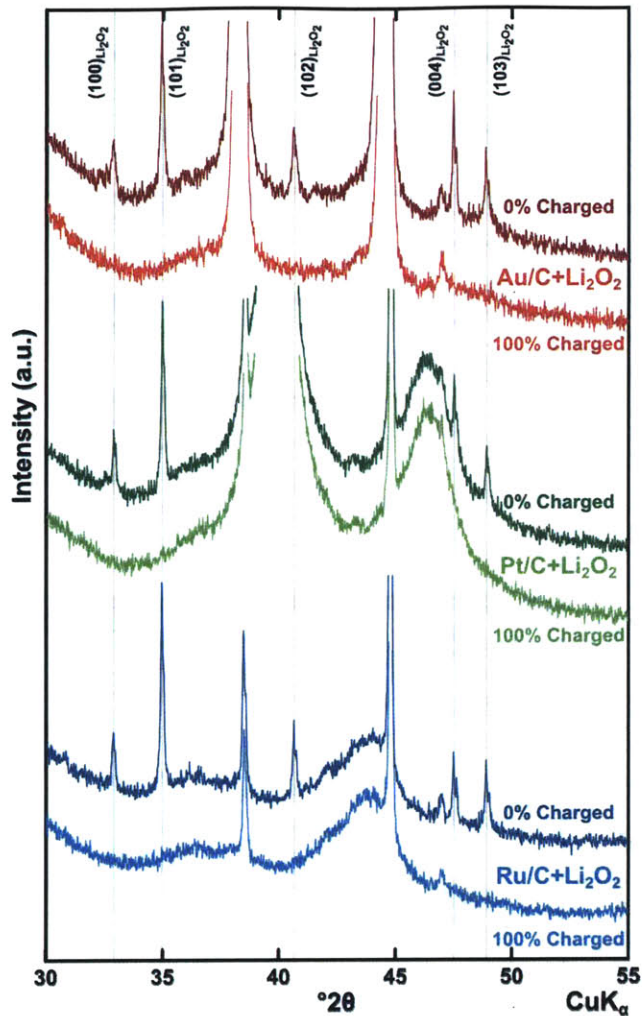
Figure 2-12. XRD spectra of pristine and ~100% charged electrodes of Au and Li_2O_2, Pt/C and Ru/C. All Li_2O_2 peaks are absent in the 100% charged electrodes. Pt/C+Li_2O_2 electrode charged at 3.7 V (~800 mAh/g_{carbon} capacity). Ru/C+Li_2O_2 electrode charged at 3.8 V (~1200 mAh/g_{carbon} capacity). Au/C+Li_2O_2 electrode charged at 4.3 V (~1300 mAh/g_{carbon} capacity).

catalyzed by Pt/C were slightly lower than the estimated capacity based on the Li_2O_2 amount in the pristine electrode (1150 mAh/g_{carbon}). Capacities of ~900 mAh/g_{carbon} were reached at 3.6 V_{Li} and higher, which corresponds to ~75% of the expected capacity. Beyond this capacity, the rise in the oxidation current densities at 3.7 V_{Li} and higher was attributed to electrolyte oxidation cata-lyzed by Pt/C, which could lead to oxidation capacities well past the expected capacity based on

48

Li$_2$O$_2$ amount in the pristine electrode. This is in agreement with recent findings of McCloskey *et al.*,[42] which have shown that electrolyte decomposition could start at ~3.6 V$_{Li}$ in the presence of Pt with a DME-based electrolyte.
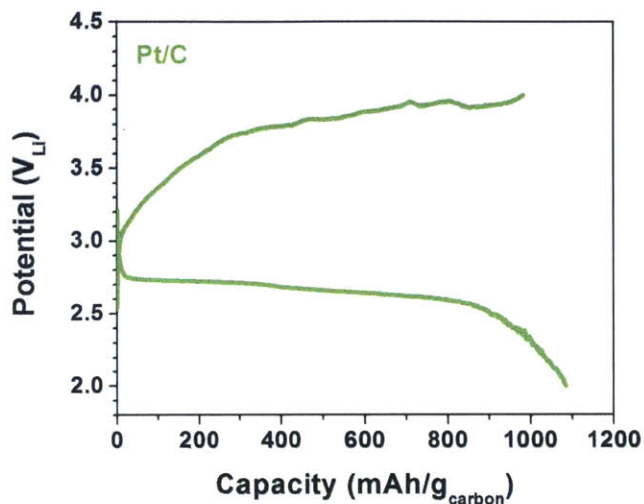
Figure 2-13. Discharge and charge profiles of Pt/C in a Li-O$_2$ cell at 100 mA/g$_{carbon}$.

2.3.3.3 Charging of Ru/C and Li$_2$O$_2$.

Ru/C was shown to exhibit high activities toward Li$_2$O$_2$ oxidation similar to Pt/C, as shown in Figure 2-11c. The oxidation current densities promoted by Ru/C reached 1000 mA/g$_{carbon}$ at 3.9 V$_{Li}$, and Ru/C remained reasonably active (providing 100 mA/g$_{carbon}$) at 3.6 V$_{Li}$. High catalytic activity of Ru/C toward Li$_2$O$_2$ oxidation was further confirmed by XRD analysis of charged electrodes, where Li$_2$O$_2$ could be oxidized and largely removed at 3.8 V$_{Li}$ (~1200 mAh/g$_{carbon}$) (Figure 2-12) as evidenced by the absence of Li$_2$O$_2$ in a fully oxidized electrode (Figure 2-14).

The capacities associated with Li$_2$O$_2$ oxidation catalyzed by Ru/C were comparable to the expected capacity based on the Li$_2$O$_2$ amount in the pristine electrode (1180 mAh/g$_{carbon}$). Like VC and Au/C, no additional oxidation was observed at the end of charging below 3.9 V$_{Li}$, which indicates that Ru/C did not significantly catalyze electrolyte decomposition.
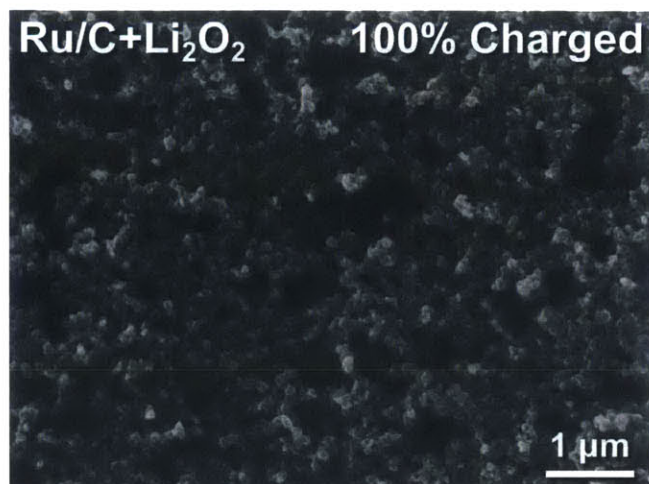
Figure 2-14. SEM of a fully charged Ru/C+Li$_2$O$_2$ electrode. No Li$_2$O$_2$ is visible, and holes in the carbon structure indicate where Li$_2$O$_2$ was originally located.

Pt/C and Ru/C were found to have comparable activities, which were significantly greater than that of VC and Au/C. The average currents of Li$_2$O$_2$ oxidation during the first 20% of the capacity (Figure 2-15) are shown as a function of applied potential in Figure 2-16, which can be used to compare the activities of Vulcan carbon and catalyzed Vulcan carbon. Interestingly, the oxidation currents from Pt/C and Ru/C are more than two orders of magnitude higher than VC and Au/C, indicative of markedly enhanced activity for Li$_2$O$_2$ oxidation. This result indicates Pt and Ru are active catalysts for Li$_2$O$_2$ oxidation; the lack of activity enhancement by Au discounts any contribution of electrical conductivity to the observed results. Additionally, a linear trend was observed between the logarithm of Li$_2$O$_2$ oxidation current and applied potential, where the Tafel slope was found to be ~250 mV/decade. As one-step, one-electron reactions give a Tafel slope of 60 mV/decade, the origin of such a high Tafel slope is not understood, and will be investigated in future studies.

50
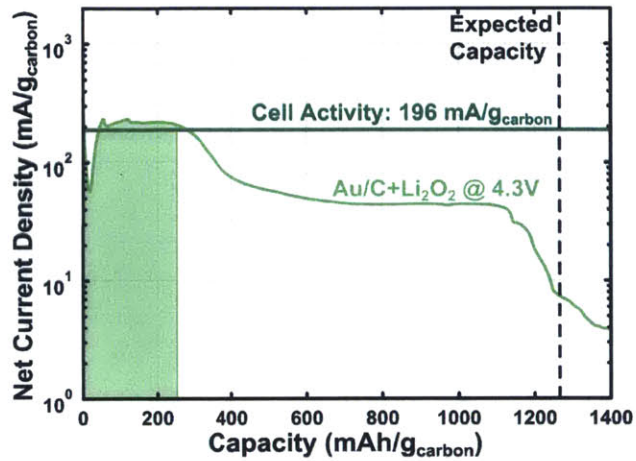
Figure 2-15. Example integration process for calculating cell activity for an example Au/C+Li₂O₂ cell at 4.3 V.
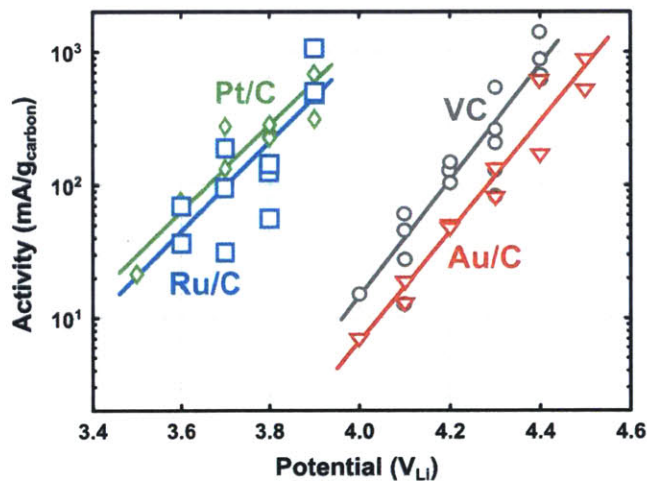
Figure 2-16. Activity *vs.* potential for all VC, Au/C, Pt/C, and Ru/C electrodes. Activity is calculated from the average current measured during the first 20% of discharge.

2.3.4 Initiation of Li₂O₂ Oxidation on Vulcan Carbon and Catalyzed Vulcan Carbon
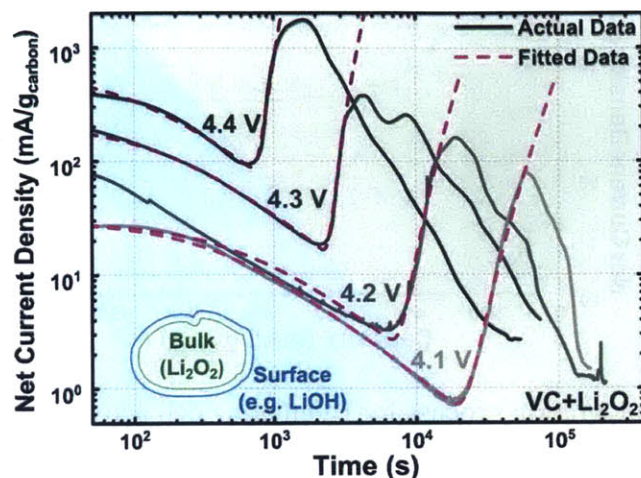
Figure 2-17. Net mass-normalized current *vs.* time for potentiostatic charging of VC+Li₂O₂ electrodes, on a log-log scale. Solid, lines are measured data. Dashed are fitted using a least squares best fit to Equation 2-1.

The oxidation currents of Li₂O₂ with VC and Au/C were found to first fall slowly and then rise sharply upon initial charging (<50 mAh/g$_{carbon}$) in Figure 2-7 and Figure 2-11a. It should be noted that the initiation takes a very long time (~10^4 s at 4.1 V$_{Li}$) for Vulcan carbon and Au/C. This initiation was fit to a simple numerical formula relating net current density (i) to time (t), containing four adjustable parameters (Equation 2-1): a, b, c, and t_0, as shown in Figure 2-17.

$$i = \frac{a}{t+b} + c(t - t_0)^3 \tag{2-1}$$

The values of the constants and quality of fit for fitted oxidation currents of Vulcan carbon in Figure 2-17 are available in Table 2-1. The first part of the formula relates current to the inverse of time plus a constant, which dominates at low times. The second portion of the equation relates current to the cube of time minus an offset, which describes the initial rise of the primary Li₂O₂ peak. The cubic form of the equation suggests 3D nucleation with a constant rate of site formation

for Li_2O_2 oxidation.[85] To account for the large time delay (t_0) observed for Vulcan carbon and Au/C, it is hypothesized that the surfaces of Li_2O_2 particles might have different chemical compositions from bulk, which have more sluggish oxidation kinetics than Li_2O_2. For example, the surfaces of Li_2O_2 particles might be covered by XRD-amorphous LiOH. This hypothesis is supported by the fact that the time delay was found to scale exponentially with potential. A linear regression between potential and the logarithm of the delay in initiation for Li_2O_2 oxidation on Vulcan carbon was found with a goodness of fit of 99.8% (Figure 2-18).

Support for the slower kinetics for Li_2O_2 particle surfaces than bulk also came from galvanostatic testing, where the 100 mA/g_{carbon} charging voltage was found to drop from ~4.4 V_{Li} initially to ~3.9 V_{Li} after ~80 mAh/g (Figure 2-19). At moderate currents, such as 500 mA/g_{carbon}, which was regularly exceeded during potentiostatic testing, cells were observed to auto-terminate

Table 2-1. Fitting parameters and goodness of fit for Equation 2-1 on the cells shown in Figure 2-17. The fit was calculated using the logarithm of current to prevent overweighting of high-current behaviors. Sampling points were evenly distributed between the decay and rise portions of the current profile, and distributed logarithmically with time in each region.

Potential (V_{Li})	a	b	c	t_0	R^2
4.4	7.4×10^4	130	1.7×10^{-5}	660	99.0%
4.3	4.1×10^4	180	1.7×10^{-7}	2100	99.5%
4.2	1.5×10^4	210	1.2×10^{-10}	5300	96.7%
4.1	1.4×10^4	420	1.3×10^{-12}	16000	99.7%

immediately after the initial voltage spike. This was observed repeatedly and consistently at the same location, and severely limited the usefulness of these galvanostatic tests. These phenomena have not been observed with the charging of Li-O$_2$ cells in literature,[37,42,76] and can be attributed to different surface compositions between the commercial, chemically prepared Li$_2$O$_2$ used in this study and electrochemically formed Li$_2$O$_2$ during Li-O$_2$ cell discharge.
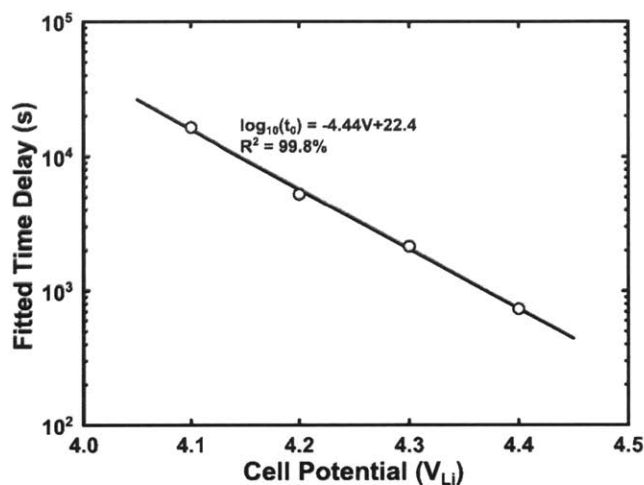
Figure 2-18. Fitted time delay *vs.* charged cell potential for the four cells presented in Table 2-1.
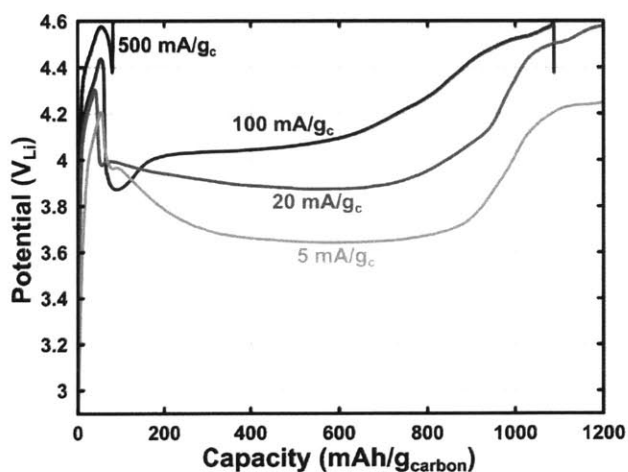
Figure 2-19. Potential *vs.* capacity for galvanostatic charging of VC+Li$_2$O$_2$ electrodes. All currents were normalized with respect to carbon mass.

54
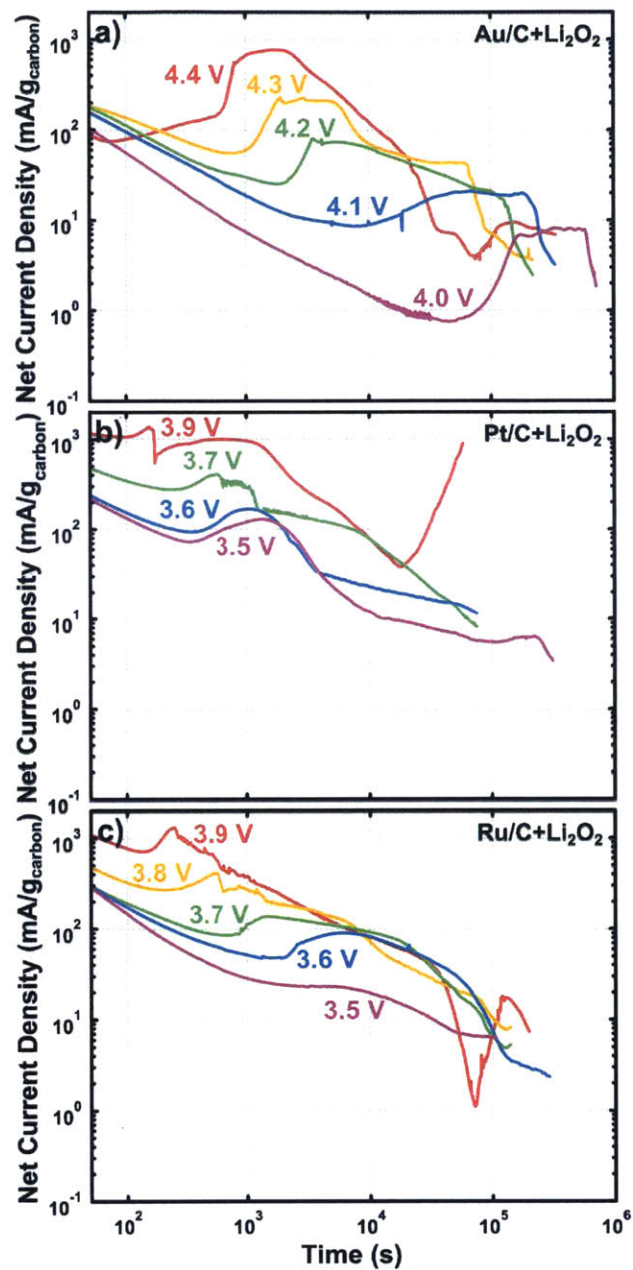
Figure 2-20. Net current vs time on a log-log scale for (a) Au/C+Li$_2$O$_2$, (b) Pt/C+Li$_2$O$_2$, and (c) Ru/C+Li$_2$O$_2$

Unlike oxidation of Li$_2$O$_2$ catalyzed by VC or Au/C, large current densities of Li$_2$O$_2$ oxidation catalyzed by Pt/C and Ru/C were noted for all applied potentials in the early stages of oxidation, where the current reached a maximum shortly after the onset of charging and then dropped

steadily (Figure 2-20). The initiation time for Li_2O_2 oxidation was much shorter for Pt/C and Ru/C than Vulcan carbon and Au/C, which might be explained by higher catalytic activities for oxidation of Li_2O_2 particle surface species such as LiOH than Vulcan carbon and Au/C.

2.4 Conclusions

The round-trip efficiency of rechargeable Li-air batteries is limited largely by the large overpotential upon charging, which can be attributed to slow oxidation kinetics of Li_2O_2 formed on discharge. In order to develop strategies into lowering the charging potentials of Li-air batteries, we have performed a systematic study to examine the effect of catalysts on the electrochemical oxidation kinetics of Li_2O_2. We have found that Vulcan carbon and Au nanoparticles supported on VC have comparable activities and only become active for Li_2O_2 oxidation at voltages greater than 4.0 V_{Li}, while Pt and Ru nanoparticles supported on VC become active at voltages greater than 3.5 V_{Li} and significantly reduce the overpotential required to oxidize Li_2O_2. As Pt appears to catalyze electrolyte decomposition more than Ru, we therefore conclude that Ru is a promising catalyst to reduce the round-trip efficiency of rechargeable Li-air batteries.

2.5 Acknowledgements

Chapter 3

Design, Construction, and Demonstration of a Differential Electrochemical Mass Spectrometer for Nonaqueous Lithium–Air Batteries

3.1 Introduction

The chemistry of Li–air and Li–O_2 batteries remains a significant challenge to the development of practical devices using these chemistries, as discussed in Chapter 1. In particular, reactions between discharge products or their intermediates with the electrolyte and electrode material have received a great deal of attention in the past several years,[53] with a number of undesirable side reactions identified for a variety of systems.[41,52,72,76,86,87] Reactions between oxygen and the electrolyte at the high potentials required to charge such batteries are also a concern (see Chapter 5),[87,88] as are any possible reactions with catalysts included to reduce the charging potential (see Chapter 2).[42,45,46,84,89] Added to these challenges is the difficulty of detecting and identifying the products of these unwanted reactions; many of these products are amorphous (preventing the use of diffraction techniques)[37,38,45,72,90,91] and lack elements heavier than oxygen (increasing the complexity of X-ray spectroscopy techniques, although not eliminating their use[40,41,47,92]). Raman[30,33,55,83,93] and Fourier transform infrared[35,41,80,94–98] spectroscopy have found wide use in characterizing these products, but these techniques cannot easily be used to quantify discharge products. For these reasons, differential electrochemical mass spectrometry (DEMS) has become popular as a tool for quantitatively determining the consumption and production of various gases during the operation of Li–O_2 batteries.[50,51,80,99–102] In spite of the importance of this technique, DEMS systems are not commercially available at the time of publication, and neither the Electrochemical Energy Lab nor the Hammond Lab have previously had access to a DEMS instrument. For these reasons, we set out the build and demonstrate a DEMS system in our lab. This chapter summarizes these efforts and shows the results of initial experiments using this tool on a number of relevant systems currently in use in our lab. Further results from this instrument are presented in Chapters 4 and 5.

58

DEMS was first developed in the 1980s[103] and became more widely popularized during the 1990s,[104–107] primarily in the context of characterizing the gases evolved in fuel cells and electrolyzers. The recent popularity of metal-air batteries, and in particular Li–O_2 batteries, has further driven the development of new types of DEMS systems suitable for characterizing those systems.[83] As a result of the gradual evolution of the DEMS technique, a number of systems with different capabilities and principles of operation all exist using the name "DEMS." In an effort to reduce the confusion between these different systems, we have defined three major classifications of DEMS systems (which themselves include variations): direct vacuum DEMS, flow-through DEMS, and discrete DEMS. We provide a brief, albeit incomplete, summary of the history and capability of each of these classes of systems in the following paragraphs.

Direct vacuum DEMS operate by using a frit or other constriction to prevent the flow of electrolyte into a vacuum chamber directly attached to the electrochemical device. Early systems, such as the one developed by Wolter and Heitbaum,[103] used a hydrophobic frit to prevent the flow of aqueous electrolyte into the vacuum system, in which a mass spectrometer (MS) was continuously probing for the presence of gases. This system was further improved by Koper and colleagues,[108] who developed a system where a small porous Teflon tip can be placed in close proximity (10-20 μm) to a single crystal electrode. These systems have a very good response time, but require well-established gas-evolving electrochemical reactions for calibration and an electrolyte that is nearly impermeable to the fit of choice. Gasteiger and colleagues developed a variation on this system for Li-air systems,[87] where the frit is replaced by a calibrated capillary leak placed in the head space of a sealed cell, which they describe as an on-line electrochemical mass spectrometer. Calibration of the capillary leak to the gases of interest allows for quantitative use of this

system, and the design allows continuous reading of the composition of the gas within a cell (rather than the rate of gas production) which motivates the use of "on-line" rather than "differential".

Flow-through DEMS systems instead rely on the quantification of gases with a stream of gas flowing through a cell. Once the gas flow rate is established, then the concentration of species within that gas can be used to infer the rate of gas production. Savinell and colleagues used this technique to characterize the production of gases in direct methanol fuel cells,[109–111] and Novák et al. constructed a system using a similar system to characterize the head gas of nonaqueous lithium-ion batteries,[112] using very large electrodes with a small head space, and work by Bruce and colleagues has applied this technique to Li–O_2 systems. While this technique dramatically simplifies quantification and maintains high response time, measuring the consumption of gas remains difficult, requiring the consumed gas to be included in the feed gas at low levels. This technique is also limited by the ability to flow gas sufficiently slowly that the gases of interest reach the detection limit of the MS.

Discrete DEMS systems are the most recent variant of the DEMS design that have been widely popularized for metal-air battery research. Air cells are connected to a system of valves and isolated for arbitrary periods of time. When a measurement is taken, a fixed volume sample of gas is removed from the cell and replaced with fresh fill gas (of known composition). This sample is then dosed into a vacuum chamber where an MS is used to characterize its composition. This technique is used by several research groups for metal–air battery research, with McCloskey and colleagues building a system capable of testing 16 cells simultaneously,[50] and the scientists at Liox Power and other companies having developed similar systems.[113] Using the discrete DEMS design allows for trivial detection of gas consumption (such as during discharge of Li–O_2 batteries) via pressure tracking. Detection of slowly produced gases can be performed by simply reducing the

60

rate that measurements are taken, and a properly designed vacuum system can eliminate the fractionation effects that occur when capillary leaks are used. This system can also allow for the efficient use of resources, as one MS can be used to analyze many different cells in turn, provided that software is developed capable of managing the different cells. Because this is a sealed system, the cell volume and volumes within the rest of the DEMS system must be known precisely for the most accurate results.

As stated above, a number of research groups investigating Li–O₂ batteries have used DEMS analyses in the past several years. McCloskey and colleagues have been very prolific in their use of DEMS,[34,39,42,50,52,71,83] investigating the consumption and generation of oxygen and carbon dioxide in many different electrolytes in an effort to understand the mechanisms of Li_2O_2 formation and oxidation and the side reactions observed in Li-air batteries. The scientists at Liox Power have also published a number of studies using DEMS analysis with amide-based electrolytes,[94,100,113–116] although their results are not calibrated to allow quantification of gas production. Gasteiger and colleagues have used DEMS to investigate oxygen production when charging Li_2O_2-preloaded electrodes,[35,36,99] and recently in investigations into the use of solvating additives in Li–O₂ batteries,[38] while Bruce and coworkers have also used DEMS extensively in their efforts to develop a combination of electrode and electrolyte that can be stably cycled without reactions in the electrode or electrolyte.[30,54,70,76,80,117] Finally recent work by Adams et al. used DEMS while characterizing the enhanced stability of a newly developed solvent for Li–O₂ applications.[51]

3.2 Design and Construction of DEMS System

After considering the different types of DEMS systems described above, we chose to construct a discrete DEMS system, based on the design published by McCloskey et al.[52,83] Discrete

DEMS systems are well suited for use in nonaqueous metal–air battery research, as the long cycling time of Li–air batteries prizes the ability to test multiple cells simultaneously over the higher time resolution of other techniques. Furthermore, unlike lithium-ion batteries, fuel cells, or electrolyzers, metal–air batteries must both consume and produce gas during normal operation, so the ability to accurately and easily measure gas consumption without use of the MS is beneficial.
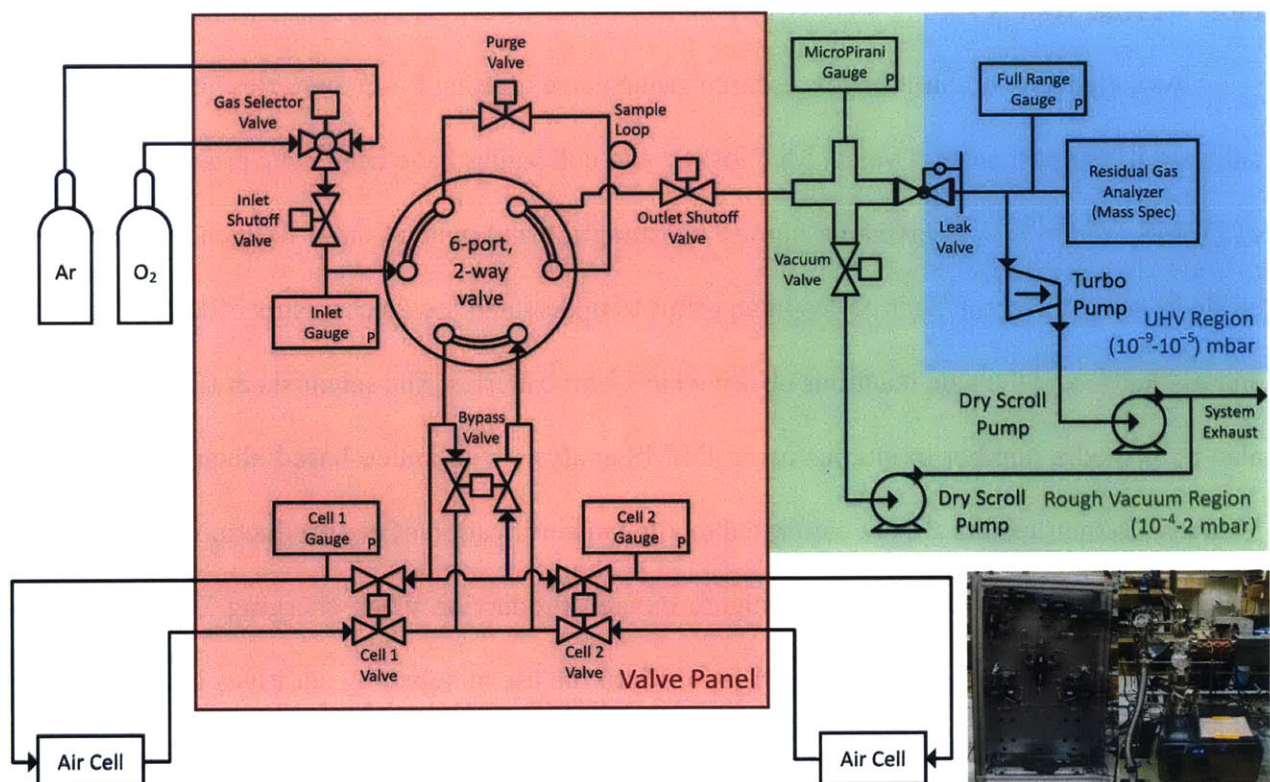
Figure 3-1. Schematic of the valves, pressure gauges, transducers, and MS for the DEMS. Blue indicates UHV, green indicates rough vacuum, and red indicates valves and gauges mounted on the valve panel. Bow-tie shapes indicate valves, and black lines indicate tubing or piping. Arcs indicate tubes that cross but are not connected, while intersections indicate connections. The section of tubing labelled sample loop holds the gas that is dosed into the vacuum region for analysis. Inset picture shows the valve panel and vacuum regions of the constructed DEMS.

3.2.2 Vacuum System & Mass Spectrometer

The vacuum system and MS comprised the majority of the expenses for the DEMS system, as the vacuum pumps and MS each represent a significant fixed cost. The vacuum system was comprised of two separate regions, noted as the rough vacuum and ultra-high vacuum (UHV) regions in Figure 3-1 (in green and blue respectively).

3.2.2.1 UHV Region and MS

The MS is a residual gas analyzer (RGA), which requires UHV conditions ($<1\times10^{-4}$ mbar) to operate. We chose to use the same RGA as McCloskey et al. used, an SRS RGA200 (Stanford Research Systems, USA), with the capability to scan up to 200 amu compounds. The RGA200 has a max operating pressure of 1.3×10^{-4} mbar and a max linear response pressure of 1.3×10^{-5} mbar. Vacuum was maintained in the UHV region by an Agilent TPS Compact Turbo pump system with TV81M Turbo pump and IDP-3 dry scroll backing pump. This Turbo pump system is rated to a base pressure of 1×10^{-9} mbar. UHV pressure is measured with an Agilent FRG-700 Inverted Magnetron Pirani (Full Range) gauge, which is capable of measuring pressures from 5×10^{-9} mbar up to atmospheric pressures, with 30% accuracy in the UHV region. This gauge is primarily used for diagnostics purposes, and is not used in analyzing the DEMS results. All connections in the UHV region are made with ConFlat fittings with a copper gasket.

3.2.2.2 Rough Vacuum Region

The rough vacuum region consists primarily of a 5-way cross with NW25 (1 in) fittings. This region is pumped by an Edwards nXDS15i dry scroll pump, with a maximum pumping speed of 15 m^3/h and a rated ultimate pressure of 7×10^{-3} mbar. The large pump was chosen to ensure that the rough vacuum region is rapidly evacuated after gas is introduced, allowing for fast turnaround between DEMS measurements. A pneumatically operated valve (LDS Vacuum Products, Inc.

PAIV-1002-NWB) separates the 5-way cross from the dry scroll pump, allowing sample gas to be held in the rough vacuum region when an MS measurement is taken. An MKS 925 MicroPirani vacuum transducer (MKS Instruments, Inc., 1.3×10^{-5} mbar to atmosphere, $\pm10\%$ accuracy) is attached to the 5-way cross, and communicates with the control computer via USB. Like the UHV pressure gauge, this gauge is used for diagnostics purposes only. One of the arms of the 5-way cross is blanked off (for future use). The remaining two arms connect to the rest of the DEMS system (described below) and to the UHV system via a variable leak valve (Agilent Model 951-5106). The variable leak valve is manually adjusted so that the maximum pressure in the sample cross when taking a reading (approx. 2 mbar) corresponds with the maximum operating pressure of the RGA (approx. 1.3×10^{-5} mbar).

3.2.3 Valve Panel and Gas Handling System

The remainder of the DEMS system is dedicated to sampling known volumes of gas from the connected cells and delivering that gas to the vacuum system for analysis (gas handling system). The valve panel contains a number of different components including valves, pressure transducers, temperature recorders, and connections to the air cells. We consider each of these in the discussion below. The red region in Figure 3-1 shows the arrangement of valves and pressure gauges used in the gas handling system.

3.2.3.1 Valves and Tubing

All valves shown in the red region Figure 3-1 are pneumatically operated, and can be controlled (along with the valve described above in the rough vacuum region) via computer. The 6-port valve is a switching valve designed for gas chromatography applications (VICI model A2C6UWE), with 1/16 in Valco® fittings and a 0.75 mm bore. Each port is connected to one of its two neighbors at all times, and these connections can be switched via the pneumatic actuator. All

64

other valves mounted on the valve panel are Swagelok® ball valves with pneumatic actuators. The Inlet Shutoff Valve and Purge Valve are both single on-off ball valves with 1/16 in fittings. The Outlet Shutoff valve is a ¼ in on-off ball valve with VCR fittings. The Gas Selector valve is a 3-way, 2-position ball valve with 1/16 in fittings, and the Bypass and Cell Valves are double on-off ball valves with 1/16 in fittings. Double valves were used so that a single actuator controls both valves, which reduced the number of actuators needed on the panel.

Stainless steel tubing (1/16 in outer diameter, type 316 stainless steel) is used to connect all the valves and fittings together. The sample loop (noted on Figure 3-1) was provided by VICI, and had an estimated internal volume of 250 µl, although this estimate is not calibrated. Fittings inserted into the 6-port valve were ordered precut and electropolished from Upchurch Scientific. Flexible stainless steel tubing is used to connect the argon and oxygen gases.

3.2.3.2 Pneumatic Valve Control

A pneumatic valve manifold (Numatics G3) was installed to control the valves listed above. Each valve actuator is connected to the manifold with plastic tubing, and entire manifold is connected to a tank of industrial grade nitrogen. The manifold interfaces with the computer over Ethernet, using the MODBUS TCP/IP protocol to probe and set the valve positions.

3.2.3.3 Atmospheric Pressure Transducers

The pressure transducers used on the DEMS panel were all Omega PX409-USBH pressure transducers with an operating range from 0-30 psia, an accuracy of ±0.08%, temperature compensation of ±0.5%, and set to take 5 samples per second. Each gauge connects independently to the computer via USB. Initially, each pressure gauge was connected to the rest of the tubing via a simple tee fitting; it was later found that doing so led to a reservoir of gas at the gauge that could only be flushed by pulling vacuum and refilling, and would otherwise slowly diffuse into the main

gas flow path. An alternative tube arrangement was devised using bored-through Swagelok fittings that allow a smaller diameter tube to be inserted into a larger one. The arrangement of tubes is shown in Figure 3-2, and was implemented on the pressure gauges connected to each cell. The inlet pressure gauge was not modified, as it can be safely evacuated whenever the supply gas is changed.
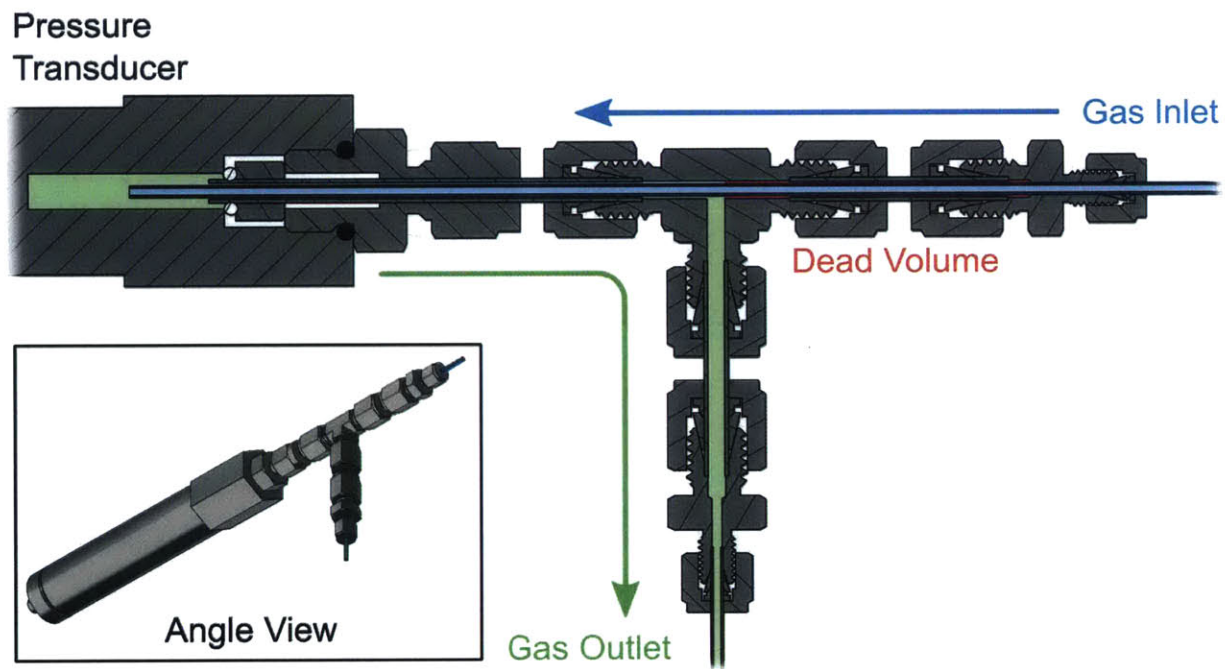
Figure 3-2. Cross-sectional view of the tube arrangement used to flush gas through each pressure gauge. Blue indicates gas flowing into the transducer, green indicates gas leaving transducer. The red region highlights the small dead volume from this arrangement. Image is to scale. Inset depicts an external view of the gauge and fittings.

3.2.3.4 Temperature Recording

After this system was initially constructed and undergoing validation, oscillations were observed in the pressure as read by all of the gauges, even when the system was flushed with argon and not expected to produce gas. Initial temperature measurements showed that these oscillations

66

corresponded to temperature changes of <0.2 °C. Thermistors (Omega TH-10-44007, 5000 Ω at 25 °C) were placed at each of the pressure gauges and attached to any cells when operating, and an ADC designed for temperature measurements (temperature measurement unit, Omega OM-USB-TEMP) was connected to the system, allowing temperature data to be collected in addition to pressure data at each pressure gauge and cell. In addition, efforts were made to stabilize the temperature on the DEMS panel (a polycarbonate enclosure with door was designed and installed around the panel) and at the cell (either by enclosure in a temperature chamber or a simple cardboard box with paper packing). The combination of stabilizing and recording the temperature allowed for improved temperature corrections (Figure 3-3), but large temperature swings (> 0.5 °C) were still found to cause slight deviations in the temperature corrected data.
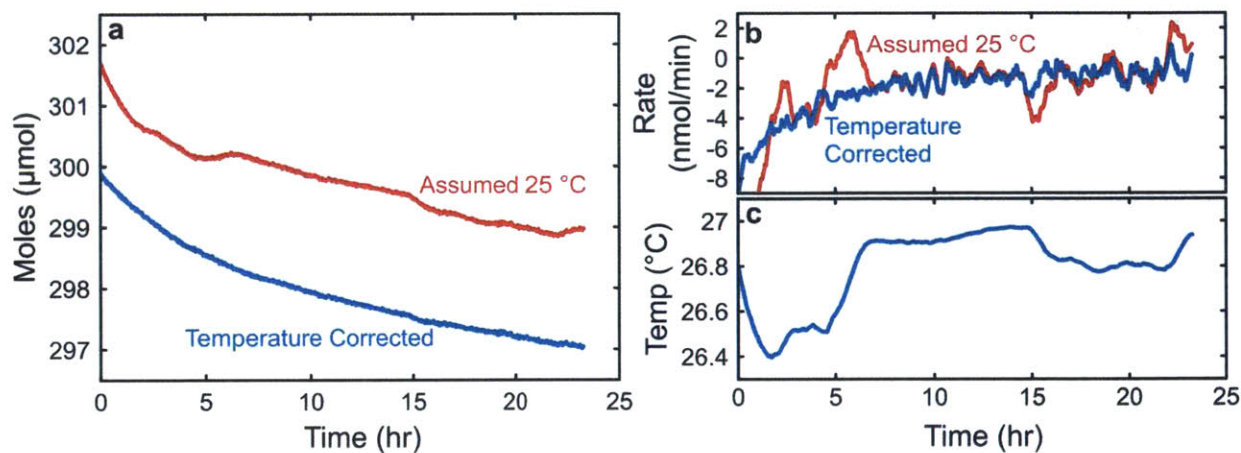
Figure 3-3. (a) Total moles of gas, (b) rate of change in moles of gas, and (c) Temperature vs. time with and without temperature correction. The cell used did not have electrolyte or electrodes. Temperature shown in (c) is the effective total temperature for the gas in the cell and at the gauge. The initial fall in total moles is attributed to temperature equilibrations inside the cell, while the long-term decline is attributed to a slight leak of 1.0 nmol/min (4.1×10^{-7} std cm^3/s).

3.2.3.5   Cell Connection System

Next, we turn to the system for connecting cells to the valve panel. To maximize the available options for future tests, it was desired to have long, flexible tubes connecting between the valve panel and cell. Furthermore, these tubes needed to be insulating, as the cells needed to maintain electrical isolation from the pressure gauges and other electronics, while also having low internal volume and low permeability to water and air. Minimizing the volume increases the sensitivity of pressure measurements and reduces the dead volume of the exhaust (which can impact the gas analysis). Commonly available materials did not meet these requirements; stainless steel is neither flexible nor insulating, while most polymers suffer from relatively high gas permeability, especially when considering long tubes with small diameter. PEEKSil™ tubing was found to be the optimal solution; a central tube of fused silica (commonly used for gas chromatography applications with low permeability) is coated with PEEK to reach the desired outer diameter. This results in flexible, nonconductive tubing that has low gas permeability and fits into normal 1/16 in Swagelok fittings. PEEKSil tubing with 1/16 in outer diameter, 530 μm inner diameter, and 50 cm length was ordered from SGE Analytical Science. 2-3 segments were connected together with Swagelok unions to reach the desired length of tubing connecting the cell to the valve panel.

In addition to the tubing, several mechanisms for attaching cells to the DEMS were considered. It was required that the fittings must be reliable and repeatable, maintain a good seal, and have minimal volume. Directly connecting and disconnecting Swagelok fittings to and from the cell was rejected as unreliable; an improperly tightened fitting could result in a leak or even damage the fitting. Use of a single-ferrule fittings (as used by McCloskey *et al.*[83]) was also rejected as unreliable, as these fittings are difficult to tighten consistently in a leak-proof manner. Initial ex-

periments used miniature quick-connect fittings (Swagelok SS-QM2 type) to make this connection. However, these fittings have a large number of seals and internal parts, which were susceptible to attack by the electrolyte solvents and cross contamination. Because of this, the quick-connect fittings were replaced with VCO fittings (Swagelok SS-4-VCO fittings), which rely on a single O-ring compressed between a stainless steel body and gland to seal. These fittings are both repeatable and reliable; once tightened, the fitting is rated have a rated leak rate of less than 4×10^{-9} std cm^3/s, suitable for high vacuum. The fittings cannot be easily overtightened, which allows users to be confident that their fittings are properly tightened, and the O-ring material can be trivially changed between each use; PTFE O-rings are preferred, and they are replaced each time a connection is remade. The one disadvantage to using VCO fittings is their relatively large internal volume. Off-the-shelf VCO fittings from Swagelok are relatively large, and the smallest ones are designed for ¼ in tubing. Each VCO fitting is estimated to be 0.25 ml in the current system, and it is suggested that custom machined and welded parts be used in the future to reduce the volume of these connections.

3.2.4 Air Cells for DEMS

Finally, we consider the design of the cell used for DEMS experiments. Although the appropriate VCO fittings can be attached to virtually any cell design, doing so may not result in the best results for this system. A new cell was designed with significant modification from the Li–O₂ air cells used in the Electrochemical Energy Lab. In additional to the requirements of any battery (electrical isolation between the electrodes), the requirements for the cell were as follows:

- The contents of the cell must remain isolated from air at all times.

- The cell should have a repeatable and reliable seal system.

- The internal cell volume should be as low as possible.

The design previously published by our group[28] uses two PTFE O-rings on either side of a PTFE spacer to seal the cell, and uses four screws to hold the top and bottom plates together. This design results in a much higher than necessary volume (DEMS volume measurements using the procedure described below estimate the cell volume to be ~6 ml excluding fittings). Furthermore, the use of two O-rings and a deformable PTFE spacer increase the number of possible leak locations, and the use of only four screws increases the likelihood of skewing between the top and
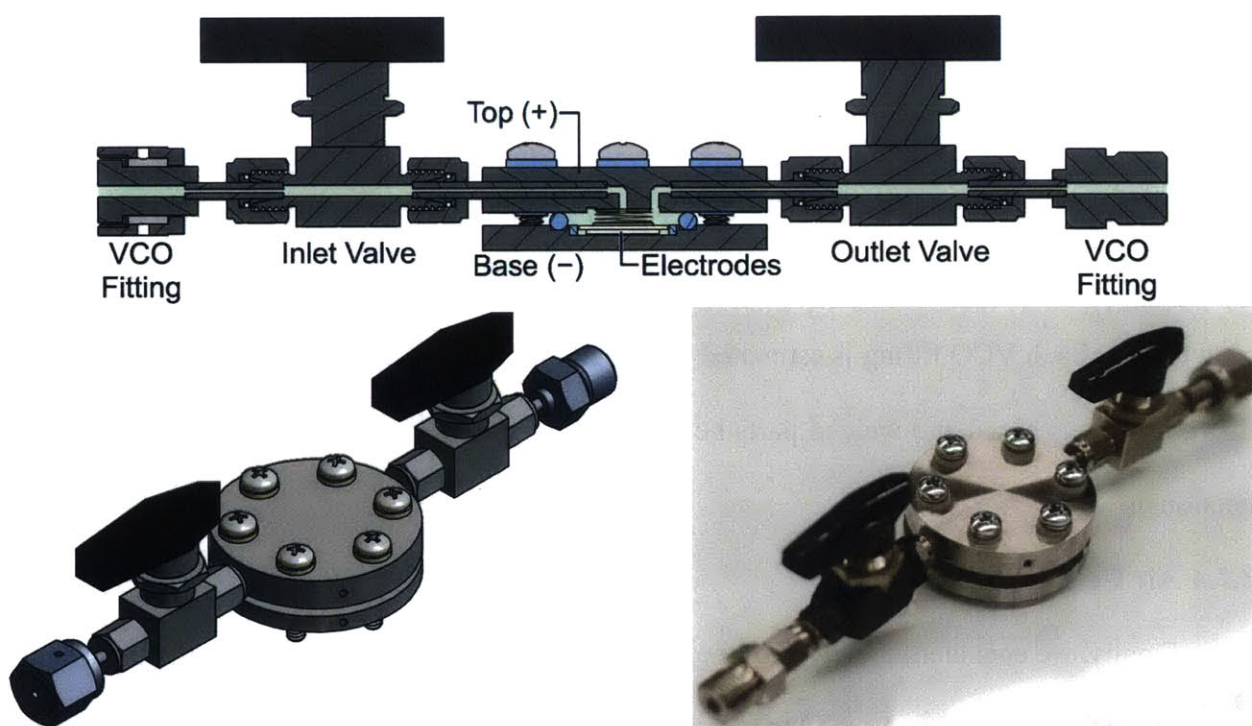
Figure 3-4. Cross-sectional (top) and angle (bottom) views of the cell designed for DEMS experiments. Grey indicates stainless steel, blue indicates insulating plastics, and cross-hatching indicates a region that has been sectioned. The black handles are used to open and close the valves which isolate the cell. Drawings are to scale (top: 2:3, bottom left: 1:2). Light green shading indicates the region that is connected to the DEMS. A picture of the cell as constructed is shown in the bottom right.

bottom plates, which also increases the chance of leaks. We designed a new cell that attempts to address all these issues (Figure 3-4).

The seal for the new cell design was changed to use a single O-ring for sealing, which is in contact with both the top and bottom of the cell. The top of the cell was changed to have an inset groove rather than a post for spring alignment, and the base of the cell has a single well to contain both electrodes. A removable PTFE ring can be installed to line the walls of this well, protecting the cell from shorting. Six screws are used, which help balance the force across the cell while tightening and prevent skewing. Finally, two valves are attached to the inlet and outlets of the cell, which are kept closed when connecting the cell to the DEMS system. To further reduce the volume, the tubes are directly brazed onto the cell body and VCO fittings rather than using standard Swagelok fittings. The volume of this cell, as measured by the DEMS system, is approx. 2.60 ml including the VCO fittings.

3.2.5 Computer Control Software

In addition to having the hardware the hardware in place, software was required to control the valves and coordinate the disparate data sources. Although the pressure transducers, temperature measurement unit, and MS each came with their own software, these applications were not designed to interface with each other or to allow programmatic control over when and how data should be recorded. We developed a LabVIEW application to control and read from all of the different devices necessary to operate the DEMS. LabVIEW was selected because the pressure transducers from Omega, the temperature measurement unit, and the MS each provided LabVIEW drivers for interfacing with these units.

The overall design of the software written is explained in Appendix B, but the software can be roughly considered as having two distinct components: a logging functionality, and a valve

71

control functionality. The logging program collects data from one or more of the devices at a user specified frequency (averaging is used when the sample frequency is lower than the device update frequency) and writes this data to a file. This functionality is primarily necessary for pressure tracking experiments, where pressure and temperature data is recorded and analyzed continuously, but is also useful when conducting instrument diagnostics. The valve control program allows the user to schedule pre-programed and custom-written sequences of valve actions, and is critical for performing volume and DEMS measurements. In addition to simple valve control, the valve control program is capable of collecting data from the various instruments at specific times during the operation of a valve sequence. This allows MS data to be recorded only when gas is being sampled to the MS, rather than requiring extraction of that data from a stream of continuously recorded data.

3.2.6 Measurement Procedure

A detailed discussion of how measurements and calibrations are performed is available in Appendix A. These techniques are briefly described here to aid in understanding the results below.

3.2.6.1 Volume Calibration

Accurate measurement of the cell volume requires accurate knowledge of the volume of various components of the DEMS system. Volumes are calibrated by attaching a variety of known-volume sample loops (supplied by VICI and Upchurch Scientific) to the valve panel at various locations. With each sample loop, a variety of measurements are performed, in which different regions of the valve panel are evacuated, and then gas is expanded from the remaining regions to fill the evacuated portions. The pressure of the gas is recorded before and after the expansion, and the ratio of the final to initial pressure (which is between 0 and 1) is recorded. Each measurement is repeated several times for each sample loop. The data for all sample loops and measurements

72

are compiled together and used to find the volumes of each of the different sections of tubing in the valve panel that best fit the data.

3.2.6.2 Volume Measurement

The principle for measuring the volume of a cell is the same as that used for calibration. Various portions of the valve panel tubing is evacuated and gas from the remaining regions (including the cell of interest) is expanded, and the ratio of final to initial pressure is recorded. The cell itself is never evacuated. Each cell can have three different measurements taken, and several repetitions of these measurements are recommended. These measurements are combined with the data from the calibration process to find a single cell volume that best fits all the measurements together.

3.2.6.3 Pressure Tracking

Pressure tracking experiments are the most conceptually simple experiments that can be performed with the DEMS. After measuring the cell volume, the cell is filled with the desired atmosphere (usually oxygen or argon) and isolated from the rest of the DEMS system. The pressure, temperature at the pressure gauge, and temperature at the cell are logged, and then the total moles of gas in the cell is calculated (using the measured volume, pressure, and temperature for the two regions) with the ideal gas law. If desired, the derivative of the calculated total moles of gas in the cell can be taken to derivate a rate of gas consumption or production. The process used for this calculation is described in Appendix A.

3.2.6.4 Leak Detection and Correction

Leaks are a significant concern for all DEMS experiments, but can be particularly deceptive during pressure tracking experiments, where there is no confirmation of the composition of the cell gas; every effort should be made to eliminate leaks before performing a test. However, very

slow leaks can be difficult to detect until long into or after an experiment has been completed, and it is desirable to be able to use this data regardless. On-line leak detection requires tracking the pressure of the cell for several hours where no production or consumption of gas is expected, and fitting an expected leak rate to this data. Once a leak rate is determined, an adjustment can be applied to the entire body of pressure data to correct for it. Refer to Appendix A for details regarding this calculation. Particular care must be taken when attempting to determine the leak rate of a cell; unexpected side reactions (such as between oxygen gas and the electrolyte) can lead to loss in cell pressure that may appear similar to a leak. Additional phenomena, such as electrolyte evaporation, temperature stabilization, and gas dissolution into the electrolyte can also cause transient changes in pressure for several hours after a cell is first connected to the DEMS. Figure 3-5 shows the results of leak correcting the same data presented in Figure 3-3.
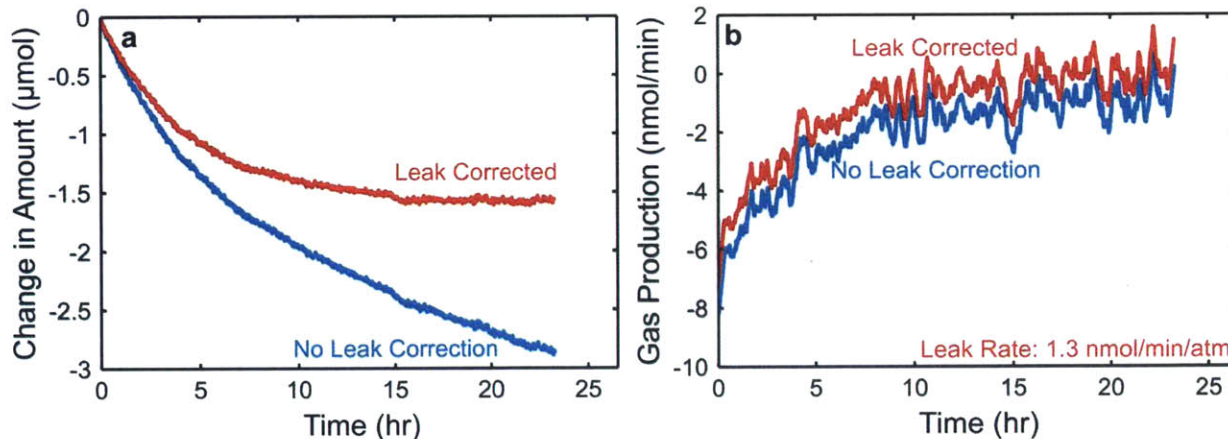
Figure 3-5. (a) Change in moles of gas and (b) gas production rate *vs.* time for the same data as presented in Figure 3-3. The leak rate fitted based on the last 8 hours of resting was 1.3 nmol/min/atm. Because the pressure is essentially uniform throughout this test, this resulted in a consistent shift of 1.0 nmol/min to the gas production rate.

3.2.6.5 DEMS Measurements

The primary objective during each DEMS measurement is to remove a known volume of gas from the cell and dose that into the vacuum system for analysis by the MS. The procedure currently used is somewhat more complicated than this simple description: MS readings are taken for the base vacuum of the UHV chamber, the composition of the fill gas, and the cell gas. The baseline UHV reading can be used to verify that the vacuum was in good condition when the measurement was taken, and partially mitigate species that are persistent in UHV chambers (H_2 and CO are generally present in UHV at higher levels than other gases). The fill gas composition is used to determine the composition of the gas entering the cell. A detailed discussion of the measurement and analysis processes is included in Appendix A. Briefly, during a DEMS measurement, the base vacuum condition is first measured. The tubing is then evacuated and filled with new fill gas (usually argon). A portion of this gas is dosed into the MS for analysis. Finally, the exhaust portion of the tubing is evacuated, and the valve isolating the cell is opened. This causes gas from the cell to flood into the exhaust tubing, and fresh fill gas simultaneously flows into the cell to replace it. A portion of the cell exhaust gas is dosed into the MS. In addition to MS data, the pressure and temperature of the cell (and its gauge) is recorded both before the valve isolating the cell is opened and after it is closed. This is used to determine the total change in moles of gas between one reading and the next, and can be used to confirm that the MS is detecting all the gases being generated. Finally, the time of each DEMS measurement is recorded (based on the opening of the cell valve), so that the time elapsed between each measurement can be determined during the analysis phase.

The raw readings collected from the measurements above are analyzed to produce the rate of production of each gas in the cell. The technique for this analysis is described in detail in Appendix A, but is summarized here. The raw base vacuum reading is subtracted from both the fill

gas and cell gas readings. The raw readings from the MS indicate intensity of signal for particular mass-to-charge (m/z) ratios, and processed via linear transformation into an absolute partial pressure of each gas in the UHV chamber. These partial pressures are summed together to produce a total pressure in the UHV chamber, and the fraction of each gas out of the total is determined. The composition of gas in the UHV chamber is then assumed to represent the composition of the gas sampled from the cell and fill gases, and is combined with the pressure and temperature data to determine the total number of moles of each gas in the cell before the sample was taken. The amount of fill gas added to the cell is then determined based on the known volume of the removed gas and known pressure of the cell after the measurement. This is used to estimate the composition of the cell gas after the measurement was taken. Finally, the measured cell gas composition is subtracted from the previous reading's post-measurement composition, and divided by the elapsed time to produce the number of moles of each analyzed gas produced since the last reading (in addition to the total moles of gas produced, using only pressure data). It should be noted that the production of any individual gas is only sensitive to changes in pressure based on its fraction of the total gas. In most experiments using DEMS measurements, a single inert gas (such as argon) makes up >99% of the cell gas composition at any given time, and so any discrepancy between the pressure and MS readings appears as the production or consumption of this inert gas. Such discrepancies usually indicate an error in the calibration or the production of a gas that is not being detected by the MS.

Two further adjustments are made reflecting the non-homogenous distribution of gas within the cell and connecting tubes. First, the volume of the tubes (including the pressure gauge) between the inlet and the cell is assumed to contain fill gas at all times. Second, the gas analyzed by the MS is assumed to be the gas in the cell at the time of the *previous* measurement (i.e. measurements are

shifted back by one). Both of these corrections are made because the gas within the cell is expected to diffuse very slowly through the 1-1.5 m of tubing between the cell and the valve panel. Shifting the measurements is experimentally validated by observations in the cell response upon sudden changes (such as the onset of charging or changing the sample rate), as can be seen in Figure 3-6.
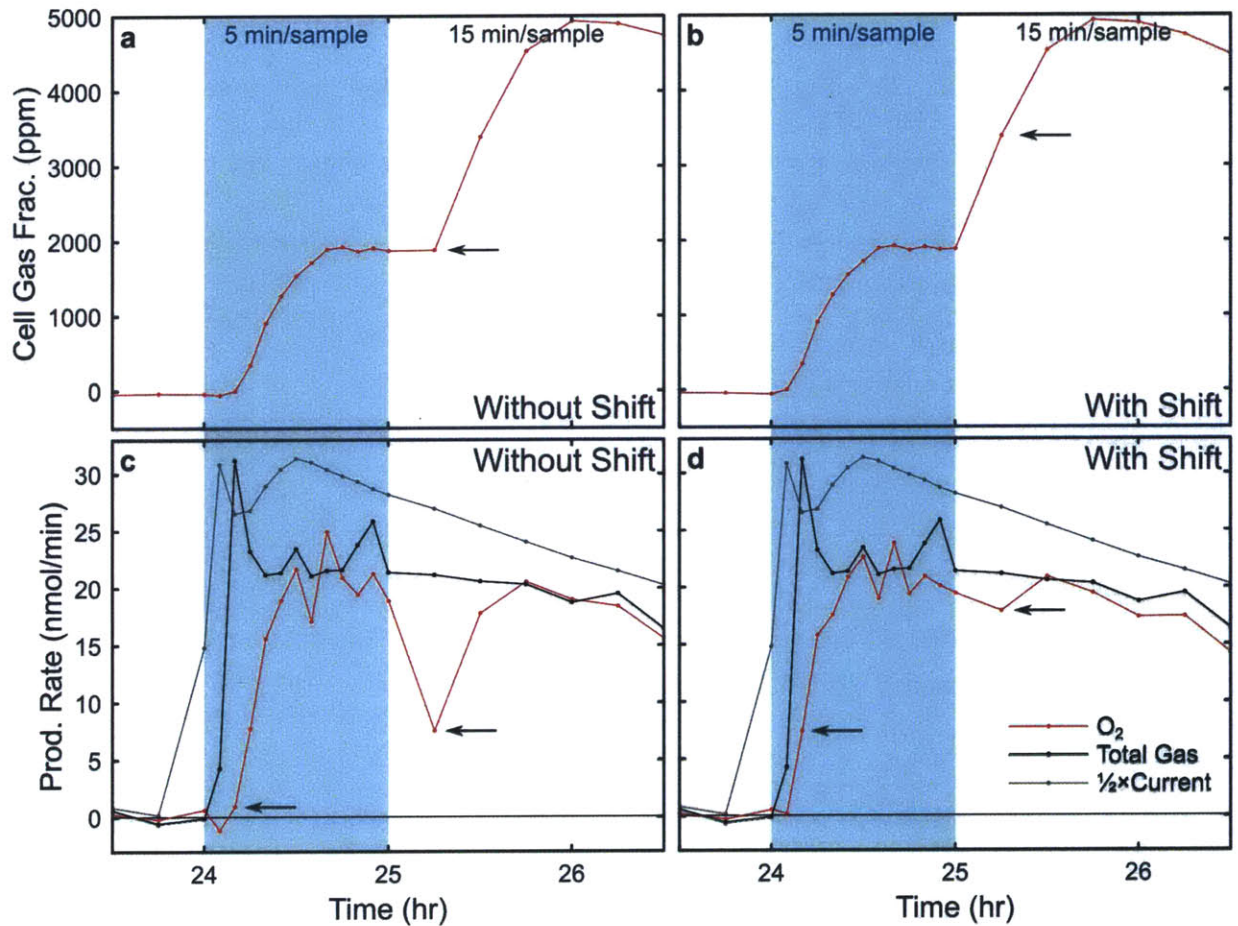
Figure 3-6. Cell gas fraction and production rate *vs.* time (a & b) without and (c & d) with shifting the cell gas readings. The blue region indicates when samples were taken every 5 minutes, white indicates 15 minutes/sample. Arrows indicate improvements in the data after shifting: there is no longer a one reading lag when charging starts or the sample rate changes and there is no dip in oxygen production once the sample rate slows.

3.3 Demonstration of Capabilities

The DEMS system was used to perform preliminary investigations of several systems that are currently under investigation in the Electrochemical Energy Lab. As discussed in the introduction, DEMS analysis has been used extensively by several groups doing research on Li–air batteries, and it is important to compare the results obtained from these preliminary results with previously published systems. We investigated the following systems using diglyme-based electrolytes (diethylene glycol dimethyl ether): Vulcan carbon (VC)-based electrodes cycled galvanostatically, carbon nanotube (CNT)-based electrodes cycled galvanostatically, and Li_2O_2-pre loaded electrodes charged potentiostatically. Diglyme was used in place of 1,2-dimethoxyethane (DME) due to its significantly lower vapor pressure. VC electrodes were used because VC-based systems have been widely used in the Li–air field as a standard air electrode material, while CNT-based electrodes were used because they have been used in several studies from our group and are a promising platform for both Li–air research and as high capacity devices, as they are both binder-free and have extremely high surface area and porosity. We chose to investigate Li_2O_2-preloaded electrodes in order to further validate the results of catalyzed oxidation of Li_2O_2 shown in Chapter 2. Additional investigations using polyethylene oxide-based electrolytes are discussed in Chapters 4 and 5.

3.3.1 Experimental Methods

3.3.1.1 Electrode Preparation

XC-72 Vulcan carbon (VC; Premetek, USA), Lithiated Nafion® (Li-Nafion; LITHIon™ dispersion, Ion Power, USA), and Celgard C480 (Celgard, USA) were obtained from their respective suppliers. VC was dried at 70 °C overnight under vacuum before storage in an argon-filled glovebox (<0.1 ppm O_2, 0.1 ppm H_2O, MBraun). VC, Li-Nafion, and isopropanol were horn sonicated

outside the glovebox until a uniform slurry was formed (approx. 15 minutes). The slurry was deposited onto Celgard C480 using a #40 Mayer rod. The resulting film was allowed to dry in air, then punched into ½ in diameter disks using a circular hole punch. Electrodes were collected and dried together under vacuum at 70 °C overnight, and transferred into the argon glovebox for storage until use.

CNT electrodes were synthesized using previously published thermal chemical vapor deposition technique,[41,118] then dried at 100 °C for >8 hours under vacuum, and finally transferred into the argon glovebox for storage until use.

Li_2O_2 (Alfa Aesar, Purity $\geq$ 90%) was ball-milled using the procedure described in Chapter 2, and stored in the glovebox before and after ball milling. Ru nanoparticles (Ru NPs, Sigma Aldrich, purity $\geq$ 98%) were dried overnight under vacuum at 100 °C and transferred to the glovebox without exposure to air. 40 wt% Pt on VC (Pt/C) was purchased from Premetek and dried overnight at 70 °C under vacuum before transfer to the argon glovebox. Li_2O_2-preloaded electrodes with Ru NPs (Ru/C+Li_2O_2) were prepared following the procedure in Yao et al.:[84] Ru NPs, VC, Li_2O_2, and Li-Nafion were mixed in a 40:60:60:60 ratio with anhydrous isopropanol (Sigma Aldrich, Purity = 99.5%) and horn sonicated in a dry glovebox (Ar with <1% O2, <0.1 ppm H2O, MBraun) until a slurry formed (30 W for 30 min with a 50% duty cycle), then cast onto aluminum foil with a #50 Mayer rod. The solvent was allowed to evaporate in the glovebox, then ½ in diameter electrodes were punched. The electrodes were dried under vacuum at 70 °C for at least 12 hours before being stored in the argon glovebox until used. Li_2O_2-preloaded electrodes with Pt NPs (Pt/C+Li_2O_2) were prepared in the same manner, except that the Pt used was deposited on the VC by the manufacturer, and extra caution was taken to minimize reactions between the Pt NPs and the solvent.

3.3.1.2 Electrolyte Preparation

All cells used the same electrolyte. Diethylene glycol dimethyl ether (diglyme, Sigma-Aldrich, anhydrous 99.5% purity) was dried over 3 Å molecular sieves inside the argon glovebox. When preparing the electrolyte, diglyme was pipetted into a scintillation vial, and sufficient $LiClO_4$ (battery grade, dry, 99.99% trace metals basis, Aldrich) was added to achieve 0.1M $LiClO_4$. This solution was stirred in the glovebox for 12 hours before use, and stored capped in the argon glovebox when not used for preparing a cell.

3.3.1.3 Cell Preparation

All cells were prepared using the DEMS cell described in Section 3.2.4. The cell was dried at 70 °C in vacuum for several hours prior to use. A 15 mm diameter disk of Li foil (Chemetall, Germany) was punched and placed in the bottom of the cell. All cells used two 18 mm diameter disks of Celgard C480 as separators. For VC- and CNT-based cells, 200 µl of electrolyte was used to wet both separators and the VC electrode, and a 400 mesh stainless steel grid added to provide electrical conductivity. For Li_2O_2-preloaded cells, 150 µl of electrolyte was used, and no electrolyte was added above the Al foil. A lightweight spring (Lee Spring, USA) was attached to the top of the cell and provided electrical contact to the top electrode. The cell was sealed using a PTFE O-ring (size AS568A-212); this O-ring was not used more than twice prior to replacement. The six screws used to close the cell were tightened in a crossing pattern until all screws were snug. The cell valves were closed prior to removing the cell from the glovebox.

Cells were connected to the DEMS shortly after removal from the glovebox. Each of the two VCO fittings were connected, using new PTFE O-rings (size AS568A-010) for each measurement, and tightened fully. A pre-programmed procedure was used to purge the lines leading the cell with

argon before the valves were opened. The exact procedure for each cell is described below. All tests were performed using argon and oxygen as described (Airgas, 99.999% Ar, 99.999% O₂).

3.3.2 Pressure Tracking during Discharge

We first consider the discharge performance of a VC-based electrode discharged in diglyme under pure oxygen. After connection to the DEMS system, the gas in the cell was exchanged for oxygen, and the cell volume was measured. After volume measurements, the cell was allowed to rest at room temperature with pressure tracking for approximately 44 hours before discharging, and an additional 13 hours after discharge. Leak estimation was performed using the last 3 hours of the post-discharge pressure tracking, at which time all electrolyte evaporation, gas dissolution, and thermal equilibration were assumed to be completed (Figure 3-7). Notably, the change in
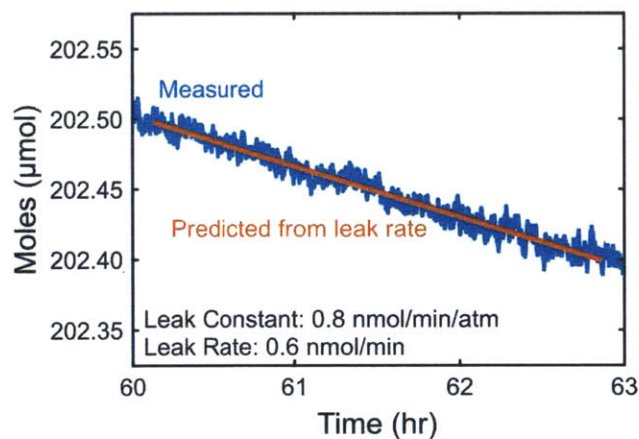
Figure 3-7. Total moles in cell *vs.* time for a VC-based cell in diglyme under oxygen. Blue indicates the measured number of moles in the cell, while orange indicates the predicted loss of moles due to the fitted leak rate. The leak rate constant was determined to be 0.8 nmol/min/atm, resulting in a leak rate of 0.6 nmol/min. The loss of gas shown here corresponded to a loss of ~0.02 psi over three hours.

moles appeared to be linear during this period, further confirming that no dynamic processes were occurring. The cell volume was estimated at 2.82 ± 0.02 ml.

This cell was discharged at 100 mA/g_{VC} to 2 V_{Li} (Figure 3-8). The discharge capacity was only 580 mAh/g_{VC}, which is significantly lower than the capacity of VC-based electrodes previously reported by our group.[47] However, the reduction in capacity is consistent with recent work showing that the presence of water in the electrolyte of Li–O_2 batteries can increase the discharge capacity; the improvements in electrolyte storage and handling developed in our group in the past several years may explain the reduction in capacity seen here. Figure 3-8b shows the leak-corrected consumption of oxygen in comparison with the flow of electrons through the circuit, and shows very good agreement with a 2 e^-:O_2 process. Figure 3-8c shows the derivative of the lines
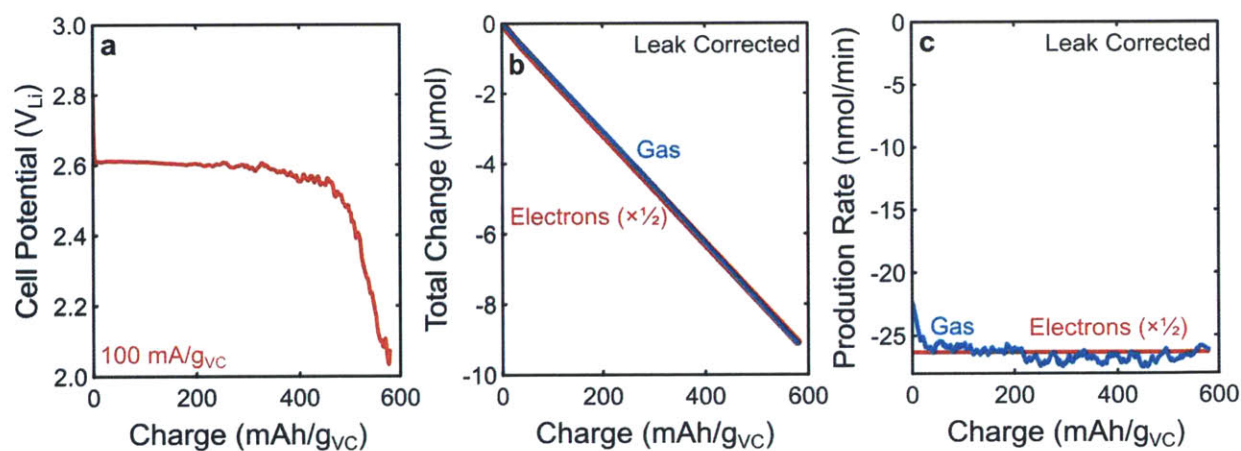
Figure 3-8. (a) Cell potential, (b) total change in moles, and (c) molar production rate vs. time of a VC-based cell discharge in diglyme. Blue indicates moles of gas, while red indicates moles of electrons (scaled by ½ to reflect a 2 e^-:O_2 process). Note that the width of the red line in (b) has been increased to make it visible. Gas consumption shown here is after the leak correction process described in Figure 3-7. The curves in (c) are the derivative of the curves in (b) (using a sample interval of 60 s and a smoothing window of 15, as described in Appendix A).

shown in Figure 3-8b, which further show that the consumption of gas was consistent with a 2 e^-:O_2 process throughout the entire discharge, within accuracy of the measurement. The overall ratio of electrons passed to gas consumed was 1.99 ± 0.01 with leak correction (without leak correction, this ratio was 1.94 ± 0.01). This result is in good agreement with published results that indicate gas consumption in DME and triglyme is very close to 2 e^-:O_2.[50,83]

A similar test was performed using a CNT-based electrode. After connection to the DEMS, the cell gas was immediately exchanged for O_2 and the volume was measured (2.69 ± 0.02 mL). Note that the discrepancy in volume between this cell and the previous one is due to the use of a different channel on the DEMS, as the head space at the two pressure gauges is slightly different. After volume measurement, the cell was allowed to rest for approx. 20 hours before discharge. The
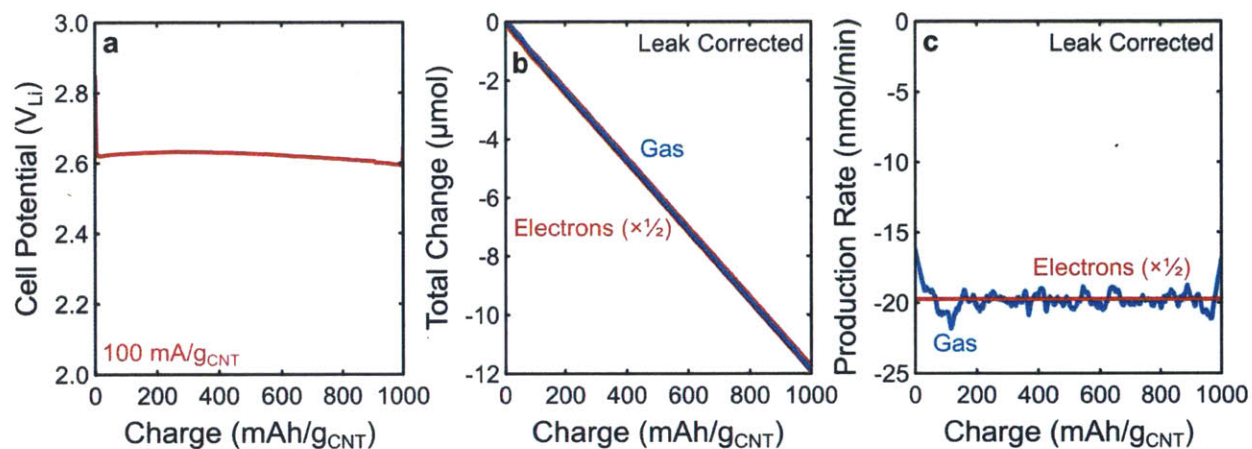
Figure 3-9. (a) Cell potential, (b) total change in moles, and (c) molar production rate vs. time of a CNT-based cell discharge in diglyme. Blue indicates moles of gas, while red indicates moles of electrons (scaled by ½ to reflect a 2 e^-:O_2 process). Note that the width of the red line in (b) has been increased to make it visible. Gas consumption shown here is after leak correction (the leak rate constant is 1.3 nmol/min/atm). The curves in (c) are the derivative of the curves in (b) (using a sample interval of 60 s and a smoothing window of 31, as described in Appendix A).

cell was discharged at 100 mA/g$_{CNT}$ for 10 hours, and allowed to rest for an additional 10 hours after discharge. The leak rate was estimated using the final 5 hours of this process; the leak rate constant was found to be 1.3 nmol/min/atm, which resulted in a leak rate of 0.9 nmol/min. Figure 3-9 shows the summary of the performance of this cell. Discharge was capacity limited, and stayed close to 2.6 V$_{Li}$ throughout discharge. Additionally, Figure 3-9b and c show that the leak corrected gas consumption agreed very well with a 2 e$^-$:O$_2$ process at all times during the discharge. The overall leak-corrected ratio of electrons passed to gas consumed is 2.00 ± 0.01 (without leak correction, this value is 1.90 ± 0.01).

3.3.3 DEMS Measurements during Charging of Discharged Electrodes

For both of the above cells, after the discharge and several hours of resting in oxygen, the cell atmosphere was exchanged to argon and DEMS measurements were taken at intervals throughout the charging process. These DEMS measurements examined the production of oxygen, carbon dioxide, nitrogen and carbon monoxide, hydrogen, and water before, during, and after the charging process.

After exchanging oxygen for argon, the VC-based cell was allowed to rest for approx. 28 hours before charging at 100 mA/g$_{VC}$ for approx. 10 hours, throughout which DEMS measurements were taken on a 13.5 minute interval. Due to the incorrect arrangement of the pressure gauge (see Section 3.2.3.3 above), a significant quantity of oxygen was observed to diffuse into the cell during this period, and the cell gas was further exchanged with argon periodically during this 28-hour rest period. Figure 3-10 shows a summary of the results of this experiment. Figure 3-10a shows the estimated gas fraction of all gases (except Ar) in the cell; this data is most closely related to the raw readings from the MS. Figure 3-10b shows the cell charging potential; the cell potential rises from ~3.6 VLi to 4.4 VLi during the charging process, where it reaches a plateau until nearly

84

completely recharged, after which the voltage rapidly rises to ~4.9 VLi, where anoxic oxidation of

glyme-based electrolytes is known to occur.[87] This continues until the end of the test. Figure 3-10c

shows the cumulative production of each gas, as well as the total production (based on pressure

measurements only), and one-half of the accumulated electrons. For this test, there is significant

disagreement between the total production of gas (as determined by the pressure gauge) and the
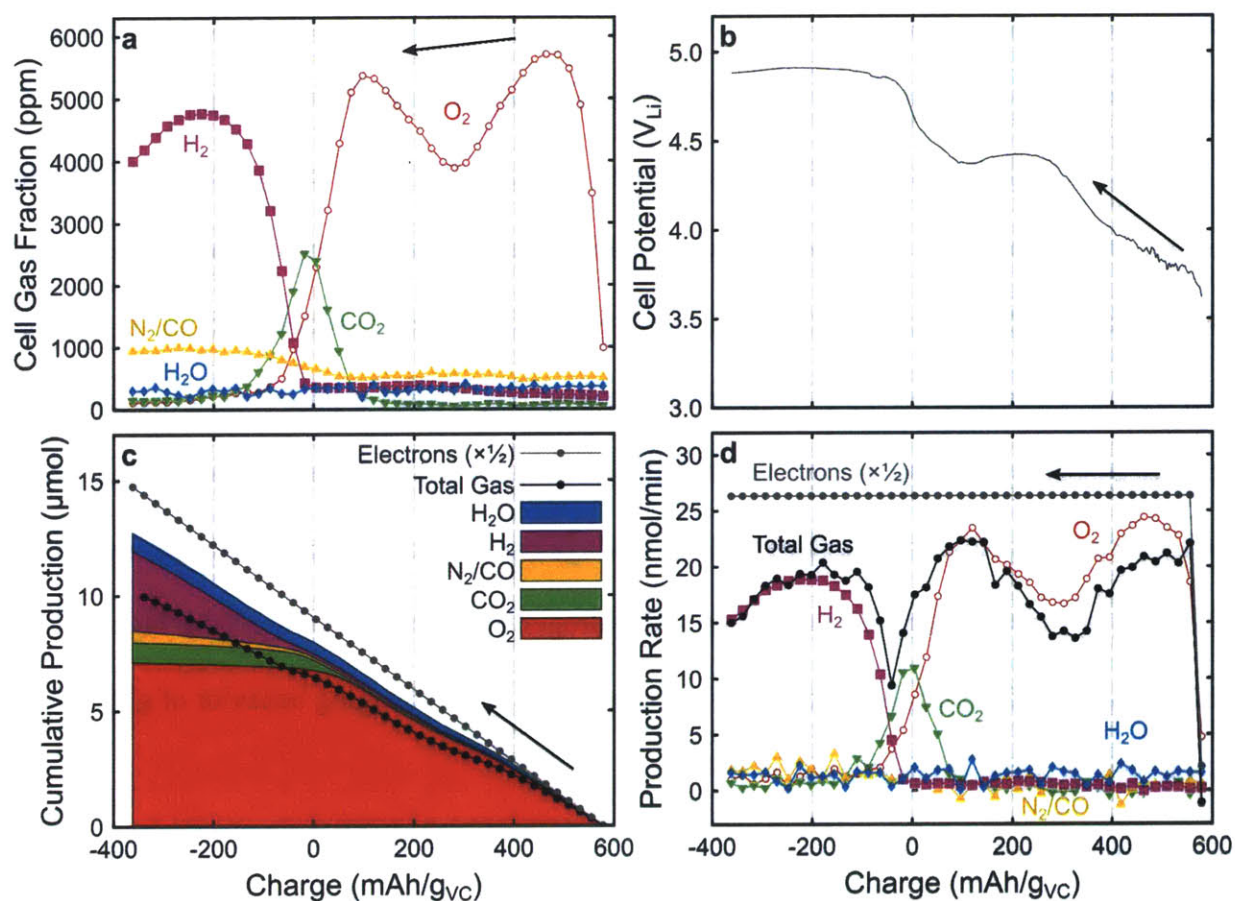
Figure 3-10. (a) Cell gas fraction, (b) cell potential, (c) cumulative production, and (d) production rate *vs.* accumulated cell charge for DEMS measurements taken during the VC-based cell charging. Graphs flow from right to left, with the right-most point equal to the right-most point of Figure 3-8. Zero charge indicates the point of complete recharge; negative charge indicates overcharging. The total gas production is not corrected for leaks.

production of each gas species (as determined by the MS). This discrepancy is primarily identified as being due to incorrect volume calibration for MS measurements on this cell. Given that the pressure tracking results during the discharge process (Figure 3-8) agreed very well with theory, we believe that the pressure tracking data (*i.e.* total gas) in Figure 3-10 is accurate, and that with proper calibration of the volumes before and after the cell (as discussed in section 3.2.6.5) the MS and pressure tracking data would come into agreement (as is the case for the cells presented in the remainder of this chapter and the next, which used a different channel on the DEMS).

Figure 3-10d shows the derivative of the data in Figure 3-10c (in reality, the opposite is true; the rate of gas production is first calculated, and then integrated over time to produce the cumulative production). It is clear here that at all times through the charge process, less gas is produced than would be expected for a 2 e^-:O_2 process. Furthermore, oxygen is produced in two waves, the first corresponding to charging at low potentials and the second to the plateau at 4.4 V_{Li}. Carbon dioxide production does not increase until the voltage rises at the very end of charge, and quickly falls back before bulk electrolyte oxidation and hydrogen production are observed at high voltages. These results are in good agreement with published data on the charging behavior of glyme-based Li–O_2 cells in argon environments.[50,71,83,87]

Finally, we note that the gas production rate in Figure 3-10d is neither a derivative nor a proportion of the cell gas fraction in Figure 3-10, although it can sometimes appear to be one or the other. A gas being produced at steady state will result in a steady state cell gas fraction as that gas is replaced during measurements. However, a sudden stop in gas production will result in a gradual decline in the cell gas fraction. Similarly, gases present at low levels may result in a highly fluctuating gas production rate simply because signal-to-noise ratio is large, which results in the

apparent production or consumption of gas between readings. It is for this reason that the cumulative gas production is recommended to analyze low levels of production (such as N_2/CO in Figure 3-10), but the rate of production may be more helpful when considering dominant products, such as oxygen.

Next, we consider the DEMS results during charging of the CNT-based electrode in diglyme previously shown in Figure 3-9. After the cell gas was exchanged to argon, DEMS measurements were taken every 15 minutes, and the cell was allowed to rest for approx. 10 hours before charging at 100 mA/g_{CNT} for 15 hours (resulting in a 50% overcharge). This cell was tested using the corrected pressure gauge arrangement, and so an order of magnitude less oxygen was produced during the resting period; no additional argon purging was considered needed, as the DEMS measurements acted to remove the oxygen. This oxygen is attributed to oxygen dissolved in the electrolyte during discharge, which was expected to be released from the electrolyte after the cell atmosphere was changed to argon. Figure 3-11 shows a summary of the charging performance; the cell voltage (Figure 3-11b) started from a low value of ~3.4 V_{Li} and rose steadily before reaching a short plateau around 4.25 V_{Li} when 75% charged, after which the voltage rose near the end of charge and stabilized at ~4.7 V_{Li} throughout the overcharging period. The charge profile is qualitatively similar to that of the VC electrode discussed above; the reduced voltages are attributed to the lower absolute and BET-surface area-normalized current (the CNT electrode contains less carbon with a higher BET surface area than that of VC). This profile is also somewhat distinct from the first charge of the same CNT electrodes previously published by Gallant et al.[41] The primary differences between these experiments are the electrolyte solvent and the discharge rate (this experiment discharged at 100 mA/g_{CNT} in diglyme, while Gallant et al. discharged at 250 mA/g_{CNT} in DME); further experiments are needed to determine the exact cause of the difference between these systems.
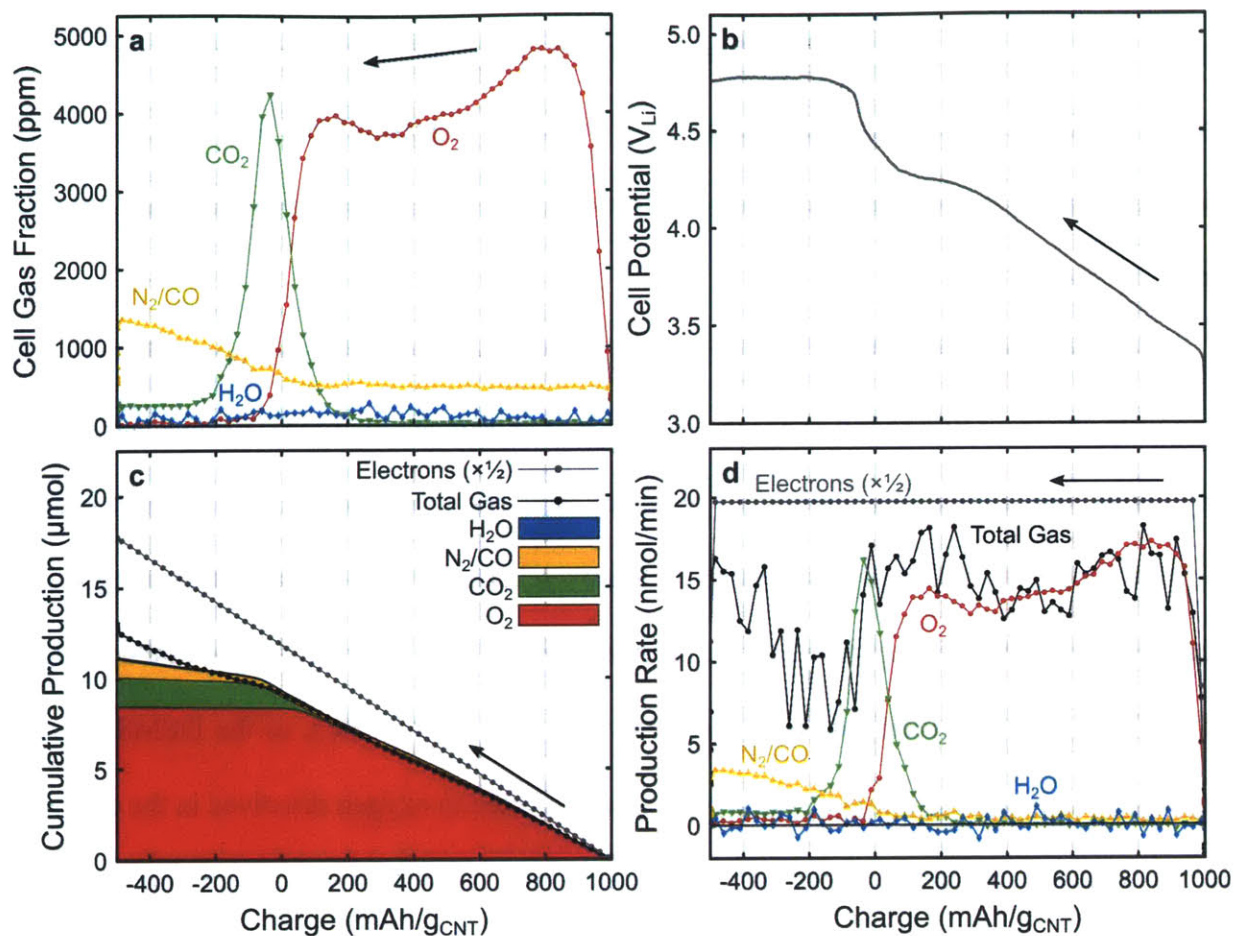
Figure 3-11. (a) Cell gas fraction, (b) cell potential, (c) cumulative production, and (d) production rate *vs.* accumulated cell charge for DEMS measurements taken during the CNT-based cell charging. Graphs flow from right to left, with the right-most point equal to the right-most point of Figure 3-9. Zero charge indicates the point of complete recharge; negative charge indicates overcharging. The total gas production is not corrected for leaks.

Unlike in the VC electrode experiment, we observe very good agreement between the total gas production (via pressure tracking) and the production of individual gases (via MS measurements), as shown in Figure 3-11c. We attribute this to better estimation of the volumes before and after the cell on this channel, which is the result of a larger number of experiments allowing more precise determination of these values. Throughout the initial period of charge, the majority of gas

produced is O_2, with trace amounts of other gases. Throughout this region, the production of oxygen was less than expected for a 2 e^-:O_2 process, as depicted by the gray line. This is in agreement with other results published using glyme-based electrolytes in Li–O_2 cells.[50,71,83,87] As the O_2 production slowed, a wave of CO_2 is produced near the point of 100% recharge, after which larger amounts N_2/CO are produced, and an excess of undetected gases are observed based on the total gas data. We attribute the CO_2 production to the oxidation of lithium carbonate/lithium alkyl carbonates formed during discharge,[50] and the production of N_2/CO and other gases to the result of anoxic electrolyte decomposition, as seen in the VC electrode and published by other groups.[87]

Figure 3-11d shows the gas production rate in the CNT electrode. This shows that, like in the VC electrode, the O_2 production rate is not constant through initial charging region, which was highest at low voltages and gradually decayed. The second wave of O_2 production is also less pronounced, which is consistent with the reduced duration of the plateau at high 4.25 V_{Li}. This is consistent with the different stages of charge that were identified by McCloskey et al.[83] for Li–O_2 batteries charged in DME; later work from the same group suggests that O_2 evolved later in charge corresponds to Li_2O_2 deposited early during discharging,[34] but that work does not specifically identify the two waves of oxygen production seen here. The maximum rate of O_2 production observed (after approximately 100 mAh/g_{CNT} charged) was 17.3 nmol/min, which corresponds to an e^-:O_2 ratio of 2.3. The total O_2 production at the point of 100% charge was 8.35 μmol, corresponding to an overall e^-:O_2 ratio of 2.83. This value is in general agreement with McCloskey et al., who report values above and below this value for the same (apparent) system in different reports.[50,83]

3.3.4 DEMS Measurements during Charging of Li_2O_2-Preloaded Electrodes

An additional set of experiments was performed where $Ru/C+Li_2O_2$ and $Pt/C+Li_2O_2$ electrodes were charged potentiostatically while connected to the DEMS. The procedure for charging was similar to that reported in Chapter 2: each cell was connected to the DEMS and the volume was measured, after which the cell was allowed to rest for 12 hours (with DEMS measurements taken every 15 minutes). Following the rest, the cell was held at 2.9 V_{Li} for 30 minutes; this ensures that the capacitive current from jumping to the experimental potential is constant between similar electrodes. No gas evolution was detected during this period. After 30 minutes, the cell potential was raised to 3.9 V_{Li} and held constant until the end of the experiment, approx. 12 hours. DEMS measurements were taken every 15 minutes throughout the experiment.

Figure 3-12 shows a summary of the results of this experiment using a $Ru/C+Li_2O_2$ electrode. Figure 3-12b plots the mass-normalized current against the mass-normalized capacity of this cell, using the same semi-log plot and axes limits as used in Chapter 2 (mass of Li_2O_2 and mass of VC are equivalent, as they were included in a 1:1 ratio in both cases). Compared with Figure 2-11, the charging profile is much lower in this experiment, with the maximum current (after initial capacitance) only reaching 210 mAh/g_{Li2O2}, *versus* more than 1000 mAh/g_{Li2O2}. In addition, the discharge profile is much flatter here, and is qualitatively similar to that of $VC+Li_2O_2$ charged at 4.2 V_{Li} in Chapter 2, although the onset time was much faster (approx. 650 s here *versus* approx. 6000 s). We attribute this reduction in performance to the use of a diglyme-based electrolyte rather than the DME-based one used in Chapter 2. We also note that the second wave of current observed for the $Ru/C+Li_2O_2$ electrode at 3.9 V_{Li} in Chapter 2 is not observed here; this is attributed to the removal of oxygen from the cell, indicating that Ru may catalyze electrolyte decomposition in the presence of oxygen at high potentials.

90
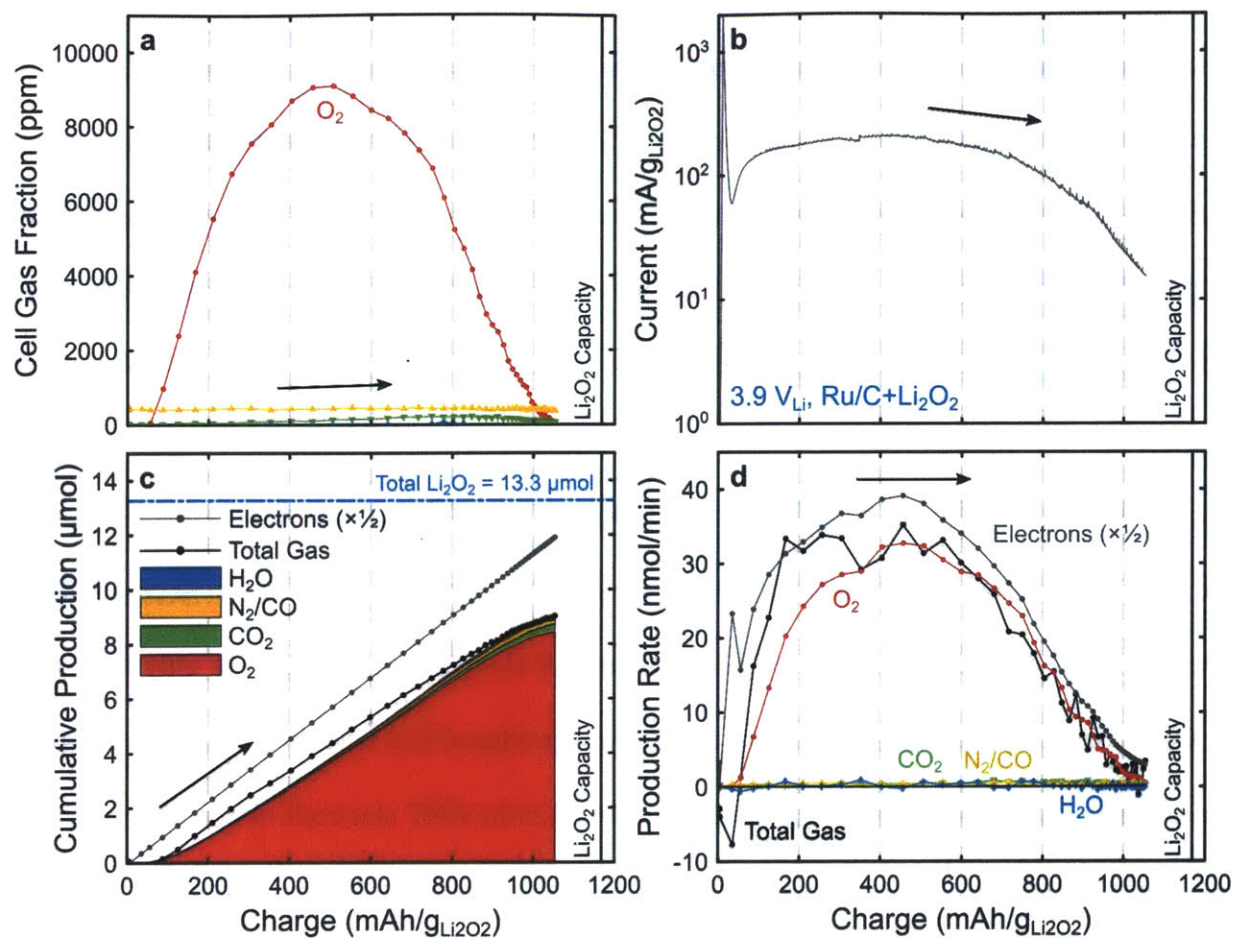
Figure 3-12. (a) Cell gas fraction, (b) mass-normalized current, (c) cumulative production, and (d) production rate *vs.* accumulated cell charge for DEMS measurements taken during the potentiostatic charging of a Ru/C+Li₂O₂ electrode. Part b is plotted using the same scale as was used for Figure 2-11. The dark vertical line on all parts indicates the expected charge for 2 electron oxidation of Li₂O₂. The dashed blue line in (c) indicates the total moles of Li₂O₂ added to the cell. Lines in (a) are identified using the same colors and shapes in (d) and in previous figures in this chapter. The total gas production is not corrected for leaks.

Oxygen was the only dominant gas observed during this test (8.46 μmol), with no unambiguous production of any other gases (Figure 3-12c). Very small quantities of CO_2 and N_2/CO (0.29 and 0.26 μmol respectively) accumulate over the course of the charge. However, there is a slight

discrepancy between the observed pressure profile and MS data; this may indicate the production of other gases that were not detected on the MS, or may simply be an artifact of experimental variation. We note that the apparent consumption of gas that is observed at the beginning of charge (Figure 3-12d) is attributed entirely to a temperature anomaly in which the temperature dipped by 0.5 °C over a 3 h period coinciding with the start of charge. As noted in Section 3.2.3.4, temperature swings of this magnitude are not accurately corrected for and can impact the apparent rate of gas production. Finally, we note that the total oxygen production is less than would be expected for a 2 $e^-:O_2$ process: the minimum $e^-:O_2$ ratio of 2.2 is observed at 750 mAh/g_{Li2O2}, while the overall $e^-:O_2$ ratio was found to be 2.81 at the end of charge, and oxidation of only 64% of the Li_2O_2 in the electrode. While much less oxygen was produced that would be desired, we note that the overall $e^-:O_2$ ratio is consistent with that observed in the CNT electrode above. The production of oxygen alone during charge is also consistent with work by Gasteiger and colleagues,[35,36,99] who have studied VC+Li_2O_2 electrodes in a variety of electrolytes, binders, and cell configurations. Their work shows a similar oxygen production rate (~2.3 $e^-:O_2$) in Li_2O_2-preloaded electrodes with a Li-Nafion binder and no catalyst, indicating that the addition of Ru does not reduce the Li_2O_2 oxidation efficiency.

Figure 3-13 shows the results of a similar experiment using a Pt/C+Li_2O_2 electrode. Several differences are immediately apparent: The discharge profile is more steeply sloped and current drops rapidly from an initially high level, which is qualitatively similar to Figure 2-11, although overall current is lower. Additionally, CO_2 is the first gas evolved during the charge process, and oxygen production is minimal until CO_2 production peaks. Finally, the overall production of gas is low, with O_2 and CO_2 combined producing only 3.41 μmol (1.88 and 1.53 μmol for O_2 and CO_2 respectively) relative to the 9.63 μmol of Li_2O_2 added to the cell. Furthermore, gas production only

92

occurs for the first 500 mAh/g_{Li2O2}; thereafter, a low level of current is passed yet only slight changes in the production of any gas is observed.
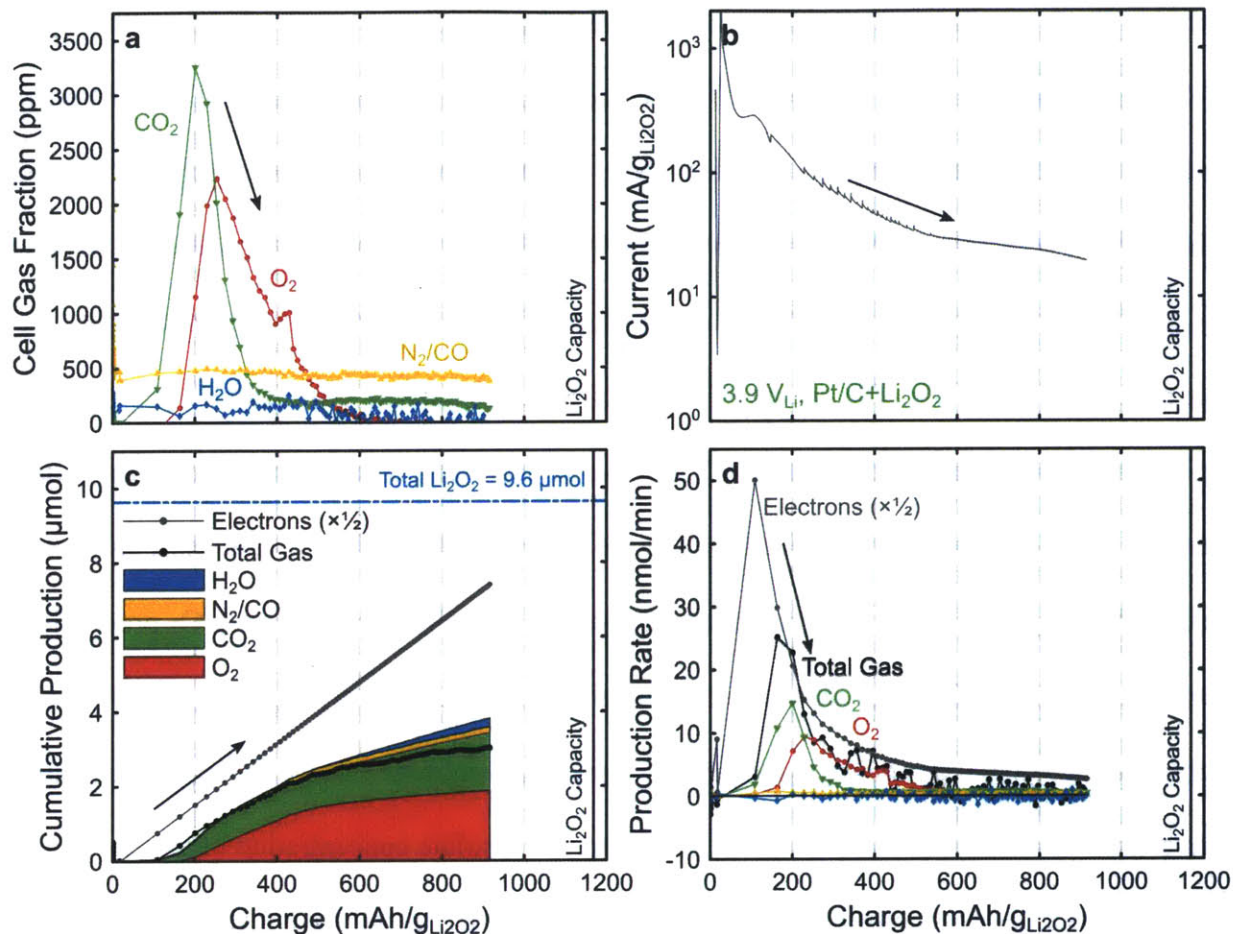
Figure 3-13. (a) Cell gas fraction, (b) mass-normalized current, (c) cumulative production, and (d) production rate *vs.* accumulated cell charge for DEMS measurements taken during the potentiostatic charging of a Pt/C+Li_2O_2 electrode. (b) is plotted using the same scale as was used for Figure 2-11. The dark vertical line on all parts indicates the expected charge for 2 electron oxidation of Li_2O_2. The dashed blue line in (c) indicates the total moles of Li_2O_2 added to the cell. Lines in (d) are identified using the same colors and shapes in (a) and in previous figures in this chapter. The total gas production is not corrected for leaks.

These results validate the hypothesis proposed in Chapter 2 that Pt catalyzes the reaction between oxygen and the electrolyte, and helps confirm that Ru does not readily promote the same reaction. These results are also consistent with work by McCloskey *et al.* who show that cycled Li–O$_2$ cells produce a small amount of O$_2$ and mostly CO$_2$, although the order of production was reversed, with O$_2$ appearing before CO$_2$. However, our observation of CO$_2$ during charging appears to be in direct contrast with Meini *et al.* who saw O$_2$ as the dominant reaction product when charging Li$_2$O$_2$-preloaded electrodes with a Pt catalyst, which was charged galvanostatically at potentials at and above 3.9 V$_{Li}$. The source of the discrepancy is unclear, but may be attributed to the concentration of oxygen in the cell: McCloskey *et al.* reported that oxygen was consumed in the presence of Pt catalysts at open circuit when the cell was filled with O$_2$. We show that CO$_2$ is produced during the period of highest total gas production, which transitions to O$_2$ production at lower rates. It is possible that when the O$_2$ concentration is sufficiently high (*e.g.* 2000 ppm, the highest concentration shown in Figure 3-13a), Pt initiates combustion of the electrolyte and rapidly converts the O$_2$ into CO$_2$. Meini *et al.* do not report the absolute concentration of any gases in the cell, and so the O$_2$ produced by their Pt/C+Li$_2$O$_2$ electrode may never have reached this threshold. If this hypothesis is correct, it implies that the activity of Pt to oxidize Li$_2$O$_2$ is separate from its activity to combust the electrolyte in oxygen, and suggests that other materials (such as Ru or transition metal compounds) may be capable of catalyzing Li$_2$O$_2$ oxidation without promoting electrolyte combustion.

3.4 Suggested Improvements and Future Experiments

Although the system as currently constructed is fully operational and the results shown above and in the next chapters demonstrate the capability to accurately measure gas production in Li–O$_2$

94

cells, several improvements are available that could increase the performance or reliability of the system.

Currently, both pressure tracking and DEMS performance are limited by the volume of the cell and other portions of the DEMS system. In particular, the VCO fittings currently used to connect the cell each contain approximately 0.5 ml, and their position near to but separate from the cell interior complicates the collection of cell gas for DEMS measurement. Using custom machined VCO fittings, either by modifying blanks purchased from Swagelok or by designing custom small-size analogs of VCO fittings, could further reduce this volume. Changes to the cell design may also be beneficial; changing the flow path inside the cell so that the regions where gas is well mixed are clearly defined will also enhance the accuracy of DEMS measurements, even if the total internal volume of the cell is slightly increased.

Further enhancements to the performance of MS measurements are possible through improvements to the procedure of taking and analyzing these measurements. As shown in Figure 3-6, dead space between the MS and the cell currently causes MS readings to be delayed by one. A careful reconsideration of the measurement process may allow for the measurement of gas currently in the cell, without further interfering with the cell gas composition (taking several samples of gas in quick succession will cause increased dilution of the cell gas). Further improvements in calibrating the MS, including with individual gases and mixtures of gases diluted in argon will enhance the quality of MS readings. Additionally, the accuracy of the volumes in the pressure gauges must be improved. This volume is not especially important during pressure tracking (as both the gauge and cell volume are determined and considered together), but becomes critical when estimating the distribution of gases during DEMS measurements, and an improved understanding

of these volumes may help explain the poor agreement between pressure and MS data in Figure 3-10.

Additional improvements could be made to the cell design used for DEMS measurements. Changing some or all of the base of the cell to copper will prevent unwanted interactions between lithium metal, the electrolyte, and stainless steel, and changing the material of the lining ring to a lithium-compatible polymer (such as polyethylene or PEEK) will further improve the reliability of the cell's electrochemical behavior. Similarly, an investigation into the cause of the leaks observed during discharge is recommended, and the cell design and handling procedures should be adjusted to eliminate them.

Finally, the results in this chapter suggest a number of additional experiments. Using a partial oxygen environment in the cell (e.g. 1% O_2 in Ar) would allow DEMS experiments to be performed during discharge that could further validate the pressure tracking data. Similarly, using partially oxygenated environments during charge could be used to study the impact of oxygen gas on the charging process; the DEMS measurements shown here continually remove oxygen from the cell, which limit the ability of oxygen to interact with the electrode and electrolyte later in the charge process. This would be especially beneficial for Li_2O_2-preloaded experiments, where it is necessary to show that any catalysts added are compatible with an oxygen environment. It should be obvious that these suggestions are only a small sample of the possible uses of the DEMS system, and that using DEMS can be a powerful addition to any Li–O_2 experiment.

3.5 Conclusions

In this chapter, we have described the design and construction of the DEMS system built in the Electrochemical Energy Lab over the past year, and describe the process for using it in both pressure tracking and DEMS experiments. We then demonstrate this system using VC- and CNT-

96

based cells in diglyme to show results that are in agreement with studies performed by other groups[50,51,70,83,87] using DEMS systems for Li–O$_2$ research. Finally, we used the DEMS system to analyze Li$_2$O$_2$-preloaded electrodes, similar to those discussed in Chapter 2, and find that oxygen is produced during potentiostatic charging of Ru/C+Li$_2$O$_2$ electrodes, and both oxygen and carbon dioxide are produced by Pt/C+Li$_2$O$_2$ electrodes. These results support the work presented in Chapter 2 and more recent work from our lab,[46,84] by demonstrating that promoting the oxidation of Li$_2$O$_2$ still results in the production of oxygen.

3.6 Acknowledgements

Chapter 4

Development of Poly(ethylene oxide)-Based Electrolytes for Lithium–Air Batteries

4.1 Introduction

As discussed in Chapter 1, Li–air batteries face many challenges that must be overcome before they can realize their potential as a high specific energy storage system. Much of the attention in the literature has focused on problems such as enhancing discharge rate and capacity,[38,39,44,78,79,81,82,119–129] reducing the charging potential,[42,46,78,81,89,90,117,122,128] and finding materials that enable cells with long cycle lives.[121,124,128,130–132] However, relatively little attention has been paid to concerns about electrolyte loss to the environment. Li–air batteries (as opposed to Li–O_2 batteries) must ultimately be open to the environment in order to be effective, but many of the electrolytes commonly used in Li–air and Li–O_2 devices in the lab are highly volatile,[58] requiring careful handling to prevent solvent evaporation. Other solvents are less volatile,[56,57,133] but have measureable vapor pressures that would lead to significant loss of electrolyte over the long-term operation of a real device. Furthermore, these solvents are almost universally toxic,[56,58,59,133] and widespread release of these chemicals into the environment would be undesirable.

The development of solid electrolyte-based Li–air batteries would alleviate many of these concerns; solid electrolytes are non-volatile, and so do not leave the cell even when open to air. Additionally, certain solid electrolytes can serve as an effective anode protection layer, and ceramic electrolytes have been developed to protect lithium metal from water as well as air.[134] Finally, solid electrolytes can be designed not to flood the void space of the positive electrode, as is common for liquid electrolytes.[47,135] This allows gaseous oxygen to travel deep into the electrode, and reduces the distance oxygen must diffuse as a dissolved species from tens of microns, where oxygen transport can be a significant limitation,[47] to nanometers.

100

There are two main classes of solid lithium-conducting electrolytes: organic polymers and inorganic ceramics and glasses.[136] Both classes have advantages and disadvantages. Some inorganic ceramics, especially sulfur-based ones, have exceptionally high lithium conductivities, which can exceed that of liquid electrolytes.[137,138] They are also generally more effective as barriers, allowing few species other than lithium ions to pass.[139] However, the rigidity of ceramics make them difficult to handle,[139] yet they must be pinhole free if used as a barrier membrane. Ceramics and glasses are also denser than organic electrolytes,[140] which negatively impacts the specific energy of devices that use them. Furthermore, many of the most performant inorganic electrolytes are also unstable in air,[141] a significant concern for Li–air batteries. Polymer electrolytes, on the other hand, are usually much easier to handle and process, and many polymers are flexible enough to be significantly deformed without cracking. In addition most polymers are significantly less dense than ceramics,[142] and can be more easily processed into thin films using various casting techniques,[143] both of which serve to enhance the specific energy of polymer electrolyte devices. The disadvantages of polymers as electrolytes are two-fold: they are much less effective as protection layers, as most polymers are gas permeable[144] and many are hygroscopic,[145] and they are generally less conductive than liquid electrolytes or high performance ceramics,[136] especially at room temperatures. On balance, these advantages and disadvantages must be carefully weighed, and the decision to use one or the other (or both) must be made for each device type and application.

In this chapter, we choose to focus on developing a solid polymer electrolyte-based Li–O$_2$ battery. Polymer electrolytes have been used previously for some Li–O$_2$ and Li–air devices,[73,146–151] including the first modern nonaqueous Li–air battery demonstrated by Abraham and Jiang,[73] which used polyacrylonitrile (PAN) gelled with propylene carbonate (PC) and ethylene carbonate

(EC) and LiPF6 as the electrolyte. While this device counts as a polymer electrolyte system, it was not a solid polymer electrolyte, as the PC/EC liquids were still susceptible to evaporation over time. Furthermore, PC/EC is now well-known to be unstable in Li–O$_2$ electrochemistry,[67,76,83,152] and we have recently shown that PAN is also unstable when exposed to Li$_2$O$_2$.[97] More recent work has developed solid-polymer Li–air devices, either with only solid polymers[148,151] or hybrid polymer ceramic membranes.[146,153] In all cases, the polymer of choice was poly(ethylene oxide) (PEO), which has also received significant attention as an electrolyte for Li–ion devices.[154–157] This is due to the high lithium conductivity of amorphous PEO, in which segmental motion of neighboring chains of the PEO backbone is believed to allow the transport of lithium ions through the electrolyte.[157] Many different materials have been developed as solid polymer lithium electrolytes, and a careful examination of them shows that most, if not all, rely on oligo-ether moieties (*e.g.*, oligo(ethylene oxide)) to provide lithium conductivity.[136,157] Additives such as nanoparticles of transition metal oxides[158] and various small-molecule plasticizers[156,159] have also been explored to enhance the conductivity of PEO electrolytes as room temperature. In addition to these additives, simple PEO-salt complexes are known to have reasonable conductivity above their melting point, which ranges from 50-65 °C depending on the electrolyte salt used.[157] These PEO electrolytes have been shown to have a large stability window, forming a stable SEI against lithium metal and no significant decomposition current below 4.9 V vs lithium (V_{Li}).[160]

In particular, Hassoun *et al.*[148] demonstrated the use of PEO when investigating Li–O$_2$ electrochemistry at room temperature, using a blend of PEO, lithium triflate salt, and ZrO$_2$ nanoparticles as the electrolyte. However, this work did not investigate the performance of PEO in the context of developing a practical device, instead using potentiodynamic cycling with galvanostatic acceleration to try to identify the onset of different reactions with changing voltage. Further, it is

102

unclear whether or not the electrolyte used was plasticized by tetraethylene glycol dimethyl ether (tetraglyme), which is referred to in the conclusion of that article but not mentioned in the experimental section. As with the PC/EC solvents discussed above, tetraglyme would be expected to evaporate during long term operation, especially if exposed to elevated temperatures.[57]

In this chapter, we set out to develop a PEO electrolyte-based Li–O$_2$ device that can achieve relatively high discharge rates and capacities. We used as a starting point an ionic liquid-plasticized electrolyte developed by Passerini and colleagues over the past decade for Li–ion devices,[159–164] which has been shown to have reasonable conductivity at room temperature. We also developed an all-solid-state electrode that uses XC-72 Vulcan carbon (VC) for structure and electrical conductivity and a PEO-based electrolyte to act as a binder and lithium conductor. We first investigated the operation of such devices as room temperature, and explored the impact of a variety of experimental parameters on cell discharge performance. We then explored the performance of cells discharged at 60 °C, and further investigated discharge performance with and without the inclusion of ionic liquid. Finally, we investigated the behavior of these cells using a differential electrochemical mass spectrometer (DEMS) to characterize the rates of gas consumption and production during the discharge and charge processes at a variety of temperatures. This work was generously funded by the Samsung Advanced Institute of Technology (SAIT), who also provided a discharge performance target for practical polymer-based Li–air devices of 1000 μAh/cm^2 at 200 μA/cm^2. This target is used as the overall performance goal throughout this chapter.

After the work shown in this chapter was completed, a similar body of work was published by Balaish et al.[151] who investigated the development of PEO-based Li–O$_2$ devices at 80 °C with carbon nanotube electrodes and lithium triflate salt. Although that work also performed some investigations on the discharge rate capability and capacity of their system, they also focused on

limited-capacity cycle life and the degradation of the PEO electrolyte during cycling. The degradation of PEO electrolyte while charging in oxygen is explored more deeply in Chapter 5, in which this aspect of the work by Balaish *et al.* is discussed.

4.2 Experimental Methods

PEO (MW ~10^5 g/mol and MW ~4×10^6 g/mol, <1000 ppm BHT as inhibitor), *bis*(trifluoromethane)sulfonimide lithium salt (LiTFSI, 99.95% trace metals basis), and poly(ethylene glycol) dimethyl ether (PEGDME, M$_n$ ~2000 g/mol, inhibitor-free) were obtained from Sigma-Aldrich. BHT was removed from the PEO via Soxhlet extraction in hexanes under flowing argon gas for at least 24 hours. Extracted PEO and as-received PEGDME were dried under vacuum at 50 °C for at least 48 hours before being transferred to a glovebox under argon for storage. 1-butyl-1-methylpyrrolidinium *bis*(trifluoromethane)sulfonamide (Pyr$_{14}$TFSI, 98% purity) was obtained from Alfa Aesar. LiTFSI and Pyr$_{14}$TFSI were dried separately under vacuum at 120 °C for 24 hours and stored in the argon glovebox without exposure to air. Fluorinated ethylene propylene (FEP) sheets of 5 mil (125 μm) thickness were ordered from McMaster-Carr, and cleaned using deionized water and ethanol before being dried under vacuum at 70 °C overnight before use. Heat-sealable bags with water vapor and oxygen transport resistance meeting MIL-PRF-131K (noted as poly/foil bags) were obtained from Sigma Aldrich, and dried under vacuum at 70 °C overnight before use. Celgard C480 was supplied by Celgard LLC. XC-72 Vulcan carbon (VC) was supplied by Premetek, and dried under vacuum at 100 °C overnight before being stored in the glovebox without air exposure. Lithium metal foil was obtained from Chemetall (Germany), and was stored as received in the glovebox.

A variety of polymer electrolytes were prepared in several different configurations. The recipe was derived from that published by Kim et al.[161] which describes the development of an electrolyte based on PEO, LiTFSI, and Pyr14TFSI (a room temperature ionic liquid). To prepare an electrolyte batch, appropriate quantities of PEO and LiTFSI were weighed and mixed in a mortar and pestle inside the glovebox (the exact ratios are listed in Table 4-1 below). The powders were gently mixed until fluffy and slightly sticky. If used, ionic liquid was added by volume (assuming a density of 1.394 g/ml)[165] directly to the mixture. The mixture was then vigorously mixed and pressed until it became a single white mass, which ranged from slightly tacky when no ionic liquid was used to very sticky when ionic liquid was present. This was then placed in a glass scintillation vial and dried under vacuum at 100 °C for 48 hours, before being returned to the glovebox. After drying, the electrolyte became clear, but maintained its original level of stickiness. The electrolyte was placed between two 4 in FEP squares and heat-sealed in a poly/foil bag. This bag was then pressed in a bench-top hot press at 100 °C with a maximum applied load of 1 t per 2 g electrolyte, slowly increasing and releasing pressure to minimize the formation of wrinkles. Shims were used to ensure that the electrolyte film thickness was approximately 150 μm. For electrolytes including an interlayer of Celgard, the once-pressed electrolyte was returned to the glovebox and cut in half. Each half was placed on opposite sides of a sheet of Celgard C480, and again protected by FEP and heat-sealed in a fresh bag. The PEO-Celgard sandwich was pressed again in the hot press at 100 °C, using the same shims as before and reaching a maximum load of 5 t per 2 grams of electrolyte. Once the pressure stabilized, the heat was turned off and the press was allowed to cool overnight under load. This allowed the PEO electrolyte to fully impregnate the Celgard film, resulting in a translucent film (if the electrolyte does not fill the Celgard, the film remains white and

exhibits poor ionic conductivity). Once cooled, pressure was very gently released, in order to minimize wrinkles, and the bag was returned to the glovebox. An 18 mm diameter hole punch was used to punch disks of the electrolyte, keeping the FEP films in place to protect the electrolyte. These were collected and stored in the glovebox until used.

Several parameters of the electrolyte recipe described above were varied in the experiments shown in this chapter. The presence of ionic liquid, the concentration of LiTFSI, the molecular weight of the PEO, and the presence or absence of Celgard were all adjusted. Table 4-1 describes the different electrolytes used, and provides a list of codes that are used in the remainder of this chapter.

Table 4-1. Electrolyte names and descriptions used in this chapter.

Electrolyte Code	PEO MW (g/mol)	LiTFSI Conc. (mol Li/mol EO)	$Pyr_{14}TFSI$ Conc. (mol Pyr_{14}^+/mol Li^+)	Includes Celgard?
P4M10IL	4×10^6	1:10	1:1	No
P4M20	4×10^6	1:20	None	No
P4M20-C	4×10^6	1:20	None	Yes
P4M10IL-C	4×10^6	1:10	1:1	Yes

VC air electrodes were prepared by mixing VC, BHT-extracted PEO or PEGDME, and LiTFSI in a planetary ball mill (Fritsch Pulverisette 6, Germany) jar, along with 5 mm diameter zirconia beads. A 50% v/v mixture of ethanol in deionized water were added to the jar before sealing and milling for at least 4 hours at 500 rpm. The resulting slurry was deposited onto aluminum foil using a Mayer rod. The amount of solvent and Mayer rod thickness were chosen to

achieve the desired carbon loading. The solvent was allowed to evaporate in air before 0.5 in diameter discs were punched. These disks were collected in a scintillation vial and dried for at least 24 hours at 100 °C under vacuum, before being directly transferred into an argon glovebox and stored until ready for use. In the final electrode, PEO/PEGDME and LiTFSI (referred to as the catholyte) were assumed to conformally coat the VC particles throughout the electrode.

As with the electrolyte, several different recipes of VC electrodes were prepared, which varied the weight fraction of VC, PEO molecular weight, and carbon loading. These variations are listed in Table 4-2.

Table 4-2. Electrode names and descriptions used in this chapter. Average carbon loading is based on the measured electrode weight rather than the loading targeted when preparing the electrodes.

Name	PEO MW (g/mol)	% VC (wt/wt)	Average carbon loading (g_{VC}/cm^2)
VC4M-60-0.3	4×10^6 PEO	60	0.3
VC4M-75-0.4	4×10^6 PEO	75	0.4
VC100k-60-0.4	10^5 PEO	60	0.4
VC2k-60-0.3	2,000 PEGDME	60	0.3
VC2k-45-0.3	2,000 PEGDME	45	0.3
VC2k-60-0.6	2,000 PEGDME	60	0.6
VC2k-60-0.9	2,000 PEGDME	60	0.9
VC4M-60-1.0	4×10^6 PEO	60	1.0

Complete cells were prepared by placing the VC electrode carbon-side down onto the PEO electrolyte, inside the protective FEP sheets. A PTFE rod was used to press the carbon into the electrolyte. The FEP was removed and the aluminum foil was carefully peeled back, leaving the VC electrode attached to the electrolyte. The mass of the VC electrode was determined by differencing the weight of the electrode/aluminum foil before and after attaching the carbon. The other protective FEP sheet was then removed from an electrolyte disk, and gently pressed into the exposed electrolyte onto a 15 mm diameter disk of lithium. Using plastic (non-conductive) tweezers, the second sheet of FEP was removed and a 316 stainless steel mesh disk (15 mm diameter, 400 mesh) was pressed on top of the VC electrode (if present) or directly onto the electrolyte (for VC-free cells). The completed stack was then placed into the body of a lithium-oxygen cell (designed and produced in our lab, as published previously),[28] a lightweight spring (Lee Spring, USA) was added to provide contact with the cell body, and the cell valves were closed to seal it. For most tests, the sealed cell was transferred to a water-free glovebox and purged with oxygen gas. The gas was allowed to flow through the cell at high rate for several seconds, to ensure that all the gas in the cell was replaced. The cell was then pressurized to 28 psig (2.9 atm absolute) and sealed, before being removed from the glovebox.

Cells were discharged using a Bio-Logic VMP3 multipotentiostat or a Solartron 1470A multipotentiostat. In all cases, cells were allowed to rest for 6 hours before discharge. Cells discharged at 60 °C were placed in an ESPEC SU-221 benchtop temperature chamber, and were held at 60 °C during the resting period. All discharges were carried out galvanostatically, with a cutoff voltage of 2.0 V_{Li}.

Electrochemical impedance spectroscopy (EIS) was performed to determine the conductivity of the electrolytes. 0.5 in diameter disks of electrolyte were punched out, and placed between two

108

0.5 in diameter stainless steel (SS) disks (0.5 mm thickness). The thickness of the electrolyte and SS disks was measured to determine the electrolyte thickness. These were then slid into a 0.5 in internal diameter plastic tube, and 2 SS slugs (0.5 in diameter, ~1 in length) were placed on either side of the electrolyte sandwich. The slugs were held in place using plastic set screws, and served to ensure good electrical contact was made to the electrodes while also providing some protection from the environment. This cell was then removed from the glovebox and connected to an EIS-capable channel on the Bio-Logic VMP-3. Measurements made at 60 °C were made using the temperature chamber, and were allowed to heat for 2 hours to reach equilibrium. Measurements made at room temperature were taken without resting. The amplitude of the applied voltage was 10 mV, and measurements were taken in single sine mode, with frequencies from 1 MHz to 10 mHz, with 10 points per decade and using the average of 5 measurements per frequency.

Grazing incidence X-ray diffraction (GIXD) was used to characterize the crystal structure of electrolytes and complete cells after discharge. All measurements were performed using a Rigaku SmartLab, with a 9 kW copper anode. Measurements were taken at room temperature under a polycarbonate dome to protect the sample from air exposure. GIXD was used (rather than traditional powder X-ray diffraction) because removing the bulk PEO electrolyte from the lithium anode was relatively destructive, and frequently resulted in significantly deformed electrodes. GIXD was performed with 2° incident angle, which was low enough to prevent any diffraction peaks from the lithium metal from appearing. Scans were performed at 1°/min from 10° to 60° 2θ, or 0.08°/min from 30° to 40° 2θ.

Several DEMS experiments were performed using P4M10IL-C electrolytes and VC4M-60-1.0 positive electrodes, where each cell was discharged at 60 °C then charged at a different tem-

perature. P4M10IL-C electrolytes were used to minimize electrolyte crystallization at low temperatures. VC electrodes with high carbon loading were used to maximize the absolute capacity. Each cell was rested for 6 hours and then discharged at 122 mA/gvc to 2 V_{Li} in oxygen at 60 °C. The total oxygen exposure for each cell was 24 hours, regardless of the duration of discharge. Pressure tracking experiments were performed during discharge using the procedure described in Chapter 3. After 24 hours, the gas in the cell was exchanged for argon and the temperature of the cell was adjusted to between 30 and 60 °C. Mass spectrometry (MS) measurements of the cell composition were taken every 15 minutes thereafter (using the procedure described in Chapter 3). A 24 hour rest between discharge and charge ensured cells were fully equilibrated before charging. Cells were charged at 122 mA/gvc to 5 V_{Li}, with DEMS measurements taken before, during, and after the charging process. A detailed discussion of the analysis technique for the DEMS measurements is available in Appendix A.

4.3 Results and Discussion

4.3.1 Electrolyte Characterization

Polymer electrolytes were characterized with and without ionic liquid at room temperature. Both electrochemical impedance spectroscopy (EIS) and grazing incidence X-ray diffraction (GIXD) were performed to evaluate the conductivity and crystallinity of these electrolytes (Figure 4-1). It was found that the addition of ionic liquids significantly reduced the crystallization and enhanced the conductivity of the electrolyte. The room temperature electrolyte conductivity was found to be 1.9×10^{-4} S/cm with IL (P4M10IL, Figure 4-1a, b), while the IL-free electrolyte (P4M20) exhibited capacitance at even very high frequencies (>1 MHz), which prevented the identification of a bulk conductivity. This is consistent with the GIXD results, which show that the IL-free electrolyte had a very large number of sharp crystal diffraction peaks, similar to that of pure

110

PEO, while the electrolyte with IL showed only a broad low-angle diffraction peak. Crystalline PEO is known to have very low lithium conductivity,[136] so the presence of large amounts of crystalline PEO in the IL-free electrolyte is consistent with the poor conductivity and high capacitance of that electrolyte.
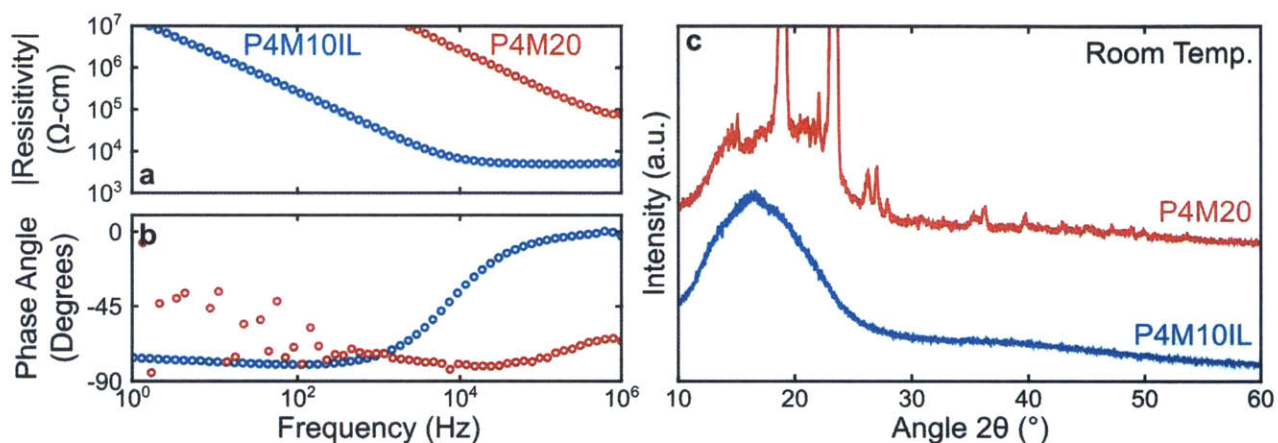
Figure 4-1. (a) Bode magnitude and (b) Bode phase plots of the EIS response of PEO electrolytes with and without ionic liquid (P4M10IL and P4M20, respectively) between stainless steel plates. (c) GIXD pattern of the same types of electrolytes shown in (a) and (b). All data was measured at room temperature. The large peaks in (c) have been truncated to increase the visibility of smaller peaks. Nyquist plots are not shown, as no significant features are visible on any length-scale for either electrolyte.

4.3.2 Room Temperature Performance

Solid polymer-based Li–air cells were discharged galvanostatically at room temperature using the P4M10IL-type electrolytes with VC2k-60-0.3 electrodes (Figure 4-2). Discharge was carried out at 10, 20, 50, and 100 mA/g$_{VC}$ to determine the rate capability of this system. It was found that capacity reached a maximum of 750 mAh/g$_{VC}$ at the lowest rate of 10 mA/g$_{VC}$. Discharge

capacity decreased with increasing discharge current, with less than half of the maximum capacity observed when discharged at 100 mA/gvc.
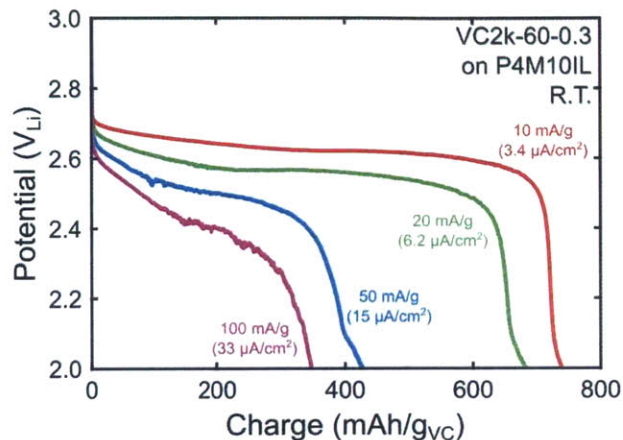
Figure 4-2. Potential vs accumulated charge for VC2k-60-0.3 electrodes discharged on P4M10IL electrolyte at room temperature at a variety of rates.

After establishing the rate capability of VC2k-60-0.3 electrodes, additional electrode types were discharged at the same rates to determine the impact of PEO molecular weight in the catholyte and VC content, using the first five electrode types listed in Table 4-2. Figure 4-3 shows a Ragone plot that summarizes the result of these investigations. In all cases, the cell capacity was observed to fall with increasing discharge rate. Cells discharged at low rates appeared to be carbon-mass limited; the final capacity of cells discharged at 10 mA/gvc was 600-800 mAh/gvc regardless of the electrode type. In contrast, cells discharged at high rate were area-limited; as shown in Figure 4-3b, cells discharged at rates above 10 $\mu A/cm^2$ largely followed the same capacity trend regardless of composition. Beyond discharge rate, the primary factor for discharge performance was found to be total carbon loading. When considering mass-normalized activity, electrodes with low carbon loading were found to have the highest performance, while area-normalized activity showed the

opposite trend: electrodes with high carbon loading had the best performance. It is clear from Figure 4-3 that further optimizations of electrode composition and structure are likely to only provide incremental improvements on the overall cell performance, as low-rate performance was limited by carbon mass, while high-rate performance was limited by the geometric area of the electrode. We note that incremental improvements are insufficient to meet the discharge performance goals offered by SAIT; the target of 1000 μAh/cm^2 at 200 μA/cm^2 is beyond the scale shown in Figure 4-3b, requiring a 3× enhancement in discharge capacity while simultaneously requiring a 5× enhancement in discharge rate.
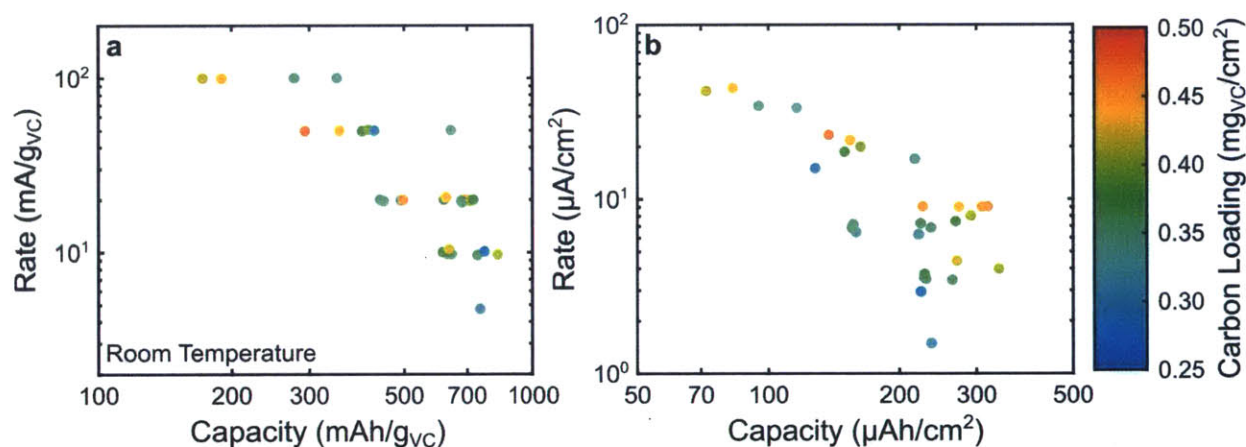
Figure 4-3. (a) Mass-normalized and (b) area-normalized Ragone plots for cells discharged at room temperature in oxygen using a variety of electrode types. Each electrode was weighed individually, and carbon loading varied between electrodes within individual batches.

4.3.2.2 Analysis of Rate and Capacity Limitations of Discharge at R.T.

In order to understand the nature of the rate and capacity limitations described above, we considered several different possible processes that could feasibly be the source of the observed rate limitation: the transport of oxygen to the surface of VC, the transport of Li$^+$ ions within the

electrode and electrolyte (*i.e.* ohmic losses), and the rate of charge transfer (*i.e.* electrochemical reaction rate). These are each considered below.

There are two stages of oxygen transport to examine when estimating the limiting rate of oxygen consumption. The first is diffusion of oxygen within the gas phase. Given that the atmosphere of the cells tested here is pure oxygen, this is effectively limitless; high rates of oxygen consumption would generate a pressure gradient that drives the bulk motion of more oxygen gas to the electrode surface. Reactions that were limited by the gas-phase transport of oxygen would quickly deplete the entire cell volume of oxygen. Because the VC electrodes used in this study were designed to have significant void volume, we expect that oxygen can remain in the gas phase throughout the electrode. However, oxygen must still be exposed to both electrons and lithium ions to be able to form Li_2O_2. This can either occur at triple-phase boundaries (between the carbon, PEO catholyte, and gas) or, if oxygen diffuses through the PEO catholyte, at the interface between carbon and catholyte. As triple phase boundaries are one-dimensional, we assume that these are negligible relative to conduction of oxygen through the catholyte. The limiting rate of oxygen consumption can be considered for oxygen diffusing through a film of thickness t, with a concentration in equilibrium with the gas on one side and zero concentration at the other (representing the instantaneous reaction of oxygen at the carbon surface). This is then easily solved by considering the permeation of oxygen through a PEO membrane:

$$N_{O_2}'' = -P_{O_2,PEO} \frac{p_{O_2}(t) - p_{O_2}(0)}{t} \tag{4-1}$$

where N_{O_2}'' is the area-specific mass flux of oxygen, $P_{O_2,PEO}$ is the permeability of O_2 through PEO, and $p_{O_2}(x)$ is the pressure of oxygen at position x, where $x = 0$ is the VC surface and $x = t$ is the catholyte surface. The permeability of oxygen in semi-crystalline PEO at 25 °C has been reported

114

at 0.26 barrer.[144] Given this permeability, a cell operating pressure of 3 atm, and a PEO film thickness of 5 nm (equivalent to ~60 wt% VC with ~40 wt% catholyte), we estimate that the diffusion limited rate of oxygen transport to the carbon surface is 5.3 mmol/(m^2 s), where the area is the true surface area of the carbon. Assuming 100 m^2/g$_{VC}$ and 2 e$^-$/O$_2$ of reaction, we estimate the oxygen transport limiting rate of discharge to be ~10^5 A/g$_{VC}$. We therefore conclude that oxygen transport is not limiting.

There are also two regions to consider when investigating lithium transport. Lithium must be conducted both through the bulk electrolyte and the catholyte. Ohmic losses in the bulk electrolyte can be easily estimated using the ionic conductivity measured above. At a discharge rate of 50 μA/cm^2, higher than any cell shown in Figure 4-3, the expected ohmic loss of a 150 μm thick electrolyte with 1.9×10^{-4} S/cm conductivity is 4 mV, indicating bulk electrolyte conductivity is not limiting cell performance. Estimation of conductivity in the catholyte is more difficult, and is dependent on the volume fraction of the catholyte, the thickness of the total electrode, and the tortuosity of the electrolyte path. We estimate the volume fraction of the catholyte by assuming that the VC deposited maintains the 85% porosity of the bulk VC powder, and that the catholyte uniformly coats the surface of the carbon. To estimate the tortuosity, we refer to Zalc et al.[166] who used Monte-Carlo simulations of porous nanomaterials to estimate the surface and void tortuosity of nanoporous catalyst materials. VC has a higher porosity than any configuration examined by Zalc et al., but in that work, the authors show that the surface tortuosity is generally in the range of 3-6 when the overall network is continuous, as is the case here. We use surface tortuosity because the catholyte is assumed to coat the surface of the VC structure; very thick layers of catholyte will have lower tortuosity values, as it may allow for shorter diffusion pathways, but this effect will only serve to reduce tortuosity. We therefore assume a tortuosity of 6 for this analysis. The effective

conductivity of the catholyte can be calculated to account for both the volume fraction of catholyte and tortuosity using Equation 4-2:

$$\sigma_{eff} = \frac{\sigma\theta}{\tau_s} \quad\quad (4\text{-}2)$$

Where σ_{eff} is the effective catholyte conductivity, σ is the bulk catholyte conductivity, θ is the volume fraction of catholyte, and τ_s is the estimated surface tortuosity of the electrode. In order to estimate the ohmic drop due to lithium conduction in the catholyte, we consider the ohmic drop associated with conducting 50 $\mu A/cm^2$ of lithium ions through the entire electrode, representing a worst-case estimate of limitations to lithium transport inside the cathode. The results of these calculations performed with a variety of possible electrode designs is shown in Table 4-3.

Table 4-3. Estimated ohmic drop due to lithium conduction within a cathode at 50 $\mu A/cm^2$. All cases assume a bulk conductivity of 1.9×10^{-4} S/cm and a tortuosity of 6. VC porosity was assumed to be 85%, with a bulk density of 0.264 g/cm^3, while the catholyte has an assumed density of 1.46 g/cm^3.

VC Mass Fraction (%)	Catholyte Volume Fraction (%)	Carbon Loading (mg/cm^2)	Electrode Thickness (μm)	Effective Conductivity (S/cm)	Ohmic drop (mV)
75	6	0.5	19	1.9×10^{-6}	**50**
60	12	0.5	19	3.8×10^{-6}	**25**
45	22	0.5	19	7.0×10^{-6}	**14**
60	12	1.0	38	3.8×10^{-6}	**50**

Although the estimated ohmic drop is large enough that we expect some inhomogeneity of discharge reaction throughout the electrode, it is not sufficient to explain the significant loss of

116

capacity at high rates; a shift of 50 mV in the discharge voltage of the lowest rate showed in Figure 4-2 would not result in the observed loss in discharge capacity at higher rates.
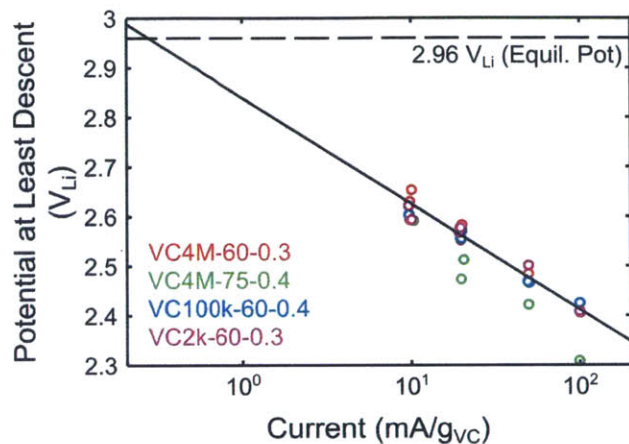
Figure 4-4. Potential at the point of least descent of the cell voltage *vs.* mass-normalized current of PEO-based Li–O$_2$ cells discharged at room temperature. The dashed line represents the theoretical reversible potential of Li$_2$O$_2$ formation. The solid line represents a best fit of the VC4M-60-0.3, VC100k-60-0.4, and VC2k-60-0.3 data points, giving a Tafel slope of 202 ± 23 mV/decade. VC4M-75-0.4 was not included in the fit owing to the large drop in voltage at high currents.

We finally consider the rate of charge transfer as a source of discharge rate limitations. We prepared a pseudo-Tafel plot (Figure 4-4), which considers the voltage of the cell during the flattest portion of the discharge profile (*i.e.* the point where the derivative of voltage with respect to time reached its most positive value, or the point of least descent) against the mass-normalized discharge rate (presented on a log scale). Electrodes with higher VC content (VC4M-74-0.4, ~75 wt% VC) were not included in this fit, as the potential deviated from the other samples, especially at high rate. The Tafel slope for the remaining set of tested electrodes (VC4M-60-0.3, VC100k-60-0.4, and VC2k-60-0.3) was 202 ± 23 mV/decade. This is in the range of values that have been

previously observed in our lab for carbon electrodes in liquid glyme-based electrolytes.[40,68] Moreover, the relationship between voltage and the log of the discharge current is linear, which is expected for kinetically controlled Butler-Volmer electrochemical reactions. We also note that the calculated value of the exchange current (the predicted current at the equilibrium potential) is 0.23 ± 0.12 mA/gvc. Assuming 100 m^2/gvc, the exchange current is 0.23 ± 0.12 nA/cm^2, approximately one order of magnitude lower than the estimated exchange current for carbon nanotube electrodes in 1,2-dimethoxyethane.[40] These results indicate that the limited discharge performance of PEO is likely controlled by reaction kinetics; further optimization of electrode design may lead to incremental improvements, but the reaction kinetics must be improved to allow for the development of a practical PEO-based Li–O$_2$ battery.

4.3.3 Discharge Performance at 60 °C

One of the most obvious and easily tested ways to improve the performance of the PEO-based Li–O$_2$ cells investigated above is to increase the operating temperature. Increasing the temperature should allow all aspects of the discharge process to occur more quickly: lithium conductivity should increase, the exchange current should increase, and the Tafel slope should decrease (reducing the rate at which voltage drops with increasing rate). In addition, large batteries such as those used in electric vehicles often operate at elevated temperatures, because the efficient removal of heat generated during discharge and charge becomes a significant engineering challenge.[135] We therefore investigated the operation of these cells at 60 °C, in agreement with SAIT, which provided funding for this research.

In addition to the performance enhancements listed above, the PEO electrolytes used in this study are melted at 60 °C. Although the bulk electrolyte used very high MW PEO ($\sim 4 \times 10^6$ g/mol), which remains extremely viscous even when melted, it was observed that cell shorting could occur

118

when allowed to discharge for extended periods. We therefore developed an electrolyte that included a Celgard interlayer; Celgard C480 was included when pressing the PEO electrolyte (refer to the Experimental Methods section for a detailed description). This allowed the PEO electrolyte to fill the void space within the Celgard (which has a porosity of 50%[167]). The Celgard interlayer does not melt at 60 °C, and so acts as a barrier preventing any portion of the positive electrode from making direct electrical contact with the negative electrode. Although this technique worked well for the purposes of this study, a realistic product would likely use advanced block-co-polymer materials that combine the conductivity of PEO with the mechanical properties of other polymers.[145,168,169] Using such polymers would also ensure that the positive electrode would not sink into the bulk electrolyte over very long-term operation.
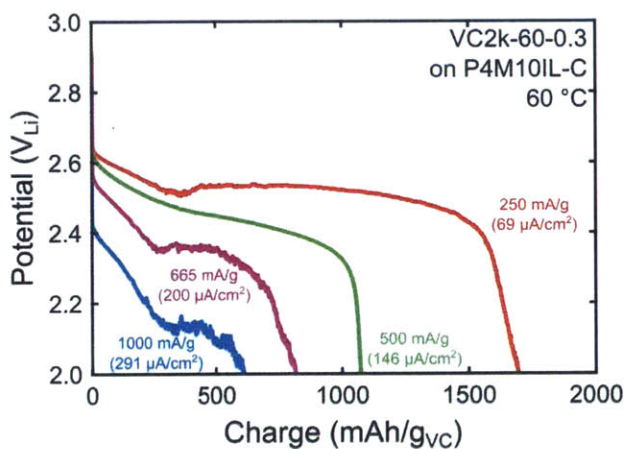
Figure 4-5. Potential vs accumulated charge for VC2k-60-0.3 electrodes discharged on P4M10IL-C at 60 °C at a variety of rates. Note that the lowest rate shown here (250 mA/gvc) is 2.5× higher than the highest rate shown in Figure 4-2. Also note that the horizontal scale extends to higher values than shown in Figure 4-2.

As was performed at room temperature, a set of VC2k-60-0.3 electrodes were discharged on a P4M10IL-C electrolyte (the "-C" indicates the inclusion of Celgard) at 60 °C at a variety of rates

(Figure 4-5). It is immediately apparent that increasing the temperature dramatically enhanced the discharge performance; an order of magnitude increase in rate capability was paired with a more than 2× enhancement of the total capacity.

We investigated whether the inclusion of ionic liquid within the bulk electrolyte was necessary to maintain good performance. Ionic liquid was initially added to the bulk electrolyte in order to inhibit crystallization of PEO, but melted PEO (as is expected at 60 °C) is not crystalline; ionic liquid is not necessary to maintain good conductivity of melted PEO. Appetecchi *et al.* showed that PEO-LiTFSI at 60 °C is only ~3× less conductive than a similar electrolyte with Pyr14TFSI, but is ~100× less conductive at 20 °C. EIS was performed on a P4M20-C electrolyte (which does not contain ionic liquid) at 60 °C, in the same manner as was used earlier in this chapter (Figure 4-6). The conductivity of the P4M20-C electrolyte at 60 °C is higher than the conductivity of the P4M10IL electrolyte tested at room temperature (3.9×10^{-4} *vs.* 1.9×10^{-4} S/cm, respectively).
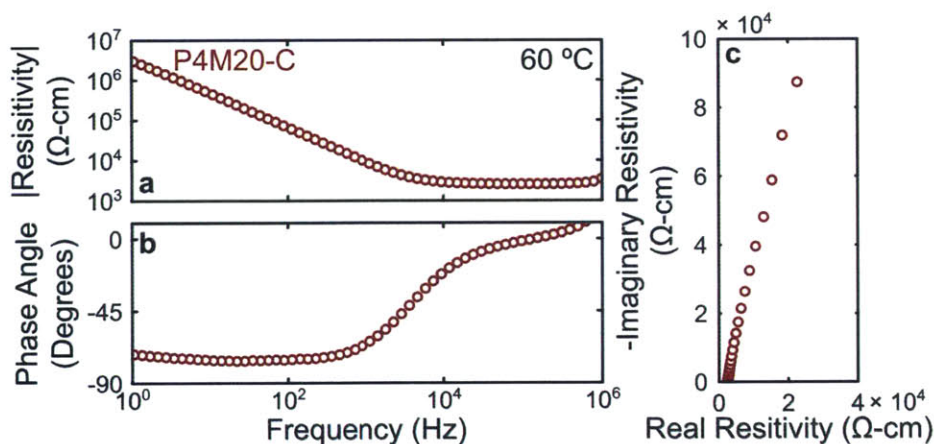
Figure 4-6. (a) Bode magnitude, (b) Bode phase, and (c) Nyquist plots of the EIS response of a P4M20-C electrolyte between stainless steel plates, measured at 60 °C.
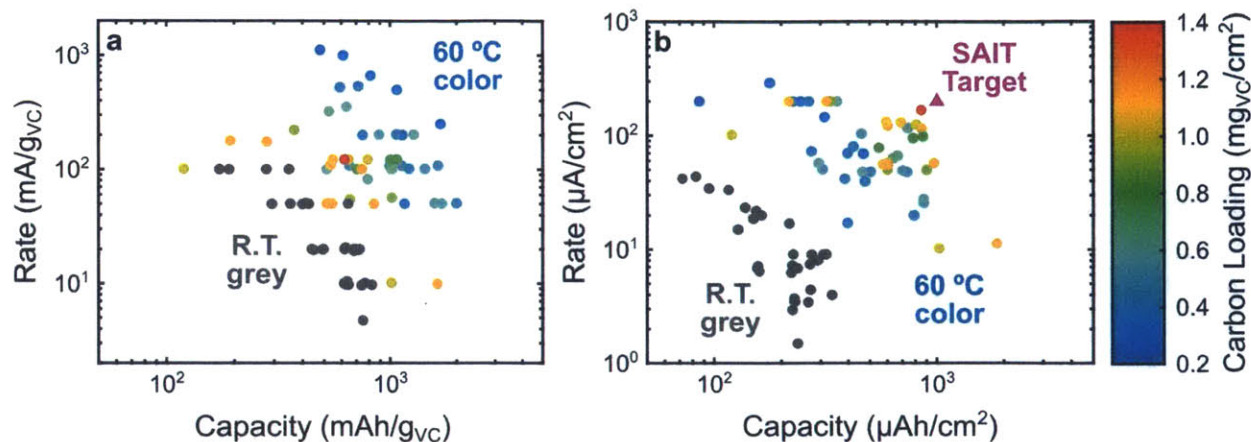
Figure 4-7. (a) Mass-normalized and (b) area-normalized Ragone plots for VC-PEO based cells discharged at 60 °C in oxygen. Note that the axes and color range in this figure are extended from Figure 4-3. The data from Figure 4-3 is reproduced in grey for comparison. The SAIT performance target (1000 μAh/cm^2 @ 200 μA/cm^2) is marked by a purple triangle in (b).

Using both electrolytes with and without ionic liquid, the performance of all of the electrode types listed in Table 4-2 was explored. A variety of different properties were varied between electrode types, including PEO molecular weight, VC weight fraction (related to the catholyte thickness over the VC particles), and total carbon loading, which was measured for each electrode. A Ragone plot showing the performance of each cell is presented in Figure 4-7. It was found that carbon loading, more than any other parameter, dominated the overall performance at most of the rates investigated. When examining mass-normalized performance, the very lightest electrodes (those presented in Figure 4-5) showed the highest rate capability, capable of discharging at as much as 1000 mA/g$_{VC}$. Increasing the carbon loading led to a reduction in observed performance. The opposite trend was observed when normalizing for geometric area; light electrodes showed relatively poor performance, with performance trending upwards with increasing carbon loading.

The heaviest electrode tested (red circle in Figure 4-7) showed only average mass-normalized performance, but nearly satisfied the performance target set by SAIT of 1000 μAh/cm^2 at 200 μA/cm^2 discharge rate. It should be noted that with few exceptions, performance at 60 °C was higher than at room temperature, regardless of normalization method or carbon loading.

Further examination shows that the maximum mass-normalized capacity observed for all carbon loadings at 60 °C was between 1600-2000 mAh/g$_{VC}$. This is more than twice the maximum capacity achieved at low rates at room temperature, which discharged to 700-800 mAh/g$_{VC}$ at low rates. It is not clear what allows for the observed increase in capacity, but one possibility is the transition of the PEO electrolyte from solid to liquid. Deep discharge capacities in liquid electrolytes are believed to require mobility of some discharge species into the bulk electrolyte.[38,39,129] In both its solid and melted phases, PEO is significantly more viscous than most liquid electrolytes, and we expect the mobility of discharge species to be quite limited. However, solid PEO may further inhibit the mobility of discharge products relative to melted PEO; the relatively high lithium conductivity of amorphous PEO relies on the chelation of lithium ions with consecutive oxygen atoms in the PEO backbone,[157] with segmental motion allowing lithium to move from one region to another. Other species, especially ionic, oxygen-rich compounds such as LiO_2, a $Li–O_2$ discharge intermediate,[33,86,170,171] are unlikely to interact in the same manner with the PEO backbone, and are therefore expected to have much lower mobility. A simple analysis allows us to convert the mass-normalized discharge capacity into a theoretical thickness of Li_2O_2 deposits on the VC surface. We assume a VC surface area of 100 m^2/g$_{VC}$ and the formation of crystalline Li_2O_2 (with a density of 2.31 g/cm^3). At room temperature, the maximum discharge capacity observed was 825 mAh/g$_{VC}$, corresponding to a Li_2O_2 thickness of 3 nm, while the maximum capacity observed at 60 °C was 2000 mAh/g$_{VC}$, equivalent to a 7.5 nm thick film of Li_2O_2. Although the

122

electronic conductivity of discharged Li_2O_2 is not well established, it has been proposed that crystalline layers of Li_2O_2 with thicknesses on the order of 3 nm would have significant resistance to electronic conduction, with an exponential increase in resistance with increasing thickness. One possible explanation of the capacity increase we observed is that in solid PEO, LiO_2 that is formed on discharge is essentially immobile, and directly forms a layer of Li_2O_2 at the discharge site (either through chemical disproportionation or a second electrochemical reduction reaction). When PEO is melted, the increased motion of the PEO chains may allow for some diffusion of LiO_2 away from the initial reaction site, allowing for a thicker deposit of Li_2O_2 to form. In the extreme, this process could result in the micron-scale toroid particles that have been widely reported in liquid electrolytes discharged at low rates.[10,31,38–40,78,96,118] Such large particles are unlikely in an electrolyte as viscous as PEO, especially as the electrode is not flooded, requiring all products to remain within a few nm of the carbon surface.

This hypothesis is also consistent with GIXD of electrodes taken at room temperature after discharge at either temperature (Figure 4-8). The diffraction patterns were inconclusive; no high-intensity peaks that could be used to fingerprint possible discharge products were observed in the wide-angle scan. A very slow scan was performed from 30-40° 2θ, which showed very slight, broad peaks at ~32° and ~35° 2θ. The peak at 35° is consistent with the primary (101) peak of Li_2O_2, and the peak at 32° is possibly consistent with the (100) Li_2O_2 peak. Further, larger peaks are observed for the sample discharged at 60 °C, although they are not as well aligned with the Li_2O_2 pattern. This may indicate that more discharge product is forming at 60 °C, as proposed above, but that much of that additional product is not in the form of crystalline Li_2O_2. It is important to emphasize that these results are inconclusive, and many possible compounds could produce the

peaks observed, but that these results are consistent with the formation of Li_2O_2 and other compounds during discharge of PEO-based Li–O_2 cells.
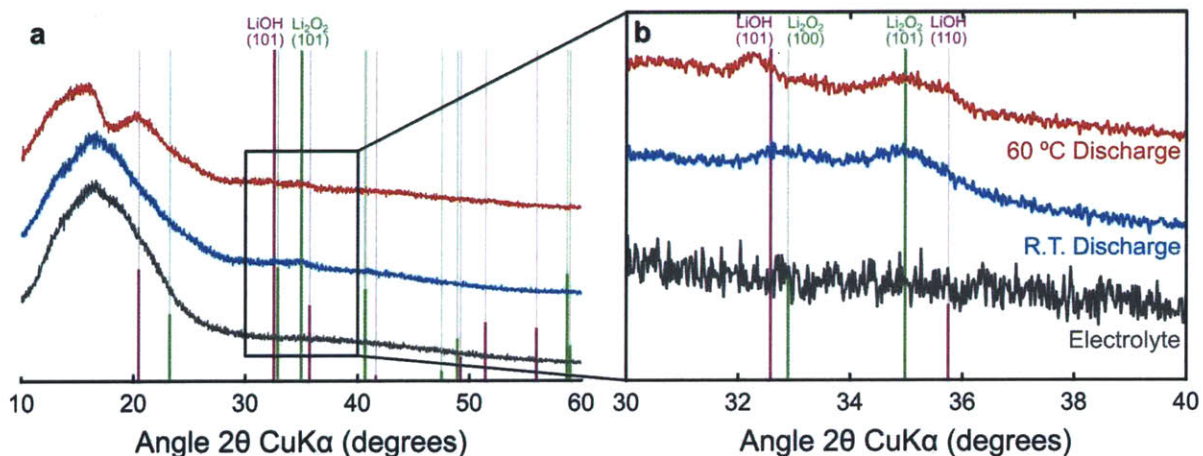
Figure 4-8. GIXD patterns of electrodes after discharge at room temperature and at 60 °C. (a) Wide-angle scans were performed at 1°/min. (b) Scans for the discharged electrodes taken at 0.08°/min from 30° to 40° (Electrolyte data is the same as in (a)). All measurements were performed at room temperature under a polycarbonate dome to prevent air exposure.

4.3.4 Analysis of Gases Produced during Charging of PEO-Based Li–O_2 Cells

In addition to the largely electrochemical characterization above, some preliminary investigations of gas consumption and production of PEO cells were carried out. Using the DEMS described in detail in chapter 3, a series of experiments were performed in which VC4M-60-1.0 electrodes were discharged at 122 mA/gvc in oxygen at 60 °C with a P4M10IL-C electrolyte, and then charged in argon between 30 and 60 °C. Pressure tracking was carried out during discharge (Figure 4-9), and MS readings were taken during the entire time that the cells were under argon (Figure 4-10). The high carbon loading was used to maximize the total gas production and consumption, enhancing the sensitivity of both pressure and MS readings.
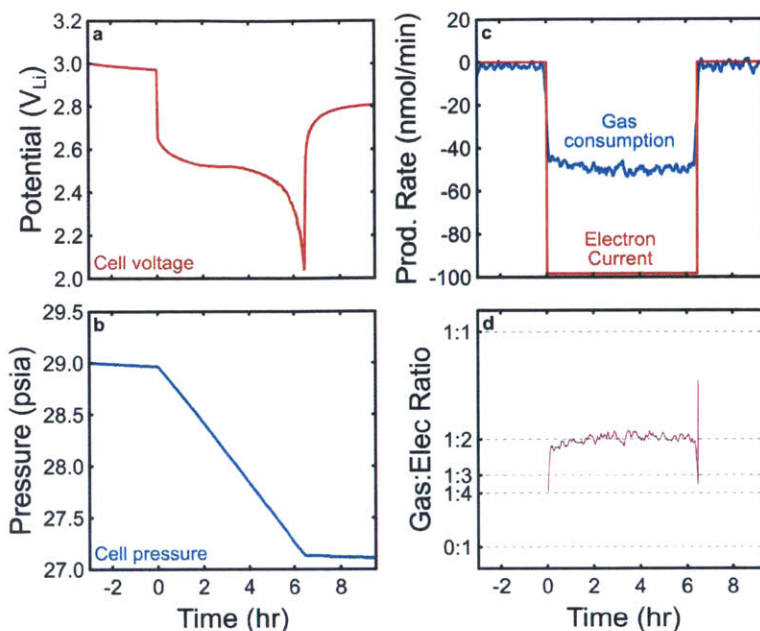
Figure 4-9. Representative results from pressure tracking a PEO-based Li-O$_2$ cell during discharge. (a) Cell voltage, (b) measured cell pressure, (c) gas production rate and electron current (converted into nmol/min), and (d) ratio of gas consumption to electron current *vs.* time. See chapter 3 for a detailed discussion of this analysis process. All plots are aligned in time, with 0 corresponding with the start of discharge.

Figure 4-9 shows representative discharge performance of the cells. The total current to gas consumption was between 1.92 and 2.00 e$^-$/O$_2$ for all four cells. The deviation from 2 e$^-$/O$_2$ is attributed to equilibration of oxygen into the PEO electrolyte, and to the PEO autoxidation reaction explored in Chapter 5. The high carbon loading caused the cells to be area-limited; the total discharge was approximately 800 µAh/cm^2, although the carbon loading varied between electrodes. This caused the exact length of discharge to vary between cells.

Figure 4-10 summarizes the results of the charging process and MS measurements. The cells charged at 30° and 40 °C showed a single plateau region between 3.5 and 4.0 V$_{Li}$, after which the voltage rapidly climbed to the cutoff of 5 V$_{Li}$. These cells also only showed the production of
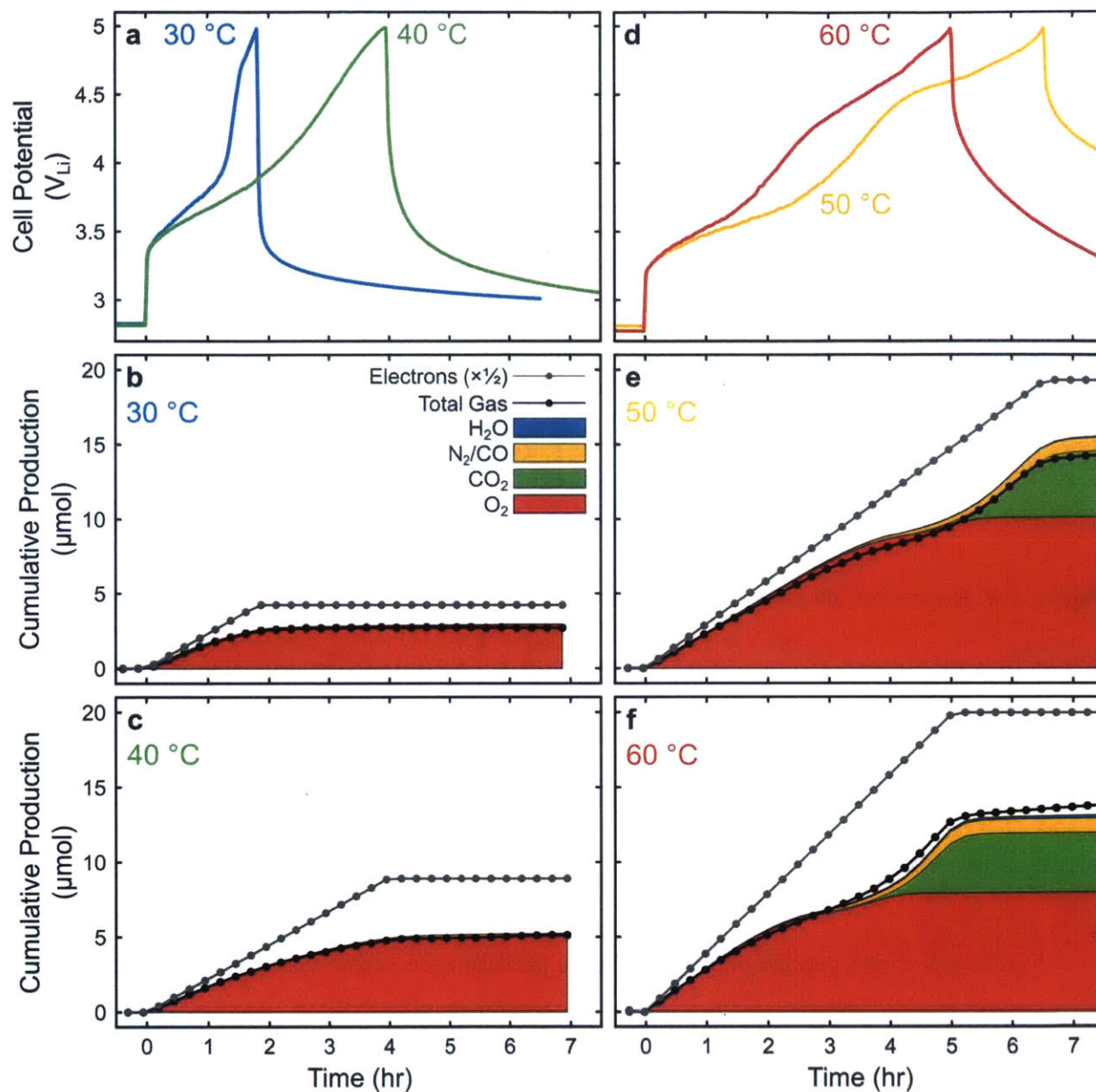
Figure 4-10. (a & d) Cell potential *vs.* time for Li–O$_2$ cells charged at (a) 30 °C and 40 °C, and (d) 50 °C and 60 °C. (b, c, e, & f) Cumulative production of gases generated during charge *vs.* time at (b) 30 °C, (c) 40 °C, (e) 50 °C and (f) 60 °C. The grey line indicates one-half of the number of electrons passed during the charge process; during a 2e$^-$/O$_2$ reaction, the grey line would align with the oxygen production area.

oxygen, with oxygen making up 100% and 98% of the evolved gas at 30 and 40 °C, respectively. There was good agreement between the total gas production (black line) and the accumulated production of each gas, indicating that all gases were detected by the MS. However, the overall efficiency of the charge process was quite poor at low temperatures. At 30 °C, the charge capacity was 21% of the discharge capacity, and at 40 °C the charge capacity was 48% of discharge, indicating that a large fraction of the products formed during discharge were not oxidized. Furthermore, the oxygen gas produced during charge was significantly less than would be expected by a 2 electrons/oxygen process. The oxygen production rate was highest at the beginning of discharge, reaching 2.6 e^-/O_2 at both 30 °C and 40 °C, then decaying gradually until almost no oxygen was produced at the end of the charge process. The total oxygen to electron ratio was 2.9 e^-/O_2 at 30 °C, and 3.5 e^-/O_2 at 40 °C, giving a total oxygen recovery of just 14% at 30 °C and 27% at 40°C.

A sharp change in charging response is observed for the cells charged at 50 and 60 °C. The charging profile changes to have a second plateau at potentials above 4.5 V_{Li}, and both cells had a total coulombic efficiency of 100%. In contrast with lower temperatures, significant production of carbon dioxide, hydrogen, and carbon monoxide were observed in addition to that of oxygen. Total gas production once again agreed with the accumulated MS readings. At low voltages, oxygen was the dominant charge product. Above 4.0 V_{Li}, a wave of hydrogen is produced, which begins to fall off around 4.5 V_{Li}, when a small amount of additional oxygen is produced. Finally, starting at 4.5 V_{Li} and continuing to the end of charge, a large amount of CO_2 is produced, reaching 2 e^-/CO_2 at the highest voltages. Total oxygen production was 3.8 e^-/O_2 and 5.0 e^-/O_2 at 50 and 60 °C, respectively, and made up only 71% and 55% of the total gas produced. CO_2 was 31% and 28%, CO was 7% and 7% of all gases at 50 and 60 °C respectively, with a small amount of unidentified gas produced at high potentials. The total oxygen recovery was 52% and 40% at 50 and 60 °C.

The marked change in charging behavior between 40 and 50 °C indicates that a transition must occur between those two temperatures. The gradual enhancement of reaction kinetics with temperature is unlikely to cause such a dramatic change in behavior, and the similarity between the charging behavior at 50 and 60 °C is inconsistent with a purely Arrhenius response. The sharp change in behaviors is more consistent with a phase transition, where properties can rapidly change over a narrow temperature window. The melting transition of the catholyte was not measured, but has been reported to be below 50 °C with this composition.[172] Above its melting point, the catholyte would be expected to flow more easily, and may allow more of the discharge product to interact with the VC surface. Additionally, intermediate species may be more mobile in the melted electrolyte as is hypothesized to be important during discharge, which could allow reactions to proceed at 50 °C that would be mass transport limited at 40 °C. An exact explanation of the sequence of gas production remains elusive; the order is likely related to the different species formed during discharge (or even earlier in the charge process), and relates to the potential at which each of them begins to break down. However, it is clear that at and above 50 °C, significantly more electrolyte and/or electrode degradation occurs during the charging process.

4.4 Conclusions

In this chapter, we have developed a PEO-based Li–O2 cell, and characterized its discharge performance at room temperature and at 60 °C. We show that at room temperature, discharge performance is limited by the charge transfer reaction, with additional limitations due to transport of lithium at higher rates. At 60 °C, we show a significant improvement in the discharge rate and capacity, and show that carbon loading is the dominant factor in controlling discharge performance. We demonstrated cells that approached the discharge performance targets set out by SAIT, which must be met to produce practical Li-air devices. Finally, we analyzed the discharge and

128

charge performance of these cells using DEMS, showing that during discharge at 60 °C oxygen is consumed at a rate consistent with the formation of Li_2O_2, but that charging at lower temperatures reduces the amount of unwanted gases produced. These results suggest the chemical stability and electrochemical performance of PEO-based $Li–O_2$ devices must be carefully balanced in future work, minimizing the operating temperature while using additives and plasticizers to maximize cell performance.

4.5 Acknowledgement

Chapter 5

Instability of Poly(ethylene oxide) upon Oxidation in Lithium–Air Batteries*

5.1 Introduction

In spite of the theoretical promise of Li-air batteries outlined in Chapter 1, many challenges must be resolved before practical devices can be produced, including low cycle life, high charging overpotential, and instability of lithium metal at the negative electrode.[19,31] In particular, electrolyte stability has proven to be a significant problem in the operation of Li-air batteries over multiple cycles, and many recent papers have focused on the search for suitable electrolyte solvents that are stable against the lithium peroxide and superoxide species that are produced during discharge.[31,49,50,53,54,83,86,98,113,114,170] Ether-based small molecules and oligomers, such as 1,2-dimethoxyethane (DME) or tetraglyme, have been shown to be moderately stable,[41,49,50,72,170] and have been demonstrated in sealed oxygen cells cycled several times at ambient conditions.[41] Other liquid electrolytes have also been recently investigated for use in Li-air batteries, including N,N-dimethylformamide,[132] N,N-dimethylacetamide,[113] and dimethyl sulfoxide,[55,173] which has been observed to react over time with lithium peroxide produced during discharge to form lithium hydroxide.[55]

Although liquid electrolytes have been the primary focus of most Li-air battery research to date, solid electrolytes offer several advantages to practical Li-air batteries, including protection of the lithium anode, prevention of electrolyte loss to the environment, and facilitation of oxygen transport to the reaction surface. Two major categories of solid electrolyte are available for Li-air cells: solid polymer electrolytes and solid ceramic electrolytes, which are varied and based on many different chemical and structural compositions.[136] Lithium conducting ceramic electrolytes have been investigated for use as both an electrolyte membrane (in aqueous and non-aqueous systems),[120,146,174,175] and as the catholyte in the air electrode where the $Li-O_2$ reaction occurs.[176] However, their high density (relative to liquid and polymer electrolytes) and difficult handling

requirements motivate research into solid polymer electrolytes, which have densities approaching that of liquid electrolytes and can be easily processed using low temperature melt or solvent techniques. Gel polymer electrolytes have been used for Li-air batteries previously,[147] including the first demonstration of a non-aqueous Li-air battery by K.M. Abraham et al.[73] However, recent results by our group have shown that many polymers used in gel polymer electrolytes for lithium-ion batteries are unstable when exposed to lithium peroxide,[97] making them unsuitable for Li-air batteries.

Polyethylene oxide (PEO) has been known as a solid state lithium conductor for more than 30 years,[154] and research during that time has aimed to increase the conductivity, reduce the operating temperature, and improve the mechanical stability of these electrolytes.[26,161,177] These PEO electrolytes have been shown to have a large electrochemical stability window, forming a stable SEI against lithium metal, and no significant decomposition current below 4.9 V vs lithium (V_{Li}).[160] Furthermore, PEO has been shown to have good conductivity above its melting point (10^{-3} S/cm at 60 °C),[136] and various additives have been used to produce functional lithium-ion batteries using a solid PEO electrolyte.[160] Recently, PEO has been investigated as a solid polymer electrolyte for use in Li-air batteries,[148,151] showing that PEO is more stable than carbonate electrolytes for Li-air batteries,[148] and demonstrating a PEO-based Li-air cell that was cycled many times under limited capacity conditions.[151]

In this chapter, we show that PEO electrolytes that are otherwise suitable for use in Li-air batteries undergo significant oxidation when exposed to oxygen and the potentials needed to charge Li-air batteries. The degradation of PEO is observed to occur regardless of the presence of a carbon-based air electrode or Li-air discharge products. The reaction is observed to proceed more

rapidly with increasing potential, resulting in significant liquefaction of the solid polymer electrolyte after less than 100 hours at 60 °C. We use NMR to identify the PEO decomposition products as those associated with PEO oxidation. Finally, we propose that the rate of spontaneous formation of radical species in PEO is accelerated with increasing potential, and conclude that PEO and PEO-derived polymers are unsuitable for elevated temperature work in Li-air batteries. These results may also have further implications about the long-term stability of ether-based small molecule liquid electrolytes (e.g., DME) at room temperature for Li-air applications.

5.2   Experimental Methods

Polyethylene oxide (PEO, MW ~4×10^6 g/mol, <1000 ppm BHT) was obtained from Sigma-Aldrich (USA). Butylated hydroxytoluene (BHT) in PEO can minimize oxidation during normal handling of PEO. For electrochemical applications it has been shown that an antioxidant in the electrolyte will interfere with the electrochemical behavior of the cell,[178] and most battery electrolytes are used without these antioxidants. For most experiments presented here, the BHT in the PEO as supplied by the manufacturer was removed from the PEO via Soxhlet extraction in hexanes under flowing argon gas for at least 24 hours. Extracted PEO was dried under vacuum at 50 °C for 48 hours before being stored in an argon glovebox (<3 ppm O_2, <0.1 ppm H_2O) until needed. Lithium bis(trifluoromethane)sulfonimide (LiTFSI, 99.95% trace metals basis) was obtained from Sigma-Aldrich (USA) and dried under vacuum at 100 °C for at least 24 hours before being transferred to an argon glovebox for storage. Separator material was Celgard C480 (Celgard, USA).

The PEO electrolyte was prepared by mixing PEO and LiTFSI (20:1 mol Li/mol EO) with a mortar and pestle inside an argon glovebox. The electrolyte was mixed until the LiTFSI dissolved in the PEO, resulting in a stiff, white mass. This mixture was then annealed under vacuum at 100 °C for at least 24 hours, after which the mixture became clear. The mixture was placed between

134

fluorinated ethylene propylene (FEP) sheets and heat-sealed in a water vapor and oxygen transport resistant bag (Sigma-Aldrich, USA; meets MIL-PRF-131K). This bag was then pressed in a benchtop hot press at 100 °C with a maximum applied load of 1 metric ton per 2 g electrolyte, slowly increasing pressure to minimize the formation of wrinkles. Shims were used to ensure that the electrolyte film thickness was approximately 150 μm. To include a Celgard interlayer, the electrolyte was cut in half, and each half was pressed separately. These were returned to the glovebox, and stacked with a sheet of Celgard C480 in between the two halves of electrolyte. This sandwich was resealed and pressed at 100 °C, with a maximum applied load of 5 metric tons per 2 g electrolyte. Heat was removed and the press was allowed to cool to room temperature overnight under load. This allowed the PEO electrolyte to fully impregnate the Celgard film, resulting in a translucent film (if the PEO does not fill the Celgard, the film remains white and exhibits poor ionic conductivity). Once pressed, the electrolyte was returned to a water-free glovebox (<0.1 ppm H_2O), removed from the bags, and punched into 18 mm diameter disks. The FEP film was left on to prevent electrolyte disks from sticking to each other. These disks were collected in a scintillation vial and stored in an argon glovebox until used.

Vulcan carbon (VC) air electrodes were prepared by mixing VC (Premetek, USA), PEO, and LiTFSI (70% w/w VC, 10:1 mol EO/mol Li) in a planetary ball mill (Fritsch Pulverisette 6, Germany) jar, along with 5 mm diameter zirconia beads. A 50% v/v mixture of ethanol in deionized water were added to the jar before sealing and milling for at least 4 hours at 500 rpm. The resulting slurry was deposited onto aluminum foil using a Meyer rod with a wet film thickness of 125 μm. The solvent was allowed to evaporate in air before 0.5 inch diameter discs were punched. These disks were collected in a scintillation vial and dried for at least 24 hours at 100 °C under vacuum,

before being directly transferred into an argon glovebox and stored until ready for use. The resulting electrodes had an approximate areal carbon density of 0.43 mg VC/cm^2 and a total carbon loading of approximately 0.54 mg in each electrode.

Electrochemical cells were prepared in two different configurations, with and without a porous VC positive electrode, inside an argon glovebox. Cells with a VC electrode were prepared by placing the VC electrode carbon-side down onto the PEO electrolyte, inside the protective FEP sheets. A PTFE rod was used to press the carbon into the electrolyte. The FEP was removed and the aluminum foil was carefully peeled back, leaving the VC electrode attached to the electrolyte. The mass of the VC electrode was determined by differencing the weight of the electrode/aluminum foil before and after attaching the carbon. Cells without a VC electrode omitted this step. For both types of cell, the other protective FEP sheet was removed from an electrolyte disk, and gently pressed into the exposed electrolyte onto a disk of lithium (Chemetall, Germany, 15 mm diameter). Using plastic (non-conductive) tweezers, the second sheet of FEP was removed and a 316 stainless steel mesh disk (15 mm diameter, 400 mesh) was pressed on top of the VC electrode (if present) or directly onto the electrolyte (for VC-free cells). The completed stack was then placed into the body of a lithium-oxygen cell (designed and produced in our lab, as published previously),[28] a lightweight spring (Lee Spring, USA) was added to provide contact with the cell body, and the cell valves were closed to seal it (see Figure 5-1). The sealed cell was transferred to a water-free glovebox and purged with oxygen or argon as appropriate. The gas was allowed to flow through the cell at high rate for several seconds, to ensure that all the gas in the cell was replaced. The cell was then pressurized to 28 psig (2.9 atm absolute) and sealed, before being removed from the glovebox.

All electrochemical tests were performed at 60 °C, using an ESPEC SU-221 bench-top temperature chamber (ESPEC NORTH AMERICA, INC.; USA) and either a Bio-Logic VMP3 multi-

136

channel potentiostat (Bio-Logic SAS, France) or a Solartron 1470A multi-channel potentiostat (Solartron Analytical, USA). Cells were placed into the heating chamber and immediately connected to a potentiostat for testing. To establish the behavior of PEO electrolytes (without BHT) without applied potential, two cells without VC air electrodes (VC-free cells) were prepared and allowed to rest with an open circuit at 60 °C for 100 hours, one in an oxygenated environment, and another in an argon atmosphere. Cells that were tested potentiostatically or galvanostatically were rested with an open circuit for 6 hours before further testing. At the end of the test, the cells were removed from the heating chamber and transferred into a dry glovebox, where the oxygen from the cell was purged out, before being disassembled and the PEO electrolyte was stored in an argon glovebox.

A detailed discussion of the methods used for pressure tracking and mass spectrometry experiments is presented in Chapter 3. Pressure tracking experiments were performed by connecting a cell to a custom-built apparatus based on the design published by McCloskey et al. for a differential electrochemical mass spectrometer (DEMS).[83] Cells were attached to the DEMS while placed inside a temperature chamber. Cells tested with the DEMS were prepared in the same manner described above, but not purged with any gas prior to connection to the DEMS. A pressure gauge (PX409-030AUSBH; Omega Engineering, INC.; USA) outside the temperature chamber was used to track the pressure of the cell throughout the test, and the temperature of both the gauge and cell were tracked throughout the test. The volume of the cell was measured by expanding the gas in the cell into an evacuated tube of known volume, while the cell was at room temperature. While full of argon gas, the cell was heated to 60 °C and allowed to rest for approximately 24 hours to allow the pressure to stabilize. Once stabilized, the cell was purged with oxygen and electrochemical tests were performed as described above. The ideal gas law was used to calculate

the total moles of gas within the cell, and the rate of gas consumption and/or production was calculated by averaging the total moles of gas over 60 second intervals and using a Savitzky-Golay filter with polynomial order 2, filter width 31, and coefficients for the 1st derivative (a detailed discussion of the analysis used for volume measurement and estimation of gas consumption/production rate is available in Appendix A).[179]

Nuclear magnetic resonance (NMR) characterization was performed by dissolving a fragment of the collected PEO electrolyte in 0.7 mL of deuterated chloroform (D, 99.8 %). The contents of the vial were rested overnight to allow the PEO electrolyte to dissolve. After resting, the fragment of undissolved Celgard was removed, and the solution was transferred to a NMR tube for ^{1}H NMR analysis. A Bruker AVANCE and Bruker AVANCE III-400 MHz NMR spectrometer was used.

Simulated ^{1}H-NMR data was calculated using the ChemNMR package provided with Chem-BioDraw Ultra (CambridgeSoft, PerkinElmer, USA), with a model solvent of $CDCl_3$ and 400 MHz.

Quantification of NMR was performed by integrating peaks in the following regions: 9.67-9.72 ppm (identified as aldehyde), 8.04-8.15 ppm (formate), 5.35-5.40 ppm (PEO-hydroperoxide/alcohol), 3.96-4.52 ppm (mixed oxidation products), and 3.42-3.90 ppm (ethylene oxide repeat unit). These areas were then converted into a relative number of each functional group, based on the number of protons predicted in that region for each functional group. Since both the aldehyde and formate groups are expected to produce peaks in the mixed oxidation products region (from the beta-carbon protons), the expected area of these protons was subtracted from the measured area in that region, with the remaining area identified as ester functional groups.

138

5.3 Results and Discussion

5.3.1 Oxidation of PEO Electrolytes

5.3.1.1 Oxidation at OCV without BHT

In order to establish the behavior of the PEO electrolyte in the Li–O_2 environment, two VC-free cells (Figure 5-1) were allowed to rest for 100 hours at 60 °C in oxygen and argon, respectively. It was observed that the open-circuit voltage (OCV) of the oxygen cell rose from 2.9 V_{Li} to more than 3.5 V_{Li} after resting, while the OCV of the cell in argon rose only slightly, from 2.8 V to 2.9 V_{Li} (Figure 5-2a).

For the oxygen cell, the OCV of the VC-free cell with BHT-free electrolyte rose throughout the duration of the test, starting around 2.95 V_{Li}, and rising to 3.53 V_{Li} after 100 hours. In contrast, the OCV of the argon cell reached a plateau after 5 hours and remained steady throughout the test. In oxygen, visible electrolyte degradation was observed in addition to the rise in OCV. Portions of the electrolyte were liquid at room temperature after resting at OCV for 100 hours in oxygen, and Celgard was required to prevent the cell from shorting. On the other hand, no significant changes in the electrolyte were observed for the cell in argon (Figure 5-2a, inset). The observed liquefaction indicates that chain scission of PEO occurred upon oxidation to break down the long backbone of
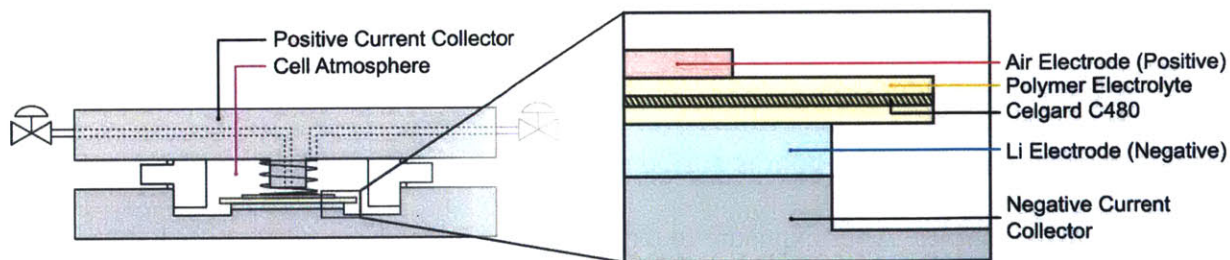
Figure 5-1. Schematic of the cell used for all tests. Inset shows the structure of the cell and polymer electrolyte, with a Celgard layer inside the polymer electrolyte. The air electrode is either an SS mesh for VC-free cells, or a VC electrode.

139
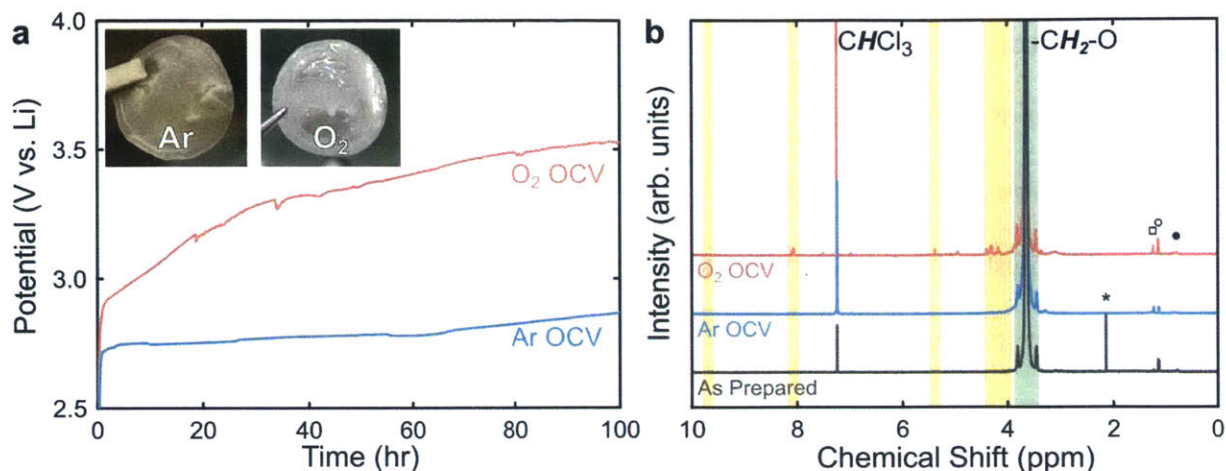
Figure 5-2. (a) OCV versus time of cells rested in oxygen and argon for 100 hours. Inset shows optical images of the electrolyte samples after the rest. (b) NMR spectra of the rested electrolytes shown in (a). Peaks for PEO and chloroform (from the NMR solvent) are labelled, and peaks from the Celgard separator are identified by an open square (□) for polyethylene and open and closed circles (○ and ●) for polypropylene. Acetone contamination (from the NMR tube) is identified by *. Additional peaks attributed to the oxidation of PEO are highlighted in gold. Each plot was normalized to the area of the primary PEO peak highlighted in green.

PEO in oxygen at room temperature, which is discussed in detail using NMR data below. ^{1}H-NMR data collected from a fragment of the rested electrolyte samples support the breakdown of the PEO electrolyte in oxygen but not in argon (Figure 5-2b). The as-prepared electrolyte shows peaks consistent with PEO, with additional peaks identified as trace amounts of Celgard, acetone, and chloroform. The sharp peak at 2.15 ppm is attributed to acetone contamination introduced while preparing the NMR samples. After exposure to oxygen, peaks were observed at shifts between 4.10–4.50 ppm, 5.35-5.40 ppm, 8.10-8.15 ppm, and 9.75 ppm.[41] In contrast, the electrolyte rested in argon shows no peaks in these regions. Although PEO is known to be susceptible to attack from atmospheric oxygen;[180–183] and the mechanism of this reaction is well understood,[42,43] we note

140

that most PEO thermal oxidation experiments have shown this reaction to be slow, requiring experiments as long as 1000 hours to show significant oxidation,[180,183] which is in contrast to the significant amount of oxidation observed in these experiments after only 100 hours.

5.3.1.2 Oxidation at OCV including BHT

Similar resting experiments were performed on PEO with the antioxidant BHT in order to suppress the oxidation of PEO in the Li–O$_2$ cell (Figure 5-3). The presence of BHT delayed the onset of the rise in OCV, but after 40 hours the OCV was found to increase in oxygen. NMR analysis confirmed the presence of comparable oxidation products observed in the BHT-free electrolytes (Figure 5-3b). The presence of BHT in the electrolyte may explain the relatively good performance of PEO-based Li–O$_2$ batteries shown in the very recent work by Balaish *et al.*[151] We note that the authors of that work do not report removing the BHT that is added to commercial PEO, and further note that the limited capacity cycling shown in that work is estimated to have
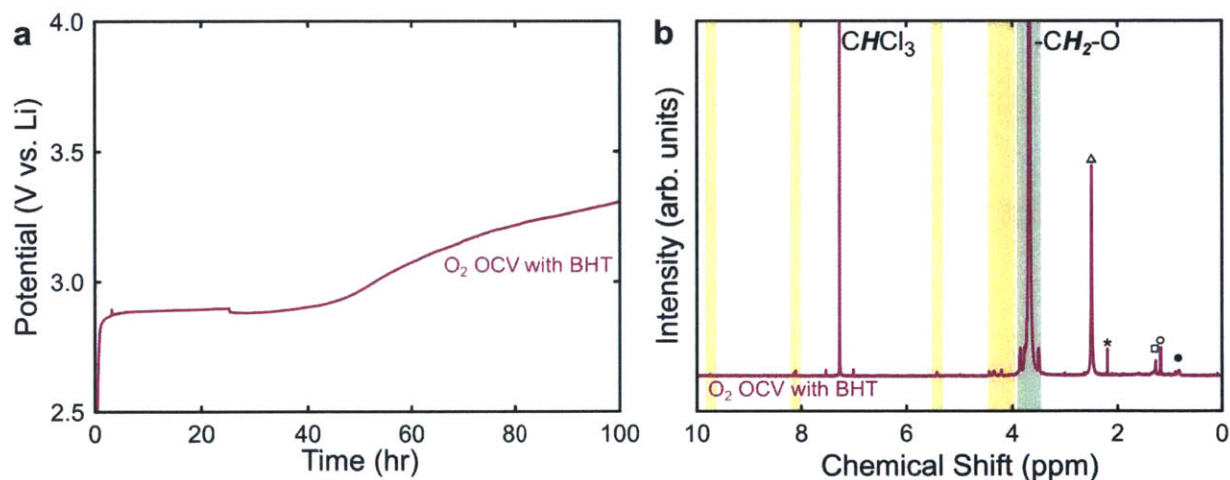
Figure 5-3. (a) Open-circuit voltage (OCV) versus time of cells using PEO with BHT, rested in oxygen for 100 hours. (b) NMR spectra of the rested electrolyte shown in (a). All scales match those used in Figure 5-2. Peaks are described as in Figure 5-2., and each plot was normalized to the area of the primary PEO peak highlighted in green.

lasted less than 40 hours. The BHT present in the electrolyte was likely irreversibly oxidized throughout the electrochemical tests presented in that work, and therefore acted to suppress the total amount of electrolyte oxidation observed.

5.3.1.3 Oxidation with Applied Potentials above OCV

We further examined the effect of potentials greater than OCV on the oxidation kinetics of PEO electrolytes. Li–O₂ cells reported in the literature[41,50,54] are frequently charged at potentials of 3.6–4.0 V_{Li} or greater, and it is desirable to determine the effect of these higher potentials on the oxidation of the PEO electrolyte. We prepared several VC-free cells and held them potentiostatically at 3.6, 3.8, and 4.0 V_{Li} for 100 hours in oxygen, along with a cell held at 3.8 V_{Li} in argon. The steady-state current (Figure 5-4a) observed for each of these cells was low (<350 nA), and was similar for cells tested in oxygen or argon, indicating that oxygen does not directly pro-
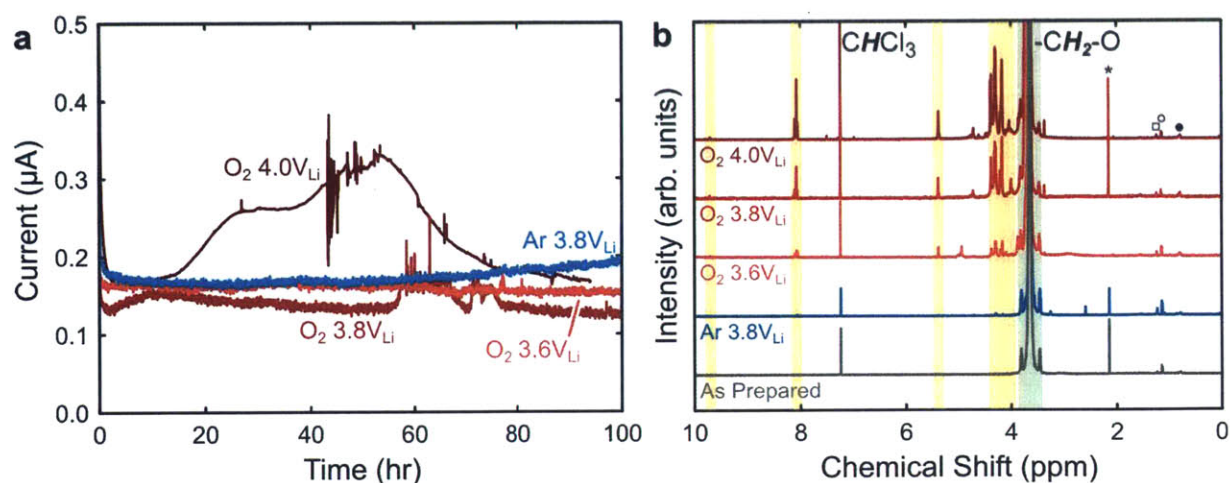
Figure 5-4. (a) Current vs. time for VC-free cells with PEO electrolytes after being charged potentiostatically for 100 hours in oxygen at 3.6, 3.8, and 4.0 V_{Li} and in argon at 3.8 V_{Li} (without BHT). (b) NMR spectra of the electrolytes shown in (a). Peaks are identified as described for Figure 5-2, and each plot is normalized to the area of the primary PEO peak (in green). The scale of (b) matches that of Figure 5-2b.

142

mote a measurable electrochemical reaction. NMR analysis of each electrolyte after oxidation at these potentials (Figure 5-4b) shows the appearance of comparable peaks with greater intensities in comparison to those identified from the OCV tests, which indicates that the amount of decomposition products upon oxidation increases with increasing potential. Similar to OCV in argon, applying potentials greater than OCV in argon produced extremely small oxidation peaks at 8.1 and 4.3 ppm.

5.3.1.4 *Pressure Tracking during PEO Oxidation*

Pressure tracking experiments showed that a significant amount of oxygen was consumed during tests both at OCV and at 4.0 V_{Li}, and that the rate of consumption varied throughout the test. A digital pressure transducer was used to track and record the pressure of VC-free cells (using BHT-free electrolyte) over the duration of tests at OCV and at 4.0 V_{Li}, which allowed for the rate of oxygen consumption to be tracked (Figure 5-5). Due to the limited range of the pressure gauge, this test was performed with an initial oxygen pressure of 1.87 bar. For both tests, the rate of
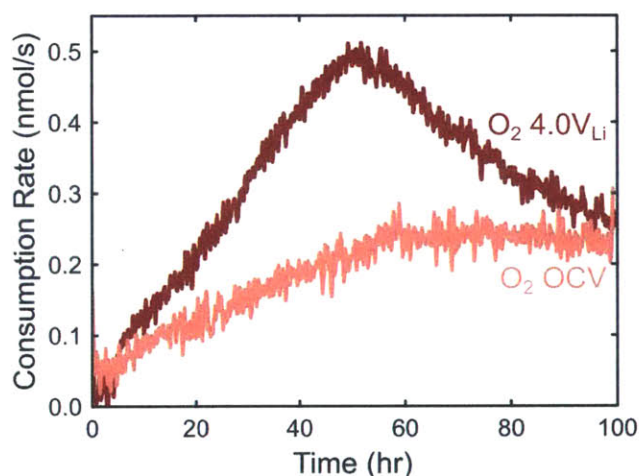
Figure 5-5. Oxygen consumption rate of VC-free cells (using BHT-free PEO electrolyte) rested at OCV and held at 4.0 V_{Li} as a function of time. Total moles of oxygen and the consumption rate were calculated as described in the experimental methods.

143

oxygen consumption was observed to be initially low, and steadily increased for several hours. For the test at OCV, the rate of oxygen consumption increased steadily for the first 60 hours, before stabilizing at 0.21 nmol/s for the remainder of the test. At 4.0 V_{Li}, the rate of oxygen consumption increased more rapidly at the beginning of the test, reaching a maximum of 0.50 nmol/s after 50 hours, after which the rate of consumption gradually fell, approaching the same steady state consumption observed at OCV. The current passed was in agreement with the potentiostatic tests discussed above and stayed below 350 nA (3.6×10^{-3} nmol electron/s) throughout the test, more than 100 times smaller than the rate of oxygen consumption.

5.3.2 Quantification and Analysis of Oxidation Products

To further analyze the NMR results, we briefly discuss the mechanism of PEO thermal oxidation that has been reported in the literature previously.[180–183] The reaction mechanism that we propose here is similar to the mechanisms reported for the oxidation of liquid glymes when exposed to superoxide during discharge in Li-air systems,[51,72,184] but does not rely on the presence of any superoxide radical species to initiate the reaction. Tsiouvaras et al. have also proposed a glyme decomposition mechanism in oxygen-free environments at very high voltages (≥ 4.9 V_{Li}),[87] a potential where PEO is already known to be unstable.[160] Similar to other auto-oxidation reactions of organic compounds, PEO is oxidized via radical chain reaction. A small number of peroxide species are formed via spontaneous reaction between PEO and molecular oxygen to form a PEO radical ($-OC\cdot HCH_2O-$) and a hydroperoxide radical (Figure 5-6, Reaction I). This reaction is also known to occur much more quickly in the presence of singlet oxygen,[185,186] which has been proposed to form during discharge and charge of Li-air batteries.[45,51,68,148] The chain reaction is prop-

Initiation

Chain Reaction

Chain Branching
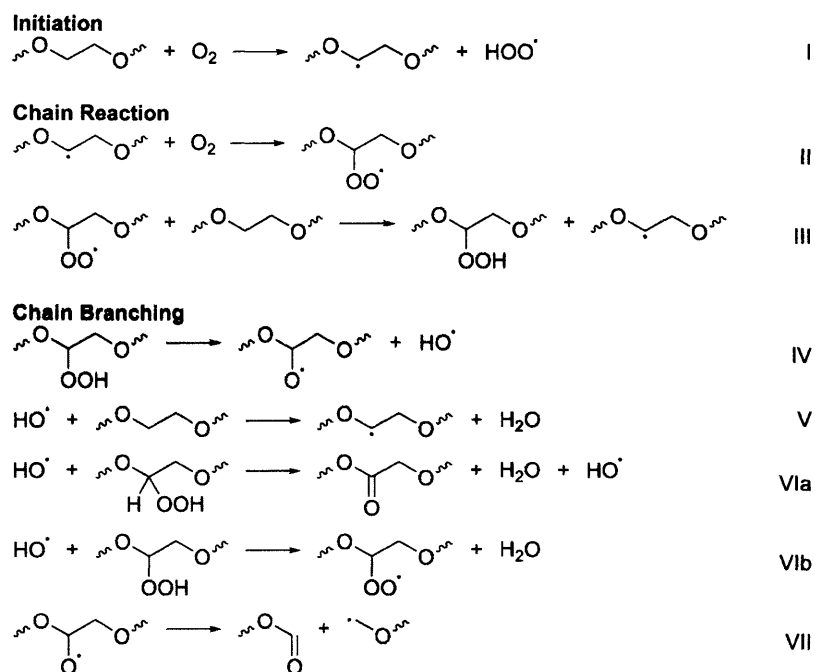
Figure 5-6. PEO auto-oxidation reaction pathway. Wavy bonds indicate the continuing PEO backbone. Termination reactions not shown.

agated when molecular oxygen reacts with the PEO radical to form a PEO-peroxyl radical (Reaction II), which then abstracts a hydrogen from another nearby ether group to form PEO-hydroperoxide and another PEO radical (Reaction III). Chain branching (which further accelerates the reaction) occurs when PEO-hydroperoxide spontaneously decomposes to form a PEO-alkoxy radical and a hydroxyl radical (Reaction IV). The hydroxyl radical can abstract a proton from a nearby PEO to form a PEO radical and water (Reaction V), or react with PEO-hydroperoxide to form an ester or a PEO-peroxyl radical (Reactions VIa-b). It has been reported that PEO-alkoxy radicals rapidly undergo β-scission to create a formate-terminated chain (Reaction VII), rather than disproportionation to create an ester.[181] Chain termination occurs when two radicals recombine or disproportionate to form non-radical species. The large number of radical species present make

listing all the possible reactions infeasible, but it has been shown that esters and formates are the dominant stable products of such PEO oxidation reactions.[181]

Little has been reported on the effect of elevated applied potentials on the auto-oxidation of PEO, such as those that occur during the charging of Li–O_2 batteries. We observed that the addition of oxygen to VC-free cells did not result in an increase in current, which remained very low with or without the presence of oxygen, indicating that the increased oxidation is not due to the bulk electro-oxidation of the PEO electrolyte, but instead results from the acceleration of one or more of the reaction steps outlined above. Therefore, a quantitative analysis of the amount and relative ratios of the different products may allow further elucidation of the impact of elevated potential on PEO oxidation kinetics.

In the ^{1}H-NMR spectra shown in Figure 5-2b and Figure 5-4b, the following peaks were associated with PEO oxidation: (i) 9.72 ppm (singlet), (ii) 8.10 ppm (group of singlets), (iii) 5.38 ppm (singlet, broadened), (iv) 4.1 to 4.5 ppm (group of many peaks). Peak (i) was identified as the proton bonded to the alpha carbon of an aldehyde-terminated PEO chain (O=CHCH$_2$OCH$_2$-, calculated shift of 9.72 ppm). Peak (ii) was attributed to the alpha-carbon proton of a formate-terminated PEO chain (O=CHOCH$_2$CH$_2$-, calculated shift of 8.10 ppm). Peak (iii) was attributed to the alpha-carbon proton of PEO-hydroperoxide and/or a secondary alcohol (–OCHOHCH$_2$O– or –OCHOOHCH$_2$O–, calculated shift of 5.60 ppm). Group (iv) was attributed to the beta-carbon protons for both aldehyde- (O=CHCH$_2$OCH$_2$CH$_2$–, calculated shift of 4.48 ppm) and formate-terminated PEO chains (O=CHOCH$_2$CH$_2$–, calculated shift of 4.28 ppm), and to in-chain esters (–OCH$_2$CH$_2$OC=OCH$_2$O–, calculated shifts of 4.20 and 4.33 ppm, respectively). Note that other reports[181] of PEO oxidation frequently report that no aldehydes are observed after oxidation, and

146

that the formation of formates is preferred over that of aldehydes when the alkoxy radical decomposes. The observation of aldehydes after oxidation in this work is consistent with these reports, as much more formate is observed than aldehyde, and the aldehyde products are only observed in the most highly oxidized samples. Integrated peak intensity was used to quantify the amount of each decomposition product. The number of each functional group relative to the number of ethylene oxide (EO) units for each of the samples shown in Figure 5-2 and Figure 5-4 is plotted in Figure 5-7a. An overall extent of reaction was calculated (Figure 5-7b), comparing the number of aldehyde, formate, peroxide/alcohol, and ester reaction products with the total number of functional groups (including the large number of ethylene oxide groups). No oxidation peaks were observed in the as prepared sample, so it is excluded from Figure 5-7.
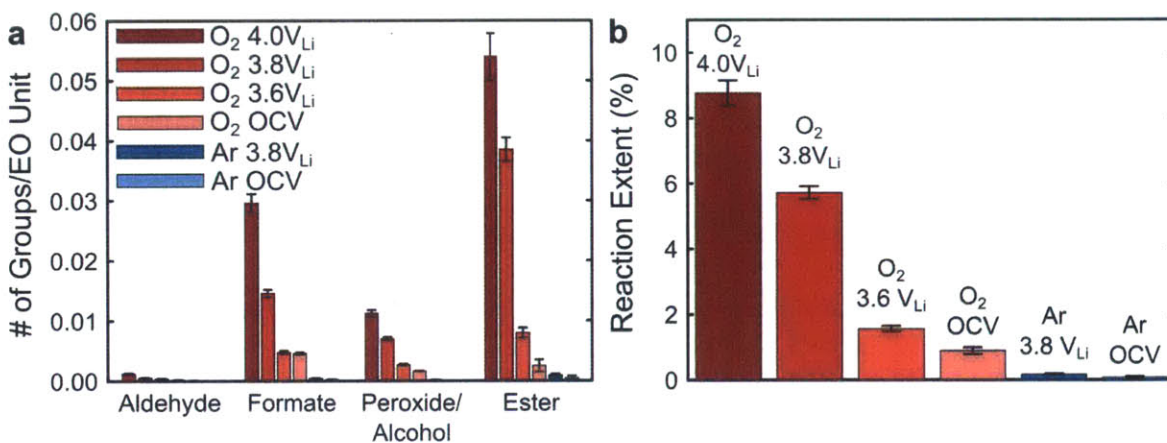
Figure 5-7. Quantification of oxidation products and total extent of oxidation. (a) Relative number of each type of functional group, shown for each of the experimental conditions. The as-prepared electrolyte exhibited no measureable peaks, and is not shown. (b) Extent of oxidation and derived reaction rate for each of the experimental conditions. Each data point represents a cell that was held at the stated conditions for 100 hours. Error bars represent the 95% confidence interval of estimated error due to integration.

Figure 5-7 clearly shows that more PEO is oxidized when exposed to potentials greater than OCV in oxygen. In contrast, samples treated in argon (with or without applied potential) are only slightly oxidized, with peaks barely rising above the background for all of the identified oxidation products. However, more careful examination of the relative amount of each oxidation product shows that applying a potential produces a different mixture of oxidation products. In particular, the potentiostatic samples have a much higher fraction of ester products, which make up 56 ± 5%, 64 ± 4%, and 50 ± 6% of all oxidation products for 4.0, 3.8, and 3.6 V_{Li}, respectively, while only 28 ± 12% of oxidation products are esters in the oxygen OCV sample. The opposite trend is observed for formates, which make up 31 ± 2%, 24 ± 1%, and 30 ± 2% of all oxidation products for 4.0, 3.8, and 3.6 V_{Li} respectively, but make up 52 ± 7% of oxidation products in the oxygen OCV sample (all uncertainties represent the 95% confidence interval).

Given the very low oxidative current relative to total oxygen consumption (as shown in Figure 5-5), we conclude that the increased potential causes more reaction chains to be created. This can be due to either an increased rate of initiation (Reaction I) or an increased rate of chain branching (Reaction IV). The primary chain reactions (Reactions II and III) cannot be directly accelerated, as this would be expected to produce a measurable current on the same order as the rate of oxygen consumption. To postulate whether Reaction I or IV is catalyzed, we consider the expected impact of increasing their reaction rates. If Reaction I were to increase in rate with increasing voltage, larger numbers of PEO radicals would be produced, steadily increasing the number of PEO chains but not driving the reaction to favor any of the products. If Reaction IV is catalyzed instead, causing PEO-hydroperoxide to breakdown more quickly and increasing the chain branching ratio, a larger number of PEO-alkoxy radicals would be produced. These alkoxy radicals would be expected to increase the fraction of formates in the oxidation products. In contrast, we observed

148

that the fraction of formates in the overall oxidation products decreases with increasing potential; an increase in the number of esters was observed instead, which is consistent with more radicals undergoing more terminating reactions towards the end of oxidation. We conclude that the application of an oxidizing potential to a PEO electrolyte exposed to oxygen results in an increase in the rate of spontaneous PEO radical formation, which results in an increase in the total rate of PEO oxidation.

5.3.3 Impact of PEO Oxidation in Li–O₂ Cells

To show the direct impact the oxidation of PEO electrolytes has on the operation of Li–O₂ cells, we present the results of a PEO-based Li–O₂ cell using a VC cathode. Two cells are considered here; one which was singly discharged, and another cycled five times (Figure 5-8). Both cells were discharged at 100 mAh/g$_{VC}$, and the cell that was cycled was subsequently charged to 4.2 V$_{Li}$. Both cells were started at the same time, and the cell that was singly discharged was held at 60 °C in oxygen until the cycling test completed. It is noted that the first-discharge capacity of a
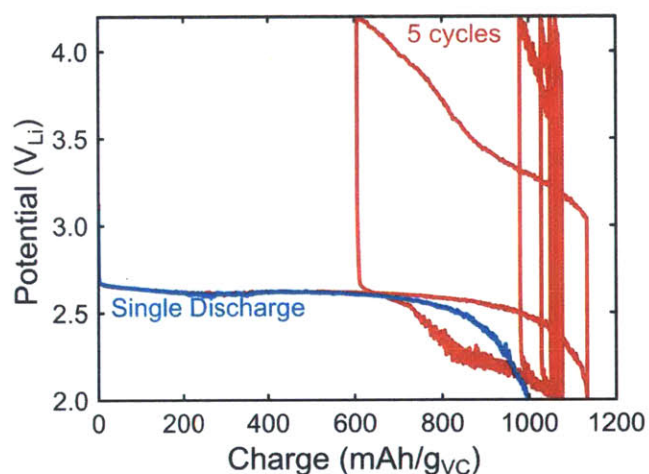
Figure 5-8. Performance of Li–O₂ cells using PEO-based electrolyte. Potential versus charge of a cell discharged once in oxygen, and a cell cycled 5 times in oxygen. Charge is normalized to the mass of Vulcan carbon in the positive electrode.

PEO-based Li–O$_2$ cell with a VC positive electrode (~1100 mAh/g$_{VC}$) is less than the capacity of similar cells using DME as an electrolyte reported elsewhere (~2800 mAh/g$_{VC}$)[47]. The reduction may result from the high viscosity of the PEO electrolyte, which may inhibit the formation of large Li$_2$O$_2$ particles observed in Li–O$_2$ cells made with liquid electrolytes,[37–39,41,45,47,118,170] which is consistent with work suggesting that dissolution and diffusion of Li–O$_2$ discharge products are required to form large Li$_2$O$_2$ particles.[38,39,129] Excluding the reduced capacity, the profile of the first discharge for the PEO-based Li–O$_2$ cell is familiar: after a brief onset, a large plateau is observed near 2.5 V$_{Li}$, after which the voltage rapidly falls to 2.0 V$_{Li}$.

During the first charge, the profile initially appears to be similar to that of previously reported Li–O$_2$ charging processes in liquid electrolytes;[19,41,68,83,113,170] the potential quickly rises above 3.1 V$_{Li}$ before rising more slowly to ~3.6 V$_{Li}$. After this point, the voltage rises more rapidly, reaching the cutoff voltage of 4.2 V$_{Li}$ (above which even liquid ether electrolytes are known to decompose).[50,70] Subsequent cycles show much poorer performance, with each subsequent cycle having lower capacity, a more sloped discharge profile, and an increasingly rapid rise in charging potential. The complete loss of cell performance after only five cycles shows that PEO degradation is significant even within the potential range that is ordinarily achievable for Li–O$_2$ batteries in literature.[19,41]

Figure 5-9 shows an additional experiment that tracked the consumption and production of gas throughout one discharge-charge cycle, using the same conditions listed above. The rate of gas consumption was near 2 electrons/O$_2$ throughout discharge (within the limit of the measurement accuracy), which is consistent with reported gas consumption rates in liquid glyme electrolytes.[50] However, the gas production during charge was far less than 2 electrons/O$_2$ which would indicate

150

reversible oxidation of Li_2O_2. The performance was worse than has been reported for glyme electrolytes as well, which have been reported to have a gas production ratio of~2.6 electrons/O_2 for LiTFSI in DME;[50,87] the rate of gas production decayed throughout charge, and even became negative as PEO auto-oxidation dominated over the expected production of O_2 due to Li_2O_2 oxidation.
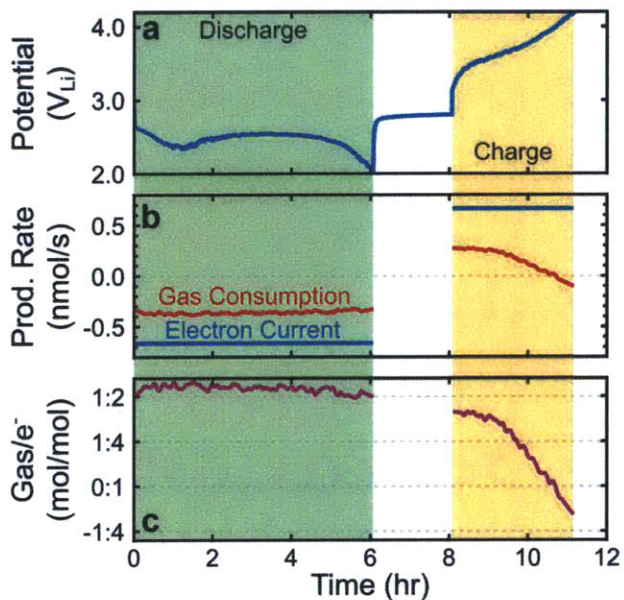
Figure 5-9. (a) Cell voltage vs. time for a Li–O_2 cell cycled in O_2 with a VC cathode. (b) Gas production rate (red) and electron current (blue, converted to nmol/s of electrons) of the same cell. Negative production indicates consumption, and negative current indicates discharge. (c) Ratio of gas consumption rate to electron current plotted in (b). This ratio stayed close to 2 electrons/O_2 throughout discharge, but deviated significantly from that value throughout charge. The negative gas to electron ratio indicates that gas is being consumed during charging.

Although mitigations may be available to extend the lifetime of a PEO-based Li–O_2 cell (such as reducing the oxygen partial pressure or removing all oxygen before charging), we assert that these techniques are neither sufficient nor feasible to protect the PEO for use as a practical

device in commercial applications. We therefore suggest that further investigations into solid electrolyte-based Li–O_2 batteries focus on either eliminating PEO from the positive electrode (such as using ceramic electrolytes in the oxygen electrode)[176] or developing a compound that permanently inhibits the oxidation of PEO without interfering with the desired electrochemical reactions.

5.4 Conclusions

Development of a stable, solid-state Li–O_2 electrolyte remains a promising goal, as a carefully engineered solid electrolyte can allow for high oxygen transport, eliminate concerns about electrolyte evaporation, and protect the anode from oxygen, water, and other contaminants from the environment. We show here that PEO, widely studied as a solid lithium-conducting electrolyte, is not stable in the fully oxygenated environment of a Li–O_2 cell. Further work on the use of PEO and PEO-derived polymers as electrolytes for Li–O_2 and Li-air cells should focus on developing compounds that permanently inhibit the oxidation of PEO (without interfering in the electrochemical process), on developing protective layers that prevent the exposure of PEO to the oxygen environment, or on using materials not based on PEO for lithium conduction. Furthermore, the results presented here are an indication that other ether-based electrolytes (such as DME,[41,47,72,83] tetraethylene glycol dimethylether,[45,68,121,127,187] or trimethylsilyl oligo(ethylene oxide)[188]) may also be susceptible to oxidation directly from the environment, in addition to the decomposition mechanisms that have already been explored for these compounds in Li–O_2 cells, and will likely be impacted by it when cycled many hundreds of times, as is commonly expected of commercially viable batteries. We conclude that the results presented here motivate further investigation into developing new oxidation-resistant electrolytes for Li-air batteries.

5.5 Acknowledgement

Chapter 6

Conclusions and Perspective

6.1 Summary

This thesis investigated two materials systems for Li–air batteries, and investigated the behavior of both of them when exposed to oxidizing conditions. In Chapter 2, we prepared porous Vulcan carbon-based (VC) electrodes with Li_2O_2 included in them during electrode preparation, using them to study the charging behavior of different noble metal catalysts without the effect of discharge. We used potentiostatic charging to establish the performance of $VC+Li_2O_2$ electrodes, observing complete oxidation of Li_2O_2 between 4.1 and 4.4 V $vs.$ Li (V_{Li}). Additional electrodes were prepared which included Au, Pt, or Ru nanoparticles as a catalyst. $Au/C+Li_2O_2$ electrodes showed no enhancement over VC, while both $Pt/C+Li_2O_2$ and $Ru/C+Li_2O_2$ electrodes were observed to oxidize Li_2O_2 between 3.6 and 3.9 V_{Li}, although signs of electrolyte oxidation were present at high voltages for both catalysts. Finally, a trend was observed that showed increasingly long delays before the initiation of Li_2O_2 oxidation as voltage decreased. We hypothesized that this trend was due to a surface layer of $e.g.$ LiOH, which oxidizes more slowly, and observed a rapid rise in current after the onset of Li_2O_2 oxidation, consistent with the nucleation and growth of Li_2O_2 reaction surfaces.

Chapter 3 covered the design, construction, and demonstration of a differential electrochemical mass spectrometer (DEMS). We reviewed the different categories of DEMS systems that have been developed, and designed a discrete DEMS system based on the design published by McCloskey et $al.$[83] We then detailed the specific design and operational methods of the DEMS system as built in our lab, and discussed problems that were found and how they were resolved over the course of construction. Finally, we demonstrated the capabilities of the DEMS, using it to measure the gas consumption and production during a single discharge-charge cycle of VC and carbon

nanotube-based (CNT) electrodes in a liquid electrolyte. We showed that both VC and CNT electrodes were observed to consume gas at rate consistent with a 2 electron per oxygen reaction. We further showed that both systems generate oxygen during the majority of the charging process, only generating carbon dioxide at high potentials near the end of charge. We also noted that the overall production of oxygen was lower than would be expected for 2 e^-:O_2 processes, indicating that additional reactions are occurring during the charging process that do not produce gas. These results were found to be consistent with those reported by other research groups.[50,87] Finally, we used the DEMS to investigate some of the Li_2O_2-preloaded electrodes initially explored in Chapter 2. We showed that Ru/C+Li_2O_2 generates oxygen as the only significant gas throughout the charge process, but that Pt/C+Li_2O_2 generates both oxygen and carbon dioxide, indicating that Pt catalyzes both the oxidation of Li_2O_2 to oxygen and the conversion of oxygen to carbon dioxide, and validating our conclusion from Chapter 2 that Ru is more stable as a catalyst for Li_2O_2 oxidation in Li–O_2 batteries.

In Chapter 4, we developed a poly(ethylene oxide)-based (PEO) electrolyte for use in Li–O_2 batteries. We based our electrolyte on the room-temperature ionic liquid-plasticized PEO electrolytes developed by Passerini and colleagues for use in Li-ion batteries at room temperature,[161] and developed a VC-based porous carbon air electrode, using PEO and LiTFSI salt as both binder and catholyte. We investigated the room temperature discharge performance of these PEO Li–O_2 cells, and after investigating a number of design parameters concluded that the charge transfer reaction limited discharge rate and capacity. We then redesigned the electrolyte for operation at 60 °C, and demonstrated significantly higher rate capability and discharge capacity, with the total carbon loading exhibiting the largest impact on discharge performance. Finally, we used DEMS to investigate the charging performance of these electrodes under argon at temperatures between 30-60 °C, and

found a significant increase in the production of carbon dioxide and hydrogen when charging at 50 °C and above. This behavior was attributed to the melting transition that the PEO electrolyte is expected to undergo near 50 °C, although further exploration of this behavior is required for a complete understanding.

Finally, in Chapter 5 we investigated the behavior of the same PEO electrolytes when exposed to oxidizing potentials in oxygen at 60 °C. We used nuclear magnetic resonance (NMR) spectroscopy and measurement of the open-circuit voltage (OCV) to show that PEO undergoes autoxidation when rested at OCV in a Li–O_2 cell at 60 °C, but does not oxidize when held at the same conditions under argon. Increasing the potential was found to increase the extent of electrolyte oxidation, although no significant increase of current was observed in oxygen *vs.* argon. We used analysis of the NMR results in combination with pressure tracking experiments performed on the DEMS to identify the reaction products and quantify the extent of oxidation at each potential, and used these results to propose that an increase in the rate of hydrogen abstraction from PEO by oxygen (*i.e.* chain initiation) was the cause of the observed increase in oxidation. Finally, we cycled PEO-based Li–O_2 cells (as developed in Chapter 4) at 60 °C in oxygen, and showed that PEO autoxidation is significant after only one charging cycle, and concluded that the observed autoxidation reaction is a potential concern for long term operation of any polyether-based Li–O_2 battery.

6.2 Perspective and Concluding Remarks

The results presented in this thesis suggest a number of additional areas of research. Since the publication of the results in Chapter 2, members of the Electrochemical Energy Lab have investigated several transition metal-based materials in Li_2O_2-preloaded electrodes, further developed a carbon-free electrode design,[46] and very recently proposed a possible reaction mechanism

158

to explain the enhancement of Li_2O_2 oxidation by metal and metal oxides through solid-solid reactions.[84] DEMS can be used to analyze these more recent results and confirm the efficiency of oxygen production with these materials, and to confirm the stability of these reaction promoters in oxygenated atmospheres, particularly to ensure that they do not catalyze electrolyte decomposition in oxygen.

Additionally, a number of open questions remain for the PEO-electrolyte system explored in Chapters 4 and 5. Although the autoxidation of PEO in oxygen at 60 °C was well established in Chapter 5, it remains unclear how this reaction changes with a decrease in temperature. Is the transition in the charging behavior seen between 40 and 50 °C in Chapter 4 also observed in the autoxidation of PEO? What is the nature of this transition, and can a system be developed that allows more complete charging (as observed at and above 50 °C) to occur without the production carbon dioxide and hydrogen (as observed at and below 40 °C)? Can an electrode be developed, using PEO or some other non-volatile electrolyte, that can be used with the bulk PEO electrolyte at room temperature and achieve high discharge performance? Are there other polymers available that can provide similar performance as PEO, but without undergoing the autoxidation reaction studied in Chapter 5?

In conclusion this thesis documents the development of several platforms for investigating Li–air batteries, conclusively identifying the catalysis of Li_2O_2 oxidation during charging, characterizing the behavior of polymer electrolyte-based $Li–O_2$ batteries, and establishing an additional requirement that Li–air battery materials must be stable to autoxidation. These efforts have advanced our understanding of Li–air battery technology and will guide further developments on the path to practical Li–air devices.

References

(1) Cubasch, U.; Wuebbles, D.; Chen, D.; Facchini, M. C.; Frame, D.; Mahowald, N.; Winther, J.-G. Introduction. In *Climate Change 2013: The Physical Science Basis. Contribution of Working Group I to the Fifth Assessment Report of the Intergovernmental Panel on Climate Change*; Stocker, T. F., Qin, D., Plattner, G.-K., Tignor, M., Allen, S. K., Boschung, J., Nauels, A., Xia, Y., Bex, V., Midgley, P. M., Eds.; Cambridge University Press: Cambridge, United Kingdom and New York, NY, USA, 2013; pp 119–158.

(2) Edmonds, J.; Wise, M.; Pitcher, H.; Richels, R.; Wigley, T.; MacCracken, C. An Integrated Assessment of Climate Change and the Accelerated Introduction of Advanced Energy Technologies - An Application of MiniCAM 1.0. *Mitig. Adapt. Strateg. Glob. Chang.* **1995**, *1*, 311–339 DOI: 10.1023/B:MITI.0000027386.34214.60.

(3) Lindzen, R. S.; Choi, Y.-S. On the observational determination of climate sensitivity and its implications. *Asia-Pacific J. Atmos. Sci.* **2011**, *47*, 377–390 DOI: 10.1007/s13143-011-0023-x.

(4) biscuitjack comments on Science AMA Series: I'm Kerry Emanuel, a Professor of Atmospheric Science at the Massachusetts Institute of Technology in Cambridge, Massachusetts. I do research on hurricanes and other types of severe weather, on climate change, a https://www.reddit.com/r/science/comments/1xsqyn/science_ama_series_im_kerry_eman uel_a_professor/cfed8oi (accessed May 4, 2015).

(5) Richard A. Muller. The Conversion of a Climate-Change Skeptic. *The New York Times*. July 30, 2012, p A19.

(6) Office of Energy Statistics. *Monthly Energy Review: March 2015*; DOE/EIA-0035(2015/03); Washington, DC, 2015.

(7) Office of Energy Statistics. *Monthly Energy Review: March 2014*; DOE/EIA-0035(2014/03); Washington, DC, 2014.

(8) Lawrence Livermore National Laboratory; US Department of Energy. Estimated U.S. Energy Use in 2013 https://flowcharts.llnl.gov/content/energy/energy_archive/energy_flow_2013/2013USEner gy.pdf (accessed Apr 1, 2015).

(9) Kanan, M. W.; Nocera, D. G. In situ formation of an oxygen-evolving catalyst in neutral water containing phosphate and Co2+. *Science* **2008**, *321*, 1072–1075 DOI: 10.1126/science.1162018.

(10) Choi, N.-S.; Chen, Z.; Freunberger, S. A.; Ji, X.; Sun, Y.-K.; Amine, K.; Yushin, G.; Nazar, L. F.; Cho, J.; Bruce, P. G. Challenges facing lithium batteries and electrical double-layer

capacitors. *Angew. Chem. Int. Ed. Engl.* **2012**, *51*, 9994–10024 DOI: 10.1002/anie.201201429.

(11) Whittingham, M. S. Materials challenges facing electrical energy storage. *Mrs Bull.* **2008**, *33*, 411–419.

(12) Simon, P.; Gogotsi, Y. Materials for electrochemical capacitors. *Nat. Mater.* **2008**, *7*, 845–854 DOI: 10.1038/nmat2297.

(13) USCAR: Energy   Storage   System   Goals http://www.uscar.org/guest/article_view.php?articles_id=85 (accessed Apr 1, 2015).

(14) Lee, S. W.; Yabuuchi, N.; Gallant, B. M.; Chen, S.; Kim, B.-S.; Hammond, P. T.; Shao-Horn, Y. High-power lithium batteries from functionalized carbon-nanotube electrodes. *Nat. Nanotechnol.* **2010**, *5*, 531–537 DOI: 10.1038/nnano.2010.116.

(15) Lee, S. W.; Gallant, B. M.; Byon, H. R.; Hammond, P. T.; Shao-Horn, Y. Nanostructured carbon-based electrodes: bridging the gap between thin-film lithium-ion batteries and electrochemical capacitors. *Energy Environ. Sci.* **2011**, *4*, 1972 DOI: 10.1039/c0ee00642d.

(16) Lee, S. W.; Kim, B.-S.; Chen, S.; Shao-Horn, Y.; Hammond, P. T. Layer-by-layer assembly of all carbon nanotube ultrathin films for electrochemical applications. *J. Am. Chem. Soc.* **2009**, *131*, 671–679 DOI: 10.1021/ja807059k.

(17) Gallant, B. M. Fundamental understanding and materials design approaches for lithium-oxygen electrochemical energy storage, 2013.

(18) Tarascon, J.-M.; Armand, M. Issues and challenges facing rechargeable lithium batteries. *Nature* **2001**, *414*, 359–367 DOI: 10.1038/35104644.

(19) Lu, Y.-C.; Gallant, B. M.; Kwabi, D. G.; Harding, J. R.; Mitchell, R. R.; Whittingham, M. S.; Shao-Horn, Y. Lithium–oxygen batteries: bridging mechanistic understanding and battery performance. *Energy Environ. Sci.* **2013**, *6*, 750 DOI: 10.1039/c3ee23966g.

(20) Gallagher, K. G.; Goebel, S.; Greszler, T.; Mathias, M.; Oelerich, W.; Eroglu, D.; Srinivasan, V. Quantifying the promise of lithium–air batteries for electric vehicles. *Energy Environ. Sci.* **2014**, *7*, 1555–1563 DOI: 10.1039/C3EE43870H.

(21) La Mantia, F.; Rosciano, F.; Tran, N.; Novák, P. Quantification of Oxygen Loss from Li[sub 1+x](Ni[sub 1/3]Mn[sub 1/3]Co[sub 1/3])[sub 1−x]O[sub 2] at High Potentials by Differential Electrochemical Mass Spectrometry. *J. Electrochem. Soc.* **2009**, *156*, A823 DOI: 10.1149/1.3205495.

(22) Li, Y.; Bettge, M.; Polzin, B.; Zhu, Y.; Balasubramanian, M.; Abraham, D. P. Understanding Long-Term Cycling Performance of Li1.2Ni0.15Mn0.55Co0.1O2-Graphite

Lithium-Ion Cells. *J. Electrochem. Soc.* **2013**, *160*, A3006–A3019 DOI: 10.1149/2.002305jes.

(23) Bruce, P. G.; Freunberger, S. A.; Hardwick, L. J.; Tarascon, J.-M. Li-O2 and Li-S batteries with high energy storage. *Nat. Mater.* **2012**, *11*, 19–29 DOI: 10.1038/nmat3191.

(24) Nishikawa, K.; Mori, T.; Nishida, T.; Fukunaka, Y.; Rosso, M.; Homma, T. In Situ Observation of Dendrite Growth of Electrodeposited Li Metal. *J. Electrochem. Soc.* **2010**, *157*, A1212 DOI: 10.1149/1.3486468.

(25) Stone, G. M.; Mullin, S. a.; Teran, a. a.; Hallinan, D. T.; Minor, a. M.; Hexemer, A.; Balsara, N. P. Resolution of the Modulus versus Adhesion Dilemma in Solid Polymer Electrolytes for Rechargeable Lithium Metal Batteries. *J. Electrochem. Soc.* **2012**, *159*, A222 DOI: 10.1149/2.030203jes.

(26) Gurevitch, I.; Buonsanti, R.; Teran, A. A.; Gludovatz, B.; Ritchie, R. O.; Cabana, J.; Balsara, N. P. Nanocomposites of Titanium Dioxide and Polystyrene-Poly(ethylene oxide) Block Copolymer as Solid-State Electrolytes for Lithium Metal Batteries. *J. Electrochem. Soc.* **2013**, *160*, A1611–A1617 DOI: 10.1149/2.117309jes.

(27) Christensen, J.; Albertus, P.; Sanchez-Carrera, R. S.; Lohmann, T.; Kozinsky, B.; Liedtke, R.; Ahmed, J.; Kojic, A. A Critical Review of Li/Air Batteries. *J. Electrochem. Soc.* **2011**, *159*, R1–R30 DOI: 10.1149/2.086202jes.

(28) Lu, Y.-C.; Gasteiger, H. A.; Parent, M. C.; Chiloyan, V.; Shao-Horn, Y. The Influence of Catalysts on Discharge and Charge Voltages of Rechargeable Li–Oxygen Batteries. *Electrochem. Solid-State Lett.* **2010**, *13*, A69–A72 DOI: 10.1149/1.3363047.

(29) Trahan, M. J.; Gunasekara, I.; Mukerjee, S.; Plichta, E. J.; Hendrickson, M. A.; Abraham, K. M. Solvent-Coupled Catalysis of the Oxygen Electrode Reactions in Lithium-Air Batteries. *J. Electrochem. Soc.* **2014**, *161*, A1706–A1715 DOI: 10.1149/2.0981410jes.

(30) Peng, Z.; Freunberger, S. A.; Hardwick, L. J.; Chen, Y.; Giordani, V.; Bardé, F.; Novák, P.; Graham, D.; Tarascon, J.-M.; Bruce, P. G. Oxygen reactions in a non-aqueous li(+) electrolyte. *Angew. Chem. Int. Ed. Engl.* **2011**, *50*, 6351–6355 DOI: 10.1002/anie.201100879.

(31) Gallant, B. M.; Lu, Y.-C.; Mitchell, R. R.; Kwabi, D. G.; Carney, T. J.; Thompson, C. V.; Shao-Horn, Y. The Kinetics and Product Characteristics of Oxygen Reduction and Evolution in LiO2 Batteries. In *The Lithium Air Battery: Fundamentals*; Imanishi, N., Luntz, A. C., Bruce, P., Eds.; Springer New York: New York, 2014; pp 121–158.

(32) Bryantsev, V. S.; Blanco, M.; Faglioni, F. Stability of lithium superoxide LiO2 in the gas phase: computational study of dimerization and disproportionation reactions. *J. Phys. Chem. A* **2010**, *114*, 8165–8169 DOI: 10.1021/jp1047584.

(33) Allen, C. J.; Hwang, J.; Kautz, R.; Mukerjee, S.; Plichta, E. J.; Hendrickson, M. a.; Abraham, K. M. Oxygen Reduction Reactions in Ionic Liquids and the Formulation of a General ORR Mechanism for Li–Air Batteries. *J. Phys. Chem. C* **2012**, *116*, 20755–20764 DOI: 10.1021/jp306718v.

(34) McCloskey, B. D.; Scheffler, R.; Speidel, A.; Girishkumar, G.; Luntz, A. C. On the Mechanism of Nonaqueous Li–O 2 Electrochemistry on C and Its Kinetic Overpotentials: Some Implications for Li–Air Batteries. *J. Phys. Chem. C* **2012**, *116*, 23897–23905 DOI: 10.1021/jp306680f.

(35) Beyer, H.; Meini, S.; Tsiouvaras, N.; Piana, M.; Gasteiger, H. A. Thermal and electrochemical decomposition of lithium peroxide in non-catalyzed carbon cathodes for Li-air batteries. *Phys. Chem. Chem. Phys.* **2013**, *15*, 11025–11037 DOI: 10.1039/c3cp51056e.

(36) Meini, S.; Tsiouvaras, N.; Schwenke, K. U.; Piana, M.; Beyer, H.; Lange, L.; Gasteiger, H. A. Rechargeability of Li-air cathodes pre-filled with discharge products using an ether-based electrolyte solution: implications for cycle-life of Li-air cells. *Phys. Chem. Chem. Phys.* **2013**, *15*, 11478–11493 DOI: 10.1039/c3cp51112j.

(37) Mitchell, R. R.; Gallant, B. M.; Thompson, C. V.; Shao-Horn, Y. All-carbon-nanofiber electrodes for high-energy rechargeable Li–O2 batteries. *Energy Environ. Sci.* **2011**, *4*, 2952–2958 DOI: 10.1039/c1ee01496j.

(38) Schwenke, K. U.; Metzger, M.; Restle, T.; Piana, M.; Gasteiger, H. A. The Influence of Water and Protons on Li2O2 Crystal Growth in Aprotic Li-O2 Cells. *J. Electrochem. Soc.* **2015**, *162*, A573–A584 DOI: 10.1149/2.0201504jes.

(39) Aetukuri, N. B.; McCloskey, B. D.; García, J. M.; Krupp, L. E.; Viswanathan, V.; Luntz, A. C. Solvating additives drive solution-mediated electrochemistry and enhance toroid growth in non-aqueous Li–O2 batteries. *Nat. Chem.* **2015**, *7*, 50–56 DOI: 10.1038/nchem.2132.

(40) Gallant, B. M.; Kwabi, D. G.; Mitchell, R. R.; Zhou, J.; Thompson, C. V.; Shao-Horn, Y. Influence of Li2O2 morphology on oxygen reduction and evolution kinetics in Li–O2 batteries. *Energy Environ. Sci.* **2013**, *6*, 2518–2528 DOI: 10.1039/C3EE40998H.

(41) Gallant, B. M.; Mitchell, R. R.; Kwabi, D. G.; Zhou, J.; Zuin, L.; Thompson, C. V.; Shao-Horn, Y. Chemical and Morphological Changes of Li–O 2 Battery Electrodes upon Cycling. *J. Phys. Chem. C* **2012**, *116*, 20800–20805 DOI: 10.1021/jp308093b.

(42) McCloskey, B. D.; Scheffler, R.; Speidel, A.; Bethune, D. S.; Shelby, R. M.; Luntz, A. C. On the efficacy of electrocatalysis in nonaqueous Li-O2 batteries. *J. Am. Chem. Soc.* **2011**, *133*, 18038–18041 DOI: 10.1021/ja207229n.

164

(43) Giordani, V.; Freunberger, S. A.; Bruce, P. G.; Tarascon, J.-M.; Larcher, D. H2O2 Decomposition Reaction as Selecting Tool for Catalysts in Li–O2 Cells. *Electrochem. Solid-State Lett.* **2010**, *13*, A180–A183 DOI: 10.1149/1.3494045.

(44) Oh, S. H.; Nazar, L. F. Oxide Catalysts for Rechargeable High-Capacity Li-O2 Batteries. *Adv. Energy Mater.* **2012**, *2*, 903–910 DOI: 10.1002/aenm.201200018.

(45) Black, R.; Lee, J. H.; Adams, B.; Mims, C. A.; Nazar, L. F. The Role of Catalysts and Peroxide Oxidation in Lithium-Oxygen Batteries. *Angew. Chemie - Int. Ed.* **2013**, *52*, 392–396 DOI: 10.1002/anie.201205354.

(46) Yao, K. P. C.; Lu, Y.-C.; Amanchukwu, C. V.; Kwabi, D. G.; Risch, M.; Zhou, J.; Grimaud, A.; Hammond, P. T.; Bardé, F.; Shao-Horn, Y. The influence of transition metal oxides on the kinetics of Li2O2 oxidation in Li-O2 batteries: high activity of chromium oxides. *Phys. Chem. Chem. Phys.* **2014**, *16*, 2297–2304 DOI: 10.1039/c3cp53330a.

(47) Lu, Y.-C.; Kwabi, D. G.; Yao, K. P. C.; Harding, J. R.; Zhou, J.; Zuin, L.; Shao-Horn, Y. The discharge rate capability of rechargeable Li–O2 batteries. *Energy Environ. Sci.* **2011**, *4*, 2999–3007 DOI: 10.1039/c1ee01500a.

(48) Wagner, F. T.; Lakshmanan, B.; Mathias, M. F. Electrochemistry and the Future of the Automobile. *J. Phys. Chem. Lett.* **2010**, *1*, 2204–2219 DOI: 10.1021/jz100553m.

(49) Schwenke, K. U.; Meini, S.; Wu, X.; Gasteiger, H. A.; Piana, M. Stability of superoxide radicals in glyme solvents for non-aqueous Li–O2 battery electrolytes. *Phys. Chem. Chem. Phys.* **2013**, *15*, 11830–11839 DOI: 10.1039/C3CP51531A.

(50) McCloskey, B. D.; Bethune, D. S.; Shelby, R. M.; Mori, T.; Scheffler, R.; Speidel, A.; Sherwood, M.; Luntz, A. C. Limitations in Rechargeability of Li-O2 Batteries and Possible Origins. *J. Phys. Chem. Lett.* **2012**, *3*, 3043–3047 DOI: 10.1021/jz301359t.

(51) Adams, B. D.; Black, R.; Williams, Z.; Fernandes, R.; Cuisinier, M.; Berg, E. J.; Novak, P.; Murphy, G. K.; Nazar, L. F. Towards a Stable Organic Electrolyte for the Lithium Oxygen Battery. *Adv. Energy Mater.* **2015**, *5*, n/a – n/a DOI: 10.1002/aenm.201400867.

(52) McCloskey, B. D.; Speidel, A.; Scheffler, R.; Miller, D. C.; Viswanathan, V.; Hummelshøj, J. S.; Nørskov, J. K.; Luntz, A. C. Twin Problems of Interfacial Carbonate Formation in Nonaqueous Li–O2 Batteries. *J. Phys. Chem. Lett.* **2012**, *3*, 997–1001 DOI: 10.1021/jz300243r.

(53) Kwabi, D. G.; Ortiz-Vitoriano, N.; Freunberger, S. A.; Chen, Y.; Imanishi, N.; Bruce, P. G.; Shao-Horn, Y. Materials challenges in rechargeable lithium-air batteries. *MRS Bull.* **2014**, *39*, 443–452 DOI: 10.1557/mrs.2014.87.

(54) Peng, Z.; Freunberger, S. A.; Chen, Y.; Bruce, P. G. A reversible and higher-rate Li-O2 battery. *Science* **2012**, *337*, 563–566 DOI: 10.1126/science.1223985.

(55) Kwabi, D. G.; Batcho, T. P.; Amanchukwu, C. V.; Ortiz-Vitoriano, N.; Hammond, P.; Thompson, C. V.; Shao-Horn, Y. Chemical Instability of Dimethyl Sulfoxide in Lithium–Air Batteries. *J. Phys. Chem. Lett.* **2014**, *5*, 2850–2856 DOI: 10.1021/jz5013824.

(56) Sigma-Aldrich. Dimethyl sulfoxide Safety Data Sheet, 2015, 1–8.

(57) Chaudhari, S. K.; Patil, K. R.; Allepús, J.; Coronas, a. Measurement of the vapor pressure of 2,2,2-trifluoroethanol and tetraethylene glycol dimethyl ether by static method. *Fluid Phase Equilib.* **1995**, *108*, 159–165 DOI: 10.1016/0378-3812(95)02683-6.

(58) Sigma-Aldrich. 1,2-Dimethoxyethane Safety Data Sheet, 2010, 1–6.

(59) Sigma-Aldrich. Tetraethylene glycol dimethyl ether Safety Data Sheet, 2015, 1–7.

(60) Read, J. Characterization of the Lithium/Oxygen Organic Electrolyte Battery. *J. Electrochem. Soc.* **2002**, *149*, A1190 DOI: 10.1149/1.1498256.

(61) Zhang, G. Q.; Zheng, J. P.; Liang, R.; Zhang, C.; Wang, B.; Hendrickson, M.; Plichta, E. J. Lithium–Air Batteries Using SWNT/CNF Buckypapers as Air Electrodes. *J. Electrochem. Soc.* **2010**, *157*, A953 DOI: 10.1149/1.3446852.

(62) Girishkumar, G.; McCloskey, B.; Luntz, A. C.; Swanson, S.; Wilcke, W. Lithium–Air Battery: Promise and Challenges. *J. Phys. Chem. Lett.* **2010**, *1*, 2193–2203 DOI: 10.1021/jz1005384.

(63) Débart, A.; Bao, J.; Armstrong, G.; Bruce, P. G. An O2 cathode for rechargeable lithium batteries: The effect of a catalyst. *J. Power Sources* **2007**, *174*, 1177–1182 DOI: 10.1016/j.jpowsour.2007.06.180.

(64) Débart, A.; Paterson, A. J.; Bao, J.; Bruce, P. G. Alpha-MnO2 nanowires: a catalyst for the O2 electrode in rechargeable lithium batteries. *Angew. Chemie Int. Ed.* **2008**, *47*, 4521–4524 DOI: 10.1002/anie.200705648.

(65) Mizuno, F. Fundamental Study on Rechargeable Reaction of Lithium-Oxygen Battery. In *Symposium on Energy Storage Beyond Lithium Ion: Materials Perspectives*; Oak Ridge, TN, 2010.

(66) Cheng, H.; Scott, K. Carbon-supported manganese oxide nanocatalysts for rechargeable lithium-air batteries. *J. Power Sources* **2010**, *195*, 1370–1374 DOI: 10.1016/j.jpowsour.2009.09.030.

(67) Aurbach, D.; Daroux, M.; Faguy, P.; Yeager, E. The electrochemistry of noble metal electrodes in aprotic organic solvents containing lithium salts. *J. Electroanal. Chem. Interfacial Electrochem.* **1991**, *297*, 225–244 DOI: 10.1016/0022-0728(91)85370-5.

166

(68) Lu, Y.-C.; Shao-Horn, Y. Probing the Reaction Kinetics of the Charge Reactions of Nonaqueous Li–O2 Batteries. *J. Phys. Chem. Lett.* **2013**, *4*, 93–99 DOI: 10.1021/jz3018368.

(69) Hummelshøj, J. S.; Luntz, A. C.; Nørskov, J. K. Theoretical evidence for low kinetic overpotentials in Li-O2 electrochemistry. *J. Chem. Phys.* **2013**, *138*, 034703 DOI: 10.1063/1.4773242.

(70) Ottakam Thotiyl, M. M.; Freunberger, S. A.; Peng, Z.; Bruce, P. G. The carbon electrode in nonaqueous Li-O2 cells. *J. Am. Chem. Soc.* **2013**, *135*, 494–500 DOI: 10.1021/ja310258x.

(71) McCloskey, B. D.; Garcia, J. M.; Luntz, A. C. Chemical and electrochemical differences in nonaqueous Li-O2 and Na-O2 batteries. *J. Phys. Chem. Lett.* **2014**, *5*, 1230–1235 DOI: 10.1021/jz500494s.

(72) Freunberger, S. A.; Chen, Y.; Drewett, N. E.; Hardwick, L. J.; Bardé, F.; Bruce, P. G. The lithium-oxygen battery with ether-based electrolytes. *Angew. Chemie Int. Ed.* **2011**, *50*, 8609–8613 DOI: 10.1002/anie.201102357.

(73) Abraham, K. M.; Jiang, Z. A Polymer Electrolyte-Based Rechargeable Lithium/Oxygen Battery. *J. Electrochem. Soc.* **1996**, *143*, 1 DOI: 10.1149/1.1836378.

(74) Lu, Y.-C.; Xu, Z.; Gasteiger, H. A.; Chen, S.; Hamad-Schifferli, K.; Shao-Horn, Y. Platinum-gold nanoparticles: a highly active bifunctional electrocatalyst for rechargeable lithium-air batteries. *J. Am. Chem. Soc.* **2010**, *132*, 12170–12171 DOI: 10.1021/ja1036572.

(75) Lu, Y.-C.; Gasteiger, H. A.; Shao-Horn, Y. Catalytic Activity Trends of Oxygen Reduction Reaction for Nonaqueous Li-Air Batteries. *J. Am. Chem. Soc.* **2011**, *133*, 19048–19051 DOI: 10.1021/ja208608s.

(76) Freunberger, S. A.; Chen, Y.; Peng, Z.; Griffin, J. M.; Hardwick, L. J.; Bardé, F.; Novák, P.; Bruce, P. G. Reactions in the Rechargeable Lithium-O(2) Battery with Alkyl Carbonate Electrolytes. *J. Am. Chem. Soc.* **2011**, *133*, 8040–8047 DOI: 10.1021/ja2021747.

(77) Gibian, M. J.; Sawyer, D. T.; Ungermann, T.; Tangpoonpholvivat, R.; Morrison, M. M. Reactivity of superoxide ion with carbonyl compounds in aprotic solvents. *J. Am. Chem. Soc.* **1979**, *101*, 640–644 DOI: 10.1021/ja00497a026.

(78) Oh, S. H.; Black, R.; Pomerantseva, E.; Lee, J.; Nazar, L. F. Synthesis of a metallic mesoporous pyrochlore as a catalyst for lithium–O2 batteries. *Nat. Chem.* **2012**, *4*, 1004–1010 DOI: 10.1038/nchem.1499.

(79) Cui, Y.; Wen, Z.; Liang, X.; Lu, Y.; Jin, J.; Wu, M.; Wu, X. A tubular polypyrrole based air electrode with improved O2 diffusivity for Li–O2 batteries. *Energy & Environmental Science*, 2012, *5*, 7893.

(80) Ottakam Thotiyl, M. M.; Freunberger, S. A.; Peng, Z.; Chen, Y.; Liu, Z.; Bruce, P. G. A stable cathode for the aprotic Li-O2 battery. *Nat. Mater.* **2013**, *12*, 1050–1056 DOI: 10.1038/nmat3737.

(81) Xie, J.; Yao, X.; Madden, I. P.; Jiang, D.-E.; Chou, L.-Y.; Tsung, C.-K.; Wang, D. Selective deposition of Ru nanoparticles on TiSi$_2$ nanonet and its utilization for Li$_2$O$_2$ formation and decomposition. *J. Am. Chem. Soc.* **2014**, *136*, 8903–8906 DOI: 10.1021/ja504431k.

(82) Xiao, J.; Mei, D.; Li, X.; Xu, W.; Wang, D.; Graff, G. L.; Bennett, W. D.; Nie, Z.; Saraf, L. V; Aksay, I. a; et al. Hierarchically porous graphene as a lithium-air battery electrode. *Nano Lett.* **2011**, *11*, 5071–5078 DOI: 10.1021/nl203332e.

(83) McCloskey, B. D.; Bethune, D. S.; Shelby, R. M.; Girishkumar, G.; Luntz, A. C. Solvents' Critical Role in Nonaqueous Lithium–Oxygen Battery Electrochemistry. *J. Phys. Chem. Lett.* **2011**, *2*, 1161–1166 DOI: 10.1021/jz200352v.

(84) Yao, K. P. C.; Risch, M.; Sayed, S. Y.; Lee, Y.-L.; Grimaud, A.; Pour, N.; Harding, J. R.; Wei, C.; Zhou, J.; Hu, Y.; et al. Solid-state activation of Li2O2 oxidation kinetics and implications for Li-O2 batteries. *Energy Environ. Sci.* **2015**, Submitted for review.

(85) Armstrong, R. D.; Fleischmann, M.; Thirsk, H. R. The Anodic Behaviour of Mercury in Hydroxide Ion Solutions. *J. Electroanal. Chem.* **1965**, *11*, 208–223.

(86) Bryantsev, V. S.; Giordani, V.; Walker, W.; Blanco, M.; Zecevic, S.; Sasaki, K.; Uddin, J.; Addison, D.; Chase, G. V. Predicting Solvent Stability in Aprotic Electrolyte Li-Air Batteries: Nucleophilic Substitution by the Superoxide Anion Radical (O2•-). *J. Phys. Chem. A* **2011**, *115*, 12399–12409 DOI: 10.1021/jp2073914.

(87) Tsiouvaras, N.; Meini, S.; Buchberger, I.; Gasteiger, H. A. A Novel On-Line Mass Spectrometer Design for the Study of Multiple Charging Cycles of a Li-O2 Battery. *J. Electrochem. Soc.* **2013**, *160*, A471–A477 DOI: 10.1149/2.042303jes.

(88) Harding, J. R.; Amanchukwu, C. V.; Hammond, P. T.; Shao-Horn, Y. Instability of Poly(ethylene oxide) upon Oxidation in Lithium-Air Batteries. *J. Phys. Chem. C* **2015**, *119*, 6947–6955 DOI: 10.1021/jp511794g.

(89) Harding, J. R.; Lu, Y.-C.; Tsukada, Y.; Shao-Horn, Y. Evidence of catalyzed oxidation of Li2O2 for rechargeable Li–air battery applications. *Phys. Chem. Chem. Phys.* **2012**, *14*, 10540–10546 DOI: 10.1039/c2cp41761h.

(90) Adams, B. D.; Radtke, C.; Black, R.; Trudeau, M. L.; Zaghib, K.; Nazar, L. F. Current density dependence of peroxide formation in the Li–O2 battery and its effect on charge. *Energy Environ. Sci.* **2013**, *6*, 1772–1778 DOI: 10.1039/C3EE40697K.

(91) Nasybulin, E.; Xu, W.; Engelhard, M. H.; Nie, Z.; Li, X. S.; Zhang, J.-G. Stability of polymer binders in Li-O2 batteries. *J. Power Sources* **2013**, *243*, 899–907 DOI: 10.1016/j.jpowsour.2013.06.097.

(92) Karan, N. K.; Balasubramanian, M.; Fister, T. T.; Burrell, A. K.; Du, P. Bulk-Sensitive Characterization of the Discharged Products in Li–O 2 Batteries by Nonresonant Inelastic X-ray Scattering. *J. Phys. Chem. C* **2012**, 120816065440008 DOI: 10.1021/jp306298e.

(93) Veith, G. M.; Dudney, N. J.; Howe, J.; Nanda, J. Spectroscopic Characterization of Solid Discharge Products in Li–Air Cells with Aprotic Carbonate Electrolytes. *J. Phys. Chem. C* **2011**, *115*, 14325–14333 DOI: 10.1021/jp2043015.

(94) Bryantsev, V. S.; Giordani, V.; Walker, W.; Uddin, J.; Lee, I.; van Duin, A. C. T.; Chase, G. V.; Addison, D. Investigation of Fluorinated Amides for Solid-Electrolyte Interphase Stabilization in Li-O 2 Batteries Using Amide-Based Electrolytes. *J. Phys. Chem. C* **2013**, 130520171032004 DOI: 10.1021/jp402844r.

(95) Veith, G. M.; Dudney, N. J. Current Collectors for Rechargeable Li-Air Batteries. *J. Electrochem. Soc.* **2011**, *158*, A658 DOI: 10.1149/1.3569750.

(96) Black, R.; Adams, B.; Nazar, L. F. Non-Aqueous and Hybrid Li-O2 Batteries. *Adv. Energy Mater.* **2012**, *2*, 801–815 DOI: 10.1002/aenm.201200001.

(97) Amanchukwu, C. V.; Harding, J. R.; Shao-Horn, Y.; Hammond, P. T. Understanding the Chemical Stability of Polymers for Lithium–Air Batteries. *Chem. Mater.* **2014** DOI: 10.1021/cm5040003.

(98) Sharon, D.; Etacheri, V.; Garsuch, A.; Afri, M.; Frimer, A. A.; Aurbach, D. On the Challenge of Electrolyte Solutions for Li–Air Batteries: Monitoring Oxygen Reduction and Related Reactions in Polyether Solutions by Spectroscopy and EQCM. *J. Phys. Chem. Lett.* **2012**, *4*, 127–131 DOI: 10.1021/jz3017842.

(99) Meini, S.; Solchenbach, S.; Piana, M.; Gasteiger, H. A. The Role of Electrolyte Solvent Stability and Electrolyte Impurities in the Electrooxidation of Li2O2 in Li-O2 Batteries. *J. Electrochem. Soc.* **2014**, *161*, A1306–A1314 DOI: 10.1149/2.0621409jes.

(100) Uddin, J.; Bryantsev, V. S.; Giordani, V.; Walker, W.; Chase, G. V.; Addison, D. Lithium Nitrate As Regenerable SEI Stabilizing Agent for Rechargeable Li/O 2 Batteries. *J. Phys. Chem. Lett.* **2013**, *4*, 3760–3765 DOI: 10.1021/jz402025n.

(101) Hartmann, P.; Bender, C. L.; Sann, J.; Dürr, A. K.; Jansen, M.; Janek, J.; Adelhelm, P. A comprehensive study on the cell chemistry of the sodium superoxide (NaO2) battery. *Phys. Chem. Chem. Phys.* **2013**, *15*, 11661–11672 DOI: 10.1039/c3cp50930c.

(102) Barile, C. J.; Gewirth, A. a. Investigating the Li-O2 Battery in an Ether-Based Electrolyte Using Differential Electrochemical Mass Spectrometry. *J. Electrochem. Soc.* **2013**, *160*, A549–A552 DOI: 10.1149/2.033304jes.

(103) Wolter, O.; Heitbaum, J. Differential Electrochemical Mass Spectroscopy (DEMS) - a New Method for the Study of Electrode Processes. *Berichte der Bunsengesellschaft für Phys. Chemie* **1984**, *88*, 2–6 DOI: 10.1002/bbpc.19840880103.

(104) Wasmus, S.; Samms, S. R.; Savinell, R. F. Multipurpose Electrochemical Mass Spectrometry: A New Powerful Extension of Differential Electrochemical Mass Spectrometry. *J. Electrochem. Soc.* **1995**, *142*, 1183 DOI: 10.1149/1.2044149.

(105) Gao, Y.; Tsuji, H.; Hattori, H.; Kita, H. New on-line mass spectrometer system designed for platinum-single crystal electrode and electroreduction of acetylene. *J. Electroanal. Chem.* **1994**, *372*, 195–200 DOI: 10.1016/0022-0728(93)03291-V.

(106) Bogdanoff, P. A New Inlet System for Differential Electrochemical Mass Spectroscopy Applied to the Photocorrosion of p-InP(111) Single Crystals. *J. Electrochem. Soc.* **1998**, *145*, 576 DOI: 10.1149/1.1838306.

(107) Jusys, Z.; Massong, H.; Baltruschat, H. A New Approach for Simultaneous DEMS and EQCM: Electro-oxidation of Adsorbed CO on Pt and Pt-Ru. *Journal of The Electrochemical Society*, **1999**, *146*, 1093.

(108) Wonders, A. H. H.; Housmans, T. H. M. H. M.; Rosca, V.; Koper, M. T. M. T. M. On-line mass spectrometry system for measurements at single-crystal electrodes in hanging meniscus configuration. *J. Appl. Electrochem.* **2006**, *36*, 1215–1221 DOI: 10.1007/s10800-006-9173-4.

(109) Wang, J.; Wasmus, S.; Savinell, R. F. Evaluation of Ethanol, 1-Propanol, and 2-Propanol in a Direct Oxidation Polymer-Electrolyte Fuel Cell A Real-Time Mass Spectrometry Study. *J. Electrochem. Soc.* **1995**, *142*, 4218–4224 DOI: 10.1149/1.2048487.

(110) Wasmus, S.; Wang, J.-T.; Savinell, R. F. Real-Time Mass Spectrometric Investigation of the Methanol Oxidation in a Direct Methanol Fuel Cell. *J. Electrochem. Soc.* **1995**, *142*, 3825 DOI: 10.1149/1.2048420.

(111) Wang, J.-T.; Wasmus, S.; Savinell, R. F. Real-Time Mass Spectrometric Study of the Methanol Crossover in a Direct Methanol Fuel Cell. *J. Electrochem. Soc.* **1996**, *143*, 1233 DOI: 10.1149/1.1836622.

(112) Novák, P.; Goers, D.; Hardwick, L.; Holzapfel, M.; Scheifele, W.; Ufheil, J.; Würsig, A. Advanced in situ characterization methods applied to carbonaceous materials. *J. Power Sources* **2005**, *146*, 15–20 DOI: 10.1016/j.jpowsour.2005.03.129.

(113) Walker, W.; Giordani, V.; Uddin, J.; Bryantsev, V. S.; Chase, G. V.; Addison, D. A rechargeable Li-O2 battery using a lithium nitrate/N,N-dimethylacetamide electrolyte. *J. Am. Chem. Soc.* **2013**, *135*, 2076–2079 DOI: 10.1021/ja311518s.

(114) Bryantsev, V. S.; Uddin, J.; Giordani, V.; Walker, W.; Addison, D.; Chase, G. V. The Identification of Stable Solvents for Nonaqueous Rechargeable Li-Air Batteries. *J. Electrochem. Soc.* **2012**, *160*, A160–A171 DOI: 10.1149/2.027302jes.

(115) Giordani, V.; Bryantsev, V. S.; Uddin, J.; Walker, W.; Chase, G. V.; Addison, D. N-methylacetamide as an Electrolyte Solvent for Rechargeable Li-O2 Batteries: Unexpected Stability at the O2 electrode. *ECS Electrochem. Lett.* **2013**, *3*, A11–A14 DOI: 10.1149/2.007401eel.

(116) Giordani, V.; Walker, W.; Bryantsev, V. S.; Uddin, J.; Chase, G. V.; Addison, D. Synergistic Effect of Oxygen and LiNO3 on the Interfacial Stability of Lithium Metal in a Li/O2 Battery. *J. Electrochem. Soc.* **2013**, *160*, A1544–A1550 DOI: 10.1149/2.097309jes.

(117) Chen, Y.; Freunberger, S. A.; Peng, Z.; Fontaine, O.; Bruce, P. G. Charging a Li–O2 battery using a redox mediator. *Nat. Chem.* **2013** DOI: 10.1038/nchem.1646.

(118) Mitchell, R. R.; Gallant, B. M.; Shao-Horn, Y.; Thompson, C. V. Mechanisms of Morphological Evolution of Li 2 O 2 Particles during Electrochemical Growth. *J. Phys. Chem. Lett.* **2013**, *4*, 1060–1064 DOI: 10.1021/jz4003586.

(119) Ryu, W.-H.; Gittleson, F. S.; Schwab, M.; Goh, T.; Taylor, A. D. A Mesoporous Catalytic Membrane Architecture for Lithium–Oxygen Battery Systems. *Nano Lett.* **2015**, *15*, 434–441 DOI: 10.1021/nl503760n.

(120) Zhang, T.; Zhou, H. A reversible long-life lithium-air battery in ambient air. *Nat. Commun.* **2013**, *4*, 1817 DOI: 10.1038/ncomms2855.

(121) Meini, S.; Piana, M.; Beyer, H.; Schwammlein, J.; Gasteiger, H. A. Effect of Carbon Surface Area on First Discharge Capacity of Li-O2 Cathodes and Cycle-Life Behavior in Ether-Based Electrolytes. *J. Electrochem. Soc.* **2012**, *159*, A2135–A2142 DOI: 10.1149/2.011301jes.

(122) Jadhav, H. S.; Kalubarme, R. S.; Roh, J.-W.; Jung, K.-N.; Shin, K.-H.; Park, C.-N.; Park, C.-J. Facile and Cost Effective Synthesized Mesoporous Spinel NiCo2O4 as Catalyst for Non-Aqueous Lithium-Oxygen Batteries. *J. Electrochem. Soc.* **2014**, *161*, A2188–A2196 DOI: 10.1149/2.0771414jes.

(123) Wang, Z.-L.; Xu, D.; Xu, J.-J.; Zhang, L.-L.; Zhang, X.-B. Graphene Oxide Gel-Derived, Free-Standing, Hierarchically Porous Carbon for High-Capacity and High-Rate Rechargeable Li-O2 Batteries. *Adv. Funct. Mater.* **2012**, *22*, 3699–3705 DOI: 10.1002/adfm.201200403.

(124) Wang, D.; Xiao, J.; Xu, W.; Zhang, J.-G. High Capacity Pouch-Type Li–Air Batteries. *J. Electrochem. Soc.* **2010**, *157*, A760 DOI: 10.1149/1.3414828.

(125) Beattie, S. D.; Manolescu, D. M.; Blair, S. L. High-Capacity Lithium–Air Cathodes. *J. Electrochem. Soc.* **2009**, *156*, A44 DOI: 10.1149/1.3005989.

(126) Thapa, A. K.; Saimen, K.; Ishihara, T. Pd/MnO2 Air Electrode Catalyst for Rechargeable Lithium/Air Battery. *Electrochem. Solid-State Lett.* **2010**, *13*, A165–A167 DOI: 10.1149/1.3481762.

(127) Laoire, C. O.; Mukerjee, S.; Plichta, E. J.; Hendrickson, M. A.; Abraham, K. M. Rechargeable Lithium/TEGDME-LiPF6/O6 Battery. *J. Electrochem. Soc.* **2011**, *158*, A302 DOI: 10.1149/1.3531981.

(128) Trahey, L.; Karan, N. K.; Chan, M. K. Y.; Lu, J.; Ren, Y.; Greeley, J.; Balasubramanian, M.; Burrell, A. K.; Curtiss, L. A.; Thackeray, M. M. Synthesis, Characterization, and Structural Modeling of High-Capacity, Dual Functioning MnO2 Electrode/Electrocatalysts for Li-O2 Cells. *Adv. Energy Mater.* **2012**, n/a – n/a DOI: 10.1002/aenm.201200037.

(129) Meini, S.; Piana, M.; Tsiouvaras, N.; Garsuch, A.; Gasteiger, H. A. The Effect of Water on the Discharge Capacity of a Non-Catalyzed Carbon Cathode for Li-O2 Batteries. *Electrochem. Solid-State Lett.* **2012**, *15*, A45–A48 DOI: 10.1149/2.005204esl.

(130) Mirzaeian, M.; Hall, P. J. Characterizing capacity loss of lithium oxygen batteries by impedance spectroscopy. *J. Power Sources* **2010**, *195*, 6817–6824 DOI: 10.1016/j.jpowsour.2010.04.064.

(131) Shao, Y.; Ding, F.; Xiao, J.; Zhang, J.; Xu, W.; Park, S.; Zhang, J.-G.; Wang, Y.; Liu, J. Making Li-Air Batteries Rechargeable: Material Challenges. *Adv. Funct. Mater.* **2012**, *201200688*, n/a – n/a DOI: 10.1002/adfm.201200688.

(132) Chen, Y.; Freunberger, S. A.; Peng, Z.; Bardé, F.; Bruce, P. G. The Li-O2 Battery with a Dimethylformamide Electrolyte. *J. Am. Chem. Soc.* **2012** DOI: 10.1021/ja302178w.

(133) Sigma-Aldrich. Diethylene glycol dimethyl ether Safety Data Sheet, 2015, 1–8.

(134) Visco, S. J.; Nimon, Y. S.; Katz, B. D. Protected lithium electrodes based on ceramic membranes, September 18, 2014.

(135) Sandhu, S. S.; Fellner, J. P.; Brutchen, G. W. Diffusion-limited model for a lithium/air battery with an organic electrolyte. *J. Power Sources* **2007**, *164*, 365–371 DOI: 10.1016/j.jpowsour.2006.09.099.

(136) Fergus, J. W. Ceramic and polymeric solid electrolytes for lithium-ion batteries. *J. Power Sources* **2010**, *195*, 4554–4569 DOI: 10.1016/j.jpowsour.2010.01.076.

(137) Kamaya, N.; Homma, K.; Yamakawa, Y.; Hirayama, M.; Kanno, R.; Yonemura, M.; Kamiyama, T.; Kato, Y.; Hama, S.; Kawamoto, K.; et al. A lithium superionic conductor. *Nat. Mater.* **2011**, *10*, 682–686 DOI: 10.1038/nmat3066.

(138) Kanno, R.; Murayama, M. Lithium Ionic Conductor Thio-LISICON: The Li[sub 2]S-GeS[sub 2]-P[sub 2]S[sub 5] System. *J. Electrochem. Soc.* **2001**, *148*, A742 DOI: 10.1149/1.1379028.

(139) Heitjans, P.; Indris, S. Diffusion and ionic conduction in nanocrystalline ceramics. *J. Phys. Condens. Matter* **2003**, *15*, R1257 DOI: 10.1088/0953-8984/15/30/202.

(140) Kitaura, H.; Zhou, H. Electrochemical performance and reaction mechanism of all-solid-state lithium–air batteries composed of lithium, Li1+xAlyGe2−y(PO4)3 solid electrolyte and carbon nanotube air electrode. *Energy Environ. Sci.* **2012**, *5*, 9077 DOI: 10.1039/c2ee22381c.

(141) Sahu, G.; Lin, Z.; Li, J.; Liu, Z.; Dudney, N.; Liang, C. Air-stable, high-conduction solid electrolytes of arsenic-substituted Li4SnS4. *Energy Environ. Sci.* **2014**, *7*, 1053–1058 DOI: 10.1039/C3EE43357A.

(142) Mark, J. *Polymer Data Handbook*; Oxford University Press, 1999.

(143) Hammond, P. T. Form and Function in Multilayer Assembly: New Applications at the Nanoscale. *Adv. Mater.* **2004**, *16*, 1271–1293 DOI: 10.1002/adma.200400760.

(144) Lin, H.; Freeman, B. D. Gas solubility, diffusivity and permeability in poly(ethylene oxide). *J. Memb. Sci.* **2004**, *239*, 105–117 DOI: 10.1016/j.memsci.2003.08.031.

(145) Singh, M.; Odusanya, O.; Wilmes, G. M.; Eitouni, H. B.; Gomez, E. D.; Patel, A. J.; Chen, V. L.; Park, M. J.; Fragouli, P.; Iatrou, H.; et al. Effect of Molecular Weight on the Mechanical and Electrical Properties of Block Copolymer Electrolytes. *Macromolecules* **2007**, *40*, 4578–4585 DOI: 10.1021/ma0629541.

(146) Kumar, B.; Kumar, J.; Leese, R.; Fellner, J. P.; Rodrigues, S. J.; Abraham, K. M. A Solid-State, Rechargeable, Long Cycle Life Lithium–Air Battery. *J. Electrochem. Soc.* **2010**, *157*, A50 DOI: 10.1149/1.3256129.

(147) Mohamed, S. N.; Johari, N. A.; Ali, A. M. .; Harun, M. K.; Yahya, M. Z. A. Electrochemical studies on epoxidised natural rubber-based gel polymer electrolytes for lithium-air cells. *J. Power Sources* **2008**, *183*, 351–354 DOI: 10.1016/j.jpowsour.2008.04.048.

(148) Hassoun, J.; Croce, F.; Armand, M.; Scrosati, B. Investigation of the O2 electrochemistry in a polymer electrolyte solid-state cell. *Angew. Chemie Int. Ed.* **2011**, *50*, 2999–3002 DOI: 10.1002/anie.201006264.

(149) Kichambare, P. Mesoporous Nitrogen-Doped Carbon-Glass Ceramic Cathodes for Solid-State Lithium–Oxygen Batteries. *ACS Appl. Mater.* ... **2011**, *4*, 49–52 DOI: 10.1021/am201513d.

(150) Zhang, D.; Li, R.; Huang, T.; Yu, A. Novel composite polymer electrolyte for lithium air batteries. *J. Power Sources* **2010**, *195*, 1202–1206 DOI: 10.1016/j.jpowsour.2009.08.063.

(151) Balaish, M.; Peled, E.; Golodnitsky, D.; Ein-Eli, Y. Liquid-Free Lithium–Oxygen Batteries. *Angew. Chemie Int. Ed.* **2014**, *54*, 436–440 DOI: 10.1002/anie.201408008.

(152) Bryantsev, V. S.; Blanco, M. Computational Study of the Mechanisms of Superoxide-Induced Decomposition of Organic Carbonate-Based Electrolytes. *J. Phys. Chem. Lett.* **2011**, *2*, 379–383 DOI: 10.1021/jz1016526.

(153) Nookala, M.; Kumar, B.; Rodrigues, S. Ionic conductivity and ambient temperature Li electrode reaction in composite polymer electrolytes containing nanosize alumina. *J. Power Sources* **2002**, *111*, 165–172 DOI: 10.1016/S0378-7753(02)00303-8.

(154) Fenton, D. E.; Parker, J. M.; Wright, P. V. Complexes of alkali metal ions with poly(ethylene oxide). *Polymer (Guildf)*. **1973**, *14*, 589 DOI: 10.1016/0032-3861(73)90146-8.

(155) Hanai, K.; Ueno, M.; Imanishi, N.; Hirano, a.; Yamamoto, O.; Takeda, Y. Interfacial resistance of the LiFePO4-C/PEO-LiTFSI composite electrode for dry-polymer lithium-ion batteries. *J. Power Sources* **2011**, *196*, 6756–6761 DOI: 10.1016/j.jpowsour.2010.10.079.

(156) Kim, Y.; Smotkin, E. The effect of plasticizers on transport and electrochemical properties of PEO-based electrolytes for lithium rechargeable batteries. *Solid State Ionics* **2002**, *149*, 29–37.

(157) Meyer, W. H. Polymer electrolytes for lithium-ion batteries. *Adv. Mater.* **1998**, *10*, 439–448 DOI: 10.1002/(SICI)1521-4095(199804)10:6<439::AID-ADMA439>3.0.CO;2-I.

(158) Appetecchi, G. B.; Croce, F.; Hassoun, J.; Scrosati, B.; Salomon, M.; Cassel, F. Hot-pressed, dry, composite, PEO-based electrolyte membranes:: I. Ionic conductivity characterization. *J. Power Sources* **2003**, *114*, 105–112.

(159) Shin, J.-H.; Henderson, W. A.; Passerini, S. An Elegant Fix for Polymer Electrolytes. *Electrochem. Solid-State Lett.* **2005**, *8*, A125 DOI: 10.1149/1.1850387.

(160) Appetecchi, G. B.; Kim, G.-T.; Montanino, M.; Alessandrini, F.; Passerini, S. Room temperature lithium polymer batteries based on ionic liquids. *J. Power Sources* **2011**, *196*, 6703–6709 DOI: 10.1016/j.jpowsour.2010.11.070.

(161) Kim, G.-T.; Jeong, S. S.; Xue, M.-Z.; Balducci, A.; Winter, M.; Passerini, S.; Alessandrini, F.; Appetecchi, G. B. Development of ionic liquid-based lithium battery prototypes. *J. Power Sources* **2012**, *199*, 239–246 DOI: 10.1016/j.jpowsour.2011.10.036.

(162) Shin, J. H.; Henderson, W. A.; Passerini, S. Ionic liquids to the rescue? Overcoming the ionic conductivity limitations of polymer electrolytes. *Electrochem. commun.* **2003**, *5*, 1016–1020 DOI: 10.1016/j.elecom.2003.09.017.

(163) Shin, J.-H.; Henderson, W. A.; Passerini, S. PEO-Based Polymer Electrolytes with Ionic Liquids and Their Use in Lithium Metal-Polymer Electrolyte Batteries. *J. Electrochem. Soc.* **2005**, *152*, A978 DOI: 10.1149/1.1890701.

(164) Shin, J. H.; Henderson, W. A.; Appetecchi, G. B.; Alessandrini, F.; Passerini, S. Recent developments in the ENEA lithium metal battery project. *Electrochim. Acta* **2005**, *50*, 3859–3865 DOI: 10.1016/j.electacta.2005.02.049.

(165) Kolbeck, C.; Lehmann, J.; Lovelock, K. R. J.; Cremer, T.; Paape, N.; Wasserscheid, P.; Fröba, A. P.; Maier, F.; Steinrück, H.-P. Density and surface tension of ionic liquids. *J. Phys. Chem. B* **2010**, *114*, 17025–17036 DOI: 10.1021/jp1068413.

(166) Zalc, J. M.; Reyes, S. C.; Iglesia, E. Monte-Carlo simulations of surface and gas phase diffusion in complex porous structures. *Chem. Eng. Sci.* **2003**, *58*, 4605–4617 DOI: 10.1016/j.ces.2003.07.008.

(167) Celgard LLC. Celgard Product Comparison Datasheet http://www.celgard.com/pdf/library/Celgard_Product_Comparison_10002.pdf (accessed Mar 17, 2015).

(168) Bouchet, R.; Maria, S.; Meziane, R.; Aboulaich, A.; Lienafa, L.; Bonnet, J.; Phan, T. N. T.; Bertin, D.; Gigmes, D.; Devaux, D.; et al. Single-ion BAB triblock copolymers as highly efficient electrolytes for lithium-metal batteries. *Nat. Mater.* **2013**, *12*, 452–457 DOI: 10.1038/nmat3602.

(169) Hu, Q.; Osswald, S.; Daniel, R.; Zhu, Y.; Wesel, S.; Ortiz, L.; Sadoway, D. R. Graft copolymer-based lithium-ion battery for high-temperature operation. *J. Power Sources* **2011**, *196*, 5604–5610 DOI: 10.1016/j.jpowsour.2011.03.001.

(170) Black, R.; Oh, S. H.; Lee, J.; Yim, T.; Adams, B.; Nazar, L. F. Screening for superoxide reactivity in Li-O2 batteries: effect on Li2O2/LiOH crystallization. *J. Am. Chem. Soc.* **2012**, *134*, 2902–2905 DOI: 10.1021/ja2111543.

(171) Herranz, J.; Garsuch, A.; Gasteiger, H. a. Using Rotating Ring Disc Electrode Voltammetry to Quantify the Superoxide Radical Stability of Aprotic Li–Air Battery Electrolytes. *J. Phys. Chem. C* **2012**, *116*, 19084–19094 DOI: 10.1021/jp304277z.

(172) Vallée, A.; Besner, S.; Prud'Homme, J. Comparative study of poly(ethylene oxide) electrolytes made with LiN(CF3SO2)2, LiCF3SO3 and LiClO4: Thermal properties and conductivity behaviour. *Electrochim. Acta* **1992**, *37*, 1579–1583 DOI: 10.1016/0013-4686(92)80115-3.

(173) Sharon, D.; Afri, M.; Noked, M.; Garsuch, A.; Frimer, A. A.; Aurbach, D. Oxidation of Dimethyl Sulfoxide Solutions by Electrochemical Reduction of Oxygen. *J. Phys. Chem. Lett.* **2013**, *4*, 3115–3119 DOI: 10.1021/jz4017188.

(174) Zhang, T.; Imanishi, N.; Shimonishi, Y.; Hirano, A.; Takeda, Y.; Yamamoto, O.; Sammes, N. A novel high energy density rechargeable lithium/air battery. *Chem. Commun.* **2010**, *46*, 1661–1663 DOI: 10.1039/b920012f.

(175) Li, L.; Zhao, X.; Fu, Y.; Manthiram, A. Polyprotic acid catholyte for high capacity dual-electrolyte Li-air batteries. *Phys. Chem. Chem. Phys.* **2012**, 2–5 DOI: 10.1039/c2cp42250f.

(176) Kitaura, H.; Zhou, H. Electrochemical Performance of Solid-State Lithium-Air Batteries Using Carbon Nanotube Catalyst in the Air Electrode. *Adv. Energy Mater.* **2012**, *2*, 889–894 DOI: 10.1002/aenm.201100789.

(177) Croce, F.; Appetecchi, G. B.; Persi, L.; Scrosati, B. Nanocomposite polymer electrolytes for lithium batteries. *Nature* **1998**, *394*, 456–458 DOI: doi:10.1038/28818.

(178) Oesten, R.; Heider, U.; Schmidt, M. Advanced electrolytes. *Solid State Ionics* **2002**, *148*, 391–397 DOI: 10.1016/S0167-2738(02)00078-4.

(179) Savitzky, A.; Golay, M. J. E. Smoothing and Differentiation of Data by Simplified Least Squares Procedures. *Anal. Chem.* **1964**, *36*, 1627–1639 DOI: 10.1021/ac60214a047.

(180) Han, S.; Kim, C.; Kwon, D. Thermal degradation of poly(ethyleneglycol). *Polym. Degrad. Stab.* **1995**, *47*, 203–208 DOI: 10.1016/0141-3910(94)00109-L.

(181) De Sainte Claire, P. Degradation of PEO in the Solid State: A Theoretical Kinetic Model. *Macromolecules* **2009**, *42*, 3469–3482 DOI: 10.1021/ma802469u.

(182) Dulog, V. L.; Storck, G. Die oxydation von polyepoxiden mit molekularem sauerstoff. *Die Makromol. Chemie* **1966**, *91*, 50–73 DOI: 10.1002/macp.1966.020910104.

(183) Yang, L.; Heatley, F.; Blease, T. G.; Thompson, R. I. G. A study of the mechanism of the oxidative thermal degradation of poly(ethylene oxide) and poly(propylene oxide) using 1H- and 13C-NMR. *Eur. Polym. J.* **1996**, *32*, 535–547 DOI: 10.1016/0014-3057(95)00182-4.

(184) Bryantsev, V. S.; Faglioni, F. Predicting autoxidation stability of ether- and amide-based electrolyte solvents for Li-air batteries. *J. Phys. Chem. A* **2012**, *116*, 7128–7138 DOI: 10.1021/jp301537w.

(185) Hu, J.; Xu, K.; Jia, Y.; Lv, Y.; Li, Y.; Hou, X. Oxidation of Ethyl Ether on Borate Glass: Chemiluminescence, Mechanism, and Development of a Sensitive Gas Sensor. *Anal. Chem.* **2008**, *80*, 7964–7969 DOI: 10.1021/ac800748m.

(186) Kaplan, M. L.; Kelleher, P. G. On the mechanism of polyethylene photodegradation: The oxidation of terminal olefins and saturated centers with singlet oxygen. *J. Polym. Sci. Part B Polym. Lett.* **1971**, *9*, 565–568 DOI: 10.1002/pol.1971.110090802.

(187) Jung, H.; Hassoun, J.; Park, J.; Sun, Y.; Scrosati, B. An improved high-performance lithium–air battery. *Nat. Chem.* **2012**, 1–7 DOI: 10.1038/nchem.1376.

(188) Zhang, Z.; Lu, J.; Assary, R. S.; Du, P.; Wang, H.-H.; Sun, Y.-K.; Qin, Y.; Lau, K. C.; Greeley, J.; Redfern, P. C.; et al. Increased Stability Toward Oxygen Reduction Products for Lithium-Air Batteries with Oligoether-Functionalized Silane Electrolytes. *J. Phys. Chem. C* **2011**, *115*, 25535–25542 DOI: 10.1021/jp2087412.

(189) Valco Instruments Co. Inc. Sample loops for 1/16" Valco injectors http://www.vici.com/vval/loops_uw16.php (accessed Mar 8, 2015).

(190) NIST/SEMATECH e-Handbook of Statistical Methods http://www.itl.nist.gov/div898/handbook/pmd/section4/pmd452.htm#uw (accessed Mar 10, 2015).

(191) Diederick. Savitzky-Golay smooth/differentiation filters and filter application - File Exchange - MATLAB Central http://www.mathworks.com/matlabcentral/fileexchange/30299-savitzky-golay-smooth-differentiation-filters-and-filter-application (accessed Mar 9, 2015).

(192) Stanford Research Systems. SRS RGA Manual http://www.thinksrs.com/downloads/PDFs/Manuals/RGAm.pdf (accessed Apr 2, 2015).

Appendix A

DEMS Analysis Methods

A.1 Terminology

Table A-1 defines the terms used throughout this appendix. Additional terms may be defined within specific portions of the appendix, but will only be used in close proximity with their definition.

Table A-1. Terms used to describe the DEMS in this appendix.

Symbol	Name	Definition
h_{Mg}	Partial peak height	Peak height contribution at mass M of gas g
n_{eff}	Effective moles	Effective number of moles in the cell after correcting for the leak rate
R_x	Pressure ratio	Ratio of final to initial pressure measured during volume calibration or measurement, for measurement x.
R_x^*	Calculated pressure ratio	
V_{AB}	AB volume	Volume contained inside the 6-port valve connecting two adjacent ports The entire valve contains three regions with this volume, and shifting the valve from position A to B will change which ports these volumes connect to.
$V_{cell,i}$	Cell volume	Volume of cell attached to position i (does not include excess cell volume)
$V_{cell,i}^*$	Total cell volume	Volume of cell excess volume and the attached cell or calibration loop.
$V_{CL,d}$	Direct calibration loop	Loop of known volume that is attached to the DEMS in order to perform a calibration. Can be attached directly to the 6-port valve (in Direct Calibration) or to any of the cell positions (Cell Calibration)
$V_{CL,i}$	Cell calibration volume	Volume of the calibration loop for cell i (does not include excess cell volume).

$V_{ex,i}$	Excess cell volume	Volume of tubing associated with cell i that is permanently attached to the DEMS Includes the volume of each cell's pressure gauge
V_{in}	Inlet volume	Volume of the inlet portion of the cell bypass system
V_{out}	Outlet volume	Volume of the outlet portion of the cell bypass system
V_{pg}	Purge volume	Tubing between 6-port valve and the purge valve, opposite the sample loop
V_{SL}	Sample loop	Loop used to collect gas that will be dosed into the vacuum system for analysis
V_{src}	Source volume	Tubing between the inlet shutoff valve and the 6-port valve (includes inlet pressure gauge)
C_{leak}	Leak rate constant	Parameter that defines the leak rate in terms of a pressure driving force. Units are given in amount/time/pressure
H_M	Peak height	Total peak height measured at mass M
P_g	Partial pressure	Partial pressure of gas g at the RGA.
S_g	Pressure sensitivity	Partial pressure sensitivity of gas g at the highest peak of that gas. This has units of amps/Torr
U_{in}	Inlet volume ratio	Ration of V_{in} to $V_{in} + V_{out}$
$V_{exhaust}$	Exhaust volume	Volume of tubes that are downstream from a cell. Equal to $V_{out} + V_{SL} + V_{AB}$
W_z	Volume ratio	Ratio of volume z (e.g. V_{src}) to V_{SL}
$\dfrac{dn_{leak}}{dt}$	Leak rate	Rate of moles escaping from cell due to leak
f_{act}	Active fraction	Fraction of cell volume that is active and accumulates gas during charging
f_{fill}	Fill fraction	Fraction of moles of gas in the active portion of a cell that is freshly added fill gas
y_i	Gas fraction	Fraction of gas i out of all gases

α_{Mg}	Fragmentation factor	Fragmentation factor of gas g at mass M. Fragmentation factor is defined as the ratio of the signal at a particular mass relative to the highest peak of a particular gas
M	Mass	Integer representing the mass (m/z) measured
g	Gas	Indicates the gases measured. When used in a subscript, indicates the variable applies to a single gas

A.2 Volume Calibration and Measurement

Accurate volume information is critical in performing any sort of experiment on the DEMS with precision. The general principle of volume measurement with the DEMS is to expand gas from a region of uncertain volume into an additional region of known volume. Measuring pressure (as a proxy for total moles) before and after this expansion allows the experimenter to estimate the volume of the unknown region. This method is complicated by the fact that the small internal diameter (ID) tubing used in this instrument has relatively high volume uncertainty (small variations in the ID can result in very large impacts on the total volume, estimated at ±5% of the rated volume for tubes used in this system).[189] To avoid propagating these errors through to the rest of the system, several different calibration volumes were used, and the entire collection of calibration experiments are analyzed through a nonlinear optimization process, in order to find the optimal estimation of all volumes present in the system.

Calibration Measurements

Direct Calibration

The first set of calibrations involved directly attaching a variety of known-volume loops to the 6-port switching valve to estimate the volume of the source and sample volumes of the DEMS. The arrangement of connections is shown in Figure A-1 below.
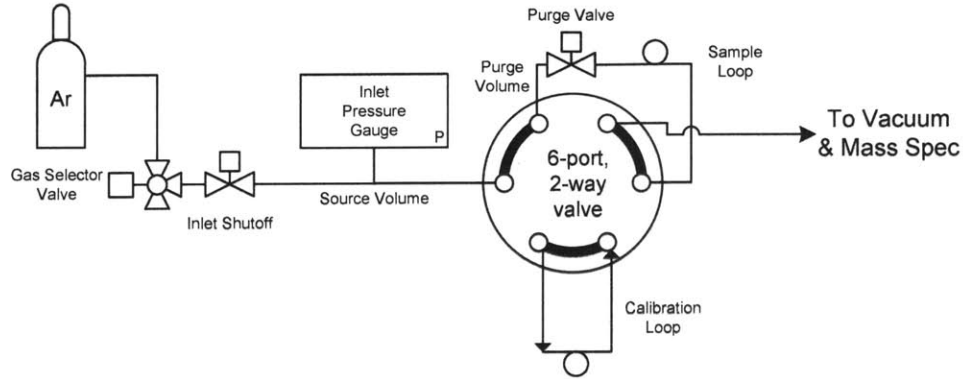
Figure A-1. Arrangement of loops connected to the 6-port valve during direct calibration.

In this arrangement, three separate measurements can be taken, while only switching the 6-port valve between positions, which are summarized in Table A-2 below. In each measurement, the volumes designated as "filled before" are filled with gas and isolated, and the "evacuated volumes" are exposed evacuated. The pressure of the filled region is recorded, and then the 6-port valve is switched so that the evacuated volumes are filled with gas from the previously filled volumes. The pressure of the expanded gas is recorded, and the ratio of the final pressure to the initial pressure (designated R_x, where x represents the particular measurement) is saved. Each measurement may involve evacuating or filling more regions than just those listed here, but those volumes are not directly accessible to the inlet pressure gauge after the measurement. Note that measurement C is independent of either $V_{CL,d}$, and so is constant across all calibrations.

Table A-2. Direct calibration measurements.

Measurement	Volumes filled before	Volume(s) evacuated	Volumes connected to Inlet Gauge after measurement
A	V_{src}, V_{AB} (×1), $V_{CL,d}$	V_{SL}, V_{AB} (×1)	V_{src}, V_{AB} (×2), $V_{CL,d}$, V_{SL}
B	V_{src}	V_{AB} (×2), $V_{CL,d}$, V_{SL}	V_{src}, V_{AB} (×2), $V_{CL,d}$, V_{SL}

Measurement	Volumes filled before	Volume(s) evacuated	Volumes connected to Inlet Gauge after measurement
C	V_{src}	V_{pg}, V_{AB} (×1)	V_{src}, V_{AB} (×1), V_{pg}

Cell Bypass Calibration

After performing the direct calibration, the cell bypass system is reconnected to the 6-port valve, which is diagrammed in Figure A-2 below. This portion of the calibration does not require any separate calibration loops, and instead expands gas into different portions of the bypass system. All of the valves that connect to individual cells are kept closed, and the measurements taken are independent of any of the cell volumes.
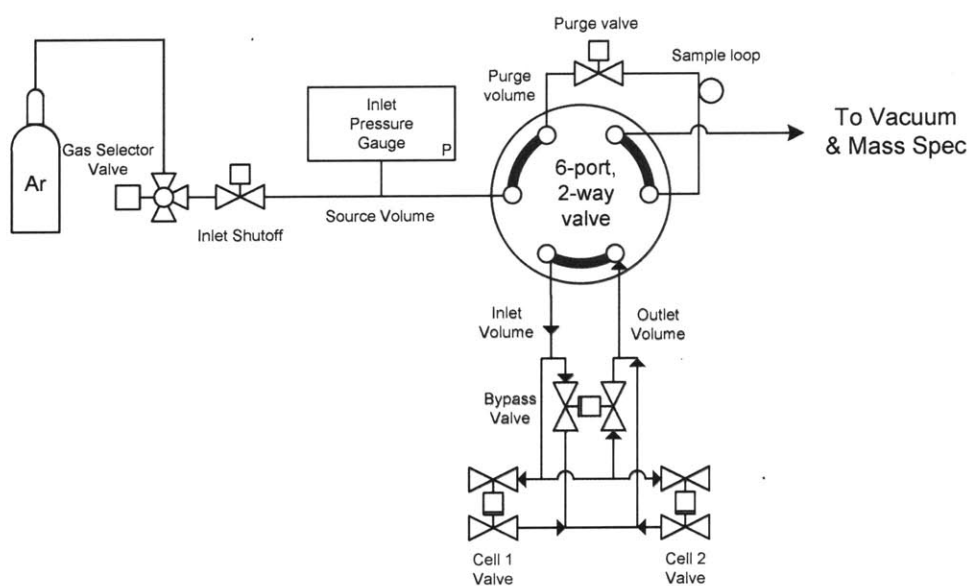
Figure A-2. Arrangement of connections used during the cell bypass calibration measurements.

Like in the direct calibration, the 6-port valve is switched between A and B positions for measurements D, E, and F. Measurement G involves opening the bypass valve instead of switching the 6-port valve. It was observed that the procedure for measurement F was not well written, and

the pressure in the evacuated volumes for this measurement were high enough to affect the accuracy of the calculation. For this reason, measurement F is neglected from the calibration analysis. Note that all four measurements do not use any calibration volumes, and are expected to be constant unless the DEMS hardware itself is modified.

Table A-3. Cell bypass calibration measurements

Measurement	Volumes filled before	Volume(s) evacuated	Volumes connected to Inlet Gauge after measurement
D	V_{src}, V_{AB} (×1), V_{in}, V_{out}	V_{SL}, V_{AB} (×1)	V_{src}, V_{AB} (×2), V_{in}, V_{out}, V_{SL}
E	V_{src}	V_{AB} (×1), V_{in}, V_{out}, V_{SL}, V_{AB} (×1)	V_{src}, V_{AB} (×2), V_{in}, V_{out}, V_{SL}
F	V_{src}	V_{in}, V_{AB} (×1)	V_{src}, V_{AB} (×1), V_{in}
G	V_{src}, V_{AB} (×1), V_{in}	V_{AB} (×1), V_{out}, V_{SL}	V_{src}, V_{AB} (×2), V_{in}, V_{out}, V_{SL}

Cell Volume Calibration

In addition to performing a Bypass calibration, calibration loops can be directly attached to the Swagelok unions on the exterior of the DEMS panel enclosure. Several different loops can be used, as was done with the direct calibration, to provide additional calibration information. Importantly, because these fittings attach with Swagelok connectors, different loops must be used from those used during direct calibration (which use Valco-compatible fittings), so calibrations with these loops can be considered independent of the calibrations performed during direct calibration. The arrangement of the system for running a calibration on Cell 1 is shown in Figure A-3 below. The same configuration could be used for Cell 2 (and any additional cells added in the future).
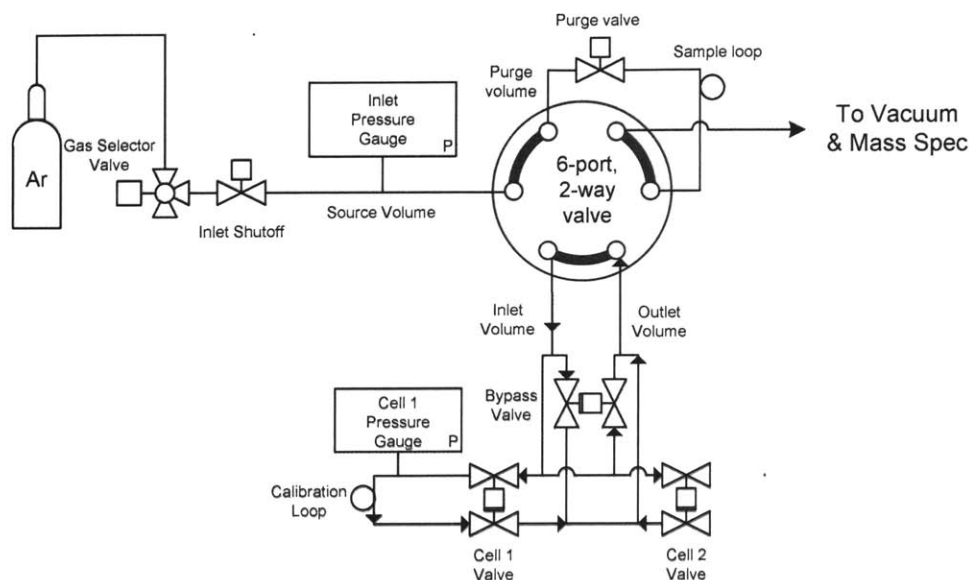
Figure A-3. Arrangement of connections used during the cell calibration measurements.

The measurements used for this calibration are listed in Table A-4. The subscript by each calibration indicates which cell was being calibrated, as each cell can undergo all of these calibrations. Measurement H_i and I_i use the 6-port valve (keeping the cell valve open), while calibrations J_i, K_i, and L_i open the cell valve to allow gas expansion. Measurement L_i uses the cell gauge to record the initial and final pressure, as the inlet pressure gauge is isolated from all the volumes involved in the measurement.

Table A-4. Cell calibration measurements

Measurement	Volumes filled before	Volume(s) evacuated	Volumes connected to Inlet Gauge after measurement
H_i	V_{src}, V_{AB} (×1), V_{in}, V_{out}, $V_{cell,i}^{*}$	V_{SL}, V_{AB} (×1)	V_{src}, V_{AB} (×2), V_{in}, V_{out}, $V_{cell,i}^{*}$, V_{SL}
I_i	V_{src}	V_{AB} (×2), V_{in}, V_{out}, $V_{cell,i}^{*}$, V_{SL}	V_{src}, V_{AB} (×2), V_{in}, V_{out}, $V_{cell,i}^{*}$, V_{SL}

J_i	V_{src}, V_{AB} (×1), V_{in}, $V_{cell,i}{}^*$	V_{AB} (×1), V_{out}, V_{SL}	V_{src}, V_{AB} (×2), V_{in}, V_{out}, $V_{cell,i}{}^*$, V_{SL}
K_i	$V_{cell,i}{}^*$	V_{src}, V_{AB} (×2), V_{in}, V_{out}, V_{SL}	V_{src}, V_{AB} (×2), V_{in}, V_{out}, $V_{cell,i}{}^*$, V_{SL}
L_i	$V_{cell,i}{}^*$	V_{AB} (×1), V_{in}, V_{out}	V_{AB} (×1), V_{in}, V_{out}, $V_{cell,i}{}^*$

Calibration Analysis

After all the calibration measurements have been taken, they are compiled together and analyzed with a nonlinear optimization to minimize the error between the measured and predicted ratios. In total, 7 + 5*(number of cells) distinct measurements are made (each should be made several times), and 6 + (number of cells) distinct parameters are fit (in the current DEMS system, this is 17 measurements and 8 parameters). These parameters can be used to define all of the volumes referenced in the tables above, and are defined in Table A-5 below. Because ratios of volumes can be much more precisely estimated than absolute volumes, most of the parameters describe the ratio (denoted as W) of a given volume to V_{SL}, which is the only parameter that describes an absolute volume (e.g. $W_{in} = V_{in}/V_{SL}$).

Table A-5. Parameters calibrated during DEMS volume calibration. All terms are arbitrary units except V_{SL}.

Parameter	Definition	Description
V_{SL}	V_{SL}	Volume of the sample loop (ml)
W_{src}	$\dfrac{V_{src}}{V_{SL}}$	Ratio of source volume to sample loop volume
W_{pg}	$\dfrac{V_{pg}}{V_{SL}}$	Ratio of purge volume to sample loop volume

W_{AB}	$\dfrac{V_{AB}}{V_{SL}}$	Ratio of AB volume to sample loop volume
W_{inout}	$\dfrac{V_{in} + V_{out}}{V_{SL}}$	Ratio of entire bypass volume to sample loop volume
U_{in}	$\dfrac{V_{in}}{V_{in} + V_{out}}$	Ratio of inlet volume to entire bypass volume
$W_{ex,1}$	$\dfrac{V_{ex,1}}{V_{SL}}$	Ratio of cell 1 excess volume to sample loop volume
$W_{ex,2}$	$\dfrac{V_{ex,2}}{V_{SL}}$	Ratio of cell 2 excess volume to sample loop volume

For any given calibration, a calibration loop may be present; this is referred to as V_{CL} in the formulas below. Depending on the calibration, this may be connected directly to the 6-port valve (where $V_{CL,d} = V_{CL}$) or to one of the cells (where $V^*_{cell,i} = V_{ex,i} + V_{CL}$). $W_{CL,d}$ and $W_{cell,i}{}^*$ are used, with the same definition of W given above.

The ratio of pressures recorded during each measurement can be used to determine the ratio of volumes before and after the measurement:

$$P_i V_i = P_f V_f = nRT \qquad \text{(A-1)}$$

$$\frac{P_f}{P_i} = \frac{V_i}{V_f} \qquad \text{(A-2)}$$

Where P_i and P_f are the initial and final pressures, and V_i and V_f are the initial and final volumes. For these equations to be valid, the following assumptions must be made: (a) the evacuated volume is entirely evacuated, and provides no additional moles of gas, (b) all of the gas in the initial volume is contained within the final volume, and (c) the temperature and pressure is uniform throughout the entire volume. With these three assumptions, we can define the calculated pressure ratios (R^*_x) for each of the measurements defined above, shown in Table A-6.

Table A-6. Formulas for determining calculated pressure ratios

Ratio	Definition (using V)	Formula (using W)
R_A^*	$\dfrac{V_{src} + V_{AB} + V_{CL,d}}{V_{src} + 2V_{AB} + V_{CL} + V_{SL}}$	$\dfrac{W_{src} + W_{AB} + W_{CL,d}}{W_{src} + 2W_{AB} + W_{CL,d} + 1}$
R_B^*	$\dfrac{V_{src}}{V_{src} + 2V_{AB} + V_{CL,d} + V_{SL}}$	$\dfrac{W_{src}}{W_{src} + 2W_{AB} + W_{CL,d} + 1}$
R_C^*	$\dfrac{V_{src}}{V_{src} + V_{AB} + V_{pg}}$	$\dfrac{W_{src}}{W_{src} + W_{AB} + W_{pg}}$
R_D^*	$\dfrac{V_{src} + V_{AB} + V_{in} + V_{out}}{V_{src} + 2V_{AB} + V_{in} + V_{out} + V_{SL}}$	$\dfrac{W_{src} + W_{AB} + W_{inout}}{W_{src} + 2W_{AB} + W_{inout} + 1}$
R_E^*	$\dfrac{V_{src}}{V_{src} + 2V_{AB} + V_{in} + V_{out} + V_{SL}}$	$\dfrac{W_{src}}{W_{src} + 2W_{AB} + W_{inout} + 1}$
R_F^*	$\dfrac{V_{src}}{V_{src} + V_{AB} + V_{in}}$	$\dfrac{W_{src}}{W_{src} + W_{AB} + U_{in}W_{inout}}$
R_G^*	$\dfrac{V_{src} + V_{AB} + V_{in}}{V_{src} + 2V_{AB} + V_{in} + V_{out} + V_{SL}}$	$\dfrac{W_{src} + W_{AB} + U_{in}W_{inout}}{W_{src} + 2W_{AB} + W_{inout} + 1}$
$R_{H,i}^*$	$\dfrac{V_{src} + V_{AB} + V_{in} + V_{out} + V_{cell,i}^*}{V_{src} + 2V_{AB} + V_{in} + V_{out} + V_{cell,i}^* + V_{SL}}$	$\dfrac{W_{src} + W_{AB} + W_{inout} + W_{cell,i}^*}{W_{src} + 2W_{AB} + W_{inout} + W_{cell,i}^* + 1}$
$R_{I,i}^*$	$\dfrac{V_{src}}{V_{src} + 2V_{AB} + V_{in} + V_{out} + V_{cell,i}^* + V_{SL}}$	$\dfrac{W_{src}}{W_{src} + 2W_{AB} + W_{inout} + W_{cell,i}^* + 1}$
$R_{J,i}^*$	$\dfrac{V_{src} + V_{AB} + V_{in} + V_{cell,i}^*}{V_{src} + 2V_{AB} + V_{in} + V_{out} + V_{cell,i}^* + V_{SL}}$	$\dfrac{W_{src} + W_{AB} + U_{in}W_{inout} + W_{cell,i}^*}{W_{src} + 2W_{AB} + W_{inout} + W_{cell,i}^* + 1}$
$R_{K,i}^*$	$\dfrac{V_{cell,i}^*}{V_{src} + 2V_{AB} + V_{in} + V_{out} + V_{cell,i}^* + V_{SL}}$	$\dfrac{W_{cell,i}^*}{W_{src} + 2W_{AB} + W_{inout} + W_{cell,i}^* + 1}$
$R_{L,i}^*$	$\dfrac{V_{cell,i}^*}{V_{AB} + V_{in} + V_{out} + V_{cell,i}^*}$	$\dfrac{W_{cell,i}^*}{W_{AB} + W_{inout} + W_{cell,i}^*}$

To perform the nonlinear least squares regression, all the measurements are separated into unique combinations of the calibration volume (if appropriate) and the measurement type; this pair defines the observation condition. The average and standard deviation of each group of measurements are stored (ignoring obvious outliers) as a single observation (for measurements that are independent of calibration volume, the volume is given as zero and all measurements of that type are combined together into a single observation). A nonlinear model function (called nonlinModel here) was written that accepts an array of the adjustable parameters, b, and x, a matrix of all the different combinations of observation conditions. nonlinModel provides a single output argument, y, which is a vector of the calculated values of R_x^* corresponding to each row of x using the parameters specified by b. The MATLAB function fitnlm, part of the optimization toolbox, is used to perform the non-linear least squares fitting of the data. fitnlm takes the compiled values of x (xSum) and the corresponding array of measurement averages (yM), and an initial guess of the parameters (b0). Additional arguments are provided to weight the regression by the inverse square of the measurement standard deviation (yS), and to exclude any set of observations that are found to be outliers (currently, measurements corresponding to R_F are excluded). The complete command is:

```
mdl = fitnlm(xSum, yM, @nlinModel, b0, 'Weights', 1./yS.^2, ...
    'CoefficientNames', b_names, 'Exclude', exclude);
```

The result of this function is mdl, an object that allows direct examination of a variety of statistics from the fit. The values of the fitted parameters and their standard errors are saved for use in later measurements, and their values as of writing are listed in Table A-7. This method was found to converge quickly (<0.03s), and was insensitive to the initial guesses provided. It is also

important to note that a relatively large number of degrees of freedom (12) are maintained with this method (relative to 8 fitting parameters), which helps prevent overfitting.

Table A-7. Current values of DEMS volume calibration parameters

Parameter	Initial Guess	Calibrated Value	Confidence Interval
V_{SL}	0.25	0.2709	$\pm1.91\times10^{-5}$
W_{src}	5	2.248	$\pm2.81\times10^{-4}$
W_{pg}	1	0.397	$\pm7.81\times10^{-5}$
W_{AB}	0	−0.00747	$\pm1.24\times10^{-4}$
W_{inout}	5	3.8229	$\pm3.64\times10^{-4}$
U_{in}	0.75	0.54419	$\pm2.70\times10^{-5}$
$W_{ex,1}$	5	2.1975	$\pm3.24\times10^{-4}$
$W_{ex,2}$	5	4.6873	$\pm6.14\times10^{-4}$

Cell Volume Measurements

Cell volume measurements are performed in a similar manner to the calibration measurements above. The particular measurements are analogs to Hi, Ji, and Ki above, as these directly involve expanding gas from the cell region into the surround tubing. Measurement Ii is not used, as this requires evacuation of the cell, and measurement Li was found to be superfluous. The exact procedure for evacuating and equilibrating was adjusted for these measurements, as the fine capillaries used to connect cells constricts the flow of gas and requires more equilibration time at each step.

Cell Volume Analysis

The technique for estimating the volume of a cell is also very similar to that of estimating the calibration parameters. The analysis process is simpler, as there are only three measurements and one volume to work with. Each measurement is collected and analyzed as before. nlinModel was rewritten to only perform calculations for the three measurements used in this analysis, and the calibration parameters are passed in as an extra argument. Only one adjustable parameter is optimized ($W_{cell,i}$), all other parameters are used as specified from the calibration process. Usually, only 1-3 repetitions of each measurement is made for measuring cell volume, which is too small to accurately estimate the measurement variance for weighting.[190] Instead, the weight factor is calculated to be $w = 1 - yM$, where yM is the average of the readings for that observation. This is more robust to variation, and accurately reflects that lower values of yM indicate a larger pressure drop, which can be measured more accurately. In general, the DEMS cell design (described in Chapter 3), results in a cell volume of ~2.70 mL, while the older EEL air cell design generally has a volume near ~7.8 ml.

A.3 Analysis of Pressure Tracking Experiments

As described in Chapter 3, pressure tracking experiments can be used on the DEMS to measure the consumption or production of gas solely through measuring the pressure and temperature of the cells. This analysis allows for data to be collected with high frequency (up to ~1 sample/sec) and without regard for the volatility of the solvent or composition of cell gas. As a result, pressure tracking does not provide any information about changes in the composition of the gas within the cell during the experiment; one must be careful to verify, as much as possible, the assumptions of what gases are consumed or produced during pressure tracking experiments.

In order to collect sufficient information for a pressure tracking experiment, pressure, temperature, and volume data must be collected in order to estimate the total moles of gas involved. The ideal gas law is then used to estimate the total moles of gas in the cell at each point in time, which can then be analyzed to estimate rates of change and other properties. The process for measuring the volume of the cell was noted in Section A.2 above.

Collection of Temperature and Pressure Data

During a pressure tracking experiment, the cell remains isolated throughout the experiment. The pressure from the appropriate pressure gauge is recorded continuously, at a rate much higher than the expected rate of the final analysis (the user can smooth or filter a large data set into a smaller one during the analysis phase). It should be noted that the DEMS software records the average of all readings received from the pressure gauge for each time point. For example, each of the pressure gauges generates a new pressure reading 5 times per second. If the user specifies a sample rate of 1 sample/s (which is commonly used throughout this document), then each reading consists of the average of 5 samples. Temperature should be recorded both at the gauge and at the cell, especially when the cell is being tested at non-ambient temperatures, as the temperature immediately around the cell is often somewhat different than the temperature at the gauge. The recommended method to record the pressure and temperatures during a pressure tracking experiment is to start a single logger in the DEMS software which records all three values, ensuring that all readings are taken at the same frequency and time.

Estimation of Total Moles of Gas in Cell

The ideal gas law is used to estimate the total moles of gas in the cell. This was chosen over other equations-of-state for simplicity, and because most other equations of state require knowledge about the composition of the gas being measured. In addition, it is assumed that the

gauge temperature represents the temperature of the cell excess volume, while the cell temperature represents the measured volume of the cell itself (including volume within the VCO fittings used to connect the cell). Pressure is assumed to be uniform throughout the cell (no adjustments for variations in elevation or possible pressure gradients are made). The number of moles for the gauge and the cell are calculated separately, using the same pressure in both cases, and then summed together to produce the total number of moles in the cell at each time point:

$$n(t) = \frac{P(t)V_c}{RT_c(t)} + \frac{P(t)V_g}{RT_g(t)} \tag{A-3}$$

Where n total moles of gas in the cell and excess volume, t is time, P is the pressure read by the gauge, V_c is the measured cell volume, R is the ideal gas constant, T_c is the temperature measured at the cell, V_g is the excess volume for the given cell, and T_g is the temperature measured at the gauge. In general, only relatively slow variations in temperature (~5 minutes or longer) are observed in the pressure log, so smoothing (*e.g.* moving average) can be applied to the temperature data prior to use in equation (A-3) if desired. In addition, there is usually a delay between changes in the temperature record and the pressure record. This delay is generally ignored, as it is sensitive to the exact placement of the thermistor relative to the cell and gauge. Future work may allow an appropriate delay for both the gauge and cell temperature to be used; the current work shows that large swings in temperature (>0.3 °C) can result in anomalies in the total moles of gas. When possible, these calculations are performed in the DEMS software (and saved alongside the pressure and temperature data), but all calculations shown in this work rely on calculations performed after-the-fact in MATLAB.

Leak Correction

Although leaks are undesired, and a properly prepared DEMS experiment will not show a measureable leak, leaks are inevitable when several critical seals must be made for each experiment. In addition, because these leaks are usually quite slow, they can be difficult to detect until long after the start of an experiment; effects such as electrolyte evaporation and gas dissolution can be significant for as long as 24 hours after connection, and temperature variations can easily hide a slight leak during a cursory examination of the pressure log. It is therefore desirable to be able to correct for leaks when they are observed, although it is important to keep in mind the potential for contamination of results due to a leak, and make every effort to prevent them in the first place.

As the pressure within the cell during a DEMS measurement may vary considerably relative to atmosphere, especially in the case of deeply discharged cells, a correction must be made to account for the change in driving force of a leak. A cell at 29 psia (0.97 atm gauge pressure) would be expected to lose pressure significantly faster than a cell at 15 psia (0.02 atm gauge), and a cell at 10 psia (−0.31 atm gauge) would be expected to *gain* pressure due to a leak. Therefore, the leak rate correction used here assumes that the rate of loss of gas is proportional to the pressure in a cell:

$$\frac{dn}{dt}_{leak} = C_{leak} \cdot (P - P_{atm}) \tag{A-4}$$

Where $\frac{dn}{dt}_{leak}$ is the rate of change in moles of gas in the cell due to a leak, C_{leak} is the leak rate constant (in units of mol/s/Pa), P is the absolute cell pressure, and P_{atm} is atmospheric pressure (assumed to be a constant of 101325 Pa). C_{leak} is generally expected to be negative. This leak rate

than can be applied to the total moles of gas calculated above to get an effective total moles of gas in the cell (n_{eff}).

$$\frac{dn_{eff}}{dt} = \frac{dn}{dt} - \frac{dn}{dt}_{leak}$$ (A-5)

$$n_{eff}(t) = n_{eff}(0) + (n(t) - n(0)) - C_{leak} \int_0^t (P(t') - P_{atm})dt'$$ (A-6)

Since $P(t)$ is not analytic, the integral must be calculated numerically. $n_{eff}(0)$ is arbitrary in equation A-6, and is usually taken to be either $n(0)$ or 0.

Calculation of Gas Production Rate

The rate of gas consumption or production can be calculated by taking the derivative of the calculated total moles of gas with respect to time. Simple derivatives of real (noisy) data are usually dominated by the variation between consecutive readings, and must be smoothed in order to bring out the overall signal. The parameters used for smoothing should be chosen to balance between minimizing noise (using more smoothing) and observing changes on shorter timescales (using less smoothing), and the exact choice of parameters may vary from experiment to experiment. In this work, a Savitzky-Golay (S-G) filter was generally used to perform the smoothing and differentiation simultaneously.[179] An S-G filter performs a least-squares fitting on the group of points surrounding each point in a data set. The filter width (i.e. the number of points used in each fitting) and the order of the fitting polynomial can be adjusted, with larger filter widths resulting in greater smoothing, and higher polynomial orders resulting in better sensitivity to high-frequency variation. Because S-G filters rely on fitting a polynomial to each point, derivatives and antiderivatives can be easily calculated while smoothing, simply by taking the derivative or integral of the fitted polynomial function.

196

Although S-G filtering can output a derivative of the original signal, that derivative must then be scaled by the sample rate. The effective gas production rate can be calculated using the following formula.

$$\frac{dn_{eff}}{dt} = -\frac{\text{savitzkyGolayFilt}(n_{eff}, o, 1, w)}{dt} \tag{A-7}$$

Where savitzkyGolayFilt is a MATLAB function for performing S-G filtering with differentiation available on MATLAB Central,[191] o is the order of the fitting polynomial, w is the filter width, and dt is the time between each sample (samples must be regularly spaced).

To reduce the computational requirements, the number of points being fit in the S-G filter can be reduced before filtering. In most of this work, the total moles of gas was usually resampled to a 60-second interval (using a time-weighted average of points within each 60-second interval) before applying the S-G smoothing and derivative filter. Table A-8 lists the parameters used for performing all S-G differentiation, unless otherwise specified.

Table A-8. Savitzky-Golay filter parameters for pressure tracking analysis.

Parameter	Unit	Value
Sample Interval	s	60
Polynomial Order	a.u.	2
Differentiation Order	a.u.	1
Filter Width	a.u.	31
Weighting Vector	a.u.	n/a

A.4 Analysis of Mass Spectrometer DEMS Experiments

Measurement Procedure

Several pieces of information are collected in a single DEMS measurement, which are all collected and analyzed through a single automated procedure in the DEMS software code. MS readings of the base vacuum are taken to determine a background for subsequent readings and ensure the vacuum remains in good condition. MS readings are also taken on the fill gas, which is used to replace the gas removed from the cell. This allows automatic calculation of gas production rates without prior knowledge of the gas being used to fill the cell. MS readings are also taken of the cell gas composition, which are used to determine the production of gas in the cell. In addition to these MS readings, pressure and temperature readings are taken before the cell isolation valve is opened and after it is closed again, to estimate a total production of gas via change in pressure. Finally, the time that the cell valve was opened is recorded and used to determine the time elapsed between readings.
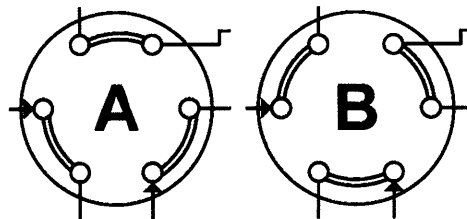
Figure A-4. Connections between ports for the 6-port, 2-way valve positions "A" and "B".

The exact schedule for taking a DEMS measurement proceeds as follows, using the valve names as used in Figure 3-1:

1. All of the tubes on the DEMS panel are evacuated for one minute, and the base vacuum reading is recorded for the last 10 seconds.

2. The purge valve is closed and the tubes on the DEMS panel are filled with fill gas (usually argon).

3. The vacuum pumpout valve is closed, isolating the rough vacuum chamber.

4. The 6-port valve is switched to position "B", which doses gas from the sample loop into the rough vacuum chamber.

5. The outlet shutoff valve is closed, fully isolating the rough vacuum chamber. The chamber is held in this condition for 15 seconds, with the last 10 of which are used to record the fill gas composition. The 6-port valve is returned to position "A".

6. The vacuum pumpout valve, outlet shutoff, and purge shutoff valves are all opened, and the exhaust tubes on the DEMS panel are re-evacuated for 50 seconds. The cell pressure before opening is recorded for the last 10 seconds of this period.

7. The purge valve is shut and the inlet valve is opened, immediately followed by opening the appropriate cell valve for 15 seconds. This allows gas from the cell to fill the exhaust lines and gas from the inlet to fully re-pressurize it.

8. Steps 3 and 4 are repeated.

9. The outlet shutoff valve is closed, fully isolating the rough vacuum chamber with cell gas inside. This condition is held for 40 seconds. During the first 10 seconds the cell pressure after opening is recorded, and the last 30 seconds are used to collect the cell gas composition. The 6-port valve is returned to position "A".

10. The vacuum pumpout valve, outlet shutoff, and purge valves are opened (evacuating the exhaust lines), and the sequence terminates.

This procedure takes 3:39 to execute in total, which prevents DEMS measurements from being taken any faster than this. In the event that faster measurements were necessary, an alternate procedure would need to be developed that omitted the measurement of the fill gas.
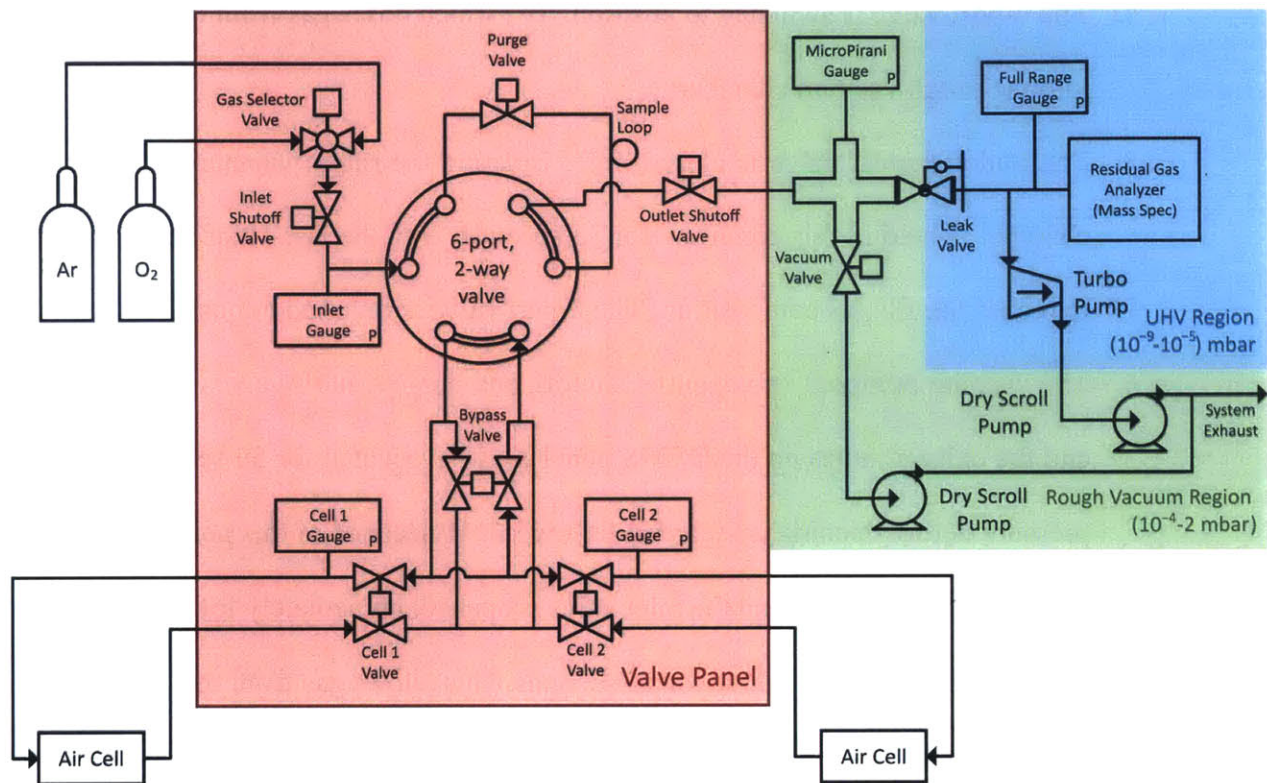
Figure A-5. DEMS system valve layout (identical to Figure 3-1).

DEMS calibration is performed using a similar measurement, which is not hard coded into the LabVIEW software. This measurement essentially only records the base vacuum and fill gas composition, where the fill gas used is the calibration gas. Logging capability can be used to record the MS data through the calibration process, which can then be analyzed manually as discussed below.

Estimation of Calibration Parameters

Gas calibration is performed using the concepts defined in Chapter 2 of the SRS RGA manual, which is available in the lab and online from the SRS website.[192] In it, they discuss the analysis principles for relating the raw readings from the MS with actual concentrations of one or more gases. These concepts are used for the analysis below. The following terms are defined for all of the equations below:

Table A-9. Terminology used for MS calibration.

Term	Definition
g	Indicates the gases measured. When used in a subscript, indicates the variable applies to a single gas
M	Integer representing the mass (m/z) measured
H_M	Total peak height measured at mass M
h_{Mg}	Peak height contribution at mass M of gas g
α_{Mg}	Fragmentation factor of gas g at mass M. Fragmentation factor is defined as the ratio of the signal at a particular mass relative to the highest peak of a particular gas
S_g	Partial pressure sensitivity of gas g at the highest peak of that gas. This has units of amps/Torr
P_g	Partial pressure of gas g at the RGA.

Several assumptions are required for analysis of MS measurements, and it is recommended to confirm that these assumptions are true if possible:

1. Gas contributions are additive (*i.e.* $H_M = \sum_g h_{Mg}$).

2. Gas sensitivity is linear (*i.e.* $h_{Mg} = \alpha_{Mg} S_g P_g$ for all relevant pressures, and S_g is not dependent on P_g of any gas).

The recommended procedure to determine the partial pressure sensitivity of a gas is to introduce that gas in a known concentration to the vacuum chamber, and compare the rise in pressure (of that gas) to the rise in signal of the primary peak:

$$S_g = \frac{\Delta H_M}{\Delta P_g} \tag{A-8}$$

For most accurate results, this should be performed in the conditions most closely resembling the experimental conditions (*e.g.* diluted in high concentrations of argon). In general, the partial pressure is assumed to be zero initially and rises to the known level based on the amount of gas added to the system, and ΔH_M is determined by subtracting the background signal from the measured peak height.

In the DEMS system developed here, the partial pressure of gas in the RGA is difficult to determine directly; although pressure gauges are available for both the UHV and rough vacuum regions, these gauges have limited accuracy and respond differently to different gases. Therefore, we use the atmospheric pressure transducers (specifically, the inlet pressure gauge) to calibrate the gas pressure, since they are both very precise and insensitive to gas composition. Using this transducer requires that exactly the same volume of gas be dosed into the vacuum chamber for each calibration reading, which the DEMS procedure described above achieves. This can be used to develop an "atmospheric partial pressure sensitivity" which relates the partial pressure of the gas of interest at atmospheric pressures to the MS response. Finally, this can be converted back into a vacuum partial pressure sensitivity by using comparing the atmospheric pressure and recorded UHV pressure for a single gas (here, N_2), and assuming that the UHV pressure gauge is accurate for that gas. Which gas is used is immaterial, as the same adjustment factor will be used for all gases.

For the data presented in this thesis, the following calibration parameters were used. Calibrations were performed using 99.999% Ar, 99.999% O_2, 99.99% CO_2, and industrial grade N_2. H_2O and CO were assumed to have the factory partial pressure sensitivity, and the H_2 sensitivity was adjusted based on the results of several experiments where significant H_2 was detected. I strongly suggest that a calibration using gases diluted in Ar to be used, and to check the linearity of responses with oxygen diluted in Ar at several concentrations.

Table A-10. Sensitivity factors used for MS analysis in this thesis.

Gas	Primary Peak (m/z)	Atmospheric Partial Pressure Sensitivity (A/Torr)	Partial Pressure Sensitivity (A/Torr)
Ar	40	7.58×10^{-13}	4.10×10^{-4}
O_2	32	4.15×10^{-13}	2.24×10^{-4}
CO_2	44	5.75×10^{-13}	3.11×10^{-4}
CO	28	3.44×10^{-13}	1.86×10^{-4}
N_2	28	5.86×10^{-13}	3.16×10^{-4}
H_2	2	2.75×10^{-12}	1.49×10^{-3}
H_2O	18	3.44×10^{-13}	1.86×10^{-4}

In addition to the sensitivity factor, which defines the height of the highest peak, many gases have a series of secondary peaks defined by a series of fragmentation factors. These factors indicate the ratio a peak has at a given value of M relative to the primary peak listed above. By definition, the fragmentation factor of the primary peak is 1 for any gas, and all other masses should have fragmentation factors between 0 and 1.

For the data presented in this thesis, the fragmentation factors used are listed in Table A-11. Fragmentation factors were determined for Ar, O_2, CO_2, and N_2 by examining the relative peak heights of each gas when dosed in a pure form. Note that this calibration requires the use of pure gas, or small secondary peaks of the carrier gas will interfere. Fragmentation factors for H_2O, CO, and H_2O were extracted from the library of fragmentation factors included in the SRS RGA software. CO is too toxic to be calibrated in pure form using the current system and pure H_2O is obviously not gaseous at room temperature and pressure, so I do not recommend that fragmentation factors be measured for any additional gases; careful re-measurement of the existing gases may be warranted, especially where overlapping peaks are frequently detected.

Table A-11. Fragmentation factors of gases detected in this thesis. Fragments for peaks generated by multiple gases are highlighted in matching colors.

Gas	Primary Peak (m/z)	Fragment #1 (m/z)	Fragment #2 (m/z)	Fragment #3 (m/z)	Fragment #4 (m/z)	Fragment #5 (m/z)
Ar	40	9.81×10^{-2} (20)	3.31×10^{-3} (36)	6.45×10^{-4} (38)	3.18×10^{-4} (18)	N/A
O_2	32	7.17×10^{-2} (16)	3.46×10^{-3} (34)	7.10×10^{-4} (33)	N/A	N/A
CO_2	44	7.21×10^{-2} (28)	7.92×10^{-2} (16)	3.94×10^{-2} (12)	1.03×10^{-2} (45)	3.43×10^{-3} (46)
CO	28	5×10^{-2} (12)	2×10^{-2} (16)	1×10^{-2} (29)	1×10^{-2} (14)	2×10^{-3} (30)
N_2	28	5.30×10^{-2} (14)	6.18×10^{-3} (29)	N/A	N/A	N/A
H_2	2	5×10^{-2} (1)	N/A	N/A	N/A	N/A

Gas	Primary Peak (m/z)	Fragment #1 (m/z)	Fragment #2 (m/z)	Fragment #3 (m/z)	Fragment #4 (m/z)	Fragment #5 (m/z)
H_2O	18	2.3×10^{-1} (17)	1.1×10^{-1} (16)	3×10^{-3} (20)	1×10^{-3} (19)	N/A

Note that there are a large number of overlapping peaks in Table A-11; care must be taken in selecting which masses are scanned when wishing to distinguish any gas whose primary peak coincides with any other gas fragment. Particularly difficult to separate accurately are water from argon and carbon monoxide from nitrogen. I suggest using an alternate carrier gas when desiring to accurately detect water (such as helium), and can only suggest not attempting to distinguish CO from N2 unless CO is present in very large quantities and CO_2 is not. As N2 is only generally a factor when leaks are present, this further motivates the elimination of leaks.

DEMS Measurement Analysis

Analyzing a series of DEMS measurements proceeds in 3 stages: gas readings are calibrated, the moles of gas in the cell is estimated, and then a gas production rate is calculated.

Calibration of DEMS Measurements

The MS data collected and recorded by the DEMS LabVIEW software is an uncalibrated pressure reading for each m/z value collected. This is the standard format that is used by the SRS RGA software and was not modified in LabVIEW. The raw current is converted into pressure units using the pre-programmed partial pressure sensitivity factor (this value is 1.86×10^{-4} A/Torr at the time of writing). **Note: the DEMS saves data in units of mbar; an oversight in the code does not record the units used.** The raw pressure readings for each m/z value should be converted into a raw current by dividing by the programmed partial pressure sensitivity factor ($1.86 \times 10-4$ A/Torr, or

1.395×10^{-4} A/mbar). After converting to pressure, the data for the base vacuum should be subtracted from both the fill gas and cell gas readings, since this reading represents the signal from gases already present in the chamber. These converted and subtracted values represent H_M for each of the masses record.

The conversion from MS readings to gas pressures can be viewed as a linear of system equations based, which can be defined with a matrix equation:

$$h_{Mg} = \alpha_{Mg} S_g P_g \quad \text{for all } M = 1..n, g = 1..k \tag{A-9}$$

$$H = AP \tag{A-10}$$

$$H = \begin{bmatrix} H_1 \\ \vdots \\ H_n \end{bmatrix} \tag{A-11}$$

$$P = \begin{bmatrix} P_1 \\ \vdots \\ P_k \end{bmatrix} \tag{A-12}$$

$$A = \begin{bmatrix} S_1\alpha_{11} & \cdots & S_k\alpha_{1k} \\ \vdots & \ddots & \vdots \\ S_1\alpha_{n1} & \cdots & S_k\alpha_{nk} \end{bmatrix} \tag{A-13}$$

This can be solved using matrix manipulation, and both MATLAB and LabVIEW offer utilities to solve such equations in a single command. For MATLAB, this command would be P = H/A; resulting in a vector P representing the solution to this system of equations. If more masses than gasses are used, the solution will be the least squares best fit to the data. This process is then repeated for each measurement taken, and for both the fill gas and cell gas readings. Doing so results in a vector of the partial pressure of each gas in the cell and in the fill gas for each reading. Finally, each of these partial pressures is converted into a gas fraction by the definition:

$$y_i = \frac{P_i}{\sum_{g=1}^{k} P_g} \quad \text{for all } i = 1..k \tag{A-14}$$

206

Gas fractions are preferred because they remove the need to have an absolute relationship between the gas partial pressure at atmospheric conditions and the MS reading. However, it implicitly assumes that the MS is detecting all gases present; the generation of significant quantities of gases not detected by the MS would cause severe distortions in the data. In practice, since argon usually makes up >99% of the cell gas, this is a safe assumption; undetected gases will still never affect the readings of other gases by more than a percentage point.

The individual gas fractions are formed into matrixes denoted as Y_{cell} and Y_{fill}, where each row represents a particular reading and each column a particular gas. Per the discussion in Chapter 3, the reading from the MS represents the composition of the cell at the time of the *previous* reading, because gas is held in the dead volume downstream from the cell. The Y_{cell} matrix is accordingly shifted up by one, and the first reading is discarded.

Estimation of Moles of Gas in the Cell

Temperature, pressure, and volume data is needed to convert the gas fractions into moles of gas. The cell volume is determined using the method discussed in Section 0, and is assumed to be constant throughout an entire test. The total moles of gas in the cell are determined before and after the gas was sampled using the ideal gas law. As with pressure tracking data, independent measures of cell and gauge temperature are used:

$$n_{before} = \frac{P_{before}V_c}{RT_{c,before}} + \frac{P_{before}V_g}{RT_{g,before}} \qquad (A\text{-}15)$$

$$n_{after} = \frac{P_{after}V_c}{RT_{c,aafter}} + \frac{P_{after}V_g}{RT_{g,after}} \qquad (A\text{-}16)$$

Where P_{before} and P_{after} represent the pressure before and after the measurement, $T_{g,before}$ and $T_{g,after}$ represent the temperature at the pressure gauge before and after the measurement, $T_{c,before}$

and $T_{c,after}$ represent the temperature at the cell before and after the measurement, and V_c and V_g represent the volumes of the cell and the tubing outside of the cell, respectively.

These values represent the total number of moles in the cell and gauge before and after each measurement was taken. This is sufficient for pressure tracking data (as the pressure is assumed to be constant throughout the cell), but the distribution of gas within this region is known to be non-uniform. We divide up the cell volume into "active" and "inactive" regions; the active region is where gas is being generated and accumulating, and the inactive region is anywhere where the gas composition does not change between measurements. The inactive volume is determined empirically, but is held constant when the same cell design is used on the same DEMS channel; almost all DEMS experiments at the time of writing were performed on the same channel with the same cell, so this value is effectively constant. For all the data published in this thesis, the active volume is assumed to be 1.445 ml less than the cell volume, making the inactive be the gauge volume (noted as $V_{ex,1}$ or $V_{ex,2}$ in Section A.2) plus 1.445 ml. It should be noted that the composition of the inactive volume does not matter; the volume upstream from the cell is generally assumed to have the fill gas composition, and the gas downstream is assumed to be the composition at the time of the last measurement, but the composition of the inactive volume as a whole is never needed. We then define the active fraction to be the ratio of the active volume to the total volume:

$$f_{act} = \frac{V_{act}}{V_{total}} \tag{A-17}$$

We can then estimate the number of moles in the active and inactive regions of the cell. By definition, we assume that the inactive moles in the cell do not change between measurements; this means that any change that occurs between measurements is due to changes in the number of moles in the active region. We first calculate the number of active and inactive moles after a measurement:

208

$$n_{act,after} = n_{after} f_{act} \qquad \text{(A-18)}$$

$$n_{inact,after} = n_{after} \cdot (1 - f_{act}) \qquad \text{(A-19)}$$

We then assume that the number of moles in the inactive region before the next measurement is constant, and use this to derive the number of active moles before the next measurement as well. We use parenthesis to indicate the reading number, such that $n_{inact,after}(i-1)$ indicates the number of moles in the inactive region after the $i-1$ measurement:

$$n_{inact,before}(i) = n_{inact,after}(i-1) \qquad \text{(A-20)}$$

$$n_{act,before}(i) = n_{before}(i) - n_{inact,before}(i) \qquad \text{(A-21)}$$

The active volume and total moles are then used to estimate a parameter defined as the fill fraction (f_{fill}), which represents the number of moles of fill gas in the active volume after a measurement divided by the total number of moles in the active volume at that time:

$$f_{fill} \equiv \frac{n_{act,fill}}{n_{act,after}} \approx \frac{n_{in}}{n_{act,after}} \qquad \text{(A-22)}$$

Where $n_{act,after}$ is the total moles in the active volume after a measurement, and $n_{act,fill}$ is the moles of fill gas that entered the active volume after the measurement. $n_{act,fill}$ can be approximated by simply assuming that all the moles of gas added to the cell are added to the active region. (It should be noted that this is an approximation: if the number of moles in the inactive region were to change significantly between measurements this assumption would be invalid.) The total number of moles added is calculated by first determining the total number of moles that leave the cell to fill the downstream tubing, and then account for the change in pressure due to the act of taking a measurement:

$$n_{out} = \frac{P_{after} V_{exhaust}}{T_{g,after} R} \qquad \text{(A-23)}$$

$$V_{exhaust} \equiv V_{SL} + V_{out} + V_{AB} \qquad \text{(A-24)}$$

The total moles of gas in the cell change before and after a measurement (because the pressure is "reset" to the pressure of the incoming gas), so the number of moles of gas entering the system must account for this change:

$$\Delta n = n_{after} - n_{before} \qquad (A-25)$$

$$n_{in} = n_{out} + \Delta n \qquad (A-26)$$

With this value, we can then estimate f_{fill} using Equation A-22, and use that to estimate the composition of the gas in the active region after the measurement was taken.

$$y_{g,cell,after} = \left(1 - f_{fill}\right) \cdot y_{g,cell} + f_{fill} \cdot y_{g,fill} \quad \text{for each } g = 1..k \qquad (A-27)$$

Equation A-27 assumes that $f_{fill} < 1$; in the event that f_{fill} is near to or greater than 1, this implies that more gas is removed from the cell than is contained in the active region. In this instance, the composition of the cell after measurement is poorly defined, and we must further consider the impact of the fill gas that is sweeping through the cell and reaching the MS.

Knowing the composition and total number of moles of the gas in the active region before and after the measurement, we can finally estimate the number of moles of each gas before and after each measurement:

$$n_{g,before} = n_{act,before} \cdot y_{g,cell} \qquad (A-28)$$

$$n_{g,after} = n_{act,after} \cdot y_{g,cell,after} \qquad (A-29)$$

Note: $n_{g,before}$ and $n_{g,after}$ do not represent the cumulative production of gas, and are not shown in the plots in the main chapters of this thesis. They simply indicate the total number of moles of each detected gas within the active region of the cell at particular points in time.

Calculation of Gas Production Rate

Finally, we can use the values of $n_{g,before}$ and $n_{g,after}$ to calculate the rate of gas production between readings. Here, we show the process of calculating the rate of gas production at the time

of reading i. As before, parenthesis are used to denote the reading number. The number of moles of gas g produced between two readings is:

$$\Delta n_g(i) = n_{g,before}(i) - n_{g,after}(i-1) \qquad \text{(A-30)}$$

The time elapsed can then be used to get a rate:

$$\Delta t(i) = t(i) - t(i-1) \qquad \text{(A-31)}$$

$$\frac{dn_g}{dt}(i) = \frac{\Delta n_g(i)}{\Delta t(i)} \qquad \text{(A-32)}$$

The same formulas can be used to determine the total rate of gas production (based only on the pressure data):

$$\Delta n(i) = n_{before}(i) - n_{after}(i-1) \qquad \text{(A-33)}$$

$$\frac{dn}{dt}(i) = \frac{\Delta n(i)}{\Delta t(i)} \qquad \text{(A-34)}$$

It is important to note that $\frac{dn}{dt}$ does not depend on f_{fill} and V_{act}, both of which are empirically estimated. It only depends on the same assumptions used in pressure tracking, and so is a reliable way to confirm the accuracy of the MS data; properly calibrated MS data in a leak-free cell should exactly track the total production of gas using $\frac{dn}{dt}$. Once $\frac{dn}{dt}$ and $\frac{dn_g}{dt}$ have been calculated, it is straightforward to integrate them to determine the cumulative production of each gas individually and the total gas production.

Appendix B

DEMS LabVIEW Software Summary

This appendix is intended to serve as a record of the structure of the LabVIEW software written to control the DEMS system developed in Chapter 3. An update to date version of this documentation should be available at https://github.mit.edu/EEL/EEL-DEMS. (This page is private and will require permission from the current DEMS maintainer to access).

B.1 Installation

The following software must be installed to load the LabVIEW project and make changes:

- LabVIEW 2014 (Professional preferred, some features cannot be edited with the Student version)
- ULx from MCC (part of the MCCDAQ installer)
- VI Package Manager (Free Edition, usually installed with LabVIEW)
- The following VI Packages:
  - NI Modbus Library
  - NI GXML Library
  - OpenG Libraries:
    - Application Control
    - Array
    - Error
    - File
    - LabVIEW Data
    - Numeric
    - String

All of the dependencies (except LabVIEW and VI Package Manager) can be downloaded from the dependencies tab on the GitHub project page, which links to the Dropbox shared folder. This folder contains the following sub-folders:

- LabVIEW Dependencies (required to load, run, and edit the LabVIEW project)
- Device Drivers (required to interface with physical DEMS hardware)
- Device Software (vendor provided software for communicating with DEMS components without using LabVIEW)
- Information (additional documents used for developing the DEMS).

LabVIEW 2014 Professional is preferred, but the project should mostly load correctly in the student version. Ask a Post-doc in lab (or Yang) to provide you with the professional key for LabVIEW.

B.2 About the Project

This repository keeps all the code necessary to operate the differential electrochemical mass spectrometer (DEMS) in the EEL at MIT. The majority of code is written in G, and should be viewed and edited in LabVIEW. The project can be loaded by opening DEMS.lvproj from LabVIEW 2014.

Files should only be moved or reorganized within the LabVIEW project management window. Moving files or folders outside of LabVIEW will likely result in a broken project.

214

B.3 Project Organization

The LabVIEW project is divided up into a number of libraries and virtual folders. Each is briefly described below.

DEMS Control Panel.lvlib

This library defines the main control panel window and the sub-vis used to run it. The vi **DEMS Control Panel.vi** should be used to operate the DEMS. When started, this VI initializes and continuously checks for updates from all devices on the DEMS. The valve control panel, the configuration page, and all instances of loggers are opened through this VI.

This library can and does reference all other libraries contained within the project, directly or indirectly.

Valve Control Panel.lvlib

This library defines the control panel for executing operations on the DEMS. It is the primary interface for changing the position of any valve and is used for executing experimental schedules. Volume, calibration, and DEMS measurements are all defined and controlled in this library.

Valve Schedule Runner.vi defines the primary window for valve measurements, and contains the logic for executing a given schedule. It also allows access to viewing and editing data saved about particular cells. It can be run independently for testing when the "Testing" button is activated (located above the default screen position).

The **Popups** folder stores VIs that show information about saved data.

The **Schedule VIs** folder contains all VIs used to define, edit, save, load, and execute Schedules (with the exception of Valve Schedule Runner.vi itself). Schedule files are identified by the .sch extension, and are XML-based text files.

The **Sequence VIs** folder contains all VIs used to define, edit, save, load, and execute Sequences, which represent individual steps in a schedule. Sequence files are identified by the .seq extension, and are XML-based text files.

This library should not reference any members of DEMS Control Panel.lvlib or Logger.lvlib, but can and does refer to all other libraries. There may currently be references to typedefs defined in DEMS Control Panel.lvlib, but these are incorrectly included if present.

Logger.lvlib

This library defines the interface for collecting and saving data from the various sources of data from the DEMS. It does not control the positions of valves or otherwise alter the overall state of the DEMS.

Main - Selector.vi defines the UI for the logger window, but is not designed to run independently of DEMS Control Panel.vi.

The **Actors** folder contains the long running subVIs that perform the primary actions of the logger. These VIs are reentrant, and each logger has a unique instance of all of them to operate.

The **VI Management** folder contains VIs that manage the Actor VIs, including loading, starting, stopping, and closing each actor instance.

The **SubVIs** folder contains subVIs that operate quickly to execute individual actions needed for running the logger. Most should not need to be reentrant, but this is not guaranteed.

UI Controls and **Typedefs** include the controls used by the logger.

This library should not reference any members of DEMS Control Panel.lvlib or Valve control panel.lvlib, but can and does refer to all other libraries. There may currently be references to typedefs defined in DEMS Control Panel.lvlib, but these are incorrectly included if present.

DEMS Calculations.lvlib

This library defines the VIs that perform various calculations on DEMS data. None of the VIs within this library are intended to be user visible, and each may be called directly by members of other libraries.

This library should only reference DEMS General Utilities.lvlib and no other libraries, but this may not be strictly obeyed at this time.

Data Saving.lvlib

This library manages all actions related to reading or writing data files during DEMS tests. This includes saving Logger data and DEMS/Volume/Calibration measurements from the Valve Control Panel.

The vast majority of instances should call **Load Cell Data.vi** and **Save Cell Data.vi**, but direct calls of the subVIs in the various folders are currently permitted.

This library should only reference DEMS General Utilities.lvlib and DEMS Calculations.lvlib, but this may not be strictly obeyed at this time.

DEMS General Utilities.lvlib

This library provides a collection of utility VIs that are used throughout the project and may be called by any other VI.

This library should not reference any other library in this project.

216

Drivers Folder

The drivers folder contains all code needed to directly communicate with any of the hardware in the DEMS. These are described below:

HW Configuration.lvlib

This library manages the editing, loading, and saving of hardware configuration data, as well as managing the status of/reading data from the various devices connected to the DEMS.

This library calls DEMS Object.lvclass and DEMS General Utilities.lvlib, but should not depend on any other library.

DEMS Object.lvclass

This class defines a generic "DEMS Object" that provides a standard interface for managing individual devices connected to the DEMS. DEMS Objects should not generally be initialized directly (one of the subclasses described below should be used instead). In addition to implementing the inherited VIs from DEMS Object.lvclass, each subclass includes all the VIs necessary to perform all communications with a particular device. This class, and all subclasses, should only refer to DEMS General Utilities.lvlib, but this is not guaranteed to be strictly observed at this time.

Agilent TPS Object.lvclass

This is a subclass of DEMS Object.lvclass that manages all communications with the Agilent turbopump system used by the DEMS. Due to issues with stalled communications between LabVIEW and the turbopump, this device is not currently active in normal DEMS operation.

MCC-Temp Object.lvclass

This is a subclass of DEMS Object.lvclass that manages all communications with the temperature reader. A single instance of this object is used to read from all connected temperature probes.

MKS 900-USB Object.lvclass

This is a subclass of DEMS Object.lvclass that manages communications with the MKS Micro-Pirani vacuum pressure gauge.

Numatics G3 Object.lvclass

This is a subclass of DEMS Object.lvclass that manages communications with the Numatics G3 pneumatic valve control panel. Additional methods are implemented to allow the Valve Control Panel direct control over the valves, in addition to the standard methods required by DEMS Object.lvclass.

Omega PX409-USBH Object.lvclass

This is a subclass of DEMS Object.lvclass that manages all communications with the Omega pressure gauges. Each pressure gauge should be read to from separate instances of this object.

SRS RGA200 Object.lvclass

This is a subclass of DEMS Object.lvclass that manages all communications with the SRS mass spectrometer. A single instance of this object is used to read all masses from the mass spec. This subclass largely relies on the LabVIEW code provided by SRS for controlling the mass spec, and an additional collection of VIs to implement the DEMs Object interface.

Configuration Files

This folder is not a part of the LabVIEW project, but contains the files used to configure and control the DEMS. The contents of this file should be edited carefully, as code may rely on hard-coded names of files and make assumptions about how those files are configured.

When compiled as a stand-alone application, the contents of this folder are copied to C:\ProgramData\Electrochemical Energy Lab\DEMS Control Panel and when run, the stand-alone application will reference the ProgramData folder rather than the version controlled Configuration Files folder.

Currently, this folder contains a large number of unused files (old .sch files, for example), but care and testing should be used before deleting them.

Appendix C

DEMS Cell Design Drawings

The following pages show to-scale drawings used to manufacture both the DEMS cell used in preparing this thesis (DEMS Cell v2) and the next generation of DEMS cells produced before I left the lab. No figure numbers are given to maximize space for drawings on each page. DEMS Cell v2 drawings are shown first, and the version number is indicated in the title block of each drawing.

DETAIL C
SCALE 3 : 1

Ø3.18 ⍌ 21.75
Ø1.59 ⍌ 3.30
Ø1.59 ⍌ 4.30
1.00
Ø3.18 ⍌ 28.00

SECTION A-A
SCALE 1 : 1

BOTTOM VIEW
SCALE 1 : 1

Ø56.00
Ø42.00
Ø6.50± .05
THRU
Ø14.50
Ø10.50

SECTION C-C
SCALE 1 : 1

9.00
Ø3.00 ⍌ 14.00
4-40 UNC - 2B ⍌ 10.00
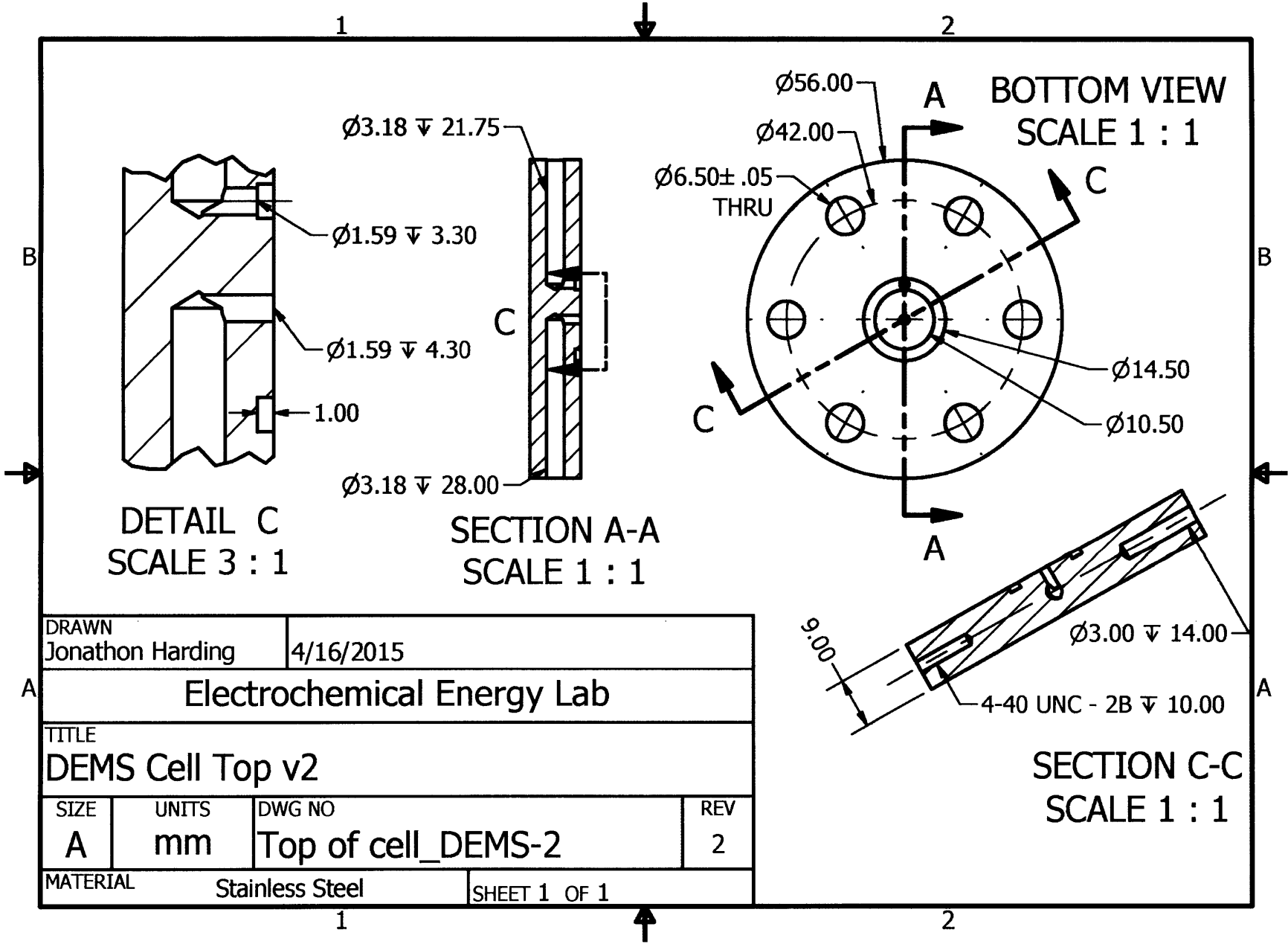
DRAWN Jonathon Harding	4/16/2015		
Electrochemical Energy Lab			
TITLE DEMS Cell Top v2			
SIZE A	UNITS mm	DWG NO Top of cell_DEMS-2	REV 2
MATERIAL	Stainless Steel	SHEET 1 OF 1	

TOP VIEW
SCALE 1 : 1

A

10-24 UNC - 2B

Ø56.00
Ø42.00

Ø28.58 [1.125 in]
Ø22.23 [.875 in]

Ø21.00

A

SECTION A-A
SCALE 1 : 1

B

4-40 UNC - 2B � 10.00

DETAIL B
SCALE 3 : 1

1.00
2.00

5.00

SIDE VIEW
SCALE 1 : 1

DRAWN Jonathon Harding	4/16/2015		
Electrochemical Energy Lab			
TITLE DEMS Cell Bottom v2			

SIZE	UNITS	DWG NO	REV
A	mm	DEMS Cell Bottom-v2	2

MATERIAL	Stainless Steel	SHEET 1 OF 1

222

TOP VIEW
SCALE 2 : 1

2.00

MODEL VIEW
SCALE 1 : 1

$\varnothing 21.00 ^{+.00}_{-.05}$

SIDE VIEW
SCALE 2 : 1

$\varnothing 18.00$

DRAWN Jonathon Harding	10/14/2014		
MIT Electrochemical Energy Lab			
TITLE DEMS Cell v2			
SIZE A	UNITS Metric	DWG NO DEMS Cell Insert-thesis	REV 2
MATERIAL		PTFE	SHEET 1 OF 1

DETAIL B
SCALE 3 : 1

SECTION A-A
SCALE 1 : 1
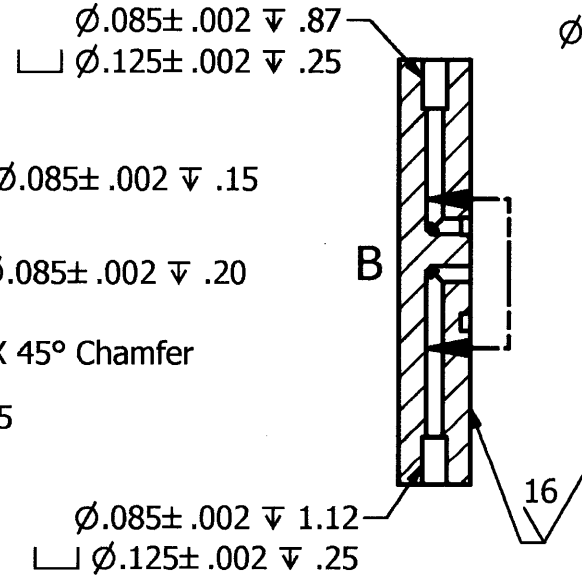
Ø2.20 [56.0 mm]

Ø1.65 [42.0 mm]

BOTTOM VIEW
SCALE 1 : 1

Ø.085±.002 ▽ .87
⊔ Ø.125±.002 ▽ .25

Ø.255±.002
THRU

A

C

Ø.085±.002 ▽ .15

B

Ø.085±.002 ▽ .20

.02 X 45° Chamfer

Ø.590

.05

C

Ø.410

Ø.085±.002 ▽ 1.12
⊔ Ø.125±.002 ▽ .25

16

A

Ø.10 ▽ .55

.375

4-40 UNC - 2B ▽ .50

SECTION C-C
SCALE 1 : 1

DRAWN Jonathon Harding	4/16/2015	
Electrochemical Energy Lab		
TITLE DEMS Cell Top v3		

SIZE A	UNITS Inch	DWG NO DEMS Cell Top-v3.1	REV 3.1
MATERIAL	Stainless Steel	SHEET 1 OF 1	
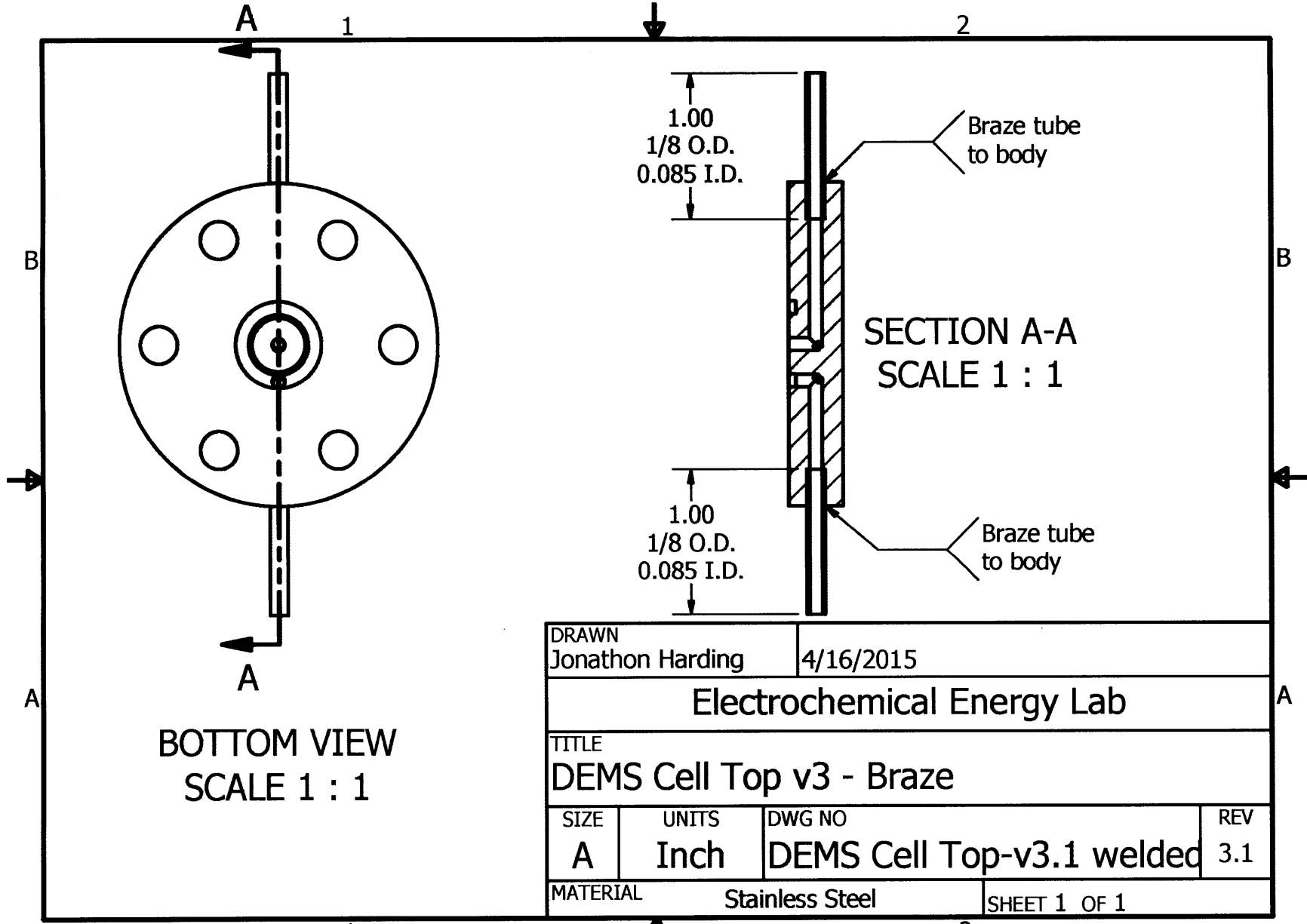
A   1   2

B   B

1.00
1/8 O.D.
0.085 I.D.

Braze tube
to body

SECTION A-A
SCALE 1 : 1

1.00
1/8 O.D.
0.085 I.D.

Braze tube
to body

A   A

BOTTOM VIEW
SCALE 1 : 1

DRAWN Jonathon Harding	4/16/2015		
Electrochemical Energy Lab			
TITLE DEMS Cell Top v3 - Braze			
SIZE A	UNITS Inch	DWG NO DEMS Cell Top-v3.1 welded	REV 3.1
MATERIAL	Stainless Steel	SHEET 1 OF 1	

1   2

A

TOP VIEW
SCALE 1 : 1

10-24 UNC - 2B

Ø56.00

Ø42.00

Ø28.88

Ø21.82

Ø21.00

Ø15.00

A

5.00

SIDE VIEW
SCALE 1 : 1

C

1.00

2.00

1.00

DETAIL B
SCALE 3 : 1

B

C

SECTION A-A
SCALE 1 : 1

4-40 UNC - 2B � 10.00

120°

120°

SECTION C-C
SCALE 1 : 1
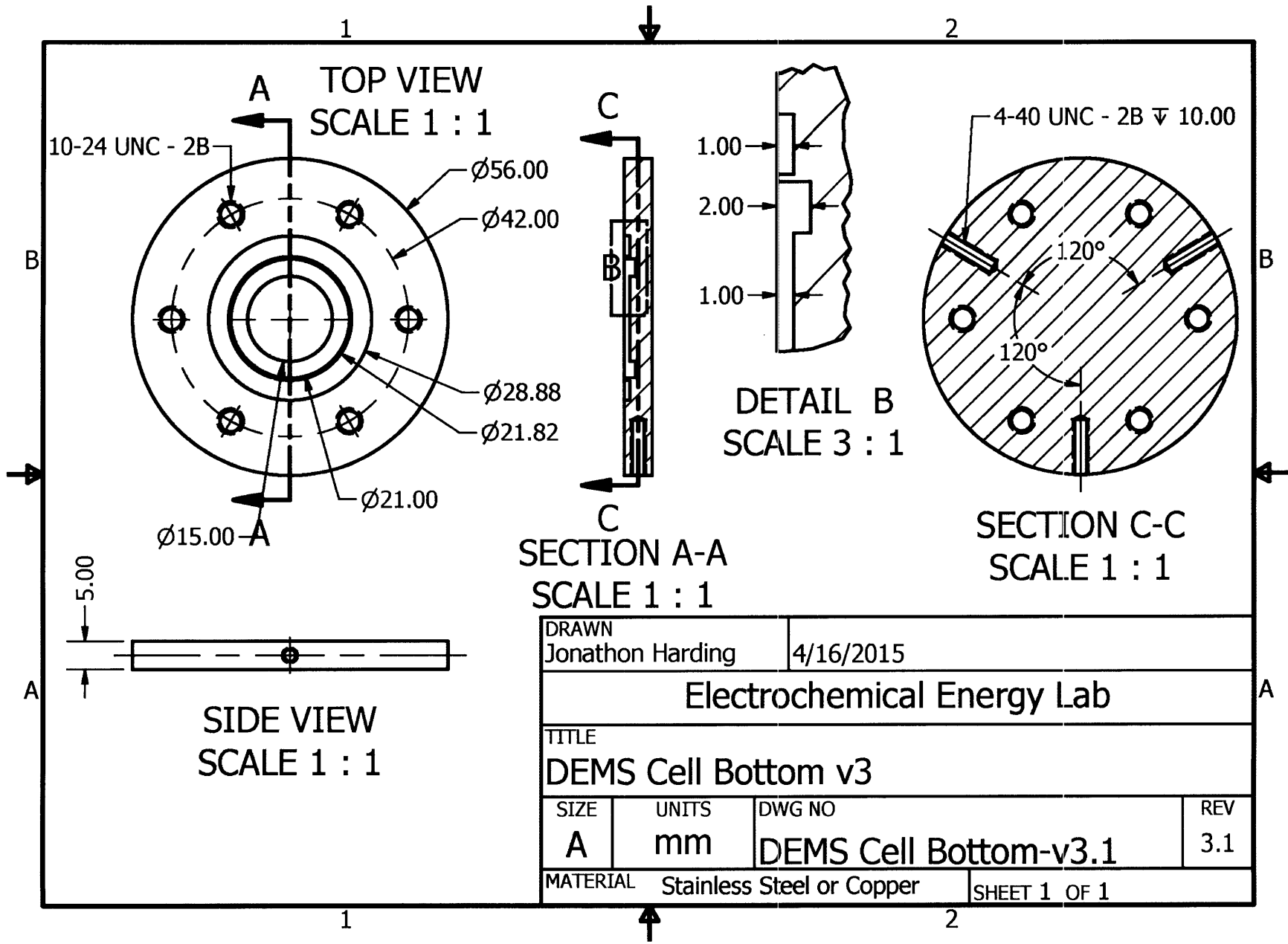
DRAWN		
Jonathon Harding	4/16/2015	
Electrochemical Energy Lab		
TITLE		
DEMS Cell Bottom v3		
SIZE	UNITS	DWG NO
A	mm	**DEMS Cell Bottom-v3.1**
MATERIAL	Stainless Steel or Copper	SHEET 1 OF 1

REV
3.1

226

Ø21.00 $^{+.00}_{-.05}$

Ø18.00

18MM ID TOP
SCALE 2 : 1

Ø21.00 $^{+.00}_{-.05}$

Ø20.00

20 MM ID TOP
SCALE 2 : 1

2.00

20 MM ID SIDE
SCALE 2 : 1

2.00

18MM ID SIDE
SCALE 2 : 1
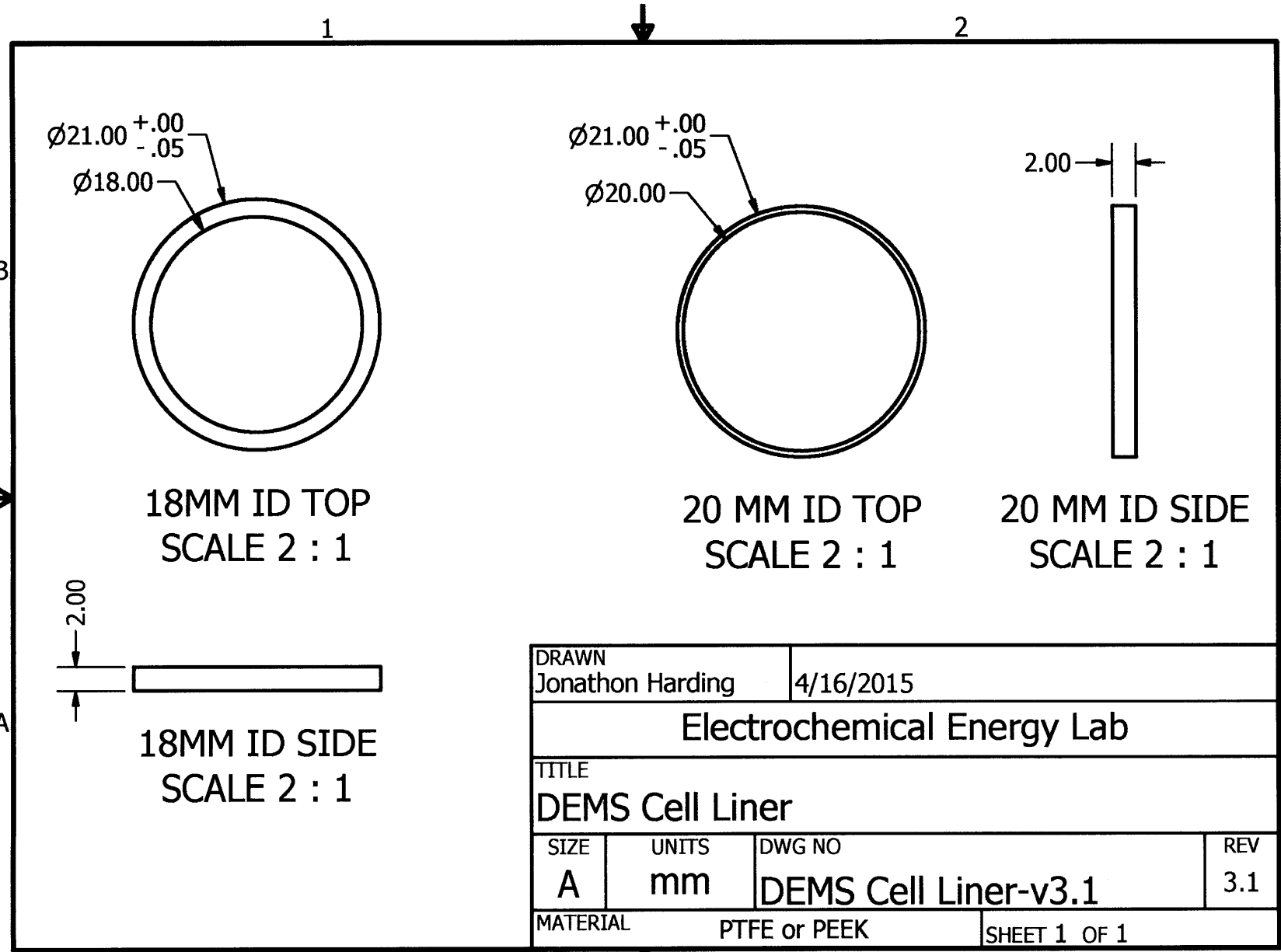
DRAWN Jonathon Harding	4/16/2015		
Electrochemical Energy Lab			
TITLE **DEMS Cell Liner**			
SIZE **A**	UNITS **mm**	DWG NO **DEMS Cell Liner-v3.1**	REV **3.1**
MATERIAL	PTFE or PEEK		SHEET 1 OF 1